Characterisation of geological storage on the UKCS from interpretation of seismic reflection data

Hector George Barnett

Doctor of Philosophy

Newcastle University
School of Natural & Environmental Science

May 2025

Abstract

This thesis investigates the impact of interpretation uncertainty on subsurface storage sites for the purposes of storing either hydrogen or carbon dioxide. 3D seismic and well data were used alongside complementary modelling methods to quantify uncertainties and sensitivities. The work investigates three themes, the interpretation of the complex internal structure of evaporites; the impact of geological uncertainties on salt cavern developments, and the variation in seismic response expected under different fluid saturations.

The internal structure of the Zechstein Supergroup shows high levels of deformation and geometries that increase in complexity basin-ward. The internal deformation was interpreted and characterised, identifying six unique deformation styles which were parametrised and mapped spatially. This has implications for storage site suitability.

Geological uncertainties were quantified for salt cavern developments, using a stochastic workflow that was developed to model potential cavern emplacement locations and hydrogen capacity. The potential hydrogen storage capacity in salt caverns in the UK sector of the Southern North Sea (80+ PWh) is far greater than any potential storage demand (100 TWh). Total energy storage demand could be met with as few as 73 caverns in an area 28 km^2.

The variation in the seismic response of siliciclastic reservoirs on the United Kingdom's continental shelf was investigated after fluid substitution of non-hydrocarbon fluids to further understand seismic monitoring approaches. The results show that typical monitoring approaches, such as 4D amplitude comparisons, may not be suitable due to the limited change in elastic properties of the reservoir rocks once substituted with the pore filling fluid.

This thesis quantifies and constrains the uncertainty of the subsurface for storage of non-hydrocarbon fluids within the UKCS for both porous media and salt caverns.

Declaration

I hereby confirm that this is my own work, except where otherwise stated, and that this thesis has not previously been submitted for the degree of Doctor of Philosophy at this, or any other University.

Signed: Hector Barnett - May 2025

'Anything that can go wrong, will go wrong'

Edward A. Murphey Jr.

Acknowledgements.

Supervisors

Mark, I do not think I can fully put communicate in words how much I appreciate your input, knowledge, and leadership over the past 4 years. From the incomprehensible (but required) amounts of red pen to the general day to day advice. You made this entire PhD possible, and perhaps might I even say enjoyable(?). For that and everything else, thank you.

Cees, I also cannot thank you enough for the expertise, support, and guidance you have provided me over the past 4 years. It has been an absolute pleasure to be your PhD student, an experience I will remember fondly.

Family

Mum, **Milo**, and **Grandma Fay**, thank you for the everlasting love, support, and patience that you have all consistently provided at every step of this journey. Special thanks to the Squires family too, and to those who are no longer with us anymore to see this accomplishment.

Spacegang

My dearest friends, **Lewis**, **Will,** and **George** (the order of names was decided by the wheel before you ask) I am deeply grateful for all the fun times we've shared. There are too many memorable moments to mention, whether it is house games, tinnies in the park, or spending that Covid Christmas together. This whole PhD would have been a much sadder affair without the friendship and questionable shenanigans you have all provided along the way.

Friends

Special thanks to the Newcastle Uni PhD trio who have helped keep me sane during the past 4 years. **Aidan** for keeping me company on the trips to Co-op and being a tactical river partner when required; **Gianluca**, for dragging me to Norway and letting me experience proper homemade Italian food; and **Andrew** for the entertainment you provide while on campus (or in the pub). A shoutout too to all those from the GNZ CDT, the evenings of field trips will be deeply missed.

Charl

You have provided nothing but kindness, support and love throughout this PhD. I will forever be grateful to you for providing me with those as they were needed to get to the end. I'm looking forward to seeing what's next for us (and Ziggy) when this is finally *finally* finished. With Love, Hector

Contents

List of Figures

List of Tables

List of Appendix

Chapter 1. Introduction

1.1 Geological storage site characterisation

Engineered storage of gasses and liquids within geological formations in the subsurface can be divided into two functional objectives: temporary used for energy storage or long-term sequestration (Krevor *et al.*, 2023; Bauer *et al.*, 2013). Storage of energy from times of excess generation for use at times of excess load allows for more efficient energy systems and better integration of renewable energy sources into the grid (Carneiro, Matos and van Gessel, 2019). Renewable energy sources, such as wind, solar, and tidal, generate energy in an intermittent and fluctuating manner that is often not matched with the energy demand of the system (Pasten and Santamarina, 2011). This intermittent and fluctuating energy supply leads to a mismatch in the supply and demand of the grid (Kueppers *et al.*, 2021). Energy storage within an energy system aids in mitigating issues relating to the fluctuating energy supply and allows for maximum efficiency and penetration of these renewable low-carbon energy sources (Evans, Strezov and Evans, 2012). When discussing the permanent sequestration of fluids in the subsurface, typically, the sole fluid being considered is carbon dioxide. Carbon sequestration enables the mitigation of carbon emissions from industries that are energy and carbon-intensive and typically seen as challenging to decarbonise (Gough and Mander, 2022).

Geological site characterisation is undertaken to mitigate risk and manage uncertainties within the subsurface (Scheidt, Li and Caers, 2018). The process of characterisation of a subsurface location, such as a geo-storage site, involves predicting the spatial variations of one or more parameters through the area of investigation. Predictions for the subsurface are derived through models, that are either conceptual, which supply qualitative predictions where a parameter can be nominal or ordinal, or numeric models which supply quantitative predictions, where a parameter is defined as any property that the subsurface exhibits that can be measured in a numeric value (Houlding, 1994; Luo, 1996). The scale and resolution of the prediction of a parameter's spatial variation is dependent on the requirement of characterisation and area in which risk is trying to be reduced (Artiola, Pepper and Brusseau, 2004).

Geoscience for site characterisation occurs at scales ranging from a nanometre to basin scale. Characterisation of the subsurface can hence encompass a range of methods at varying scales of investigation. With a broad spectrum of scales within geoscience, the acquisition and integration of data for decision making purposes can be extremely costly. Understanding the value of information within subsurface can aid in making a subsurface project viable or not, as it allows for clear objectives to be set and understood for the area to be characterised (Häggquist and Söderholm, 2015). Taking into account these factors allows for a suitable level of resolution in data acquisition, analysis to be applied, and model design (Sprecher, 1997).

Fully capturing the complexity and heterogeneity of the subsurface becomes increasingly challenging as scale decreases and resolution of data increases due to both measurement and sampling limitations (Fitch *et al.*, 2015). The nature and limitations of subsurface measurement methodologies and resources (both human time and financial) mean that in practice fully capturing all information within the subsurface is impossible and that all knowledge to an extent will be imperfect (Hetényi *et al.*, 2022). Therefore, a fundamental aspect of site characterisation is understanding what we do not know about the site, and what areas can be targeted for risk reduction and uncertainty quantification (Benson and Yuhrm, 2015).

A suitable characterisation of the subsurface allows for the prediction about how the subsurface may react when interacting with external simulation e.g. the pathways and velocity of fluid flowing through a subsurface reservoir (Houlding, 1994). The predication of parameters usually involves building models from the available data and using the built model to forward simulate and provide scientifically valid results for the input data. 'All models are wrong, but some are useful' Box (1976) is especially applicable to the geosciences, as there are often high levels of uncertainty due to data and computational limitations, robust models drive forward the understanding of the subsurface, being heavily utilised in typical subsurface operations (Holdaway and Irving, 2017). However, the models built must be of suitable standard and quality checked to ensure that they do not give erroneous results, as incorrect models will give incorrect predictions, or in other words, the quality and relevant use of any analysis, analytics or output is a direct function of the quality of the model (Kilkenny and Robinson, 2018).

1.1.1 Properties of site characterisation

This thesis focuses on the site scale characterisation for subsurface storage. The characterisation involved covers scales from ≈ 15 cm to ≈ 100's km. For perspective, this scale encompasses the range from individual beds to basin scale features, or from a data perspective, well logs to merged 3D seismic surveys.

1.1.1.1 Solid Geological Framework

In terms of characterisation, the properties of rocks in the subsurface are both pseudo-continuous and discrete in terms of their spatial variability (Houlding, 1994). The classification of a rock mass is dependent on the scale at which it is viewed (Bokulich, 2021). What appears to be a homogenous section of sandstone at core scale (< 1 m), can appear a heterogenous formation with baffles that impede fluid flow at outcrop scale (< 50 m) (Fitch *et al.*, 2015). An effective site characterisation should aim to comprehensively quantify all uncertainties and then evaluate all risks relevant to the site's intended purpose to allow for informed decisions to be made (Sollie *et al.*, 2011).

Depending on the purpose of the area being characterised, risks will be present that are aimed to be reduced (where possible), and hence different properties within the rocks will need to be quantified (Sprecher, 1997). Understanding the 3D heterogeneity together with associated uncertainties of these properties will allow for more reliable models to be developed helping reduce risk (Schweizer, Blum and Butscher, 2017).

The 3D variability of rock properties is a function of many different factors, including but not limited to the lithology, depositional setting, burial history, and diagenetic history. Although these factors individually affect the properties of a rock, they are also influenced by larger scale phenomena, such as tectonics, sea level, and climate (Boggs, 2011). A robust understanding of a subsurface site will incorporate information from the larger scales of geoscience that have influenced the rocks being investigated, as it allows for a more comprehensive understanding of the processes occurring at smaller scales.

Dependent on the approach taken, rock properties being characterised within a model may be set as either deterministic or stochastic values. A stochastic model will supply the resultant predictions probabilistically. A model producing results from a stochastic approach allows for

the quantification of the uncertainty with the associated parameter and how it interacts within the whole subsurface system (Li *et al.*, 2016).

1.1.1.2 Fluid properties

Similar to rocks, the properties of fluid within the subsurface vary spatially (Phillips, 2009). Fluid properties require characterising as they include various attributes which can modify fluid behaviour such as physical properties, migration characteristics, and phase conditions. Fluids that are contained within a rock's pore space will modify the bulk properties of the host rock they are contained within, so further understanding of the subsurface fluid can aid with understanding the rocks (Isah *et al.*, 2022). The properties of a fluid within the subsurface can be modified by several factors. Pressure-temperature conditions of the host rock can modify the state of the fluid (Danesh, 1998). Fluid rock interactions at the rock-fluid interface can influence a fluid's mobility, either attracting or repulsing it (Anderson, 1987). Fluid mixing, where the properties of the fluid mixture will need to be calculated to account for the different properties of each fluid present (Smalley *et al.*, 2004). Characterising these factors which can modify subsurface fluids will provide a better understanding to the overall properties of fluids in situ (Smalley *et al.*, 2004).

1.2 Energy Storage and carbon sequestration

Natural gas and oil have historically been the medium for subsurface energy storage, with the first subsurface storage facility storing natural gas initiating operations in Ontario, in 1915 (Muhammed *et al.*, 2022). However, more recently, hydrogen has been considered as an energy vector for subsurface energy storage. Hydrogen provides a versatile energy storage medium as it can be produced through electrolysis using excess renewable energy or from natural gas using methane (Muhammed *et al.*, 2022; Yu, Wang and Vredenburg, 2021). Compared with other energy mediums, such as natural gas, the relative energy density of hydrogen is low at atmospheric conditions (20 °C, 1 atm) at 10 MJ/m^3 compared with methane under the same conditions at 33 MJ/m^3 (NIST Chemistry WebBook, 1997).

For the sequestration of carbon dioxide within a geological formation, the permanent trapping of the carbon dioxide within the reservoir formation is required (Gunter, Bachu and Benson, 2004). Trapping of the carbon dioxide allows for permanent sequestration and mitigates the likelihood of subsurface migration. In most scenarios, carbon dioxide is injected

into the target geological reservoir as a supercritical fluid, as it is most dense within this phase (Massarweh and Abushaikha, 2024). Initially, structural and stratigraphic trapping mechanisms trap most of the carbon dioxide within the reservoir. Over time, it dissolves into the pore-fluid brine (solubility trapping) and finally precipitates out as a carbonate mineral (mineral trapping), however this mineral trapping phase can depend upon the rock type, temperature, fluid composition and injected carbon dioxide phase (Snæbjörnsdóttir *et al.*, 2020; Kim *et al.*, 2023; Massarweh and Abushaikha, 2024) (Figure 1-2). Each phase transition increases storage security as the mobility of the injected carbon dioxide is reduced (Massarweh and Abushaikha, 2024). Reaching the mineral trapping phase, where the carbon dioxide precipitates out of solution as calcite, can take 100s – 1000s of years, and as such sites will require constant monitoring to reduce the risk of surface leakage or leakage into other undesirable locations (Snæbjörnsdóttir *et al.*, 2020).

There are two types of storage containers I investigate within the subsurface within this thesis: porous media storage and salt cavern storage (Figure 1-3, 1-4).

1.2.1 Porous Media

Storage in porous media relies upon storing the fluid within the pore space of the host rock (Heinemann *et al.*, 2021; Bachu, 2008; Bachu, 2000). Oil and gas fields are natural examples of subsurface porous media storage as they have been proven storage containers for geological periods of time (Heinemann *et al.*, 2021). Safe and reliable storage within porous media requires a suitable geological storage complex, which includes a permeable and porous reservoir, a sealing lithology, a structural, stratigraphic, or hydrodynamic trapping mechanism, and no migration pathways or discontinuities (Nediljka and Karolina Novak, 2019).

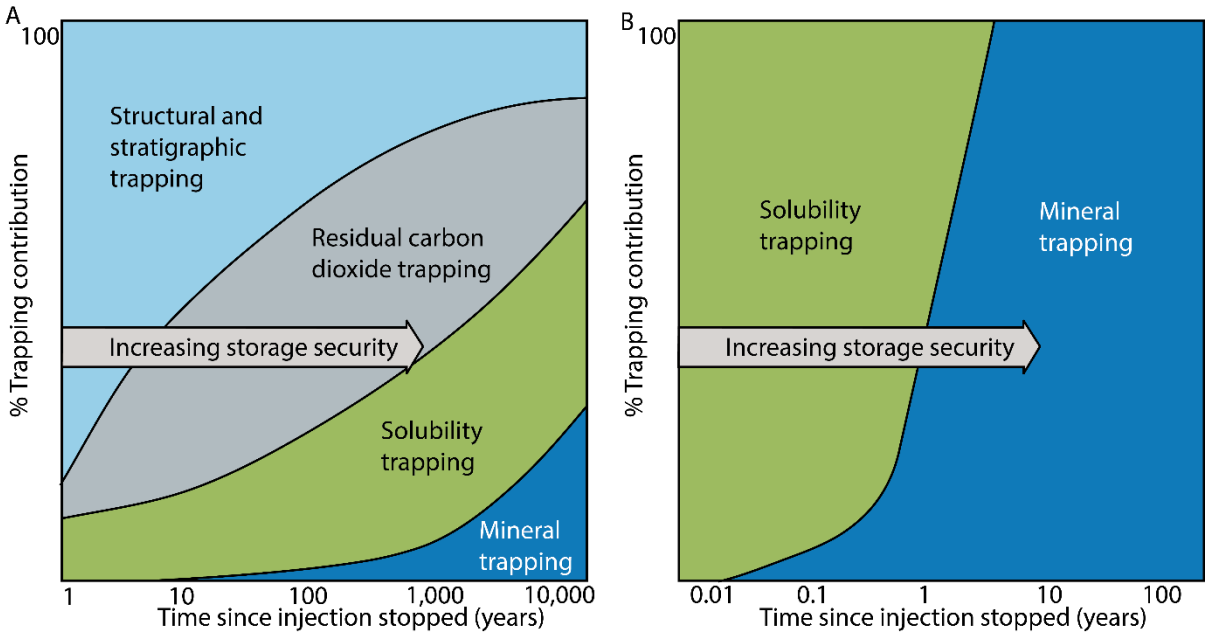

FIGURE 1-1 CARBON DIOXIDE TRAPPING MECHANISMS WITHIN POROUS MEDIA. TIMESCALE FOR MECHANISM TO TAKE EFFECT ARE LISTED ALONG WITH THE INCREASED LEVEL OF SECURITY AGAINST CARBON MIGRATION THAT THEY PROVIDE. AFTER (SNÆBJÖRNSDÓTTIR ET AL., 2020)

Sandstone is the typical chosen lithology for porous media storage, as it has favourable porosity and permeability properties. Typical reservoir parameters that must be met include high porosities, normally those greater than 20 %, permeability >300 mD, a suitable trap and seal mechanism, away from any subsurface discontinuities such as faults which may act as fluid migration pathways (Payton Ryan *et al.*, 2021; Bachu *et al.*, 2010).

For a working subsurface storage system in porous media, a sealing lithology directly above the planned reservoir zone is required. Seal integrity should be sufficient to withstand the buoyant forces exerted by the injected fluid column, preventing capillary forces from causing migration (Kaldi *et al.*, 2013). Lateral extent should cover the zone of injection to avoid migration around the sealing lithology (Kaldi *et al.*, 2013). Typical seal lithologies for planned subsurface storage containers are evaporites or homogenous mudstones.

The target trap must avoid fluid migrating laterally around it, so anticlinal or tilted fault block traps are those favoured (Muhammed *et al.*, 2022). Trap configurations targeted will depend on storage type; for energy storage, migration away from the well injection site is unwanted, so antiformal traps are the best use, for long-term sequestration sites, a combination of migration away from the well injection site is desired (Muhammed *et al.*, 2022). The

deformation caused by salt structures often causes advantageous trapping geometries within nearby reservoirs, and as such are often initial targets (Jackson and Hudec, 2017). Simple trap and seal configurations are desired to reduce unnecessary complications and risk.

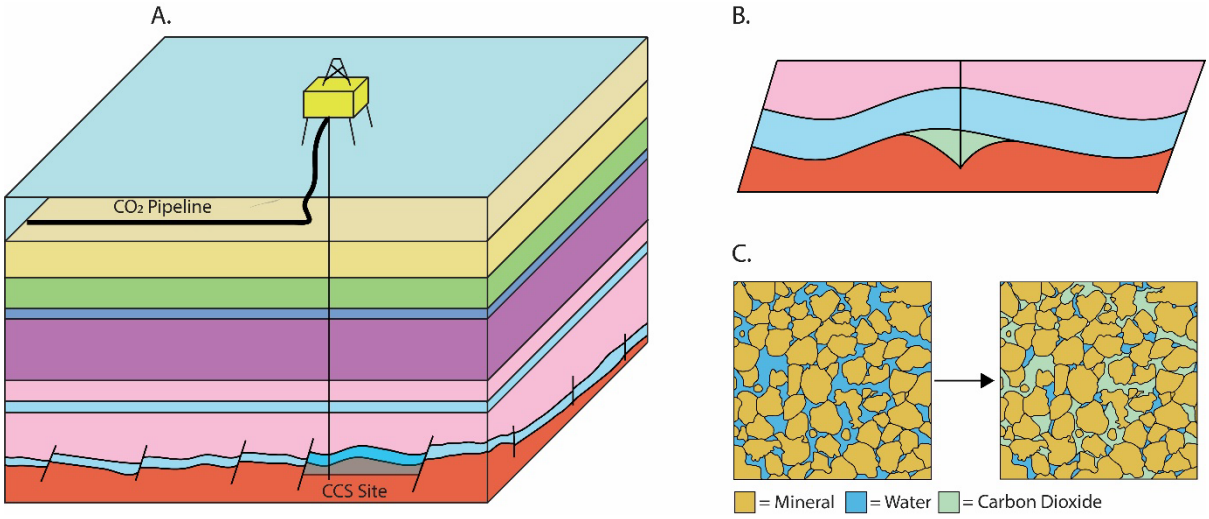

FIGURE 1-2 A) POROUS MEDIA STORAGE EXAMPLE WITH CARBON DIOXIDE AS STORE FLUID. B) SCHEMATIC 2D TRAP AND SEAL CONFIGURATION WITH CARBON DIOXIDE PLUME PRESENT. C) PORE SCALE INTERACTIONS OF POROUS MEDIA STORAGE, WITH CARBON DIOXIDE DISPLACING THE CURRENT PORE FLUID (WATER)

1.2.2 Salt caverns

A salt cavern is a large, engineered void within a geological salt layer (Figure 1-4). Salt caverns are developed via solution mining, a process where water is pumped down a borehole to dissolve the salt, and the resultant brine is pumped up and disposed of (Caglayan *et al.*, 2020; Ozarslan, 2012). They have been in use since the 1950s for storing natural gas, oil, or hydrogen (Tarkowski and Czapowski, 2018; Warren, 2016). Salt caverns are often developed in clusters, with several caverns solution mined at the same site (Warren, 2016). Cavern volumes can vary in size depending on the requirement and availability of salt; typical volume ranges for individual caverns are around 100,000 m^3; however, they can range from 10,000 m^3 to 17,000,000 m^3 (Warren, 2016; Horváth and Schneider, 2018).

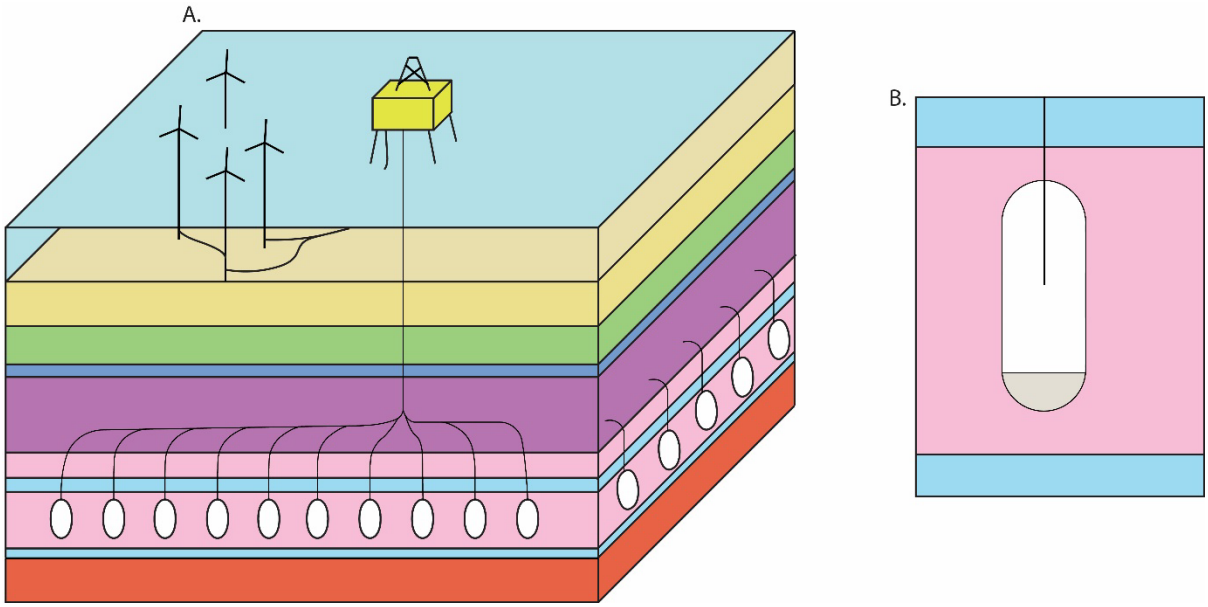

FIGURE 1-3 A) 3D SCHEMATIC DIAGRAM OF SALT CAVERN STORAGE COMPLEX WITH THE SURROUNDING GEOLOGY AND INFRASTRUCTURE. B) 2D SALT CAVERN SCHEMATIC SHOWING CAVERN (WHITE), SUMP FILLED WITH INSOLUBLES (BROWN) AND SALT IT HAS BEEN DEVELOPED WITHIN (PINK)

Certain site characteristics need to be met for a unit of salt to be suitable for cavern emplacement. The geometry of the salt needs to be thicker than 200 m to allow for an adequately sized cavern for storage (Caglayan *et al.*, 2020; Smith, Evans and Andrews, 2005). The depth of emplacement must be between 500 m and 2000 m deep, the upper depth requirement ensures the cavern can operate at suitable pressure levels, while the lower depth requirement limit avoids salt becoming too mobile and causing the cavern to lose volume (Caglayan *et al.*, 2020; Lux, 2009). Salt structures such as diapirs and walls can provide ideal geometrical parameters for salt cavern emplacement as they have mobilised to a shallow depth below the surface and are often very thick (Tarkowski and Czapowski, 2018).

Halite is the principal evaporite lithology targeted for salt cavern emplacement. It is chosen due to its solubility and the sheer quantity of halite often associated with evaporite deposits (Warren, 2016; Jackson and Hudec, 2017). The most homogenous intervals of halite are targeted, as vertical lithological heterogeneity within evaporite units has implications for cavern emplacement (Warren, 2016). An over soluble lithological layer (a layer which is more soluble in respect to halite), such as carnallite, will cause dissolution to occur in excess, leading

to cavern-side instability and possible cavern collapse. Whereas and an under-soluble layer will lead to limited dissolution with respect to the surrounding halite, causing overhangs in the cavern wall, loss of cavern volume and possible cavern collapse (Lux, 2009). If a porous and permeable layer is present in the target salt formation, such as a carbonate, it may act as either a leakage pathway for the stored substance to escape or a pathway for contaminants to enter the stored substance. Any insoluble content present during the dissolution mining process will be left in the sump of the cavern, limiting storage volume (Caglayan *et al.*, 2020; Williams *et al.*, 2022).

1.3 Reproducibility, replicability and reliability

Reproducibility, replicability, and reliability are seen as problems within the geosciences, as research often fails to provide sufficient repositories of the data, accessible ways to the data, or crucial methodology items (such as code) (Ireland *et al.*, 2023; Steventon *et al.*, 2022). The meaning and application of reproducibility, replicability and reliability are also often confused with one another. As such definitions are given by The Turing Way (2022) as follows: Reproducibility: the same analysis performed on the same dataset consistently produces the same answer; Replicability: the same analysis is performed on different datasets produces qualitatively similar answers; and Reliability: the same dataset is subjected to different analysis workflows (to answer the same research question) and a qualitatively similar or identical answer is produced. The ability to describe methodologies and work undertaken such that they are reproducible, replicable, and reliable allows for others to re-create, scrutinize or build upon it (Nüst and Pebesma, 2020), providing more robust scientific outputs.

This thesis has aimed to align with the ideals of open science, so all research produced is reproducible, replicable, and reliable. As such, all data, code and other material produced are available within the supplied data repositories. All publications originating from the research within this thesis have been or will be published as open-access articles.

1.4 Study Area

The areas researched in this thesis are located within the United Kingdom's Continental Shelf (UKCS). The UKCS is defined as the area inside and extending beyond the United Kingdom's territorial waters, where the United Kingdom possesses the mineral rights (*The Continental Shelf (Designation of Areas) Order*, 2013). The UKCS is split into subsections, these subsections

are in part informed by the regional geology of the major geological basins, but also the administrative and licensing needs of the local authority. These subsections include the Northern North Sea, Central North Sea and the Southern North Sea. This research investigated two separate basins;

1.4.1 South Permian Basin

The South Permian Basin is an east-west trending basin located within the Southern North Sea, reaching from the east coast of the United Kingdom over to eastern Poland (Ziegler, 1990) (Figure 1-4). The South Permian Basin developed over a period of 380 million years, consisting of a complex geological history with several rift and post-rift phases (Ziegler, 1990; Glennie, Higham and Stemmerik, 2003). Extension initiated with the collapse of the Late Devonian Variscan orogenic belt (Schulmann *et al.*, 2014; Pharaoh *et al.*, 2010) and subsequent Late Carboniferous inversion (Hodgson, Farnsworth and Fraser, 1992; Ziegler, 1990). Subsidence then initiated during the early Permian, with large levels of sediments >2700 m accumulating within the basin depocenter. Following Permian subsidence Late Triassic and Early Jurassic crustal extension began, after this short-lived period of subsidence, a period of domal uplift occurred in the Middle Jurassic, leading to widespread erosion (Cameron, 1992). The thermal doming was superseded by a period of renewed rifting and rapid subsidence in the Late Jurassic, this subsidence had slowed by the Early Cretaceous to allow marine sedimentation to occur across the majority of the Southern Permian Basin(Cameron, 1992; Ziegler, 1992a). When rifting ceased in the Middle Cretaceous, the basin experienced a short-term period of thermal subsidence, which lasted until the Late Cretaceous (Pharaoh *et al.*, 2010). This was followed by a period of tectonic inversion, which was initiated in the Campanian and continued to the Early Cenozoic (Erratt, Thomas and Wall, 1999). As inversion ended, it was replaced by thermal subsidence once again; as the Cenozoic sediments began to be deposited into the North Sea thermal Sag basin, leading to up to 3 km of Cenozoic sedimentation in areas (Ziegler, 1990; Wong *et al.*, 2007).

1.4.2 The East Irish Basin

The East Irish Sea Basin is located within the East Irish Sea, off the west coast of England and North of Wales (Figure 1-4). It is one of the largest and deepest basins in western Britain and contains numerous sub-basins (Knipe, Cowan and Balendran, 1993; Williams *et al.*, 2018). The East Irish Sea Basin current structural setting originates from E – W to NW – SE extensional

tectonics associated with Permian and Triassic rifting events, which resulted in a series of N-S trending structural highs and grabens (Williams *et al.*, 2018; Jackson *et al.*, 1995; Knipe, Cowan and Balendran, 1993). Minor extensional phases continued into the Jurassic, causing small depositions of sediment to accumulate (Williams *et al.*, 2018). By the cretaceous extensional tectonics had stopped, and post-extensional regional subsidence initiated (Chadwick, Kirby and Baily, 1994). Inversion initiated during Paleocene, causing widespread erosion of much of the basin sediments, leaving only Permo-Trassic stratigraphy (Knipe, Cowan and Balendran, 1993).

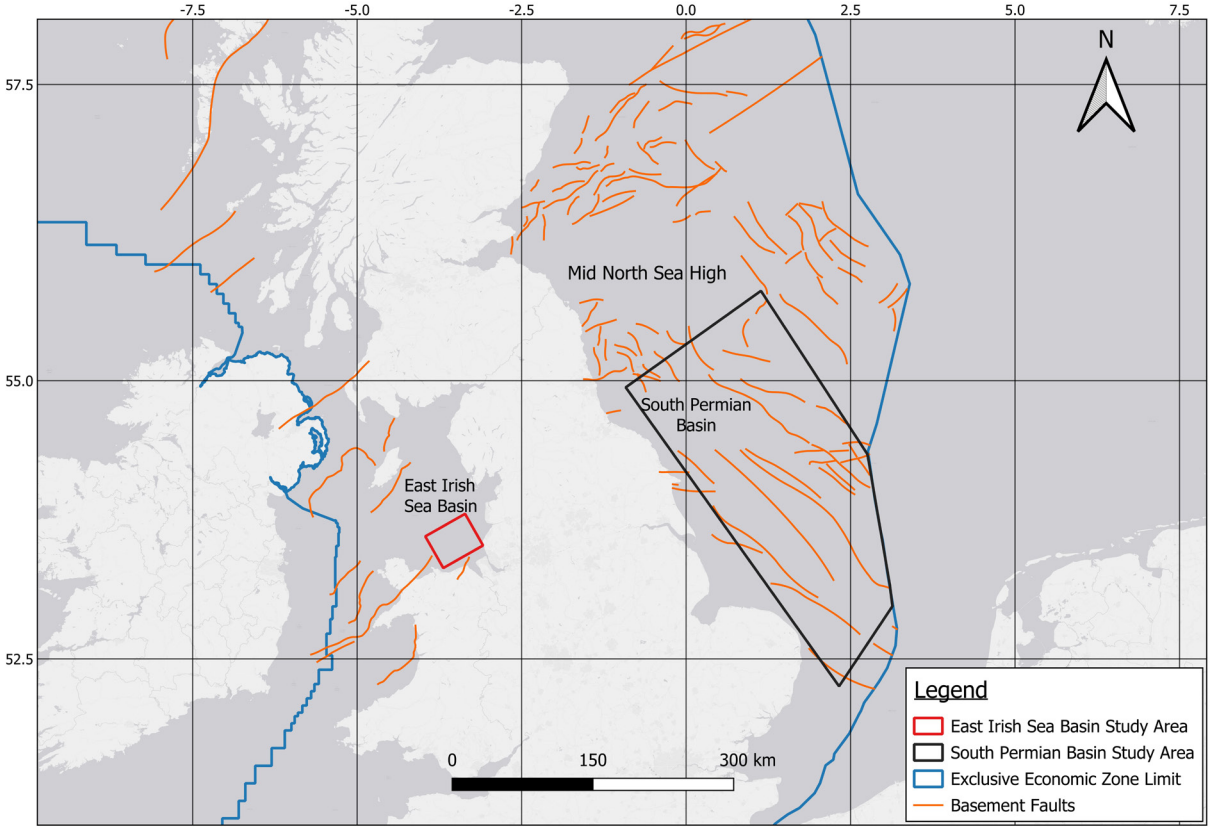

FIGURE 1-4 MAP OF STUDY AREAS WITHIN THIS THESIS. MAP DETAILS THE EXTENT OF THE UNITED KINGDOM'S EXCLUSIVE ECONOMIC ZONE AND THE MAIN BASEMENT BOUNDING FAULTS.

1.5 Thesis Aims and Outline

This research examines aspects of site characterisation for geological storage of fluids in both porous media and salt caverns. This research investigates, using seismic data, the geological interpretation of potential storage sites, associated uncertainties and sensitivities required to better characterise subsurface sites. It also further explores investigations and development of workflows and methodologies to improve the use of data in such investigations.

The aims and objectives of this thesis are as follows:

Chapter 3's aims are to investigate, characterise and map the three-dimensional internal structural deformation of the Zechstein supergroup throughout the UK sector of the Southern North Sea. Provide further understanding as to the controlling mechanisms of the lateral and vertical deformation geometries observed.

Objectives

- Identify Zechstein lithologies and cycles within well data and constrain against 3D seismic reflection data.
- Interpret the 3D geometry of the Zechstein and internal marker reflections of the Z2 and Z3 cycles within the study area using 3D seismic data.
- Characterise, map and define the different intra-Zechstein deformation styles throughout the study area.
- Compare findings with known models of intra-salt deformation.

Chapter 4's aims are to capture and quantify the geological uncertainties and sensitivities of potential salt cavern sites for the purpose of hydrogen storage in the offshore of the Southern North Sea. Additionally, it investigates the potential of different salt cavern cluster site configurations and locations in relation to the United Kingdom's energy requirements.

Objectives

- Develop a stochastic workflow that calculates salt cavern placement and volumetric values, allowing for input variables to be discrete or distributions depending on data available.

- Create geological models of varying resolutions and spatial extent to test how these factors modify the developed workflows output.
- Undertake a sensitivity analysis per site investigated to determine what geological parameters require further uncertainty quantification.

Chapter 5's aims are to quantitatively define the seismic responses of siliciclastic reservoirs from important stratigraphic intervals on the UKCS for differing non-hydrocarbon fluids and fluid fill percentages. Ascertain as to if the change in elastic properties from the change in fluid is enough to generate a detectable change in seismic response.

Objectives

- Model elastic properties of chosen reservoirs within the UKCS with data from wells.
- Forward model the change in elastic properties of reservoirs rocks having undergone fluid substitution to non-hydrocarbon fluids.
- Utilise quantitative seismic analysis methods (such as timeshift or amplitude analysis) on the modelled elastic properties to identify change in responses.

1.6 Publications

Below is a list of the publications generated from this research:

Chapter 3 has been published as 'Characterising the internal structural complexity of the Southern North Sea Zechstein Supergroup Evaporites' in *Basin Analysis (doi.org/10.1111/bre.12768).* Over 90% of the final chapter is my own work, with the remaining 10% from other authors. The contributions to the chapter are as follows; Barnett (conceptualization, data curation, formal analysis, investigation methodology, project administration, visualisation, writing – original draft, writing – review and editing), Ireland (conceptualization, funding acquisition, supervision, writing – review and editing), Van der Land (supervision, writing – review and editing).

Chapter 4 has been published in the journal *ES3* and is titled as 'Capturing geological uncertainty in salt cavern developments for hydrogen storage' *(https://doi.org/10.3389/esss.2024.10125).* Over 90% of the final chapter is my own work,

with the remaining 10% from other authors. The contributions to the chapter are as follows; Barnett (conceptualization, data curation, formal analysis, investigation methodology, project administration, software, visualisation, writing – original draft, writing – review and editing), Ireland (funding acquisition, supervision, writing – review and editing), Van der Land (supervision, writing – review and editing).

Chapter 5 has been submitted as an article for peer review within the Journal Geoenergy, and is currently available as a preprint on EarthArXiv as 'Low computational cost stochastic Gassmann fluid substitution modelling of hydrogen and carbon dioxide in clastic storage reservoirs' (*https://doi.org/10.31223/X5QB0C*). Over 90% of the final chapter is my own work, with the remaining 10% from other authors. The contributions to the chapter are as follows; Barnett (conceptualization, data curation, formal analysis, investigation methodology, project administration, software, visualisation, writing – original draft, writing – review and editing), Ireland (funding acquisition, supervision, writing – review and editing), Dunham (writing), Van der Land (supervision).

Chapter 2. Data and Methodology

The Southern North Sea of the United Kingdom is one of the most data-dense sedimentary basins in the world, due to over 60 years of hydrocarbon exploration (Rouillard *et al.*, 2020). As well as the study area being incredibly data-rich, the data is readily available and can be accessed without restriction. This PhD project was possible in part due to the North Sea Transition Authority (NSTA) and the National Data Repository (NDR), a resource which allowed access to all required subsurface data within the UKCS.

2.1 Data types

3D reflection seismic surveys and petrophysical well log data are the two most utilised data types in this scientific research. The following sections cover the background principles regarding the acquisition and science of these data types.

2.1.1 Seismic Data

Seismic data provides the ability to image and quantitatively analyse both structural and stratigraphic features within the subsurface and the elastic properties of the constituent geology (Bacon, Simm and Redshaw, 2003). The ability to map basin architectures in areas with no surface expression or inaccessible features, such as deep marine settings, reduces subsurface uncertainty and improves geological understanding in remote areas (Kearey, Hill and Brooks, 2013). The reflection seismic method of seismic image acquisition originates within the oil and gas industry, where it was developed and continues to aid in hydrocarbon exploration and production. However, more recently, seismic data has been utilised for renewable projects, such as carbon capture and storage, nuclear waste curtailment, and energy storage (Han, Cader and Brownless, 2021).

2.1.1.1 Seismic Acquisition

Seismic acquisition relies upon measuring the time taken for a seismic wave from a known source point to reflect from a geological interface and return to a known receiver point (Bacon, Simm and Redshaw, 2003). The most basic form of a recordable reflection seismic response is from a single source to a single receiver in the same position. The result of capturing this reflected seismic wave from this configuration would be a vertical 1D reflection profile (strength and time taken of the reflections) of the subsurface at that exact point, and

this is referred to as a seismic trace (Bacon, Simm and Redshaw, 2003). For a seismic reflection to be recorded three criteria need to be met: 1) There needs to be a source of the initial seismic wave (Figure 2-1), 2) There needs to be a geological boundary with an acoustic impedance contrast and hence a reflection coefficient, so that the seismic wave is reflected towards the surface (Figure 2-1,2-2). The acoustic impedance is given by:

$$Ai = \rho_{bulk} * v_p \qquad \textit{EQUATION 1}$$

where ρ_{bulk} is the bulk density of the rock the seismic wave is propagating through, and V_p is the velocity of the compressional wave. The reflection coefficient is given as:

$$Rc = \frac{Ai_2 - Ai_1}{Ai_2 + Ai_1} \qquad \textit{EQUATION 2}$$

where Ai_2 represents the geological layer below Ai_1, and 3) There needs to be a recording device for the reflected seismic wave (Bacon, Simm and Redshaw, 2003).

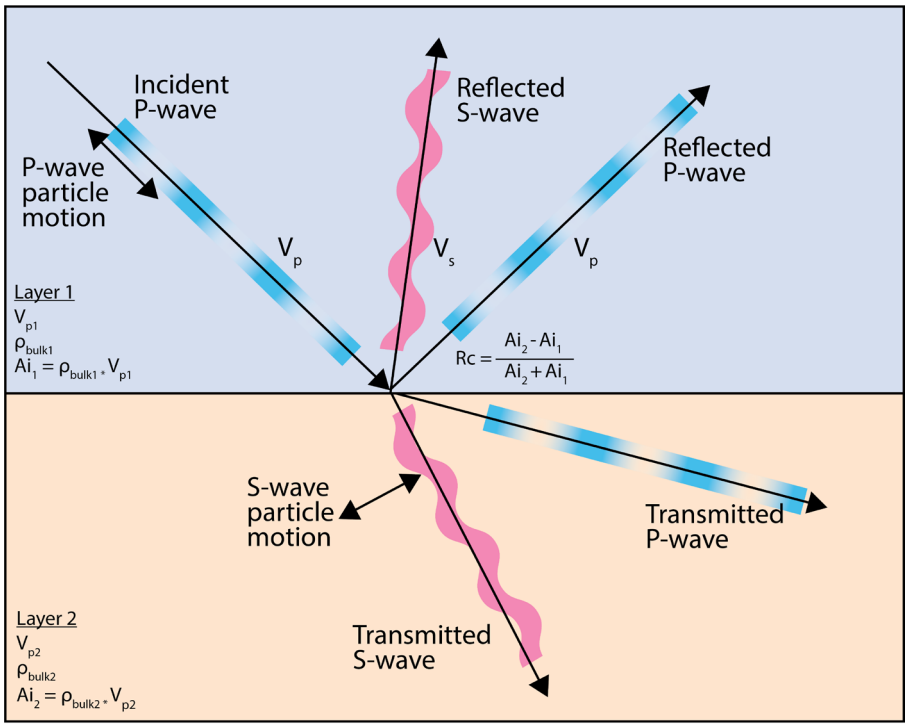

FIGURE 2-1 REFLECTED AND TRANSMITTED COMPONENTS OF PRIMARY (P) AND SECONDARY (S) WAVES WHEN REACHING A GEOLOGICAL BOUNDARY MARKING DIFFERING ACOUSTIC IMPEDANCES IN STRATA OR ROCKS. P-WAVE AND S-WAVE INTERACTIONS ARE SHOWN (BARKVED ET AL., 2004).

While a single seismic trace is helpful for a 1D view of the subsurface, the full potential of seismic imagining of the subsurface begins when single seismic traces are used in conjunction with other seismic traces. A 2D seismic line involves the recording of a seismic reflection by several receivers placed in a straight line. Using a single source and multiple receivers in a line results in a two dimensional seismic section for each line taken, with the resultant's reflection amplitude having two joint parameters, distance Y, and depth Z (Alsadi, 2017) (Figure 2-3). 2D seismic data gained prominence in the 1930s, with digital recording and processing occurring in the 1960s (Davies *et al.*, 2004a). 2D seismic surveys are typically acquired in grid formations, allowing for a coarse 3D representation of the subsurface (Alsadi, 2017). In 1967, Exxon took this step further, producing the first 3D seismic survey, however the first commercial 3D seismic survey was shot in 1975 with prominence rising to mainstream commercial usage in the late 1980's and 1990's (Davies *et al.*, 2004b; Dragoset, 2005). In a typical 2D acquisition, the 3D wavefield created by the source is recorded by a two-dimensional array of receivers. The 2D array manages to only capture a small portion of the 3D wavefront, leaving large quantities of information about the subsurface unrecorded. 3D seismic acquisition captures the full 3D wavefield seismic reflection using a three-dimensional grid of receivers (Alsadi, 2017). The benefit of 3D data over 2D is the ability to cut, splice or extract valid data from any orientation or plane within the seismic cube. While it is possible to have 2D grids of sufficient close enough spacing to mimic these properties, spatial aliasing problems (such as low frequency features appearing to be higher frequency), features dip being incorrect, features missed between grid lines) will still be encountered (Davies *et al.*, 2004a; Lonergan and White, 1999).

This thesis specifically uses marine 3D seismic data. Marine-based seismic uses P-wave reflection over S-wave reflection, as P-waves can propagate through liquids (such as water), unlike S-waves (Kearey, Hill and Brooks, 2013). In marine settings, a seismic vessel is used for acquisition. These vessels tow several cables with a seismic source (typically airguns) and a large array of receivers for the reflected seismic wave (Figure 2-2). The configuration of seismic sources and receivers will change dependent on the requirements of the survey being taken. As the recording of marine seismic data typically involves several sources and many

times this number as receivers (Figure 2-2), the raw recorded data is noisy, in the incorrect position and challenging to interpret (Bacon, Simm and Redshaw, 2003).

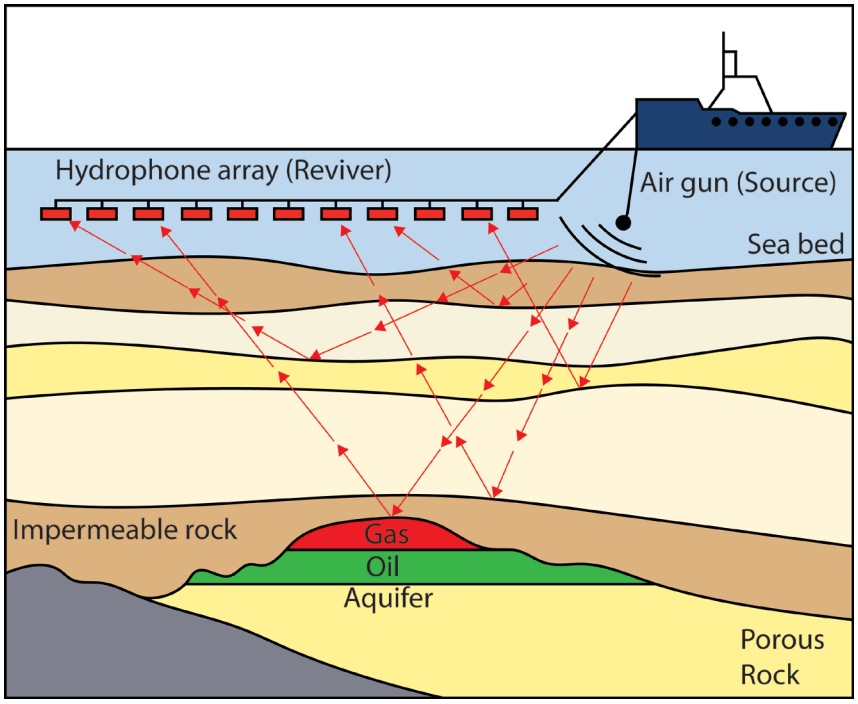

FIGURE 2-2 SCHEMATIC OF MARINE SEISMIC ACQUISITION. THE BOAT IS LOCATED IN A MARINE SETTING WITH BOTH SEISMIC SOURCES AND RECEIVERS TOWED BEHIND. THE AIRGUN EMITS A SEISMIC SIGNAL (COMPRESSIONAL WAVE) THAT PROPAGATES THROUGH THE WATER AND IS REFLECTED AT A GEOLOGICAL BOUNDARY. THIS REFLECTION PROPAGATES TOWARDS THE HYDROPHONE ARRAY, WHERE A RECEIVER RECORDS IT. AFTER SARAIVA ET AL. (2021)

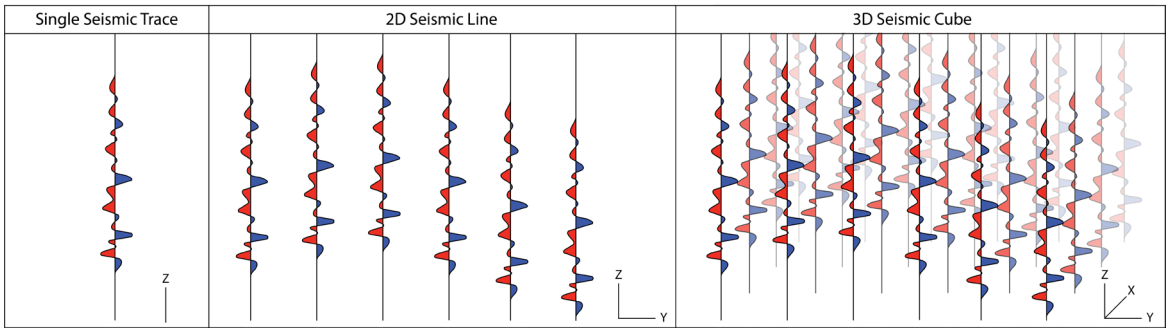

FIGURE 2-3 EXAMPLE OF CONSTITUENT TRACES IN SEISMIC DATA; 1D SEISMIC TRACE, 2D SEISMIC LINE AND A 3D SEISMIC CUBE. 3D SEISMIC DATA PROVIDES A MORE COMPREHENSIVE COVERAGE OF THE LATERAL EXTENT OF FEATURES WITHIN THE SUBSURFACE COMPARED WITH 1D OR 2D SEISMIC.

2.1.1.2 Processing of seismic data

The recorded data must be processed to account for the inherent acquisition characteristics processed by the raw seismic data. Seismic data processing can involve many steps before reaching the final processed seismic product (Bacon, Simm and Redshaw, 2003; Kearey, Hill and Brooks, 2013).

The following are key steps in the processing of seismic data;

- Binning: Data binning is the process of assigning every trace a mid-point location between the source and receiver. These traces are then assigned a common mid-point (CMP) at the centre of the bin. Ideally, all recordings taken would have CMPs at the centre of these bins, however, due to real-world conditions, this does not occur. A process known as flexi-binning can also be used, which modifies the bins, accounting for the real-world positions (Bacon, Simm and Redshaw, 2003; Sheriff, 2002).

- Stacking: Stacking is the process of combining multiple traces with different offsets that have the same CMP within the subsurface. Stacking seismic traces with the same CMP aims to reduce the signal-to-noise ratio and improve the end seismic survey product. The number of traces which have been added together to create a stack is called the fold (Bacon, Simm and Redshaw, 2003; Sheriff, 2002).

- Migration: Seismic migration is the repositioning of seismic data to its true location. During a seismic survey, after a source is shot, the respondent seismic waves are recorded by the receivers. Reflection data from a specific point within the subsurface may be recorded by coincident receivers. As waves reflected from a point in the subsurface can follow many ray pathways, the data recorded by coincident receivers may appear to be located incorrectly. Migration adjusts or 'migrates' the data to beneath the correct receiver location, thus providing a clearer image of the true geometries within the subsurface (Bacon, Simm and Redshaw, 2003; Sheriff, 2002).

When new seismic data acquisitions overlap with legacy seismic data or multiple legacy seismic datasets cover overlapping areas, the datasets can be merged, through a process known as survey merging. The merging process allows for more comprehensive seismic

coverage of the area of investigation, facilitating better interpretations and understanding (Zhou, Sun and Xuening, 2014). The following are important processing steps typically used in seismic merging processing.

- Re-binning: A master grid of bins is created that covers all seismic data sets to be merged. The original datasets are then converted or re-binned into the new master grid so that the traces are now equally spaced within the master grid. Where original bin sizes are greater than the new master grid, traces may have to be interpolated. The re-binning process allows for consistent application of further processing steps (Bacon, Simm and Redshaw, 2003).

- Amplitude matching: Differing seismic datasets are likely to be acquired under different conditions from one another, such as different source and receiver hardware or different processing workflows. As such, the amplitudes present within the seismic surveys are likely to be different from one another. Normalising amplitudes between surveys or using a survey's max amplitude as reference and modifying the surveys to be merged as appropriate allows for different survey's amplitudes to be comparable (Zhou, Sun and Xuening, 2014).

- Static Correction: Surveys may have minor differences in relative time or depth points for specific geological reflections. Static corrections allow for the shifting of traces upward or downward in the time domain to match those of the survey they are being merged with (Mousa and Al-Shuhail, 2011). For marine seismic, this is to ensure that all seismic data are at the same referenced sea level datum.

- Phase matching: Phase for a seismic survey refers to the position of the seismic wave within its cycle at the time of the reflection event (Nanda, 2021). Different surveys may utilise different phases when recording seismic data. Phase matching involves aligning the phase of all surveys to be merged to a common zero-phase wavelet or a designated wavelet of choice so that the same subsurface features have the same reflection characteristics (Deepa *et al.*, 2012). Features having the same reflection

characteristics allows for easier and more consistent interpretation across survey boundaries.

2.1.1.3 Seismic Data Resolution

The resolution at which 3D seismic can differentiate two closely spaced features within the subsurface is limited, both in horizontal and vertical orientations (Bacon, Simm and Redshaw, 2003). The limit of seismic resolution means that information at the sub-resolution scale is unable to be recorded, so knowing the scale of resolvable features within seismic data is important for geological understanding and interpretation purposes. The limitations of seismic resolution are controlled by the wavelength of the seismic wave, which is in-turn determined by the frequency content of the wave.

$$\lambda = \frac{v}{F} \qquad \textit{EQUATION 3}$$

The frequency of the seismic source controls the vertical resolution of seismic data, as the velocity through the medium is controlled by the lithology of the host rock. As the frequency of seismic waves decreases with depth, the resolution of seismic data will decrease deeper within the subsurface (Batzle *et al.*, 2005; Lines and Newrick, 2004).

The vertical resolution of seismic reflection data is defined as the minimum vertical distance between two interfaces that have distinct seismic reflections (Alsadi, 2017). To resolve two interfaces that are closely spaced they must be larger than ¼ the wavelength to be distinguishable from one another, otherwise seismic reflections interfere with one another hence (Kallweit and Wood, 1982):

$$Vertical\ seismic\ resolution = \lambda/4 \qquad \textit{EQUATION 4}$$

Vertical resolution of a seismic survey should not be confused with the detection limit. The detection limit represents the scale below which the only characteristic that changes is seismic amplitude, making it impossible for changes in thickness to be detected (Widess, 1973). Detection limit is defined as;

$$Vertical\ seismic\ detection\ limit = \lambda/8 \qquad \textit{EQUATION 5}$$

As a seismic wave propagates outwards from its source spherically (Figure 2-2) the further the distance from the source, the larger the radius of the seismic wave (Chopra *et al.*, 2007).

As waves reflect from a horizontal interface, they constructively interfere with one another in an area known as the Fresnel zone (Kearey, Hill and Brooks, 2013); this zone is approximated to be equal to the wavelength/2 and hence controls the horizontal resolution:

$$Horizontal\ seismic\ resolution = \lambda/2 \qquad \textit{EQUATION 6}$$

The Fresnel zone is only applicable to unmigrated seismic data, as the process of seismic migration collapses the Fresnel Zone (Alsadi, 2017)

2.1.2 Well Data

Well data allows for the tying and calibrating of seismic reflection data to specific rock and stratigraphy intervals within the subsurface (Vernik, 2016). Well data is gathered from a borehole during or after drilling into the subsurface. Well data allows for a highly detailed understanding of the geology at a specific point in the subsurface. Data taken from boreholes can take any number of forms from physical, for example, cuttings or core, to measure readings in the form of petrophysical parameter recordings, such as radioactivity or bulk density.

2.1.2.1 Petrophysical logs

Petrophysical logs are continuous recordings of geophysical parameters from within a borehole. The recorded measurement is plotted continuously against the depth of the wellbore at that point (Rider and Kennedy, 2011). The recording of geophysical parameters occurs either while drilling or post-drilling by having measuring tools lowered into the wellbore and measurements taken from the side of the wellbore along the well path. Petrophysical data relies on logging tools that are designed to measure specific geophysical properties of rocks in the subsurface. Typical vertical resolutions for such tools are every 0.5 ft; however, this is dependent on the logging tool (Bourke *et al.*, 1989). Hundreds of different logging tools are available, each with the ability to measure a unique geophysical property of the rock within the subsurface. The most common well logs are present in Table 2-1. This is not an exhaustive list, and there are many other types of well logs for specific purposes.

Log Name	Common Abbreviations	Purpose
Calliper	CAL, CALI, HCAL, MCAL	Diameter of the borehole
Gamma-ray	GR, GAM, NGAM, CGR	Natural gamma-ray emission of the formation
Density	RHOB, DEN, FDC	Bulk density measurement of the formation
Sonic	DT, DTC, AC, BHC	Interval transit time for a compressional seismic wave to travel within the formation
Resistivity	RES, LLS, ILD, LLD	Formation resistivity to electricity, typically investigated for multiple depths (near, mid, and far)
Neutron porosity	NPHI, NPOR, CNL	Porosity of the formation derived from the hydrogen index

TABLE 2-1 – COMMONLY USED WELL LOGS WITH ABBREVIATIONS AND PARAMETERS MEASURED, FROM DARLING (2005)

2.1.2.2 Accompanying well reports

A composite well log (also known as a completion log) serves as a comprehensive summary of the geology present within the well. A geologist creates a composite log once they can analyse all relevant data from the well bore, such as petrophysical logs and core/cuttings. A composite well log contains a depth track, specific well logs such as gamma-ray and sonic or density, cutting/core descriptions of the well, and a geologist's interpretation of all this data. The geologist's interpretation would typically include a lithology column, local formation names, and formation tops in correlation to the known geology of the local area (UK Government, 2016).

Once a well has been completed, a well report is made. A well report is a highly detailed document containing all information relating to the activities and results of drilling the well. Well reports contain a more in-depth geological analysis of the separate formations drilled through. They also contain a summary of the more specialised analysis that may have been undertaken, such as lab porosity measurements or mineralogical analyses of the core. Alongside geological information, further engineering aspects and other information are also contained.

2.1.2.3 Checkshot well data

Checkshots are direct measurements of travel time between the surface and a given depth. A source is located on the surface, and recorders are located at several points within the wellbore. The resultant checkshot data provides time-depth relationship data for the wellbore location, allowing for more accurate calibration of well data against seismic data in the time domain (Sheriff, 2002).

2.1.3 Relinquishment reports

Relinquishment reports can be used in specific areas to gain a further understanding of the geology of the subsurface. A relinquishment report contains the geology findings of an area when a hydrocarbon exploration company surrenders its exploration license within a UK exploration block. Relinquishment reports typically contain generalised information on the petroleum systems of an area and hence may contain geophysical and well interpretation. The use of these was found to give further context to the data that investigated. The NSTA provides a relinquishment report database.

2.2 Methodology

This section overviews the methodologies used within this thesis that underpin the interpretation of well and seismic data for further analysis.

2.2.1 Well lithology interpretation

The physical properties of rocks can be used to interpret the lithology, as different lithologies have different geophysical properties (Schön, 2011). Since well log data records different physical properties of the rocks that a wellbore passes through (2.1.2 Well Data), an integrated approach using both petrophysical and composite well logs was used to interpret the lithology within each well. A lithology was applied to a specific section within the well where the petrophysical measurements had been correlated to known values for similar lithologies (Table 2-2); when there was uncertainty present with the chosen lithology, the interpretation was checked against well cuttings and information present within the composite well log and lithology applied accordingly. This was done for all wells.

The main software used for petrophysical well interpretation was SLB's Petrel, however SLB's Techlog, and Python were also used. The resolution of interpreted lithology changed depending on the need, with areas of low interest, such as areas in the overburden, being interpreted at formation scale resolution, whereas areas with high interest have lithologies interpreted to petrophysical tool level resolution.

Lithology	Gamma Ray (gAPI)	Density (g/cm^3)	Sonic Velocity
Sandstone	0 - 40	≈ 2.65	5490 – 5950 (compact sandstone)
Limestone (Carbonate generalised)	10 - 40	2.71	6400 - 7010
Mudstone	80 - High	2.3 – 2.7	1790 - 5805
Halite	0	2.04 – 2.2	4,540
Carnallite	220	1.57	3,850
Polyhalite	180	2.79	5,300
Anhydrite	0	2.98	6,250
Sylvite	300 - 500	1.99	4,110

TABLE 2-2 – LITHOLOGY PETROPHYSICAL VALUES GUIDE. VALUES MAY VARY DEPENDING ON SPECIFIC PROPERTIES OF THE FORMATION BEING MEASURED AND THE LOGGING TOOL USED. FROM (JACKSON AND HUDEC, 2017; MORTON-THOMPSON AND WOODS, 1992; JONES AND DAVISON, 2014)

2.2.2 Seismic to well ties

A seismic well tie correlates the reflectivity from a seismic survey to that of a well, based on calculated reflectivity from the measured physical properties of bulk density and compressional velocity. This allows for both seismic and well data to be compared with one another and features interpreted within the well data to be correlated with those on the seismic data or vice versa (White and Simm, 2003). As seismic responses are dictated by the density and acoustic properties of the subsurface (Seismic Acquisition - 2.1.1.1), if a well has density and acoustic logs present (Petrophysical logs - 2.1.2.1), a representative seismic response for the well can be calculated (Sheriff and Geldart, 1995).

Seismic well ties were calculated in SLB's Petrel, using the seismic-well calibration suite of tools. For a well tie to be undertaken, a well must have density data and sonic data, checkshot data can also be used. While checkshot data is not mandatory for calculating seismic-well calibrations, only wells with sufficient checkshot coverage present were used for seismic well-tying as it allowed for more accurate results. The following steps outline the seismic to well tie process;

The well that is being tied to the seismic data is checked to ensure all required data is present and is of good quality with no gaps in the logs or erroneous values present. The sonic data is smoothed to remove spikes that may affect the well-tie procedure. The de-spiking procedure used a standard deviation threshold of three to identify spikes, once identified, values were replaced within the log with interpolated values. The smoothed logs were then checked to ensure no false smoothing had occurred. The acoustic impedance and reflection coefficient are then calculated using the smoothed sonic data and density data for the well (Seismic Acquisition - 2.1.1.1). The calculated acoustic responses are plotted in time according to the values with the checkshot data and calibrated with knee points at major stratigraphic intervals. A wavelet is created to be convoluted through the calculated reflection coefficient log. The wavelet is initially created as a ricker wavelet with its frequency chosen as to match the seismic data frequency (20 – 50 Hz). A synthetic seismogram is created after convoluting the wavelet with the calculated reflection coefficient (Figure 2-4). The synthetic seismogram is then plotted against the seismic data from the exact co-ordinate location as the wellbore to compare the synthetic and real seismic data. Adjustments are undertaken to best match the synthetic seismogram to the seismic data. Firstly, the wavelet is modified, and a range of modifications are undertaken, such as changing the wavelet type and frequency or extracting a wavelet from the seismic data in the well location. The synthetic seismogram can then be bulk shifted up or down vertically, if required, so that reflections in the seismogram match those in the seismic data, this is often used to correct datum inaccuracies.

2.2.3 Seismic horizon interpretation and surface creation

Seismic interpretation relies on picking and tracking seismic reflectors that are laterally continuous to create maps of geological structure, stratigraphy or other features of interest (Avseth, Mukerji and Mavko, 2005). SLBs Petrel software was used to manipulate and interpret seismic data related to seismic horizon interpretation and surface creation.

Bias from the interpreter will be encountered when interpreting seismic data (Alcalde and Bond, 2022). The bias introduces uncertainty to the interpretations of the seismic reflections and consequently the resultant data. While the methodology used to interpret the seismic data is provided, it is unlikely that another party following our exact methodology would have the same resultant interpretation of stratigraphic reflections and discontinuities within the subsurface.

Modern 3D marine seismic data can be visualised using four different orientation methods for interpretation: inlines and crosslines, time slices, and arbitrary lines. Inlines and crosslines represent a vertical cut of the seismic data cube, inlines are oriented in the same direction as the orientation of the receiver streamers towed by the marine acquisition vessel, and crosslines are perpendicular to the inlines (Ebrom *et al.*, 1995). Time slices are horizontal slices through the seismic data, providing a plan view. Arbitrary lines are cut in any orientation that the seismic interpreter needs (Bacon, Simm and Redshaw, 2003). The seismic horizon interpretation was initiated by using the seismic-well ties to identify reflections within the 3D seismic data that represent a feature of interest to be extracted, such as a geological boundary. Once a feature and the characteristics of its reflection have been identified (+'ve or –'ve, amplitude), tracking of the horizon is initiated.

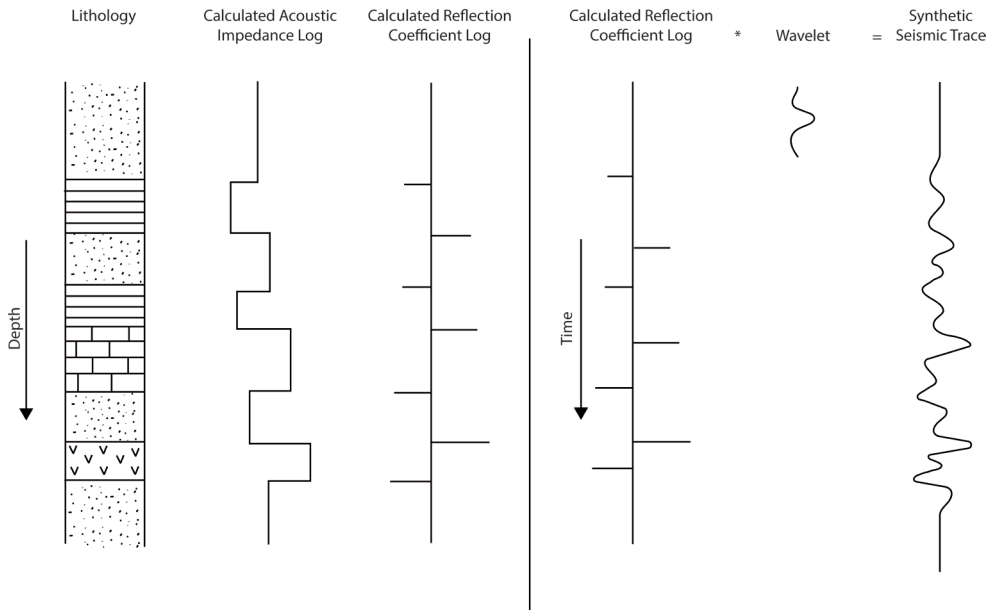

FIGURE 2-4 STEPS IN SYNTHETIC SEISMIC WELL TIE FROM (KEAREY, HILL AND BROOKS, 2013)

Initially, a horizon of interest was interpreted in 2D cross sections (Figure 2-5), firstly inlines, then crosslines at set interval steps of a geometric progression with a ratio of 2 (i.e. 64, 32, 16). The usage of this geometric progression allowed for the creation of an initial coarse interpretation grid which could be further refined; this allowed the course interpretation to act as an interpretation guide. Seeded 2D guided auto-tracking was the initial tool used for horizon mapping (Table 2-3). Once an adequate grid of interpretation had been created in inline and crossline orientations, any areas that were difficult to interpret were cut using an arbitrary line to see if the chosen reflection could be interpreted at a different orientation. Once a sufficient grid had been produced using the seeded 2D auto-tracking tool, the 3D auto-tracking tool (Table 2-3) in Petrel was used to track the horizon between areas of the interpreted grid. Once 3D auto-tracking had been completed, areas that failed auto-tracking due to lack of continuity or poor seismic data quality were retraced using the 2D auto-tracking tool at smaller grid intervals (Figure 2-5). After the second phase of 2D auto-tracking, 3D auto-tracking was again repeated. These stages were repeated until a grid of sufficient quality and coverage was created. If any small gaps remained after, the manual interpretation and guided auto-tracking tools were used in small intervals until the interpretation grid was deemed suitable.

A surface can be created once a horizon has been interpreted of suitable quality. To create a surface in Petrel, the horizon file and a surface boundary are required. A boundary defines the area in which the surface would be created. Petrel offers many different options and algorithms for surface creation. The grid increment size used was typically 50x50; however, if surfaces of different data densities were required, this was changed as appropriate. The default algorithm for surface creation was convergent interpolation, which was used for all surfaces created. No pre-processing or well adjustment was made to the surfaces in the creation process. As the seismic data is in the time domain, the generated surfaces are also in time.

Tool	Description
Manual Interpretation	Click and drag to create horizon interpretation. No locking to horizons present.
Guided Auto-tracking	Two points on a seismic horizon are chosen, the software automatically tracks the amplitude of the reflection as a guide, choosing the most fitting route.
Seeded 2D Auto-tracking	A single point is chosen on a seismic horizon, horizon is then tracked in both directions until break in horizon continuity or the software is uncertain of the interpretation
Seeded 3D Auto-tracking	Used in either 2D settings or as a tool. In 2D, click on horizon interpretates horizon in 3D, tracks until unconfident or no continuity in horizon. As tool, pre-interpreted horizon entered, 3D auto-track, interprets horizons between pre-interpreted grid (Figure 2-5)
Parameters: All auto-tracking tools can have the same parameters modified to dictate how the auto tracking is calculated. Parameters include, quality, signal feature, dip continuity, wavelet tracking, correlation quality	

TABLE 2-3 – SEISMIC HORIZON INTERPRETATION TOOLS. (SCHLUMBERGER, 2019)

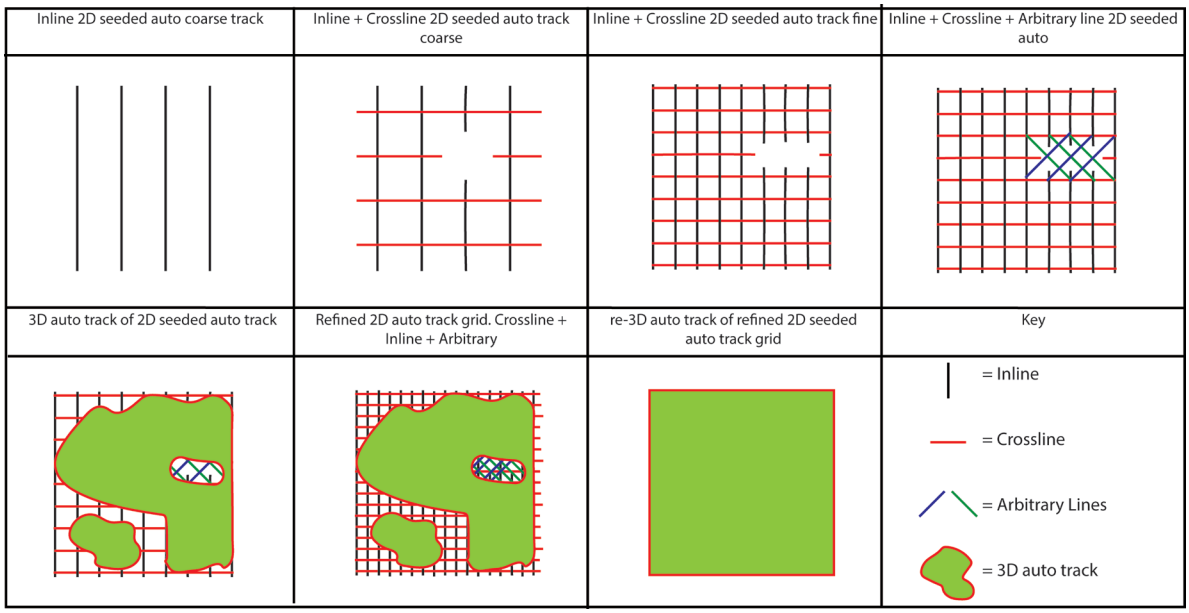

FIGURE 2-5 ORDER OF SEISMIC INTERPRETATION AND GRIDDING. STEPS TAKEN TO INTERPRET A SEISMIC HORIZON

2.2.4 Seismic attributes

A 3D seismic volume can be considered a volume of seismic amplitude values in time (Bacon, Simm and Redshaw, 2003). The amplitudes of seismic traces, while interpreted qualitatively in Section - 2.2.3, can be quantitatively analysed to measure seismic characteristics of interest and, in doing so, enhance features within the seismic data that may be difficult to interpret by identifying specific patterns or properties (Chopra and Marfurt, 2005; Barnes, 2016). Seismic attributes were applied to seismic volumes to aid the interpretation and identification of the features of interest (Figure 2-6). The most used seismic attributes were:

- RMS Amplitude: Computes the root mean squared on instantaneous trace samples over a specified window (Schlumberger, 2019; Koson, Chenrai and Choowong, 2021).

$$x_{rms} = \sqrt{\frac{1}{N}\sum_{n=1}^{N} w_n x_n^2} \qquad \textit{EQUATION 7}$$

- Dip Illumination: Highlights structural geology with a dip field estimation (Schlumberger, 2019; Barnes).

$$I_d = sin\gamma_r sin\gamma_s \cos(\emptyset_r - \emptyset_s) + cos\gamma_r cos\gamma_s \qquad \textit{EQUATION 8}$$

- Chaos: computes the local chaos, which is the lack of organisation in the structural estimate (Schlumberger, 2019; Randen, 1999)

$$C = \frac{(\lambda_{mid} + \lambda_{min})}{\lambda_{max}} \qquad \textit{EQUATION 9}$$

- Variance: estimation of local variance within the seismic signal (Schlumberger, 2019; Taner *et al.*, 1994)

$$\omega_v^2 = \frac{\int_{\omega=0}^{\varphi} (\omega - \omega_c)^2 P(\omega) d\omega}{\int_{\omega=0}^{\varphi} P(\omega) d\omega} \qquad \textit{EQUATION 10}$$

2.2.4.1 Attribute Mapping

Attributes can aid in the classification and mapping of depositional features. The geometries formed from sedimentary depositional features are captured within 3D seismic data (Bacon, Simm and Redshaw, 2003). While these geometries are recorded, they can be difficult to

interpret. The use of seismic attributes can aid in highlighting and enhancing these depositional features and allow for more confident interpretation.

Initially, an area of interest and interval were chosen to examine depositional features within the system. Seismic attributes were applied to the seismic volume to enhance the depositional features that were present. Both time slice and cross-section viewpoints of the seismic data are utilised. Flattening the seismic cube, a process where the horizon of the base interval of interest is set to horizontal, can enhance the appearance of depositional features, as it allows the time slice to cut the feature more parallel to the initial deposition of the feature. Once a feature was found, a boundary was mapped around it to record its exact extent. To ensure the maximum extent of the feature was recorded, the features were interpreted at every depth they were located.

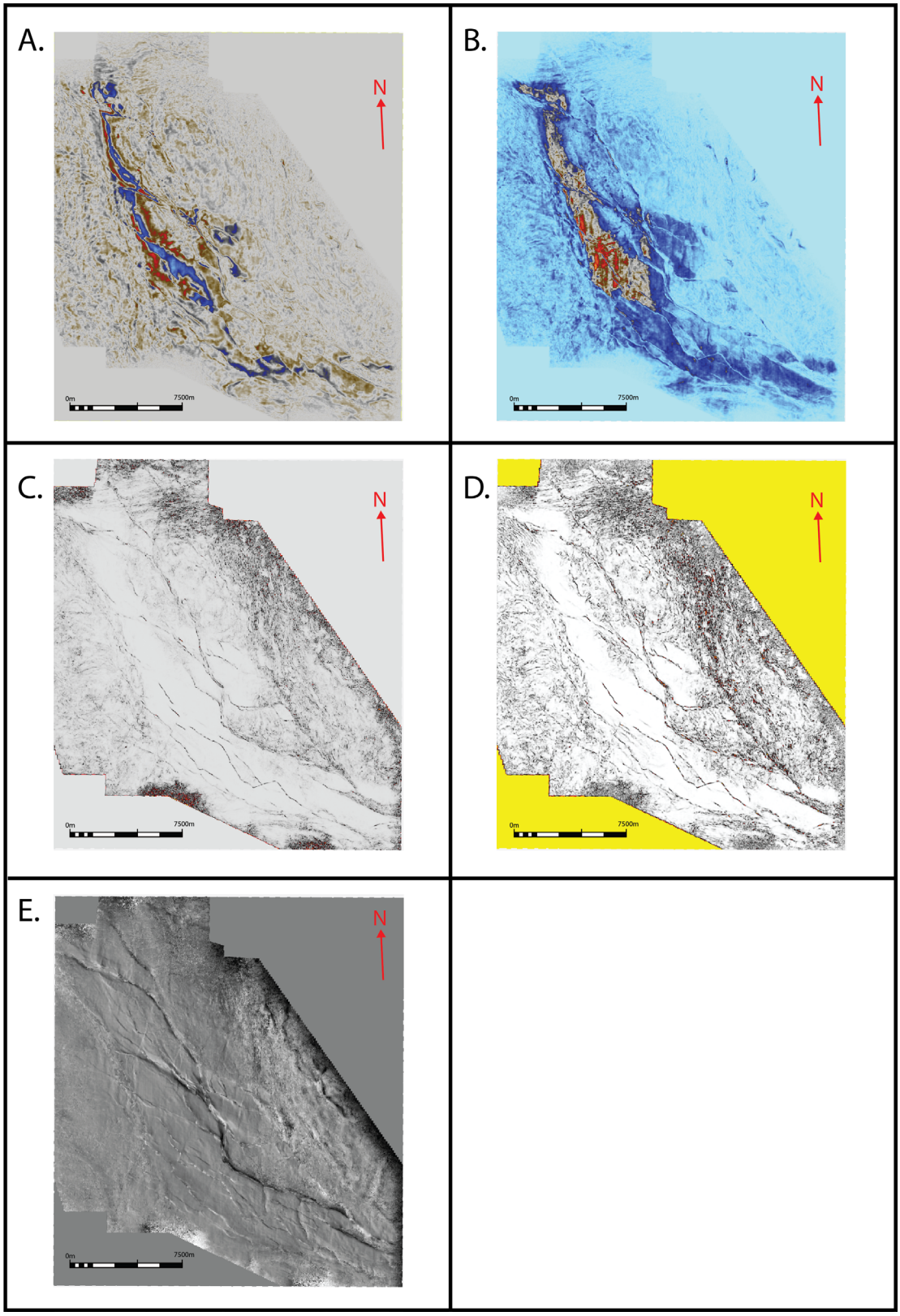

FIGURE 2-6 EXAMPLES OF SEISMIC ATTRIBUTES ON SEISMIC TIMESLICE. A) ORIGINAL SEISMIC. B) RMS AMPLITUDE C) CHAOS. D) VARIANCE E) DIP ILLUMINATION

2.2.5 Fault Mapping

Geological faults cause discontinuities within the geology of the subsurface and hence are expressed as discontinuities in seismic horizons, which lead to gaps, overlaps, or vertical offsets in the mapped surfaces (Groshong, 1999). Seismic time slices and generated time surfaces were used to locate faults that required mapping. To aid in locating faults, seismic attributes were used with time-surfaces with a seismic dip attribute applied. The dip attribute calculated the angular dip at any point of a surface and coloured it according to the applied colour bar and dip severity, this allowed for areas of sudden change in dip (typical near faults) to be located more easily.

Once the location of the faults had been identified, they could be mapped using the seismic data. An arbitrary seismic line was cut perpendicular to the strike of the fault, which allowed the true geometry of the fault to be viewed within the subsurface. SLBs Petrel was used for fault mapping, with the 'interpret faults tool'. The fault structure was traced in the initial arbitrary seismic cross-section. Once this had been completed, the cross-section was moved forward along strike, and the fault structure was retraced. This was a similar process to that of horizon interpretation (Section - 2.2.3), where a geometric progression of arbitrary line steps was used, starting at 32 steps and decreasing until a suitable interpretation of the fault had been covered.

2.2.6 Depth Conversion

As features interpreted from the seismic data are in the time domain and do not accurately represent the subsurface, they need to be depth-converted using a velocity model (Al-Chalabi, 2014). A velocity model represents the velocity of a seismic wave within the subsurface at any given point (Sheriff, 2002). For 3D seismic data, a velocity model has the same dimensions as a 3D seismic cube.

Depending on the data available, different approaches can be taken for building an appropriate velocity model, and these approaches can range from the application of a uniform velocity to the creation of a complex heterogeneous velocity cube (Al-Chalabi, 2014; Bacon, Simm and Redshaw, 2003).

SLBs Petrel was used to create a velocity model for the depth conversion process. The representative velocity data needed for the velocity model was extracted from the time-depth relationships of the wells with seismic-well-ties. Well-tops (Z points within a well that define a stratigraphic boundary) were used to calculate residuals between the generated depth surfaces and known depths, this helped in the calibration of the velocity model. Surfaces of geological boundaries created from the seismic data were used as the boundaries of the layers within the velocity model.

As each layer within the velocity model comprises different geological formations with different elastic properties, each layer requires specific parameters that best fit its vertical velocity profile. Petrel offers 3 different velocity algorithms to choose from:

1) Where at each XY location, the velocity is constant through the zone (Schlumberger, 2019),

$$V = V_o = V_{int} \qquad \textit{EQUATION 11}$$

2) At each XY location, the velocity changes vertically by a factor of k. V_o represents the velocity at the datum, and Z, the distance (m) of the point from the datum (Schlumberger, 2019).

$$V = V_o + kZ \qquad \textit{EQUATION 12}$$

3) At each XY location, the velocity changes in the vertical direction by a factor of k. V_o represents the velocity at the top of the zone and (Z-Zo) represents the distance between the point and the top of the zone. A negative value of k results in velocities that increase downwards. Typical k values range between 0 and -0.2 (Schlumberger, 2019).

$$V = V_o + k(Z - Z_o) \qquad \textit{EQUATION 13}$$

Building a velocity model is an iterative process, initially, layer 1 is added by defining parameters and the velocity algorithm. The residuals for the first layer are then checked to see if they are within the acceptable margins for error, if so, the next layer to the velocity model is added, and parameters and residuals are checked. These steps continue until all layers of the velocity model are present. If the residuals of a layer within the velocity model are outside the acceptable range, then parameters are modified and adjusted until they are within suitable ranges.

2.2.7 Rock physics modelling

The elastic properties and geophysical responses of a rock are controlled by properties such as, but not limited to, the porosity, mineralogy, pore fluid type, pore fluid mixture, and pore pressure (Avseth, Mukerji and Mavko, 2005). As seismic responses can be quantified if the velocity and density of the subsurface are known through the calculation of the acoustic impedance and reflection coefficient (2.1.1.1 - Seismic Acquisition), being able to model elastic properties of the rock allows forward modelling of seismic responses. It allows for investigating how changing rock properties will modify a rock's seismic response.

Fluid substitution is an area of rock physics modelling that involves modifying the pore-filling fluids and calculating the new elastic properties to forward the model of the change in geophysical responses (Smith, Sondergeld and Rai, 2003). For fluid substitution to be undertaken, the new velocity and bulk density of the rock with modified pore-filling fluid needs to be calculated. These are calculated by:

$$V_p = \sqrt{\frac{k_{sat} + \frac{4}{3}G}{\rho_{bulk}}} \qquad \textit{EQUATION 14}$$

and,

$$G = \rho_{bulk} * Vs^2 \qquad \textit{EQUATION 15}$$

and

$$\rho_{bulk} = \rho_g(1 - \Phi) + \rho_{fl}\Phi \qquad \textit{EQUATION 16}$$

k_{sat} is the bulk modulus and G is the shear modulus of the rock. Where ρ_g is the grain bulk density, ρ_{fl} is the pore-filling fluid density, and Φ is the porosity. While the shear modulus, grain bulk density, and porosity remain constant for the calculation of the new compressional velocity and bulk density, new values of bulk modulus and fluid bulk density are required to be calculated for the fluid-substituted rock. To calculate the new bulk modulus the Gassmann equation can be used as follows (Smith, Sondergeld and Rai, 2003):

$$K_{sat} = K^* + \frac{(1 - \frac{K^*}{K_O})^2}{\frac{\Phi}{K_{fl}} + \frac{(1 - \Phi)}{K_O} - \frac{K^*}{K_O^2}}$$ *EQUATION 17*

The Gassmann equation relates the bulk modulus to the porosity, dry rock frame bulk modulus (K^*), bulk modulus of the mineral matrix (K_O), and the bulk modulus of the pore-filling fluids (K_{fl}) (Smith, Sondergeld and Rai, 2003).

The density of the new fluid is calculated with:

$$\rho_{fl} = S_w * \rho_w + (1 - S_w)\rho_{fn}$$ *EQUATION 18*

Where ρ_{fn} is the bulk density of the new fluid being substituted into the rock.

The Gassmann equation requires the bulk modulus of the porous rock frame (K^*) as an input parameter. However, while the bulk modulus of the rock frame is independent of pore-filling fluid, it cannot be directly derived from well log data. Hence, the initial steps in performing Gassmann fluid substitution involve calculating bulk modulus of the porous rock frame from the known well data (Figure 2-7). As the initial bulk modulus can be calculated from well-log data as such,

$$K_{sat} = \rho_{bulk}(Vp^2 - \frac{4}{3}Vs^2)$$ *EQUATION 19*

, and the bulk modulus of the mineral matrix can be obtained from lab results within the published literature. The initial parameters for the Gassmann equations can be acquired from well logs and work forward to calculate the bulk modulus of the porous rock frame then work backwards again as the bulk modulus of the porous rock frame is independent of the pore filling fluids.

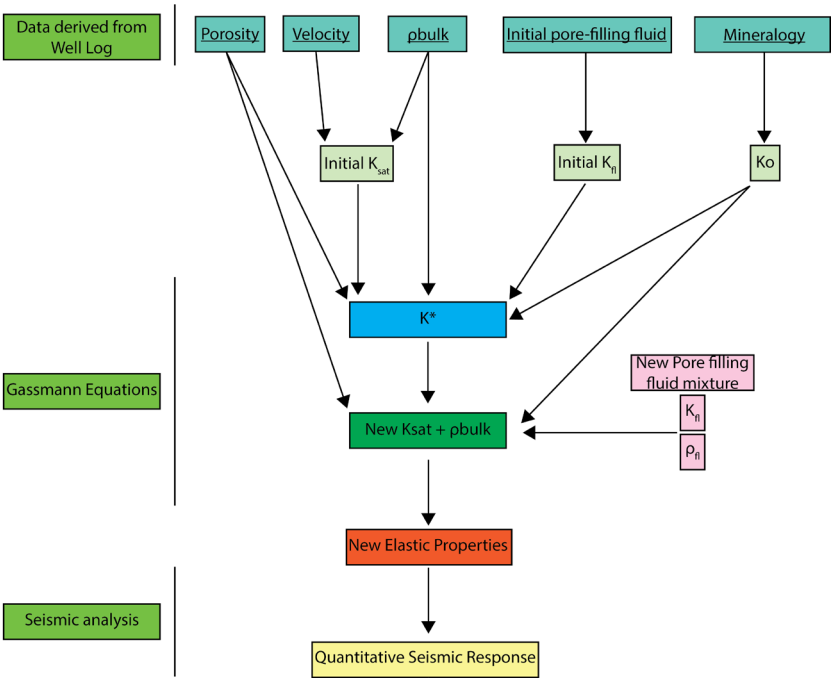

FIGURE 2-7 GASSMANN EQUATION WORKFLOW FOR CALCULATING QUANTITATIVE SEISMIC RESPONSE

2.3 Data utilised

Reproducibility and replicability is a significant challenge faced within subsurface geoscience, as often it is hindered by limited access to data, undocumented methods and poor access to code (Steventon *et al.*, 2022). Fortunately, there has been increase in efforts in recent years by journals to promote more open science by providing guidance on data and software sharing (Ireland *et al.*, 2023). To allow for full transparency, all data used within this thesis is publicly available at the named repositories. A comprehensive repository of all data produced and used within this thesis is given in Data availability.

The seismic data used within this study required no further processing upon acquisition from the National data repository. The NSTA supplied all seismic surveys with adequate information about the data, such as acquisition reports and processing reports.

2.3.1 Seismic Data

2.3.1.1 Southern North Sea Mega Merge

The Southern North Sea Mega Merge survey is located at its most westerly point 15km off the eastern shore of the United Kingdom (Figure 2-8). The total area covered is 25,561 $km^{2,}$ encompassing most of the United Kingdom's Southern North Sea basin. It includes 86 surveys

that were merged with the following steps: resampling and quality checking, re-binning to a new master grid, amplitude matching, static correction, phase matching, and a merge window between seismic surveys over an area of 40 traces (Seismic Acquisition - 2.1.1.1).

The finalised merged survey had a bin size of 12.5 m with a sample interval of 4 ms and a record length of 5632 ms. The survey was zero phase time migrated data to the European standard polarity, where an increase in acoustic impedance is represented as a decrease in displayed amplitude.

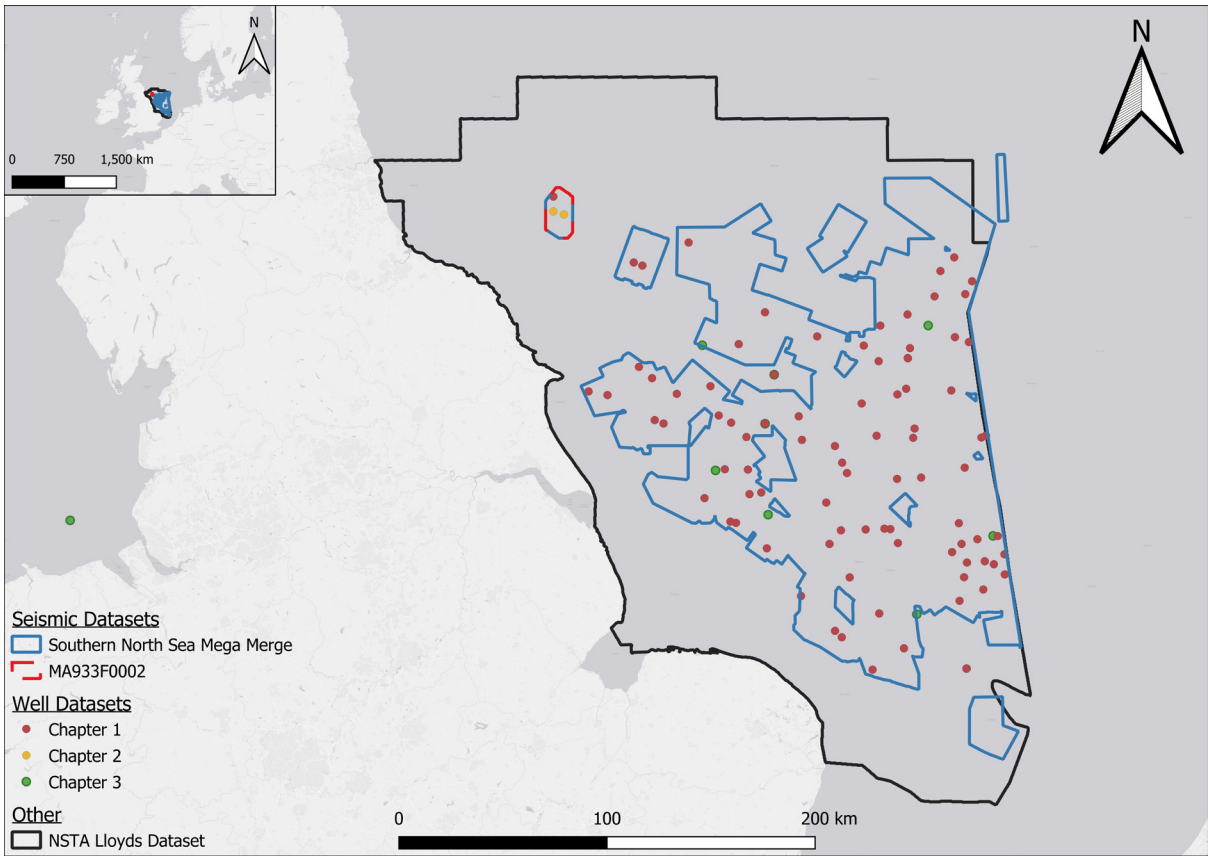

FIGURE 2-8 LOCATION MAP OF DATA USED WITHIN THIS THESIS.

2.3.1.2 Survey MA933F002

Survey MA933F002 was acquired in 1993 and is located 40 km off the eastern shore of the United Kingdom. It is located just south of the mid-North Sea high, on the northern edges of the South Permian Basin's depo-centre and covers an area of 238 km^2.

The survey is time migrated with a sample rate of 4 ms and a bin interval of 12.5 m. It is a zero-phase survey with European standard polarity where an increase in acoustic impedance is represented as a decrease in displayed amplitude. Wavelengths in the data range from 10 ms at the top intervals towards 70 ms towards the lower seismic sections, as such, vertical resolution ranged from 2.5 ms to 17.5 ms.

Name	Type	Used for	Notes*
Southern North Sea Mega Merge (OA__2019seis0001)	Seismic	Surface Interpretation Fault Interpretation Structural deformation interpretation Velocity model building	Used in Chapters 1,2
MA933F0002	Seismic	Surface Interpretation Fault Interpretation Depositional feature interpretation	Used in Chapter 2

TABLE 2-4 – SEISMIC DATASETS UTILISED WITHIN THESIS

2.3.2 Well Data

The wells used within this study were a mixture of those drilled for production and exploration and totalled 104 within this thesis (Figure 2-8).. Wells ranged in age from 1960s – 2010s, with the log recording tool dependent on the company which recorded the well logs. Each chapter of the thesis had different spatial and log content requirements for well data. As such, separate well-datasets have been constructed for each study within this thesis, and an overview of well use case can be found in Table 2-5.

2.3.3 Interpretation products

As this thesis produced and used a number of different data formats and datasets for different areas of research, a comprehensive list of all data utilised and created within this thesis can be found in Table 2-6.

Name	Number of Wells	Used for
Well Data Set – Chapter 1	92	Synthetic Seismic Well Tie, Velocity Extraction, Lithology Interpretation, Overburden modelling, Solubility modelling
Well Data Set – Chapter 2	3	Solubility Model, Lithology Interpretation, Overburden modelling
Well Data Set – Chapter 3	9	Rock Physics modelling, Lithology Interpretation, Fluid Substitutions

TABLE 2-5 – WELL DATASETS USED WITHIN THESIS

2.4 Usage of large language models on code development

This thesis used Python coding language for data manipulation and analysis, which industry-standard software, such as Petrel, was not suitable for. Large language models were used in part to aid in developing sections of code. A key emphasis within this thesis is transparency, and as such, noting the large language models used to generate code for this research should be included within the methodology. The following models were utilised, including OpenAI's ChatGPT-3, ChatGPT-4 and ChatGPT-4o; Anthropic's Claude Sonnet 3 and Claude Sonnet 3.5; Meta's LLaMa 2,3, and 3.1; and Google's Gemma 2. A range of models were utilised as computational generative AI has seen vast improvements during the time this research and thesis have been undertaken (2020 - 2024), and as such, different models were used to keep up to date. It should be noted that at no point was any large language model or generative AI used to write or generate parts of the thesis, AI was solely used for code generation or code bug fixing.

Name	Type	Source / Interpreted From	Contains	Notes
South Permian Basin Surface Dataset	Surface	Southern North Sea Mega Merge	Base Cenozoic, Base Cretaceous, Base Jurassic, Base Triassic, Base Zechstein	Self-interpreted. TWT + Z(m), depth converted using velocity model
MA933F0002 Surface Dataset	Surface	MA933F0002	Base Triassic, Base Z4 Zechstein,Base Z3 Zechstein,Base Z2 Zechstein, Base Z2- Polyhalite Zechstein, Base Z1 Zechstein	Self-interpreted. TWT + Z(m), depth converted using velocity model
South Permian Basin Fault Dataset	Faults Lines	Southern North Sea Mega Merge		Self-interpreted
Structural Deformation Styles Extent	Polygon Area	Southern North Sea Mega Merge	Deformation styles of internal Zechstein deformation	Self-interpreted
Depositional heterogeneities	Polygon Area	MA933F0002	Polygons of heterogeneities within the Zechstein	Self-interpreted
NSTA Lloyds Data Set	Surface	Taken from NSTA open data (https://www.data.gov.uk/dataset/c39cc5dd-36b3-40db-95e7-290379dbd27e/nsta-and-lloyd-s-register-sns-regional-geological-maps-open-source)	Base Triassic Base Zechstein	Low resolution surfaces in Z(m) encompassing the entire Southern North Sea Area.
Southern North Sea Velocity Model	Velocity Model	South Permian Basin Surface Dataset and Well Data set – Chapter 1	3D Velocity Cube, same spatial extent as South North Sea Mega Merge	Self-Calculated. Residuals of 7%
Southern North Sea Bathymetry Surface	Surface	From Emodnet (https://emodnet.ec.europa.eu/en)		Cut to fit the same spatial extent as the Southern North Sea mega merge

TABLE 2-6 – DATA-SETS CREATED AND USED WITHIN THESIS

2.5 Data availability

2.5.1 Data availability Chapter 3

The data for 2.5 is available in the following data repositories:

Barnett, Hector (2023). Zechstein_Internal_Structural_Facies. Newcastle University. Dataset. https://doi.org/10.25405/data.ncl.21252771.v1

Barnett, Hector (2023). Surfaces_TWT_SNS. Newcastle University. Dataset. https://doi.org/10.25405/data.ncl.21269658.v1

Barnett, Hector (2022). Welltops_SNS. Newcastle University. Dataset. https://doi.org/10.25405/data.ncl.21270309.v1

2.5.2 Data availability Chapter 4

The data for Chapter 4 is available in the following data repositories:

Barnett, Hector (2024). Workflow Code from the manuscript 'Capturing geological uncertainty in salt cavern developments for hydrogen storage: Case study from Southern North Sea'. Newcastle University. Software. https://doi.org/10.25405/data.ncl.24623961.v2

Barnett, Hector (2024). Output geospatial data from paper 'Capturing geological uncertainty in salt cavern developments for hydrogen storage: Case study from Southern North Sea'. Newcastle University. Dataset. https://doi.org/10.25405/data.ncl.24967767.v2

Barnett, Hector (2024). Input Geological data/models for paper 'Capturing geological uncertainty in salt cavern developments for hydrogen storage: Case study from Southern North Sea'. Newcastle University. Dataset. https://doi.org/10.25405/data.ncl.24968754.v2

2.5.3 Data availability Chapter 5

The data for Chapter 5 is available in the following data repository: https://figshare.com/s/01c10efe1839c03c28ff

Chapter 3. Characterising the internal structural complexity of the Southern North Sea Zechstein Supergroup Evaporites

3.1 Abstract

This chapter concentrates on the Zechstein Supergroup evaporite deposits within the Southern North Sea of the United Kingdom's Continental Shelf. This analysis of the internal structural complexity and stratigraphic heterogeneity utilises 26,000 km^2 of 3D seismic data together with 97 wells from the Southern North Sea. Characterisation of the different intra-Zechstein deformation styles was undertaken alongside mapping their spatial distribution to understand the relationship they have with one another and the structural evolution that may have been taken.

This work has characterised and mapped 6 different internal deformation styles present within the Zechstein with increasing levels of deformation. Shown the internal lithological heterogeneity is indicative of variations in the vertical strength profile of layered evaporite sequences. Identified discontinuous high amplitude reflections within the Zechstein are because of the geometries being too steeply dipping for the seismic data to image. Hypothesised the ability to predict the internal heterogeneity of areas of poorly imaged salt, such as within large diapiric salt structures, from surrounding intra-Zechstein deformation styles. These findings suggest that there is significant internal complexity even within areas of the basin with minor mobilisation to the external salt geometry.

3.2 Introduction

Laterally extensive salt deposits are never solely comprised of halite but rather form interbedded sequences of halite and other evaporite and non-separate lithologies. These variable evaporitic formations are referred to as layered evaporite sequences (Rowan *et al.*, 2019). Evaporite sequences are common features of many sedimentary basins around the world (Butler *et al.*, 2015); notable examples include the Zechstein Supergroup of Northern Europe, the Messinian of the Mediterranean, and the Iren of the Precaspian Basin (Jackson and Hudec, 2017).

Some evaporite lithologies, most notably halite, are mobile in the subsurface, typically reacting to external changes in stress (Jackson and Stewart, 2017) or, alternately, responding to internal stresses arising from variations in density differences. Three types of loading can lead to force-driven salt flow: gravitational, displacement and, to a much lesser extent, thermal (Hudec and Jackson, 2007). This ability of evaporite formations to flow causes the formation of geological structures such as salt diapirs, salt-cored anticlines and salt welds. Internal structures which do not modify the external geometries of the evaporite formation can also form, the most common structures formed being folds (Rowan *et al.*, 2019).

The mechanical behaviour of evaporite sequences is partly controlled by the proportion and layering order of the constituent lithologies present (Adamuszek *et al.*, 2021). Interbeds, such as carbonates and anhydrites are much stronger in both compression and extension than halite (Table 3-1), which undergoes flow at stresses of < 5 Mpa (Zulauf *et al.*, 2011). The mode of deformation for these interbeds also differs from halite as they can undergo both a combination of brittle (breaking apart) and ductile deformation (competent deforming) to accommodate strain (Strozyk *et al.*, 2014). In contrast, halite rarely undergoes brittle deformation because it is ductile under low strain rates (Jackson and Hudec, 2017). These mechanically strong lithologies influence the strain patterns within an evaporite sequence (Strozyk *et al.*, 2014). Differing quantities and distributions of mechanically strong interbeds influence the structural style and how internal strain is partitioned in mobile evaporites (Stewart *et al.*, 1996; Stewart and Harvey, 1998; Rowan *et al.*, 2019). Interbeds modify not only the behaviour of evaporite sequences but also aid in defining the strain and kinematic record of the evaporite sequence in both outcrops and on seismic data by acting as marker

beds, which aid in helping to quantify levels of strain which have occurred (Zulauf and Zulauf, 2005).

Stringers are blocks of non-halite material with different flow properties commonly consisting of the original interbedded lithologies (Jackson and Hudec, 2017). Stringers have been observed in many different evaporite sequences (Edgell, 1996; Giles and Rowan, 2012; Al-Siyabi, 2005; Jenyon, 1989) and previously recognised and described in the Zechstein of North West Europe (Jenyon, 1989; Van Gent, Urai and de Keijzer, 2011). Boudinage is a common mode of failure of competent layers, such as anhydrites and carbonates, that are enclosed within a weak, ductile matrix, such as halite, and which undergo layer-parrel extension (Rowan *et al.*, 2019), as generally competent rocks are more likely to undergo brittle failure in extension than compression.

Lithology	Compressive Strength (MPa)	Tensile Strength (MPa)
Anhydrite	70 – 120	5 – 12
Carbonate - Dolomite	80 – 250	3 – 25
Carbonate - Limestone	4 – 250	1 – 25
Halite	24	2
carnallite	10	0.5

TABLE 3-1 LITHOLOGIES PRESENT WITHIN LAYERED EVAPORITE SEQUENCES. ANHYDRITE AND CARBONATE VALUES FROM GUDMUNDSSON (2012), HALITE VALUES FROM JACKSON AND HUDEC (2017) AND CARNALLITE VALUES FROM LUANGTHIP ET AL. (2017)

While previous work has investigated intra-salt deformation (Burliga, 1996; Davison, Alsop and Blundell, 1996; Cartwright *et al.*, 2012; Strozyk *et al.*, 2012; Jackson *et al.*, 2014; Butler *et al.*, 2015; Jackson *et al.*, 2015), there has been a limited emphasis on distinguishing the different styles and distributions of deformation, especially on the scale of a basin. In some cases, the ability to distinguish the internal deformation of an evaporite sequence is limited by the quality of the available seismic data, with halite-dominated evaporitic sequences often described as having a chaotic or transparent appearance (e.g. Jones and Davison, 2014; Hanafi *et al.*, 2022). However, improvements in the seismic processing of evaporite sequences are

leading to coherent reflectivity within these formations, potentially leading to an evolution in the interpretation of evaporite sequences' internal structural heterogeneity.

Much of the current understanding of evaporite sequences has come from their association and the subsequent data acquisition with prolific hydrocarbon provinces, such as the Precaspian Basin (Rowan *et al.*, 2019), the South Atlantic conjugate margins (Blaich, Tsikalas and Faleide, 2008; Wen *et al.*, 2019), the Zagros basin (Amthor *et al.*, 2005; Bordenave and Hegre, 2010) and the North Sea (Peryt *et al.*, 2010), where sequences are important for both trapping geometries and seals (Sarg, 2001; Archer *et al.*, 2012). Similarly, evaporite formations will likely be important components in many subsurface developments required for the energy transition, in particular for geological storage sites (Duffy *et al.*, 2022).

This study uses observations and interpretations from 3D seismic and well data from the Southern North Sea to examine the style and distribution of the internal deformation within the layered evaporite sequences of the Zechstein. The findings here have implications for understanding the deformation within layered evaporites.

3.3 Geological Setting

The Zechstein Supergroup of Northern Europe is an laterally expansive group of layered evaporites that were deposited during the Lopingian of the Late Permian. The Zechstein has been studied extensively throughout the North Sea due to its importance in petroleum systems (Glennie, 1998). On the United Kingdom Continental Shelf (UKCS), the Zechstein is most commonly either the sealing sequence for the underlying Rotliegend natural gas reservoirs of the Southern North Sea (Bailey *et al.*, 1993) or has led to the formation of structural trapping geometries for intervals within the North Sea, such as for the Paleocene turbidites, Cretaceous chalk, Triassic and Jurassic reservoirs (Fraser *et al.*, 2002; Evans *et al.*, 2004; Jackson and Stewart, 2017; Baniak *et al.*, 2020).

3.3.1 Tectonic evolution

Two major east-west trending rift basins are present on the eastern side of the UKCS: the South Permian Basin and the North Permian Basin (Figure 3-1). The two basins are separated by the Mid-North Sea High and the Ringkøbing-Fyn High (Clark, Stewart and Cartwright, 1998) (Figure 3-1). These two larger basins host numerous smaller sub-basins, such as the Forth

Approaches Basin (Cartwright, Stewart and Clark, 2001) and the Silverpit Basin (Bailey *et al.*, 1993), located in the North and South Permian basins, respectively.

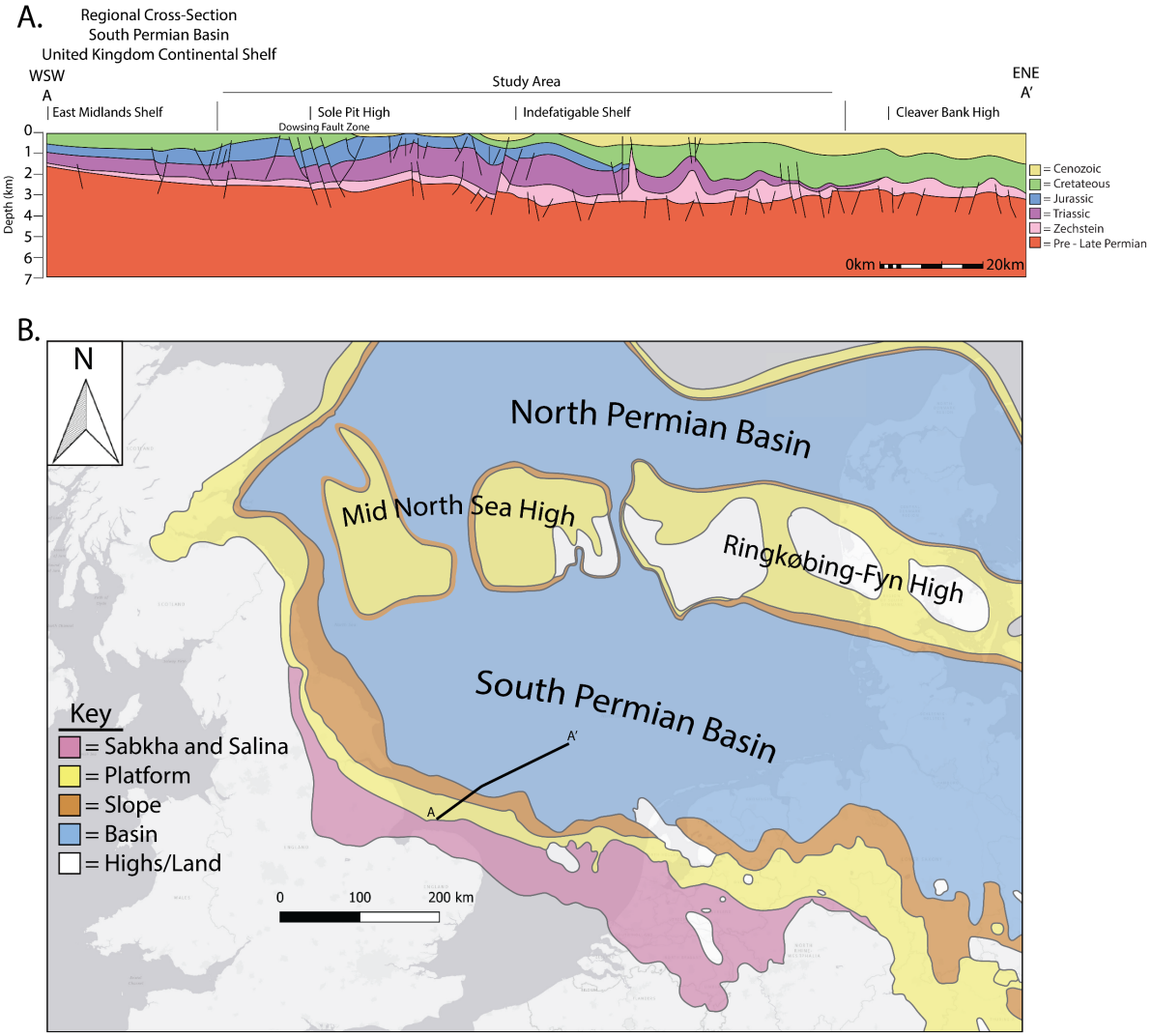

*FIGURE 3-1 - **A.** WSW - ENE TRENDING REGIONAL CROSS-SECTION OF THE SOUTH PERMIAN BASIN FROM JUST OFFSHORE THE UK TO THE EDGE OF THE UK CONTINENTAL SHELF. THE MAIN STRUCTURAL ELEMENTS AND STRATIGRAPHY (QUATERNARY - PRE-PERMIAN) WITHIN THE SOUTH PERMIAN BASIN ARE VISIBLE. REDRAWN FROM PHARAOH ET AL. (2010).**(B.)** PALEO-GEOGRAPHY MAP OF THE ZECHSTEIN'S DEPOSITION, REDRAWN FROM SŁOWAKIEWICZ ET AL. (2018). IMPORTANT GEOLOGICAL AREAS ARE NAMED, AND CROSS-SECTION A – A' IS MARKED.*

The South Permian Basin of the UKCS has developed over a period of 380 million years, consisting of a complex geological history with several rift and post-rift phases (Figure 3-2). Extension initiated with the collapse of the Late Devonian Variscan orogenic belt (Schulmann

et al., 2014; Pharaoh *et al.*, 2010) and subsequent Late Carboniferous inversion (Hodgson, Farnsworth and Fraser, 1992; Ziegler, 1990). Early-Permian rifting saw the two Permian basins of the North Sea open up and begin to develop (Hodgson, Farnsworth and Fraser, 1992; Glennie, Higham and Stemmerik, 2003). This rifting phase continued until the Middle Triassic, only briefly interrupted in the Late Permian by a phase of post-rift thermal subsidence (Hodgson, Farnsworth and Fraser, 1992; Geluk, 2007; Pharaoh *et al.*, 2010). Tensional stresses that developed during the period of Triassic rifting reactivated pre-existing faults and formed new fault systems, including those defining the East Irish Sea (Glennie and Underhill, 1998; Zanella and Coward, 2003a). Another rifting phase occurred from the Jurassic up into the Early Cretaceous (Erratt, Thomas and Wall, 1999), this phase of rifting thinned the lithosphere, allowing for a thermal anomaly which caused thermal doming and uplift (Zanella and Coward, 2003a; Pharaoh *et al.*, 2010; Ziegler, 1992b). However, this uplift event was short-lived, lasting until the Late Jurassic as rifting continued (Thomas and Coward, 1996). When rifting ceased in the Middle Cretaceous, the basin experienced a short-term period of thermal subsidence, which lasted until the Late Cretaceous (Pharaoh *et al.*, 2010). This was followed by a period of tectonic inversion, which was initiated in the Campanian and continued to the Early Cenozoic (Erratt, Thomas and Wall, 1999). As inversion ended, it was replaced by thermal subsidence once again; as the Cenozoic sediments began to be deposited into the North Sea thermal Sag basin, leading to up to 3 km of Cenozoic sedimentation in areas (Ziegler, 1990; Wong *et al.*, 2007).

The current day maximum horizontal stress field of the South Permian Basin is orientated in a North-North-West – South-South-East direction, resulting from a combination of North Atlantic ridge push and the collisional coupling of the foreland lithosphere with the Alpine-Carpathian Orogen (Hillis and Nelson, 2005; Pharaoh *et al.*, 2010). There are different stress provinces occurring within the North Sea and South Permian Basin, as it is suggested that the Zechstein salt units allow for stress detachment of basement from sediment fill in the basin (Hillis and Nelson, 2005).

The current day maximum horizontal stress field changed over geological time, during the Triassic dominant stress fields suggested to be North West – South East with minor East – West trending components, however minor variations occurred locally within the Basin (Zanella and Coward, 2003b; Williams *et al.*, 2015). This changed in the Jurassic – Early

Cretaceous where stress field changed to be North East – South West dominated (Zanella and Coward, 2003b). In the Late Cretaceous the maximum horizontal stress changed again to be North West – South East dominated (Williams *et al.*, 2015).

3.3.2 Zechstein Supergroup gross depositional environment

Prior to the deposition of the Zechstein Supergroup Evaporites, the Permian Rotliegend aeolian sediments were deposited during the early phases of thermal subsidence (Maynard and Gibson, 2001). During this phase of aeolian sedimentation, the basin was entirely landlocked, isolated from all surrounding ocean bodies (Peryt *et al.*, 2010). Subsidence of the basin was greater than that of the sedimentation rate, leading to an underfilled basin (Glennie, Higham and Stemmerik, 2003). The basin remained underfilled into the Late Permian due to the continued Permo-Triassic subsidence; this led to the centre of the basin being as much as 300 m below average sea level by the Late Permian, by the the onset of the Zechstein Supergroup deposition (Glennie, 1998).

The Zechstein ocean formed due to an influx of marine water into the underfilled Permian basins of Europe (Smith, 1979) after a significant transgression occurred from the Barents Sea to the north (Strozyk *et al.*, 2017). Both basins had restricted exchange of waters from the Northern Boreal Ocean and Southern Tethys Ocean (Pancost, Crawford and Maxwell, 2002), leading to little influx of marine water. Despite the initial influx of large amounts of oceanic water, the sedimentation rate during this period remained low, which, combined with the high temperature, arid environment, and limited water supplies, led to the Zechstein Ocean becoming a giant evaporite production area in both of Europe's Permian basins (Glennie, 1998). This period of evaporite deposition occurred in the Late Permian from 258 to 251 Ma, according to chemical analysis of fluid inclusions found within Zechstein halite (Lippolt, Hautmann and Pilot, 1993; Menning, 1995). The original depositional extent of the evaporite basin is represented by the modern-day distribution of the Zechstein (Jackson and Stewart, 2017).

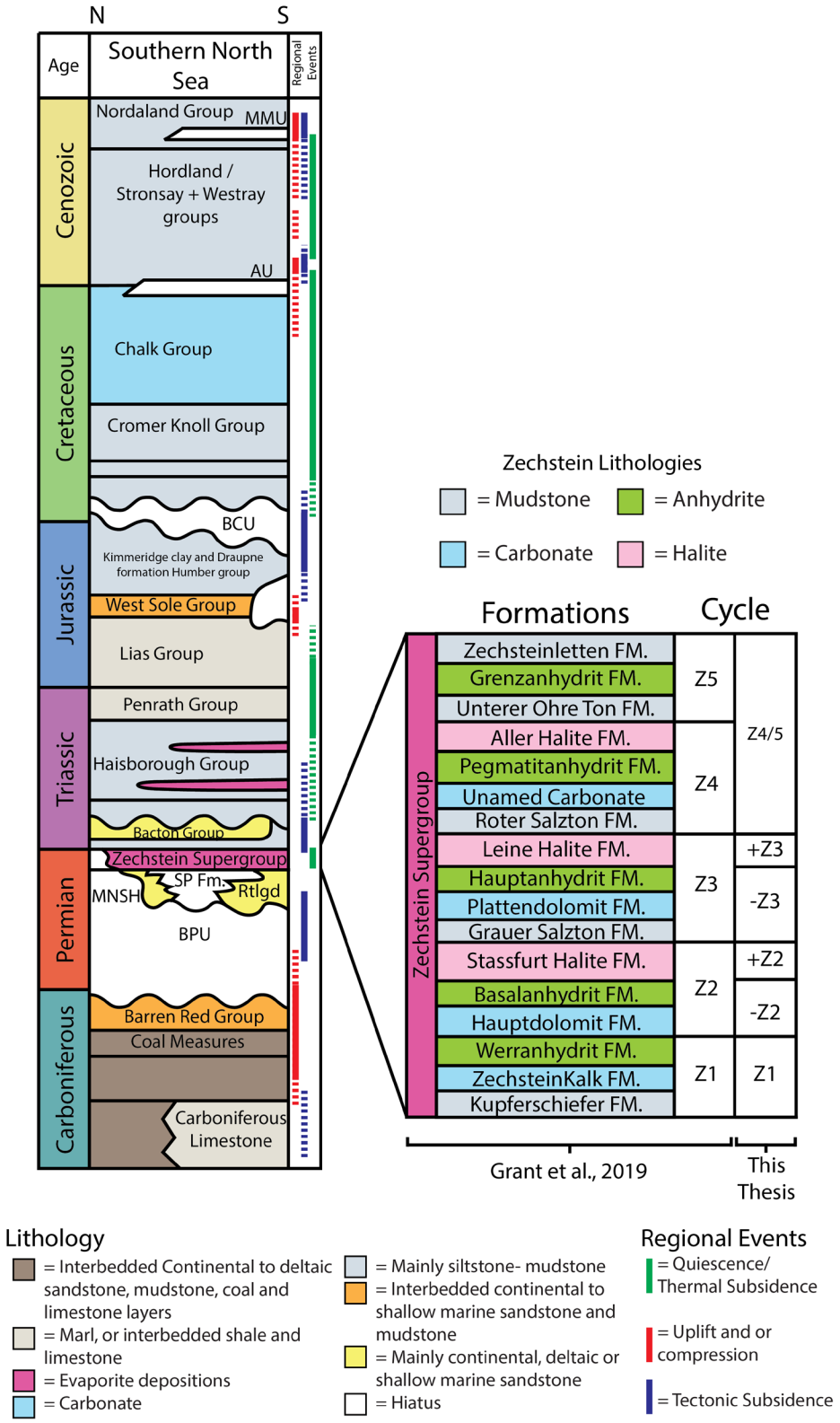

FIGURE 3-2 CHRONOSTRATIGRAPHIC CHART OF THE SOUTHERN PERMIAN BASIN STRATIGRAPHY RUNNING N – S THROUGH THE BASIN CENTRE MODIFIED FROM PATRUNO, KOMBRINK AND ARCHER (2022). ALL MAJOR STRATIGRAPHIC

SUCCESSIONS ARE SHOWN, AS WELL AS UNCONFORMITIES. REGIONAL GEOLOGICAL EVENTS FOR THE NORTH SEA PERMIAN BASINS ARE ALSO PRESENT. THE LITHOSTRATIGRAPHY OF THE ZECHSTEIN SUPERGROUP, ALONGSIDE THE ZECHSTEIN CYCLES, ARE INCLUDED. THE NOMENCLATURE FOR THE ZECHSTEIN FORMATIONS AND CYCLES IS FROM (GRANT ET AL., 2019), NEXT TO THIS NOMENCLATURE IS THE MORE DETAILED NOMENCLATURE USED TO DESCRIBE THE CYCLES IN THIS THESIS CHAPTER. THE ZECHSTEIN CYCLES ARE SUBDIVIDED INTO CYCLE COMPONENTS (+/-) USED IN THIS STUDY. MMU = MID MIOCENE UNCONFORMITY, AU = ATLANTEAN UNCONFORMITY, BCU = BASE CRETACEOUS UNCONFORMITY, SP FM = SILVERPIT FORMATION, RTLGD = ROTLIEGEND, MNSH = MID NORTH SEA HIGH, BPU = BASE PERMIAN UNCONFORMITY.

The Zechstein Supergroup's lithostratigraphy is separated into Zechstein cycles, commonly referred to as Z cycles, with either 5 or 7 in total, depending on the nomenclature used (Bailey *et al.*, 1993; Geluk, 2007) (Figure 3-2). The cycles' characterise cyclic evaporation, and hence depositional sequences relating to periods of transgression and regression within the restricted basin (Pharaoh *et al.*, 2010). Each depositional Zechstein cycle begins at maximum sea level with lithologies associated with depositional environments in settings of low salinity, such as carbonates. As the progressive evaporation of the marine waters occurs, the salinity of the brine in the basin increases, and so do the subsequently deposited lithologies (Peryt *et al.*, 2010). At the end of each Zechstein depositional cycle, total evaporation of the brine will likely have occurred, leading to the ground surface being completely dry until the next subsequent influx of water (Glennie, 1998).

3.4 Data

The study area (Figure 3-3) is located within the South Permian Basin of the UKCS, a mature gas basin that has been explored and exploited for the last 50 years (Rouillard *et al.*, 2020). The study area has the same extent as the seismic data used, covering a total area of 26,386 km^2. The western limit is ~20 km offshore the east coast of England and extends east to the easternmost edge of the UK sector of the Southern North Sea. The most northern extent of the study area is defined by the Mid-North Sea high and stretches south from this margin for 280 km. The seismic and well data are available from the North Sea Transition Authority

National Data Repository [https://ndr.nstauthority.co.uk/] under an Open Government Licence.

3.4.1 Seismic data

The seismic data used in this study was the Southern North Sea Mega Survey Revision.2 (SNSMSR2) (Figure 3-3), which was merged and processed by Petroleum Geo-Services (PGS) in 2015. This 3D merged seismic data set is comprised of 86 individual surveys from the UK sector of the Southern North Sea. The original datasets used in the merge were generally zero-phased 3D time-migrated seismic surveys, each constituent survey was resampled to 4 ms, and inline/crossline grids interpolated to 12.5 m if they were not already. Before the final merging process, cleaning was accomplished using a time-variant filter to avoid miss-stacking to reduce noise in deeper sections. Phase matching for the surveys within the merge was not undertaken; however, polarity and amplitude matching were in order to decrease edge effects. The survey was generally zero-phased and displayed using the European polarity standard so that a negative amplitude represents an increase in acoustic impedance, and a positive amplitude represents a decrease in impedance. The vertical resolution of the SNSMSR2 varies throughout the data set due to the constituent surveys having different original acquisition parameters, however, it varies between ~12 m in the Cenozoic and ~52 m in the Zechstein (Table 3-2.). The full processing report can be found at [https://ndr.ogauthority.co.uk/].

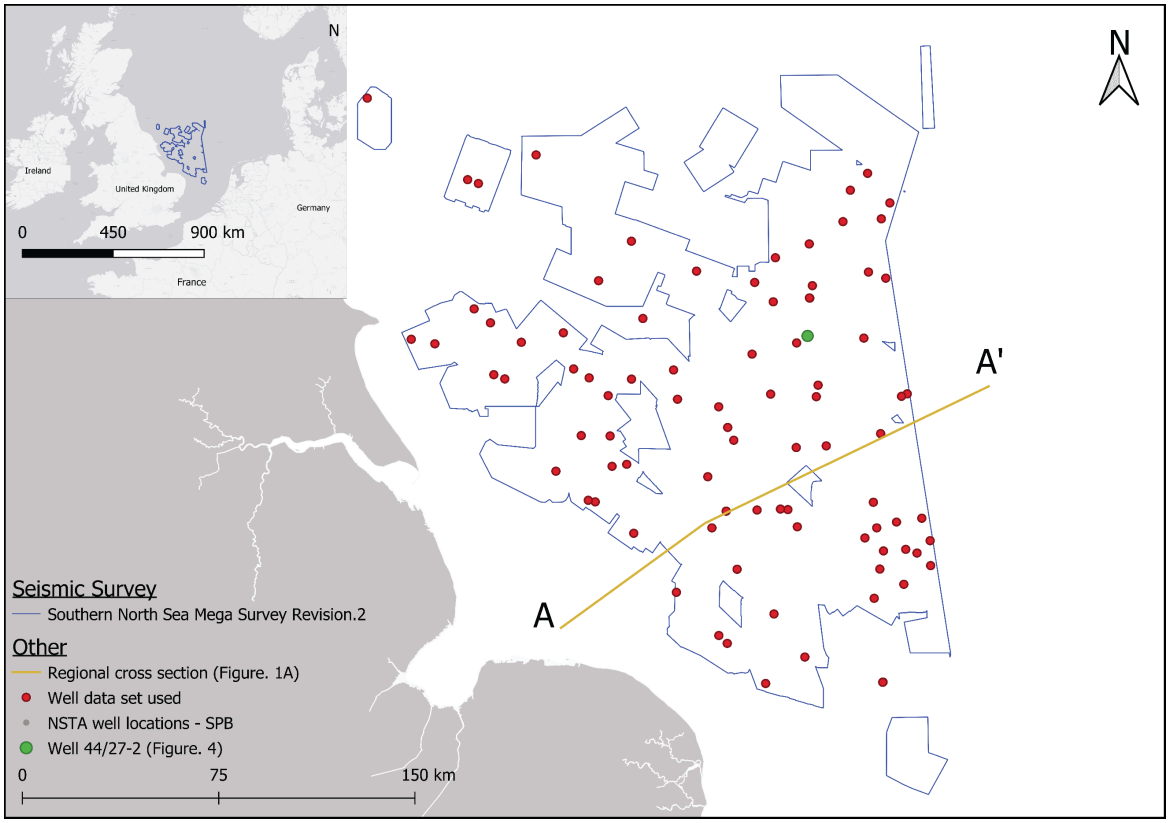

FIGURE 3-3 LOCATION AND DATA MAP FOR THE STUDY AREA. SUMMARY OVERVIEW OF ALL DATA USED WITHIN THIS STUDY AND ITS GEOGRAPHICAL LOCATION. THE TOP LEFT MAP SHOWS THE STUDY LOCATION WITH RESPECT TO THE UK AND EUROPE. THE SOUTHERN NORTH SEA MEGA SURVEY REVISION.2 SEISMIC SURVEY OUTLINE (BLUE) IS PRESENT ALONGSIDE THE LOCATIONS OF ALL WELL DATA USED WITHIN THIS CHAPTER. WELL 44/27-2'S LOCATION (FIGURE 3-4) IS MARKED ON. NSTA = NORTH SEA TRANSITION AUTHORITY, SPB = SOUTH PERMIAN BASIN.

3.4.2 Well data

96 wells were used during this study (Figure 3-3). The wells used within this study were selected based on whether the well penetrated the Zechstein Supergroup; the availability of petrophysical logs, specifically density, sonic and gamma ray, and the availability of checkshot data. Wells without these complete petrophysical logs were occasionally used in areas with poor data availability. A full list of the wells used in this study can be found in Supplementary Table A.

Main Unit	Depth (ms)	Dominant Frequency (Hz)	Seismic Velocity (m/s)	Vertical Seismic Resolution (m)	Notes
Cenozoic	-110 to -900	45	1872	12	Velocity extracted from wells in this study
Cenozoic	-110 to -900	40	1777	11	Velocity from (van Dalfsen *et al.*, 2016)
Cretaceous, Jurassic, Triassic	-900 to -1700	35	3186	18.2	Average Velocity extracted from wells
Cretaceous, Jurassic, Triassic	-900 to -1700	35	2548	32	Average Velocity from (van Dalfsen *et al.*, 2016)
Zechstein	-1700 to -2300	26.5	4500	42	Zechstein Low Seismic Velocity (van Dalfsen *et al.*, 2016)
Zechstein	-1700 to -2300	26.5	5500	51	Zechstein High Seismic Velocity. (van Dalfsen *et al.*, 2016)

TABLE 3-2 SEISMIC RESOLUTION EXAMPLES FOR SLICE INLINE 31000 – 35000, CROSSLINE 32000 – 35000 FROM THE SNSMSR2. RESOLUTIONS HAVE BEEN CALCULATED FOR SPECIFIC TIME VALUES. VELOCITIES USED WERE EXTRACTED FROM WELLS AND TAKEN FROM LITERATURE, AS DENOTED IN THE TABLE.

3.5 Methodology

3.5.1 Well interpretation

Lithologies and stratigraphic boundaries were interpreted for the Zechstein Supergroup (Figure 3-4) using a combination of petrophysical properties, lithology composite logs and cuttings descriptions. Lithologies for the Zechstein Supergroup were defined for the minimum thickness interval possible using the petrophysical data, which, while dependent on the logging tool used, was between 0.3 and 2.5 m (Bourke *et al.*, 1989). Lithologies for younger stratigraphy were also interpreted to enable a consistent seismic stratigraphic framework to be constructed across the study. Synthetic-seismic well ties were generated for 60 wells to correlate lithological and seismic-stratigraphic boundaries interpreted from wells to the seismic data. A full list of wells for which synthetic-seismic ties were generated is available in

Supplementary Table A. These well ties were generated using sonic and density logs, together with checkshot data. Synthetic traces were generated using an analytical 30Hz ricker wavelet and extracted wavelets, which were compared with the original seismic data to determine which wavelet was the best fit. In some cases, synthetic-seismic traces required time-shifting or stretching to account for mismatch in datums, largely a result of using a merged seismic volume. The synthetic is compared to multiple traces from the surveys as many of the wells throughout the study area are deviated (e.g Figure 3-4). The most prominent responses within the generated synthetics are from halite-carbonate and halite-anhydrite interfaces (Figure 3-4 - e.g. 2307 ms – 2356 ms), for example the +Z3 - -Z3 and +Z2 - -Z2. The large reflection coefficient resulting from the boundary between these two lithologies/cycles gives a strong seismic response and as such the strong resultant reflections can be utilised as marker beds in the SNSMR2. In Figure 3-4, only a few beds have both top and base fully resolvable within the generated synthetic, notably the 77 m thick k-salt bed within the +Z3 (3037 – 3114 m) and the 100 m thick -Z3 anhydrite bed (3400 – 3500 m).

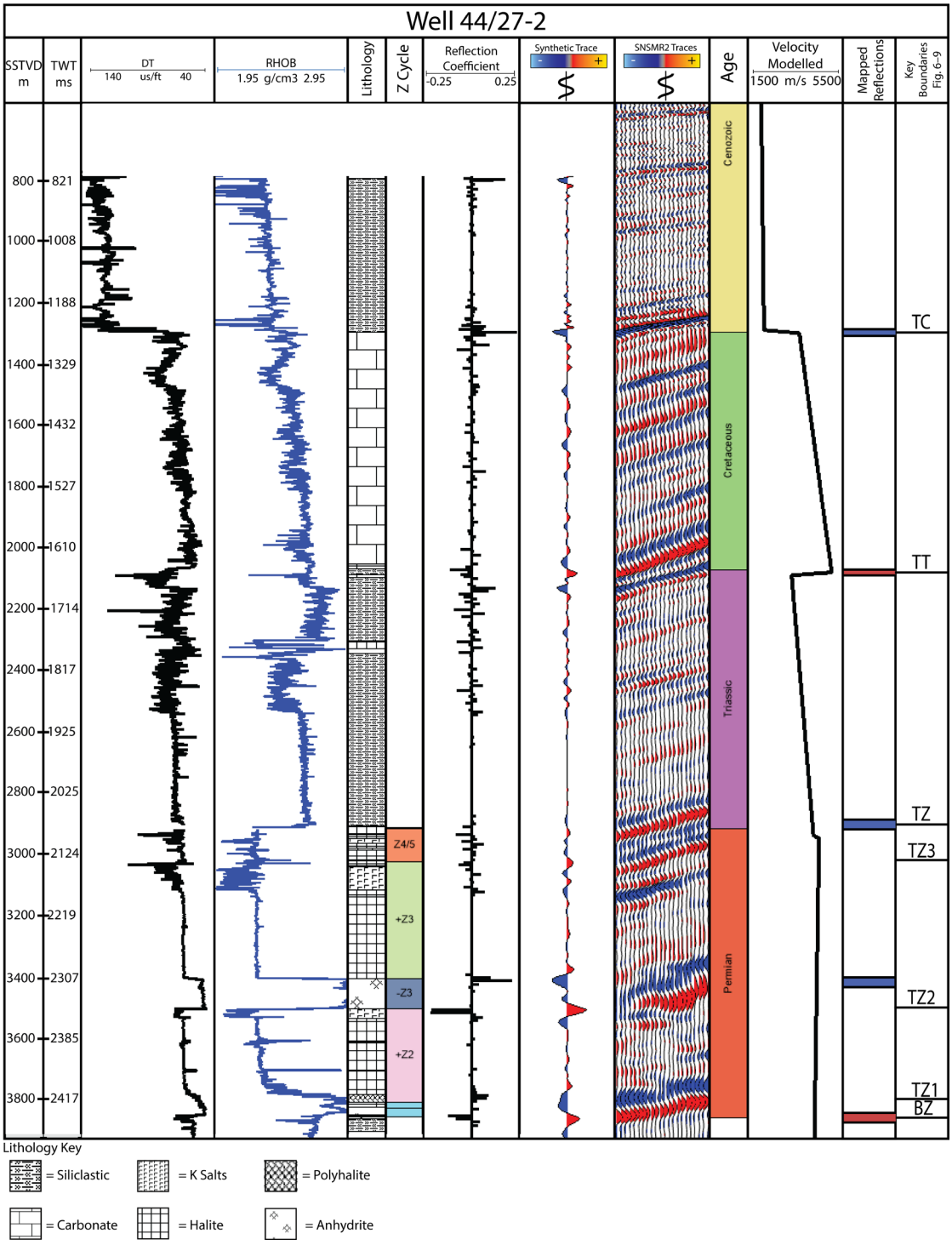

FIGURE 3-4 PETROPHYSICAL LOGS, INTERPRETED LITHOLOGY LOG, ZECHSTEIN CYCLE, SYNTHETIC-SEISMIC WELL TIES, FORMATION AGE AND CALCULATED VELOCITY MODEL EXTRACT OF WELL 44/27-2 IN THE SOUTHERN NORTH SEA. 44/27-2 IS LOCATED WITHIN THE DEPOCENTER OF THE SOUTH PERMIAN BASIN (FIGURE 3-3). PETROPHYSICAL LOGS SHOWN ARE SONIC (DT) AND DENSITY (RHOB). AN INTERPRETED LITHOLOGY LOG IS PRESENT, AS WELL AS INTERPRETED ZECHSTEIN CYCLES AND STRATIGRAPHIC AGES. LITHOLOGICAL INTERPENETRATION FOR THE ZECHSTEIN WAS

UNDERTAKEN AT THE SAME RESOLUTION AS THE PETROPHYSICAL LOGS ALLOWED. THE INTERVAL VELOCITIES FOR THE WELL USED WITHIN THE VELOCITY MODEL ARE PRESENT; NOTE THE CHANGE IN VELOCITY AT MAJOR LITHOLOGICAL BOUNDARIES. KEY SEISMIC REFLECTIONS ARE ALSO SHOWN.

3.5.2 Seismic interpretation

Major stratigraphic as well as lithological boundaries identified in the well data were subsequently interpreted in the 3D seismic, based on the seismic–well ties (Figure 3-4). Reflections were initially mapped using an inline and crossline spacing of 1250 m and then auto-tracked and quality-controlled, areas with low auto-tracking confidence were mapped at a reduced inline/crossline spacing, typically between 125 m and 250 m to improve the confidence in 3D auto-tracking. Surfaces were generated from the auto-tracked horizons using a convergent gridding algorithm with a grid spacing of 50 x 50 m to create seamless surfaces (Figure 3-5A). A common problem with the SNSMSR2 survey is the lack of continuity of the sea bed reflection. This issue, also observed by Grant *et al.* (2019), was likely due to survey vintage and age, these issues were particularly problematic in areas of shallow water depth. To counter this problem, instead of using the water bottom reflection, bathymetry data from EMODnet was used and converted to two-way travel time, assuming a water velocity of 1494 m/s, a similar approach to previous studies (e.g. Grant *et al.*, 2019).

The Zechstein cycles can be interpreted in seismic data, where the cycle thickness is above the tuning thickness (Strozyk *et al.*, 2012). Thick halite units act as the final lithology deposited for each of the Z2, Z3 and Z4 cycles (Figure 3-2); the relative acoustic properties of the halite juxtaposed with anhydrite and dolomites leads to high acoustic impedance contrasts and hence these cycles are clearly differentiated on seismic data (Grant *et al.*, 2019). Critical cycles within this analysis are the Z2 and Z3 cycles, notably the +Z2 and +Z3 cycles (Figure 3-2), which are the thickest halite units present within the Zechstein of the South Permian Basin and the -Z3 anhydrite/carbonate cycle, which, due to its distinct strong seismic response, acted as the primary marker reflection.

Dip attributes were generated for surfaces of interest, notably the top of the Zechstein Supergroup and the -Z3 surface. This attribute measures the dip in degrees of the surface at

each point and applies a colour relating to the dip level; darker areas relate to higher levels of dip (Figure 3-6 - 9). This attribute aids in highlighting structural features and changes.

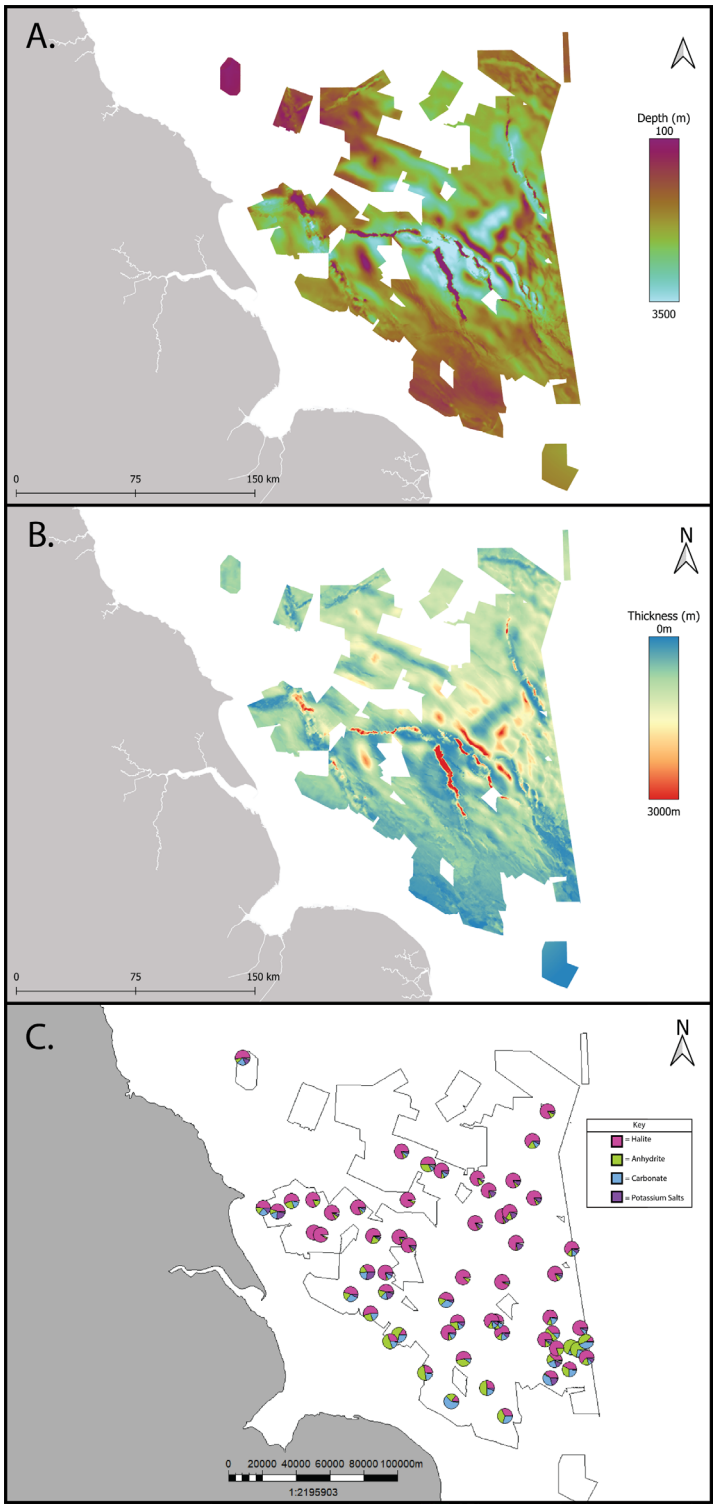

FIGURE 3-5 ZECHSTEIN PROPERTY MAPS GENERATED FROM THE SEISMIC DATA FOR THE STUDY. ***(A.)*** *DEPTH MAP TO THE TOP OF THE ZECHSTEIN SUPERGROUP EVAPORITES. THE TOP ZECHSTEIN SURFACE WAS ORIGINALLY MAPPED WITHIN THE SOUTHERN NORTH SEA MEGA MERGE REVISION 2. IN THE TIME DOMAIN AND THEN CONVERTED TO DEPTH USING THE*

GENERATED VELOCITY MODEL. ***(B.)*** *TRUE VERTICAL THICKNESS MAP OF THE ZECHSTEIN SUPERGROUP EVAPORITES. THE THICKNESS MAP WAS GENERATED BY CALCULATING THE DISTANCE (M) BETWEEN THE TOP ZECHSTEIN DEPTH SURFACE AND THE BASE ZECHSTEIN DEPTH SURFACE (TOP ROTLIEGEND). NOTE THE TREND AND ORIENTATION OF SALT STRUCTURES ARE VISIBLE.* ***(C.)*** *LITHOLOGY PERCENTAGE DISTRIBUTION MAP OF THE ZECHSTEIN SUPERGROUP EVAPORITES. LITHOLOGY % MAPPED AS PIE CHARTS FOR WELLS IN WHICH LITHOLOGIES HAD BEEN INTERPRETED. THE PRIMARY EVAPORITIC LITHOLOGIES ARE INCLUDED.*

3.5.3 Depth Conversion and Velocity Modelling

As the SNSMSR2 was in the time domain, a velocity model was created to convert the generated seismic surfaces to the depth domain. A layered velocity model was generated, constrained by the six key stratigraphic surfaces mapped from the seismic data and using the bathymetry for the seabed surface. The model uses time/depth relationship from 75 wells across the survey area. Residuals between the generated velocity model and well tops were used to quantify the accuracy and precision of the model.

The velocity model was built using an iterative process; each time aiming to reduce the residuals to a maximum of 5% for the top and base of the Zechstein. This process involved quality control checking the time-depth data in the wells, removing spurious velocity data, and changing the weighting of different wells' influence spatially on surrounding surfaces. Further information on the velocity modelling and building process can be found in the data repository.

3.5.4 Intra-Zechstein structural deformation styles interpretation

To interpret the internal deformation of the Zechstein evaporites, the internal reflection geometries were classified, principally constrained by the geometry of the prominent seismic reflections of the -Z3 Plattendolomit and the -Z3 Hauptanhydrit (Figure 3-4). Based on these interpretations of the 3D seismic data, the intra-Zechstein deformation styles were characterised based on the following characteristics; observable internal folds and associated geometries such as amplitude and wavelength, reflection terminations, faults present and where they were located and where in the Zechstein cycles have these features observable. A nomenclature was derived to classify the internal Zechstein geometries based on these

observed features, which are named as follows; planar and continuous, gently folded and continuous, open and continuous, closely folded and poorly imaged, areas of withdrawal and the chaotic reflections. The structural deformation styles interpretation included both cross-section views of the seismic data and from the geometries observed on interpreted surfaces in map view. While the nomenclature for the Zechstein used in (Strozyk *et al.*, 2012) and (Grant *et al.*, 2019) can be applicable to the deformation styles interpreted within this work, they are not detailed enough to allow the distinction of the separate layers and lithological and rheological groups undergoing structural deformation within the Zechstein, hence a new nomenclature was derived.

Internal shortening for seismic reflections within the Zechstein was calculated using the following equation;

$$Shortening\ \% = \left(\frac{Original\ length - Final\ length}{Original\ length}\right) * 100 \qquad \textit{EQUATION 20}$$

Shortening calculations were undertaken only on depth surfaces a 1x vertical exaggeration.

3.6 Data observations and Results

The base Zechstein is a prominent positive zero phase reflection across the study area (Figure 3-4). Frequently small-scale extensional faults can be interpreted to displace the reflection (Figure 3-6A, B); these faults do not propagate to the top of the Zechstein being isolated to the Z1 cycle and the base of Z2. The top Zechstein reflection is a negative reflection; however, since there is no significant velocity contrast (Figure 3-4) between the overlying Triassic interval and the Zechstein, the event is generally of low-amplitude (Figure 3-4). The steep dip of the strata at the flanks of both internal and external salt structures makes it challenging for seismic data to correctly image these features' geometries, which exacerbates the difficulty in interpretation. Within the Zechstein interval, the internal geometries vary significantly (Figure 3-6, 3-7, 3-8, 3-9). In areas that are absent of major salt structures, the thickness of the Zechstein Supergroup ranges from less than <47 m i.e. below seismic resolution to >1.5 km (true vertical thickness) (Figure 3-5 A-B). In the core of major salt structures characterised by salt diapirs and anticlines, the thickness of the Zechstein can be >3 km thick (true vertical thickness) (Figure 3-5.B). This current-day thickness varies from the original depositional gross thickness of the Zechstein Supergroup due to salt mobilisation that has occurred.

The net to gross of halite to non-halite lithologies varies spatially throughout the basin (Figure 3-5C) In the more proximal areas of the basin, higher quantities of anhydrite and carbonates are present, with halite usually consisting of only <25% of the Zechstein's lithology, halite being 12.6% in well 48/30-6, for example. However, this changes further towards the basin depocenter with the highest halite % in none structured areas typically >75% halite, 81.3% in well 44/22-5 for example.

3.6.1 Intra-Zechstein deformation styles characterisation

The following subsections describe the five defined deformation styles' characteristics. These sections are ordered by the magnitude of kinematic deformation that has been observed. The terminology used to define the deformation styles is derived from the coherent reflectivity observed from the -Z3 formation, which is the key marker bed used within the Zechstein.

3.6.1.1 Planar and continuous structural deformation style

The top Zechstein reflection normally has a planar geometry with little to no structure. Where strata is dipping it follows the base Zechstein reflecting the regional geology, however, rare anticlines are present throughout these areas, and these have large-scale wavelengths of 2.5 - 10 Km (Figure 3-6 A), with dip angles of limbs being <2°. No deformation is observed in the overlying Triassic, Cretaceous or Cenozoic intervals above this deformation style.

Reflections within the Zechstein are typically laterally continuous and planar with a dip parallel to the underlying Z1 unit and the uppermost Rotliegend group (Figure 3-6.A). All reflections show a continuous reflection character throughout the area (Figure 3-6.A). The seismic reflection amplitude of the -Z2 is lower than those of the Z3 and Z4 (Figure 3-6.A). A thickness decrease of 60ms can be identified within the Z2 towards the west of the cross-section (Figure 3-6.A), where the seismic reflections terminate. The overlying +Z3 also exhibits minor thickness changes, with a decrease in thickness towards the west, correlating with those observed in the +Z2 (Figure 3-6.A). The Z4/5 has subtle thickness changes between 12.5 – 20 ms; however, these are distinct from thickness changes or features of the Zechstein below. In these areas, the reflections' dip and dip direction change relate to the dip of the underlying Z1 Zechstein cycle sediments rather than due to the influence or formation of salt-related structures. The average dip of the -Z3 in this area is 2°, with a maximum dip of 4°. There are no observed faults of folds within the salt in these areas.

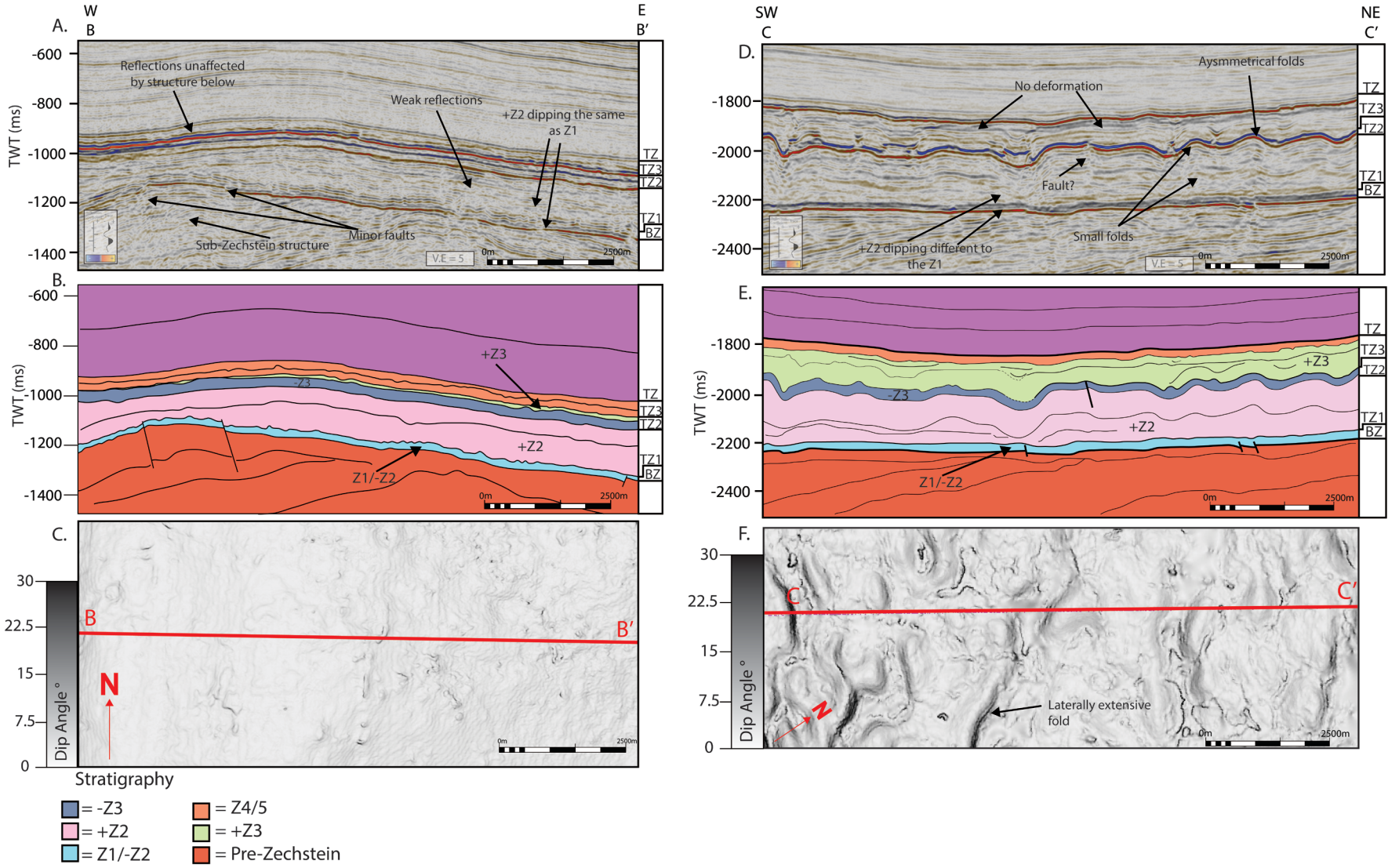
A.
W
B
E
B′
-600
-800
-1000
-1200
-1400
TWT (ms)
Reflections unaffected by structure below
Weak reflections
+Z2 dipping the same as Z1
Minor faults
Sub-Zechstein structure
V.E = 5
0m
2500m
TZ
TZ3
TZ2
TZ1
BZ
B.
+Z3
-Z3
+Z2
Z1/-Z2
C.
30
22.5
15
7.5
0
Dip Angle °
B
B′
N
Stratigraphy
= -Z3
= +Z2
= Z1/-Z2
= Z4/5
= +Z3
= Pre-Zechstein
SW
C
NE
C′
D.
-1800
-2000
-2200
-2400
No deformation
Aysmmetrical folds
Fault?
+Z2 dipping different to the Z1
Small folds
E.
F.
C
C′
Laterally extensive fold

FIGURE 3-6 SEISMIC SECTIONS OF B – B' AND C – C' OF THE ZECHSTEIN FROM THE SNSMSR2, ***(A.)*** *UNINTERPRETED AND* ***(B.)*** *INTERPRETED (A.) SEISMIC SECTION RUNNING W – E IN AN AREA CHARACTERISED AS PLANAR AND CONTINUOUS. THE VERTICAL AXIS IS IN TWO–WAY TRAVEL TIME.* ***(C)*** *DIP SURFACE OF THE -Z3 REFLECTION OF THIS CROSS-SECTION, WITH THE LOCATION OF THE CROSS-SECTION MARKED IN RED.* ***(D)*** *UNINTERPRETED AND* ***(E)*** *INTERPRETED (**D**.) SEISMIC SECTION RUNNING SW – NE IN AN AREA CHARACTERISED AS GENTLY FOLDED AND CONTINUOUS. THE VERTICAL AXIS IS IN TWO–WAY TRAVEL TIME.* ***(F)*** *DIP SURFACE OF THE -Z3 REFLECTION OF THIS CROSS-SECTION IN A PLANE VIEW, WITH THE LOCATION OF THE CROSS-SECTION MARKED IN RED. THE SURFACE VIEW OF THE -Z3 SHOWS THE GEOMETRIES IN 3D SPACE AND MAKES THE ASYMMETRICAL FOLDS VISIBLE. SEE FIGURE 3-10 FOR LOCATION. IMPORTANT REFLECTIONS ARE MARKED ON THE RIGHT-HAND SIDE OF A,B,D AND E; TZ (TOP ZECHSTEIN), TZ3 (TOP Z3), TZ2 (TOP Z2), TZ1 (TOP Z1) AND BZ (BASE ZECHSTEIN). SEISMIC POLARITY CARTOONS USED IN ALL SEISMIC SECTIONS ARE MODIFIED FROM AGILE-SCIENTIFIC (2012)GENTLY FOLDED AND CONTINUOUS STRUCTURAL DEFORMATION STYLE*

3.6.1.2 Gently folded and continuous structural deformation style

The top salt within this area is commonly folded. These folds have large wavelengths of 2.5 – 15 km and a trend of NW – SE (Figure 3-5.A). A large open syncline can be seen in Figure 3-6E. In areas where top salt forms anticlines or synclines, the -Z3 follows this geometry, forming folds of the same wavelength independent of the smaller folds within the -Z3. While internally, the Zechstein shows evidence of significant deformation, the top of the interval remains relatively undeformed. As the deformation is entirely within the Zechstein Supergroup, there is no observed deformation in the overlying Triassic, Cretaceous or Cenozoic.

The internal reflections within the Zechstein are parallel to those of the base Zechstein, however, there are distinct areas where the reflections display deformation in the form of folds (Figure 3-6D). These folds are asymmetric and are observed to affect the +Z2 as well as the reflections of the -Z3 (Figure 3-6D). The folds have a wavelength of 1 – 3 km, an amplitude of 50 – 100 ms, and limbs which dip ranging from 5 - 14°. The axial plane of the folds are typically gently inclined. The traces of the fold axis are 1 – 5 km within this area and have no preferred orientation (Figure 3-6E). Folds are not observed in the +Z3 and Z4/5 Zechstein units

(Figure 3-6 D,E). Line length comparison of the top Zechstein and -Z3 was measured and compared, the -Z3 was 2.3% longer than the top Zechstein (12.38 km vs 12.67 km).

The reflections of the +Z3 and Z4/5 are continuous and can be traced extensively across the basin. The +Z3 and Z4/5 Zechstein cycles remain comparatively undisturbed by the deformation occurring in the +Z2 and -Z3. Despite minor localised deformation within the +Z3 above the folds in the -Z3, the seismic reflections are parallel with one another, and the top and base Zechstein reflections. The interval from the top -Z3 reflection to the top Zechstein thins across anticline crests and thickens into synclines, with areas above synclines being up to 200m thicker than above the anticlines (Figure 3-6E).

The base Zechstein Z1 has occasional extensional faults (Figure 3-6D). The top termination for the faults occurs at the top Z1 reflection, unaffecting the Z2, and the base terminate into the sub-Zechstein strata below, with the maximum level of displacement occurring at the Z1 level. The faults have a throw ranging between 35 – 65 m, and a heave between 40 – 200 m.

Rare extensional faults are observed (Figure 3-6D) within the +Z2 and -Z3, displacing the top of the +Z2 and the base of the -Z3. The faults termination points are within the +Z2 and -Z3. These faults are 380 - 450 m and a displacement of up to 95 m. Alternatively, these features could be interpreted as monoclines with steeply dipping limbs, as the surrounding folds being compressional, it would be unlikely for extensional faults to be present.

3.6.1.3 Open folded and continuous structural deformation style

The top Zechstein is commonly undeformed, remaining parallel with the base Zechstein. However, some areas of the top Zechstein form rare anticlinal and synclinal structures, which trend NW – SE (Figure 3-5A), similar to observations seen in section 4.1.2. in Figure 3-7.A the top Zechstein defines a gentle syncline with a wavelength of 7.2 km. The deformed -Z3 follows the top Zechstein's geometry to form gentle anticlines and synclines of the same wavelength, independent of the asymmetric folds present in the -Z3.

The intra-Zechstein units exhibit prominent levels of deformation, specifically within +Z2 and -Z3 units (Figure 3-7A.). The seismic reflections of the lower +Z2 are increasingly discontinuous, with asymmetrical folds visible, which are also present in the -Z3. By comparison, the top +Z3 and Z4/5 are relatively undeformed (Figure 3-7.A).

The folds in +Z2 and -Z3 are asymmetrical, have inclined axial planes and are similar to those seen in the gently folded structural domain (Figure 3-7.A). The asymmetrical folds have wavelengths of 0.4 – 1 km, amplitudes from 100 – 300 ms and dip on the fold limbs typically ranging from 10 - 35°, with a maximum dip of 38°. The fold traces of the structures range in length from 1.5 – 9 km (Figure 3-7.C). This area shows the fold axis trends in an NE – SW orientation; however, the orientation has been observed to be different in other parts of the basin, with orientations trending closer to N - S. Line length of the top Zechstein and -Z3 was measured and compared, the -Z3 was 8.6% longer than the top Zechstein (9.78 km vs 10.62 km).

Units +Z3 and Z4/5 is 350 – 420 m thick within the synclines and only 270 -300 m thick above the flanking anticlines of the -Z3.(Figure 3-7.A). Within the Z4 Zechstein unit, there are isolated reflections which terminate onto the stratigraphically lower sections of Z4 (Fig 7.A.); there are two possible interpretations to these features; 1) Strain-induced thickness changes from salt mobility, or 2) These terminations represent intra-Zechstein onlap features, which would suggest a small level of salt mobility syn-depositionally.

Very rare faults are present within the Zechstein, displacing the -Z3 and the top of the +Z2 within the Zechstein in this area (Figure 3-7.A). Reverse faults (Figure 3-7.A) are observed, which terminate downwards in the basal part of the +Z2 Zechstein and upwards in the base of the +Z3. These faults have throws of ~120 m, a heave of ~240 m, a length of ~400 m and a displacement of ~230 ms.

The base Zechstein Z1 is deformed by NW – SE trending extensional planar faults; however, they are more common and are larger than those observed in the gently folded and continuous structural deformation style (Figure 3-7.A). The faults continue to terminate downwards at the top Z1 reflection, with the top of the Z1 having been juxtaposed against the Z2. The basal termination for these faults is still pre-Zechstein strata, however, the length of these faults is greater than those present within in the gently folded and continuous structural style, being < 1km. The faults have a throw ranging between 60 - 80 m and a heave between 50 – 150 m. The faults do not have any spatial relationship with the deformation occurring above within the Zechstein, as faults within the Z1 occur below both anticlines, synclines and limbs of the folding in the above Z2 and -Z3.

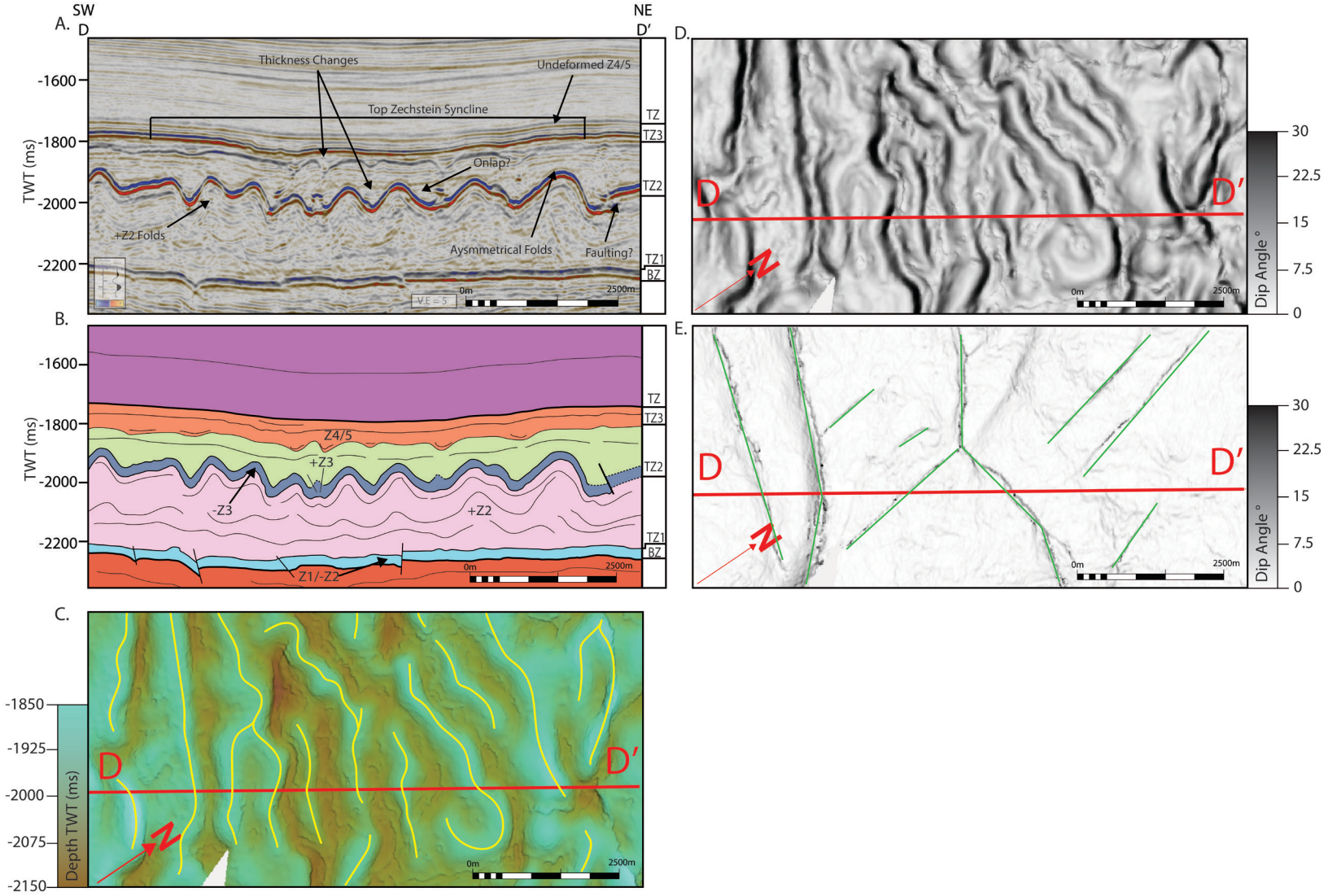
A.
SW
D
NE
D′
Thickness Changes
Undeformed Z4/5
Top Zechstein Syncline
Onlap?
+Z2 Folds
Aysmmetrical Folds
Faulting?
TWT (ms)
-1600
-1800
-2000
-2200
TZ
TZ3
TZ2
TZ1
BZ
V.E = 5
0m
2500m
B.
Z4/5
+Z3
-Z3
+Z2
Z1/-Z2
C.
-1850
-1925
-2000
-2075
-2150
Depth TWT (ms)
D
D′
N
D.
E.
Dip Angle °
30
22.5
15
7.5
0

FIGURE 3-7 SEISMIC SECTION D – D' OF THE ZECHSTEIN FROM THE SNSMSR2. ***(A.)*** *UNINTERPRETED AND* ***(B.)*** *INTERPRETED (A.) SECTIONS RUNNING SW – NE IN AN AREA CHARACTERISED AS OPEN FOLDED AND CONTINUOUS. THE VERTICAL AXIS IS IN TWO–WAY TRAVEL TIME. SEE FIGURE 3-10 FOR LOCATION. IMPORTANT REFLECTIONS ARE MARKED ON THE RIGHT-HAND SIDE OF BOTH A AND B, TZ (TOP ZECHSTEIN), TZ3 (TOP Z3), TZ2 (TOP Z2), TZ1 (TOP Z1) AND BZ (BASE ZECHSTEIN).* ***(C.)*** *TWT DEPTH SURFACE (MS) OF THE -Z3 REFLECTION WITHIN THE OPEN FOLDED AND CONTINUOUS STRUCTURAL STYLE. THE AXIAL TRENDS OF THE FOLDS PRESENT ARE MARKED IN YELLOW.* ***(D.)*** *DIP SURFACE OF THE -Z3 REFLECTION OF THIS CROSS-SECTION IN A PLANE VIEW, WITH THE LOCATION OF THE CROSS-SECTION MARKED IN RED.* ***(E.)*** *A DIP SURFACE MAP OF THE Z1/-Z2 ZECHSTEIN UNIT, DEMONSTRATING THE FAULTS PRESENT WITHIN THE BASE ZECHSTEIN, FAULTS ARE MARKED WITH A GREEN LINE.*

3.6.1.4 Closely folded and poorly imaged structural deformation style

The top Zechstein is commonly deformed, forming anticlines and synclines with wavelengths of 3 – 15km and fold trend orientations of NW - SE. Some anticlines have ruptured, developing into areas in which the Z2/Z3 salt units are seen to pierce the overburden forming diapiric salt structures. The mobile salt that has intruded upwards into the overburden has thinned. The sections where the overburden has been pierced occurs at the hinge of anticlines in the top Zechstein or in areas where faults within the overburden come into contact with the top Zechstein.

The Z1 is heavily deformed by NW – SE striking extensional faults (Figure 3-8.A,C). The faults are apparent every ~.75m - ~3.5 km; they have a greater displacement than previous Z1 extensional faults described in the gentle/open folded continuous structural style, with displacements of ~100 – 150 ms. The Z1 reflections are displaced significantly, juxtaposed against the above +Z2 (Figure 3-8.A).

The +Z2 is dominated by low amplitude, chaotic, discontinuous seismic reflections (Figure 3-8.A). However, individual reflections within the +Z2 can be differentiated. The reflections have varying high dips up to the ability of the seismic to correctly image them at ~66°. Asymmetric folds are visible within the +Z2; however, it is challenging to differentiate any continuous structures due to the seismic imaging (Figure 3-8.B).

The -Z3 seismic reflections that were continuous in the other previously identified deformation styles no longer have a continuous appearance, resulting in the +Z2 and +Z3 not being differentiable in places (Figure 3-8.A). Sections with asymmetric folds are present within the -Z3, forming open and tight folds. These folds have amplitudes of 65 – 195 ms, wavelengths of 1.1 – 1.6 km present and fold limb dips up to ~66°. Isolated high-amplitude reflections can be observed when the trajectory of the visible to none visible dipping limb is followed (Figure 3-8 A,B). Some none continuous sections of -Z3 may have no folds present; however, they have planar geometries that have been rotated to a high level of dip, the same dip levels as those observed fold limbs. Isolated areas of the -Z3 within this structural style typically have areas of 0.02 to ~ 10 km^2 (Figure 3-8.C). No preferred orientation within the hinge line of the folds, with both symmetrical and asymmetrical folds, can be observed, although this is likely due to the data quality. The top Zechstein in this section was measured to be 24.5 km while -Z3 was measured to be 31.6 km long, meaning a shortening of 26.1% has occurred.

The Z4/5 does not have the same level of intra-cycle deformation as the lower Zechstein units. The seismic reflections remain parallel, with a constant thickness; however, the geometry of the Z4/5 unit has been deformed as it now follows the geometry of the top Zechstein (Figure 3-8A, B). No faulting is observed within the Z4/5 units. Both the -Z2 and the +Z3 show significant inflation around the fold hinges, with the +Z3 increasing in thickness at its maximum point by 400 ms and the -Z2 by 300 ms.

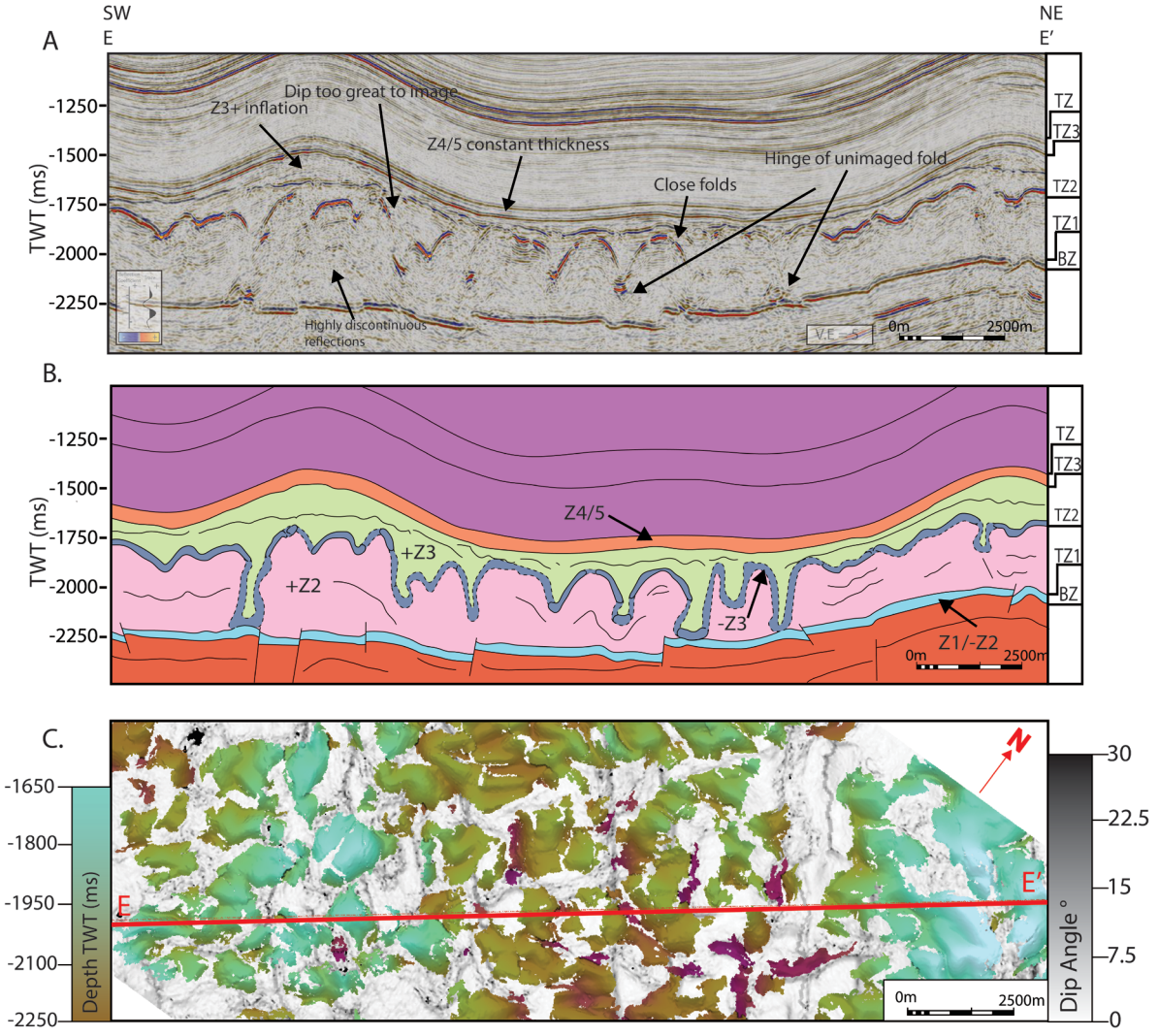
A
SW
E
NE
E'
-1250
-1500
-1750
-2000
-2250
TWT (ms)
Dip too great to image
Z3+ inflation
Z4/5 constant thickness
Close folds
Hinge of unimaged fold
Highly discontinuous reflections
V.E. ~5
0m
2500m
TZ
TZ3
TZ2
TZ1
BZ
B.
Z4/5
+Z3
+Z2
-Z3
Z1/-Z2
C.
-1650
-1800
-1950
-2100
-2250
Depth TWT (ms)
E
E'
N
30
22.5
15
7.5
0
Dip Angle °

FIGURE 3-8 A SEISMIC SECTION E – E' OF THE ZECHSTEIN FROM THE SNSMSR2, ***(A.)*** *UNINTERPRETED AND* ***(B.)*** *INTERPRETED (A.) RUNNING SW - NE IN AN AREA CHARACTERISED AS CLOSELY FOLDED AND POORLY IMAGED. THE VERTICAL AXIS IS IN TWO–WAY TRAVEL TIME. SEE FIGURE 3-10 FOR LOCATION. IMPORTANT REFLECTIONS ARE MARKED ON THE RIGHT-HAND SIDE OF BOTH A AND B, TZ (TOP ZECHSTEIN), TZ3 (TOP Z3), TZ2 (TOP Z2), TZ1 (TOP Z1) AND BZ (BASE ZECHSTEIN). (C) TWT DEPTH SURFACE (MS) OF THE -Z3 REFLECTION OF THIS CROSS-SECTION IN A PLANE VIEW, WITH THE LOCATION OF THE CROSS-SECTION MARKED IN RED.*

3.6.1.5 Area of withdrawal structural deformation style

These areas are typically found adjacent to major salt structures, such as salt diapirs and anticlines. These areas form predominantly elongate oval-shaped areas that align with the salt structures they flank, for example, the middle basin salt walls are completely encased by this structural style, which also occurs in WNW – ESE trending belts (Figure 3-5.B).

The Z2 is thinner than elsewhere in the basin, being only 42-47 m thick. In some sections, the lack of -Z2 is such that the Z5 and Z1 could be interpreted as being in contact with one another (Figure 3-9.A). The visible patches of Z2 salt have planar seismic reflections present within the Zechstein. Small areas of high amplitude reflections are present in the remnants of the Z2 salt (Figure 3-9.A). The +Z3 unit is not visible, unlike the other deformation styles observed within the basin(Figure 3-9.A), thinning until it is no longer seismically resolvable. The isolated high amplitude patches in these areas may be remnants of the -Z3 having undergone brittle deformation.

Post-Zechstein strata are thickened above these deformation areas, especially within the Cenozoic sedimentary deposits (Figure 3-2). The strata above the fringes of the area of withdrawal structural style always show dips pointing towards the lowest point of top salt, forming large-scale synclines ranging from 0.1 - 10's kms scale.

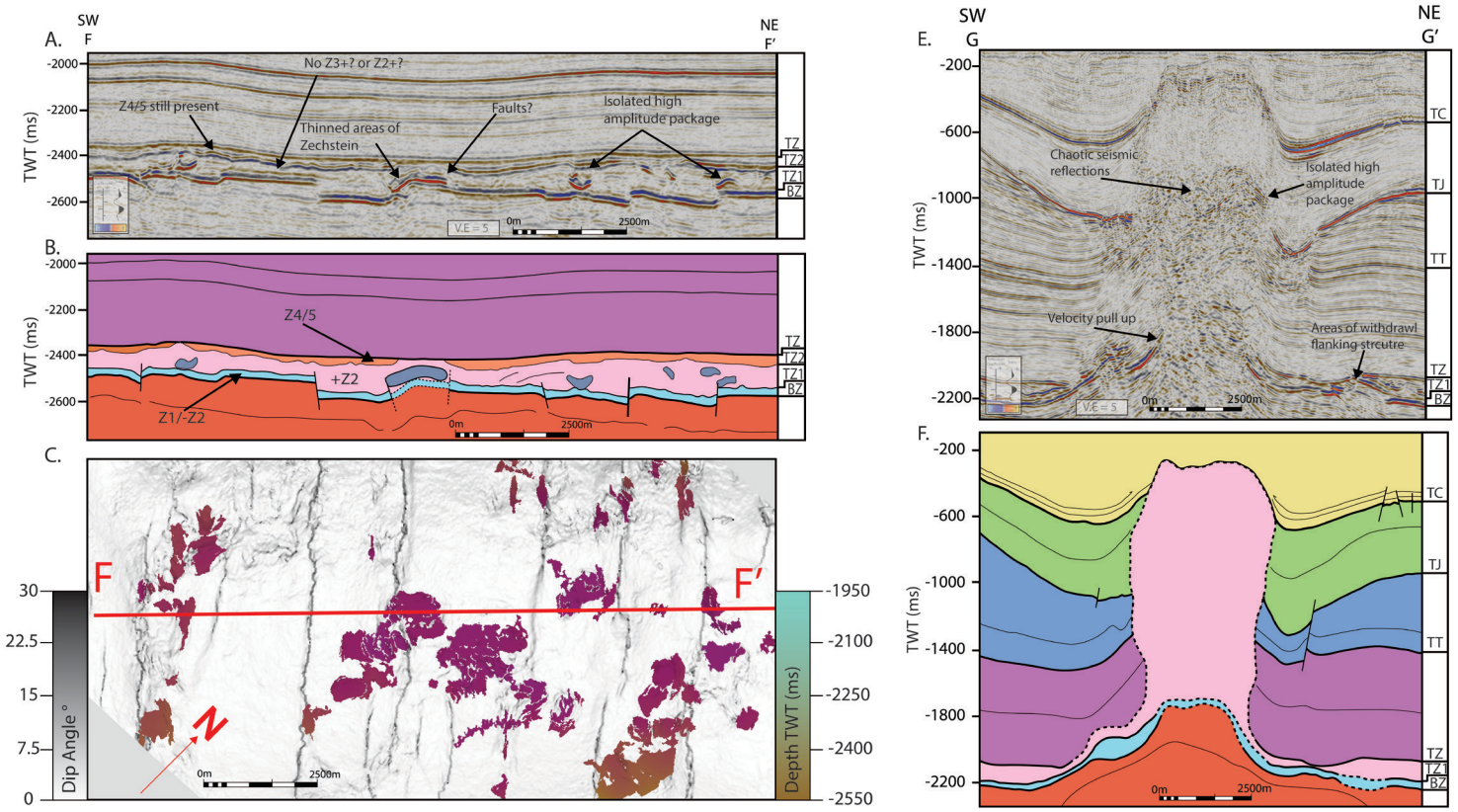

FIGURE 3-9 A SEISMIC SECTIONS OF F – F' AND G – G' OF THE ZECHSTEIN FROM THE SNSMSR2, ***(A.)*** *UNINTERPRETED AND* ***(B.)*** *INTERPRETED (A.) RUNNING SW - NE IN AN AREA CHARACTERISED AS AREA OF WITHDRAWAL. THE VERTICAL AXIS IS IN TWO–WAY TRAVEL TIME.* ***(E.)*** *UNINTERPRETED AND* ***(F.)*** *INTERPRETED (E.) RUNNING SW - NE IN AN AREA CHARACTERISED AS UNDIFFERENTIABLE INTERNAL DEFORMATION. THE VERTICAL AXIS IS IN TWO–WAY TRAVEL TIME. SEE FIGURE 3-10 FOR LOCATION. IMPORTANT REFLECTIONS ARE MARKED ON THE RIGHT-HAND SIDE OF BOTH A AND B, TC (TOP CRETACEOUS), TJ (TOP JURASSIC), TT (TOP TRIASSIC), TZ (TOP ZECHSTEIN, TZ1 (TOP Z1) AND BZ (BASE ZECHSTEIN).*

3.6.1.6 Chaotic reflections structural deformation style

Seismic reflections are not continuous for any section of the Zechstein within this structural domain, this incoherency could be any number of features, such as the internal stratigraphy still being competent and isoclinally folded, the internal stratigraphy no longer being competent and consisting of unimaged stringers, breccia or the likely highly complex internal structures are not resolvable by the conventional processing used for the SNSMSR2 (Figure 3-9.E). These deformation styles typically coincide with salt structures, such as NW trending salt diapirs or large anticlines (Figure 3-5.B). The flanks of these areas are typically surrounded by the withdrawal deformation structural style (Figure 3-9.E).

In rare areas, small packages of more continuous, high amplitude reflections are visible (Figure 3-9.E); these small packages are only visible on seismic for less than 1 km and have low dips. Wells that have drilled through these deformation styles and used within this study show more heterogeneity than in the seismic data. Interbeds of greater than the seismic resolution are present but have not been imaged correctly.

3.6.2 Well – Seismic correlations

Seismic well correlations were located through an area interpreted to be the closely folded and poorly imaged deformation style. The specific wells within the correlations were chosen to further understand the nature and distribution of the -Z3 reflection internally within the Zechstein Supergroup. The chosen wells for the correlation intercept the high amplitude reflection interpreted to be the -Z3, however, the choice of wells available was limited due to the required time-depth relationship data availability for wells in close proximity to one another.

The seismic section I-I' and associated well correlation (Figure 3-10) correlates four wells to the seismic survey in a trending NW – SE orientation. All wells present in the correlation contain stratigraphy which is interpreted to be the -Z3 interval. It should be noted that it is uncertain as to if there is any -Z3 stratigraphy present within the 44/21-1 well. A section of polyhalite has been labelled as '-Z3?' in Figure 3-10. This section has been marked as a possible -Z3 interval as current interpretations from well log and completion logs list the interval as polyhalite, however this may be incorrect as: 1) Within this interval the calliper log is of poor quality, suggesting borehole quality issues within this section and petrophysical

readings may not be correct, and 2) the borehole and '-Z3?' interval coincides with high amplitude reflections on the seismic data that could be interpreted to be the -Z3. Correlating this reflection with both wells 44/21a-5 and 44/22b-8 (Figure 3-10) aids in this argument, as both contain -Z3 for the same reflection if traced to the other wells. 44/21a-5's -Z3 section is ≈30 m and intersects on the edge of a linear high amplitude reflection. 44/22b-8's -Z3 section is ≈155 m thick and located within the axis of a recumbent syncline. 44/28-3 -Z3 section is ≈15 m thick and intercepts a weak dipping reflection. The well-seismic relationship shown in Figure 3-11,12 demonstrates that the vertical thickness of the -Z3 varies over relatively small distances, and that the dip of also varies greatly, thus both having an impact on the ability of seismic data to correctly image the reflector. Figure 3-11 shows high amplitude reflections of the -Z3 stratigraphy that are discontinuous and have folding geometries the same as previously described in section 3.6.1.3.

The wells in correlation panel Figure 3-11B show -Z3 that is interpreted to be at significantly different height locations within the Zechstein as well as large variations in thicknesses being present. The correlation of -Z3 stratigraphy to reflection on seismic data is different for each of the wells. While 44/26c-6 has a ≈30 m section of -Z3 stratigraphy present, there is no apparent seismic reflection present within the seismic data. 44/26-3 has a ≈130 m section of -Z3 stratigraphy present towards the base, this 130 m section of -Z3 correlates with a weak horizontal seismic reflection. 44/26-4 has a ≈62 m section of the -Z3 present, this section of -Z3 correlates with a dipping high reflection amplitude event either side of the well path (Figure 3-11). The high amplitude reflection shows a decrease in amplitude as the dip increases towards the top of the Zechstein and an increase of amplitude as the dip decreases towards the bottom of the Zechstein.

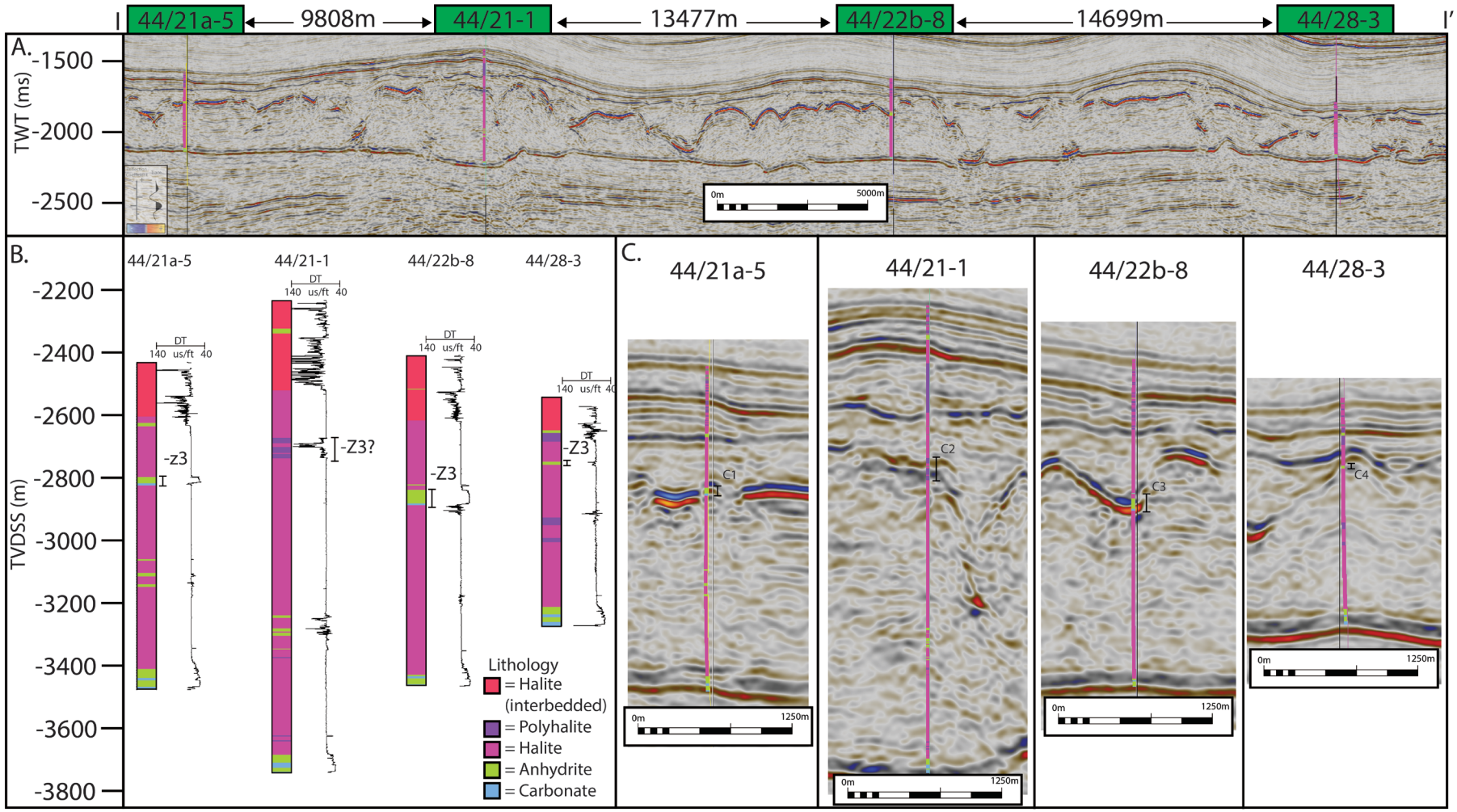

FIGURE 3-10 ***A.*** *WELL CORRELATION CROSS SECTION I – I' THROUGH THE ZECHSTEIN SUPERGROUP.* ***B.*** *LITHOLOGY COLUMN OF WELLS 44/26C-6, 44/26-3 AND 44/26-4 ALONG WITH A SONIC LOG.* ***C.*** *CLOSE UP OF WELL 44/26-4 OVERLAID ON SEISMIC SECTION*

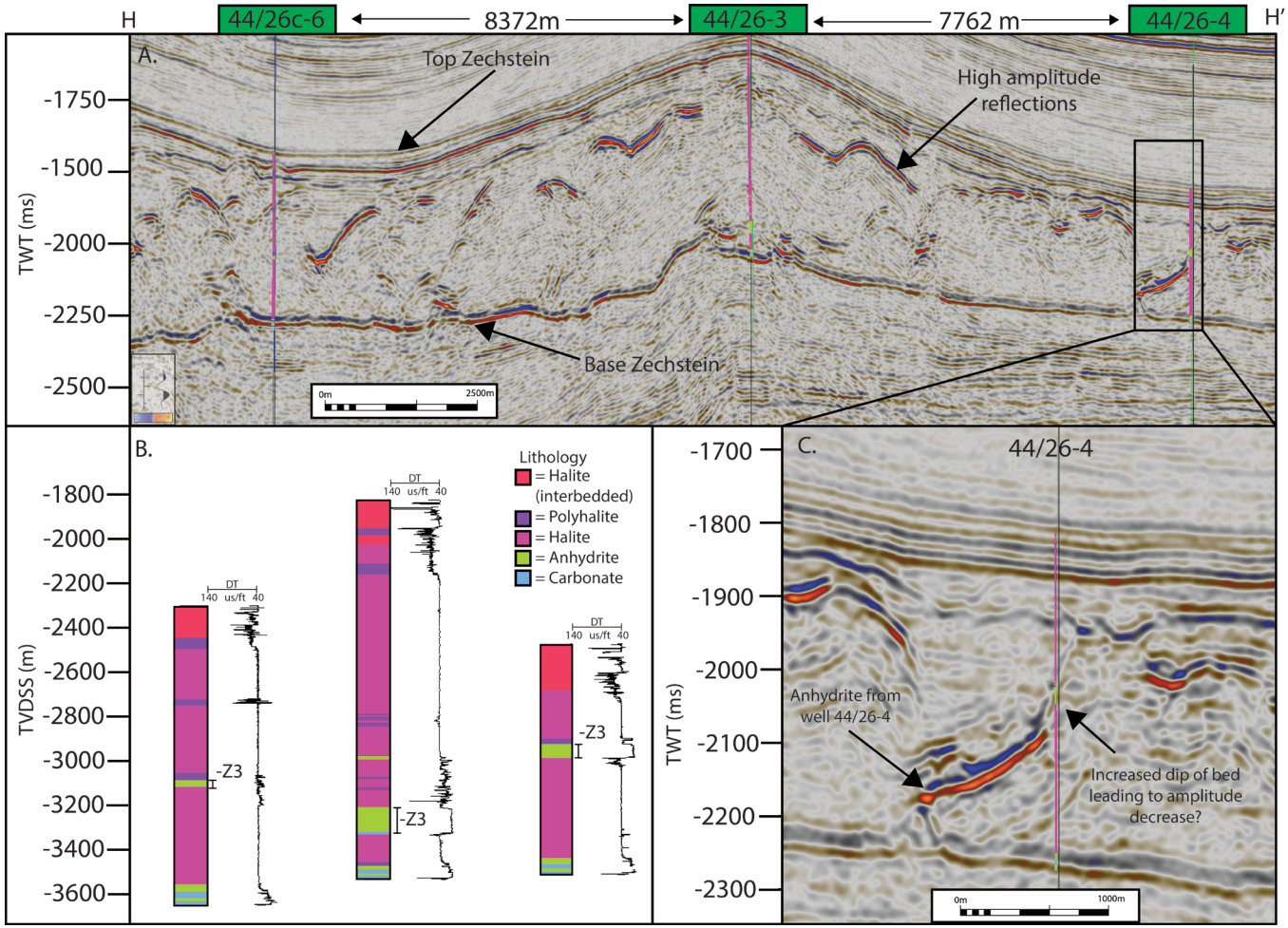

FIGURE 3-11 ***A.*** *WELL CORRELATION CROSS SECTION H – H' THROUGH THE ZECHSTEIN SUPERGROUP. B. LITHOLOGY COLUMN OF WELLS 44/26C-6, 44/26-3 AND 44/26-4 ALONG WITH A SONIC LOG.* ***C.*** *CLOSE UP OF WELL 44/26-4 OVERLAID ON SEISMIC SECTION*

3.6.3 Distribution of internal Zechstein deformation styles

The spatial distribution of the different internal deformation styles of Zechstein deformation is shown in Figure 3-10. The distinct deformation styles commonly coincide with styles of the adjacent deformation levels; however, the chaotic reflection deformation style appear enclosed within all other deformation styles identified, this is due to salt-cored structures being present within all identified domains.

The deformation styles identified provide evidence of spatially varying and a continuum in strain style and magnitude within the Zechstein Supergroup (Figure 3-6, 3-7, 3-8, 3-9). The distribution of the six identified deformation styles can be broadly split into three distinct structural domains (Figure 3-10). Domain A is located in the proximal area of the basin, it is characterised by the planar continuous and the gently folded deformation style. Small areas of chaotic reflection deformation style are present sporadically throughout this domain. Domain B, within the central region of the study area, is dominated by the withdrawal and undifferentiable deformation style, trending NW – SE (Figure 3-5A,B, Figure 3-10). This domain is characterised by large salt structures, including areas of salt expulsion which have fed these structures. Finally, domain C is located in the most distal part of the basin and is dominated by the closely folded and poorly imaged deformation style. Domain C is the most diverse of the observed domains, with every characterised deformation style present within it.

The spatial distribution of deformation styles and hence domains is complex. A very generalised trend could be inferred with increasing levels of internal deformation from proximal areas of the basin towards the distal regions of the basin, with several salt structures in the middle transitional areas of the basin.

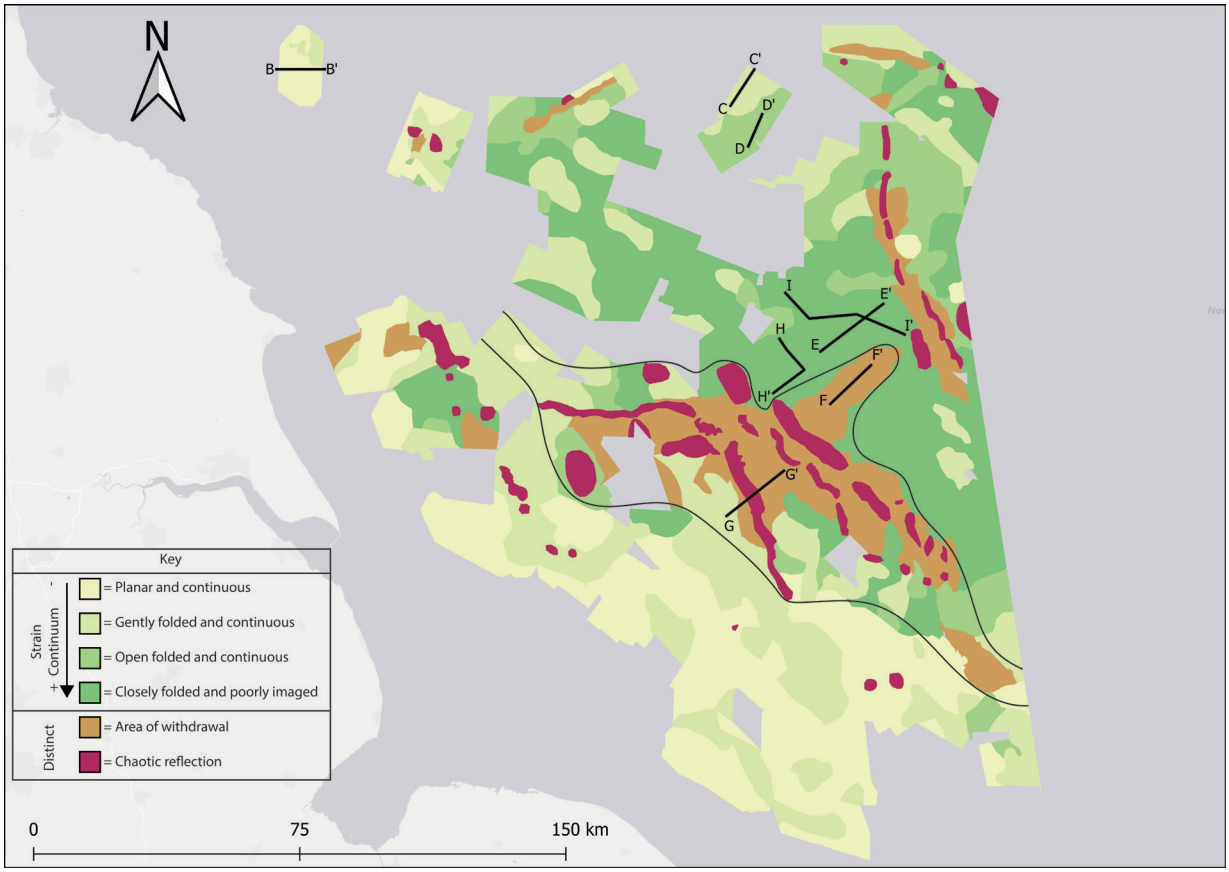

FIGURE 3-12 INTERNAL DEFORMATION STYLES MAP OF THE ZECHSTEIN IN THE SOUTH PERMIAN BASIN. THE SIX DIFFERENT DEFORMATION STYLES CHARACTERISED IN THIS STUDY ARE GEOSPATIALLY MAPPED. TRANSECTS FOR CROSS SECTIONS B – G ARE LOCATED ON THE MAP. THE WESTERN SECTION OF THE MAP IS DOMINATED BY THE PLANAR AND GENTLY FOLDED AND CONTINUOUS STRUCTURAL STYLE, WHEREAS FURTHER EASTWARDS, TOWARDS THE BASIN DEPOCENTRE, THE CLOSELY FOLDED AND POORLY IMAGED STRUCTURAL STYLE DOMINATES.

3.7 Discussion

3.7.1 Variation in structural styles

This study has observed a generalised trend for the intensity of internal deformation of the Zechstein to increase basinward (Figure 3-12), alongside the orientation of -Z3 folds being perpendicular to the basin depocentre in nonstructured salt areas. We interpret deformation styles in sections from sections 3.6.1.1 to 3.6.1.4 as a continuum of deformation, with the strain level increasing from one deformation style to the next, as evidenced by the fold amplitude increasing, wavelength decreasing and a higher level of shortening in the -Z3 per deformation style (Figure 3-6, 3-7, 3-8). However, it is important to note that layer thickness

can control fold geometries, as typically the thicker the interbed the larger the initial size of fold wavelength (Rowan *et al.*, 2019). While the % of carbonates and anhydrite decreases basinward (Figure 3-5C), the thickness of the -Z3 does not vary enough to quantify the change in levels of folding, with the thickness of the -Z3 interval to fold amplitude remaining constant. Thus, layer thickness is unlikely to be responsible for the change in fold parameters observed.

Given that gravity gliding and spreading are interpreted as an important driving mechanisms within the South Permian Basin (Stewart and Coward, 1995) it is suggested that the primary driver for the internal structures observed is salt mobilisation (flow) towards the basin depocenter. This model would be consistent with the northwest to southeast trending fold axis observed internally within the Zechstein and with the increase in fold magnitude towards the basin depocenter. We cannot rule out that the observed shortening may also be related to strain partitioning during the Early Cretaceous inversion phase within the basin. Density inversion is also an alternate explanation to the formation of such internal Zechstein fold features, however, the orientation of the internal folds indicates an association with a regional stress field, an observation that density inversion does not explain(Figure 3-6 , 3-7).

3.7.2 Vertical strain distribution and flow regimes

Figure 3-2 and Figure 3-4 show that the Zechstein supergroup is highly heterogenous, comprised of four primary different lithologies repeating in the Zechstein 1-5 cycles (Figure 3-2). These cycles and changes in lithology lead to a rheological stratification which is often seen in evaporite sequences and is present within the Zechstein (Figure 3-13. E, F) (Rowan *et al.*, 2019). This rheological stratification and hence mechanical stratigraphy affects how intra-salt units accommodate stresses applied to them (Evans and Jackson, 2021). These parameters in-part control the structural styles that develop within an evaporite sequence.

Two observations consistent throughout the basin for the characterised internal deformation styles of the Zechstein are; 1) the observed vertically varying levels of deformation. Each Z cycle, e.g., +Z2,-Z3, Z4/5, has undergone a different magnitude of strain. The vertical stratification and partitioning of deformation is likely a result of two separate factors, lithology and hence rheology, as different lithologies have different rheology (Burliga, 1996), and types of flow that have occurred internally within the Zechstein (Davison, Alsop and Blundell, 1996); and 2).The relatively undeformed overburden in areas of intense internal deformation within the Zechstein (Figure 3-6, 3-7). One interpretation for this formation is

the occurrence of thin-skinned tectonics, where mechanical decoupling of the intra-Zechstein from the overburden has occurred, allowing for flow internally within the salt and hence subsequent shortening of the intra-Zechstein stratigraphy. An alternative interpretation for this observation is that the internal deformation formed prior to the deposition of the overburden. Deformation occurring before overburden deposition would allow for the difference in the deformation magnitude between cycles and also explain the observed possible internal Zechstein onlap observed in section 3.6.1 However, further investigation into syn-depositional Zechstein mobilisation would be needed and is outside the remit of this study.

The observed internal deformation of the Zechstein (Figure 3-6, 3-7, 3-8, 3-9) is likely indicative of the dominant flow regime within the salt (Figure 3-13 A - D). Nearly all flows occurring within salt units are hybrids, however, comparing them to ideal flows provides a good base point for identifying the type of flow occurring (Jackson and Hudec, 2017). The observations made in the study area show that the that the stratigraphic middle of the Zechstein, where the -Z3 is located has undergone significant shortening compared with the +Z3,Z4/5 (up-to 26.1% within the closely folded and poorly imaged structural style), and hence has experienced the highest magnitudes of longitudinal strain (Figure 3-13 A,C,E,F), with lower magnitudes occurring stratigraphically below and above. The structures that are resolved in the -Z3 and the adjacent +Z2 indicate a higher magnitude of strain at the base of the Zechstein compared with the Z3+, Z4/5 (Figure 3-6, 3-7, 3-8, 3-9), which is unusual for typical flow deformation styles as typically it is higher towards the top (Figure 3-13 A,B,C). The +Z2 commonly has asymmetrical folds (Figure 3-6, 3-7, 3-8) present and deformed seismic reflections directly below the Z3+, Z4/5 reflections which are undeformed. The observed geometries of the Zechstein, could be explained by a number of possible different flow profiles are; 1) Simple Couette flow (Simple Shear) (Figure 3-13 B, E) of the +Z2 and -Z3 with the Z3+/4/5 mechanically acting as the overburden and the Z1 and-Z2 and acting as the underburden. For this explanation a shear zone will have developed in the upper salt units to decouple the lower -Z3 from the overburden, the competency difference between the -Z3 and +Z3 will have aided in the development of the shear zone. The Observations supporting this possible flow profile include the increasing strain from the +Z2 into the -Z3, the lack of deformation with seismic reflections remaining parallel to one another in the Z3+/4/5, and

no deformation in the -Z2 and Z1. This flow profile would also explain the geometry that Z4/5 take in Figure 3-7, where it has been uniformly deformed and behaves like the overburden. The lithological and hence rheological differences of the Zechstein can further help to explain this possible flow profiles; the -Z2 and Z1 act as the underburden as they are comprised of competent carbonates and anhydrites, the above -Z2, consisting of pure halite, as the halite is acting as a décollement between the two surfaces.

2) Asymmetric Poiseuille flow (Figure 3-13C, F) could also be an alternate dominant flow profile. Observations in support of this interpretation are maximum strain being constrained to the middle -Z3 unit, with it allowing for asymmetric levels of deformation stratigraphically, with greater levels of deformation occurring in the +Z2 over the Z3+/4. In this flow profile, there is still a décollement between the -Z2 and +Z2, and the upper Z4/5 is behaving as part of the overburden.

The gently/open folded continuous and closely folded and poorly imaged deformation style have experienced compressional stresses, as seen by the folded features observed in each style (Figure 3-6, 3-7, 3-8, 3-9). These internal compressional folds often occur; without affecting the overburden, with a lack of structure to the top salt, without compressional faults in the overburden and no syn-kinematic thinning strata above these areas. The lack of such apparent compressional features below or above the Zechstein suggests that much of this compression may have been restricted to solely within the Zechstein. The trend of the deformation styles and the distribution of these suggests a lateral distribution of the compressional stress increasing with distance down dip.

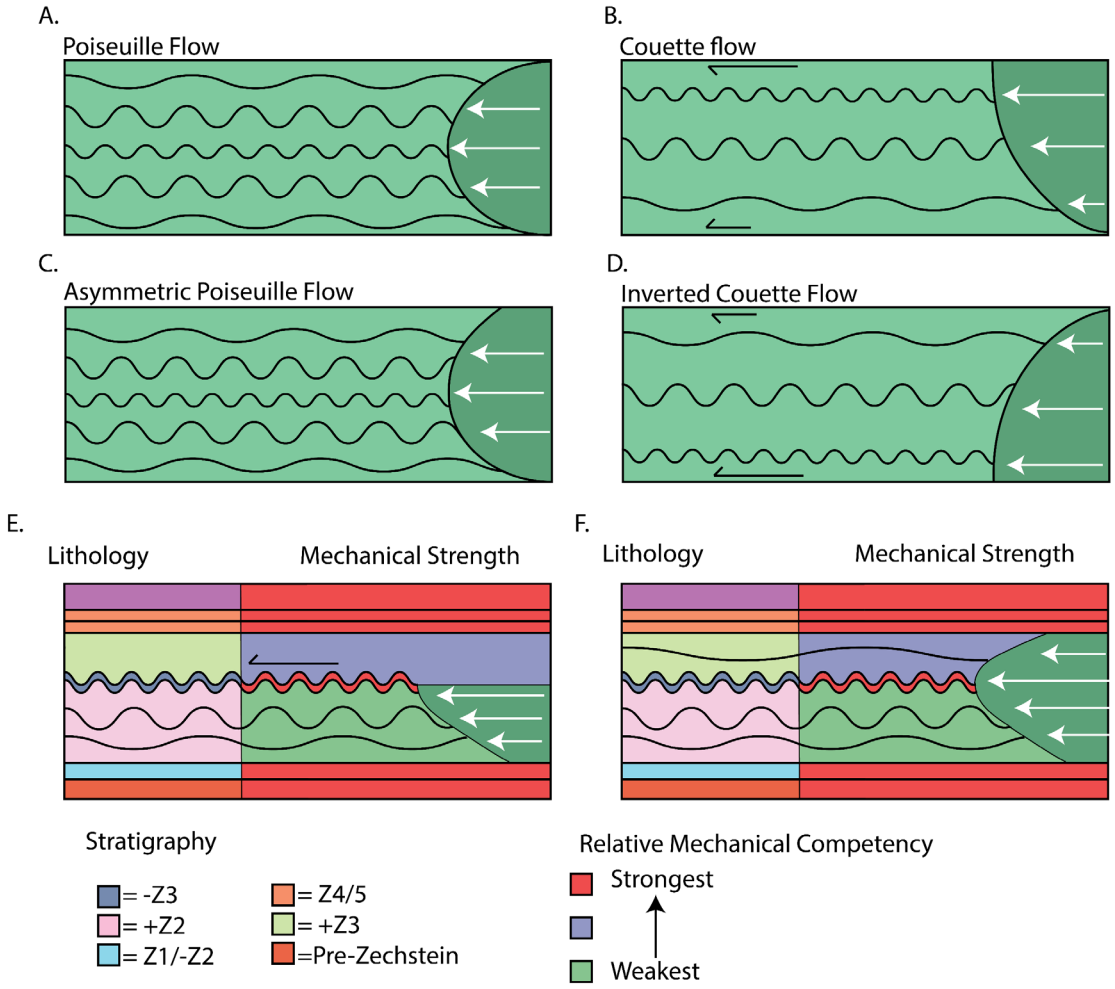

FIGURE 3-13 INTERNAL FLOW TYPE DIAGRAM DEMONSTRATING THE DIFFERENT TYPES OF FLOW. A – E REDRAWN FROM CARTWRIGHT ET AL. (2012). F AND G SHOW POSSIBLE FLOW PROFILES OBSERVED WITHIN THE ZECHSTEIN SUPERGROUP OF THE UNITED KINGDOM SOUTHERN NORTH SEA, COLOURED TO REPRESENT BOTH THE STRATIGRAPHY AND THE DIFFERENT RELATIVE MECHANICAL STRENGTHS OF THE ZECHSTEIN SUPERGROUP.

3.7.3 Alternate presence of discontinuous stringers

The closely folded and poorly imaged deformation style is the end member of the continuous compressional deformation observed throughout the research area (Figure 3-12). The maximum dip that was interpretable on any feature within the seismic data was > ~49°. Within the closely folded and poorly imaged deformation style, we observe folds with dips up to 49° after this, the reflections cannot be mapped as they have a discontinuous appearance. The ability of the seismic data to resolve high dip features, therefore, leads to questions about the observed lack of continuity within the -Z3 in this deformation style, in that, whether the -

Z3 is present and not just imaged correctly or if the -Z3 has undergone brittle deformation and formed stringers, and, if they do, how did they develop. We believe that the -Z3 is continuous and has not undergone brittle deformation, as is collaborated by borehole data (Figure 3-10, 11) and suggest two alternate scenarios for why these features appear on seismic data as they do;

1). The -Z3 is continuous and has not undergone brittle deformation within the interpretations. The observed lack of continuity between the -Z3 is due to the fold limbs being steeply dipping so that the seismic data cannot image it (Figure 3-8A, Figure 3-9D). The folds now have tight/fan geometries with limbs dipping >49°. Further evidence is opposing fold limbs dipping towards high amplitude reflection packages while no longer being visible on seismic data as the dip of the -Z3, likely as the dip becomes too great to image (Figure 3-8A). This explanation fits well with our proposed nomenclature for the observed deformation styles, in that the magnitude of folding is increasing basinward's and just not well imaged. This is further supported by the style's line length changes, which show an increasing % in shortening within the -Z3 in our measured examples of the deformation styles in section 3.7.1.1 to 3.7.1.4, going from 0.84%, 1.8%, 3.1% and finally 26.1% (Appendix 2). Mined Zechstein structures that can be used as analogues have been observed to have features dipping as steeply as 90°, suggesting that folds with dips greater than the seismic can image are possible within evaporite formations. (Figure 3-14).

Alternatively, 2). The -Z3 is continuous and has not undergone brittle deformation within the scope of the interpretations. As the fold magnitude has increased from the higher magnitude of strain basinward, the fold limbs of the -Z3 have thinned, and the fold hinges thickened. The fold limbs being thinned to below the thickness below that of the seismic resolution combined with how steeply dipping they are would explain why they are not observed on the seismic data. The thickened fold hinges would also explain why we see isolated high amplitude packages of -Z3 where we would expect the fold hinges to be (Figure 3-8A, B). This possible explanation is also consistent with our observation of increased shortening towards the basin depocenter.

To note these interpretations do not preclude the occurrence of brittle deformation occurring elsewhere within the -Z3.

However, these alternate explanations of the appearance of the -Z3 reflection on the seismic data do not preclude the ability of this formation from being over-pressured, a common observation for stringers in evaporite sequences. Laterally extensive overpressure within evaporite lithologies is possible (Dale *et al.*, 2021), so it should not be seen as a defining diagnostic feature suggesting stringers are present. Extra to this, as suggested in explanation 2, if the fold limbs have thinned, they may have undergone diagenetic changes making them impermeable and allowing further mechanisms for over-pressure to occur in fold hinges.

We are, however, more confident with the interpretation of stringers being present within the area of withdrawal deformation style, as the lack of salt in these areas due to expulsion means that the -Z3 stringers are unable to have dips >48°so lack of appearance on seismic is unlikely due to poor imaging. Furthermore, areas of withdrawal have experienced extensional forces from salt flow as salt was expulsed to feed surrounding salt structures, causing boudinage and brittle deformation to occur with the -Z3.

3.7.4 Model-driven internal deformation of salt structures

Conceptual models help determine the different internal structures that can form within chaotic reflection areas. The best analogues for the internal structural heterogeneity of diapirs originate from mined evaporite structures that have been mapped, with those such as the Hanigsen – Wathlingen salt dome, which shows boudinaged and incoherent Z cycles within the salt, or the Bartensleben Diapir, where the internal Zechstein units are deformed but still competent and distinguishable (Figure 3-14).

We suggest a model-driven process for interpreting the internal heterogeneity when seismic data does not distinguish coherent reflections. The model is driven by the closest deformation style to the area of chaotic reflections that has a resolvable internal heterogeneity, often the area of withdrawal style. Assumptions are made that the competent layers, such as anhydrites and carbonates, within an evaporite sequence are either brittlely deformed or competently deformed as salt flows to feed the surrounding salt structure. Thus, structures surrounded by the withdrawal deformation style with high amplitude packages (Figure 3-9, 3-14), interpreted as brittlely deformed competent layers, have these brittlely deformed stringers present within. Alternately, for structures next to areas where the competent layer has undergone ductile deformation, the layer remains competent as it is mobilised to feed the growing salt structures (Figure 3-14). To a lesser extent the model could also be used to

identify what residual components that may remain within the specific areas of the withdrawal style by observing the surrounding deformation styles.

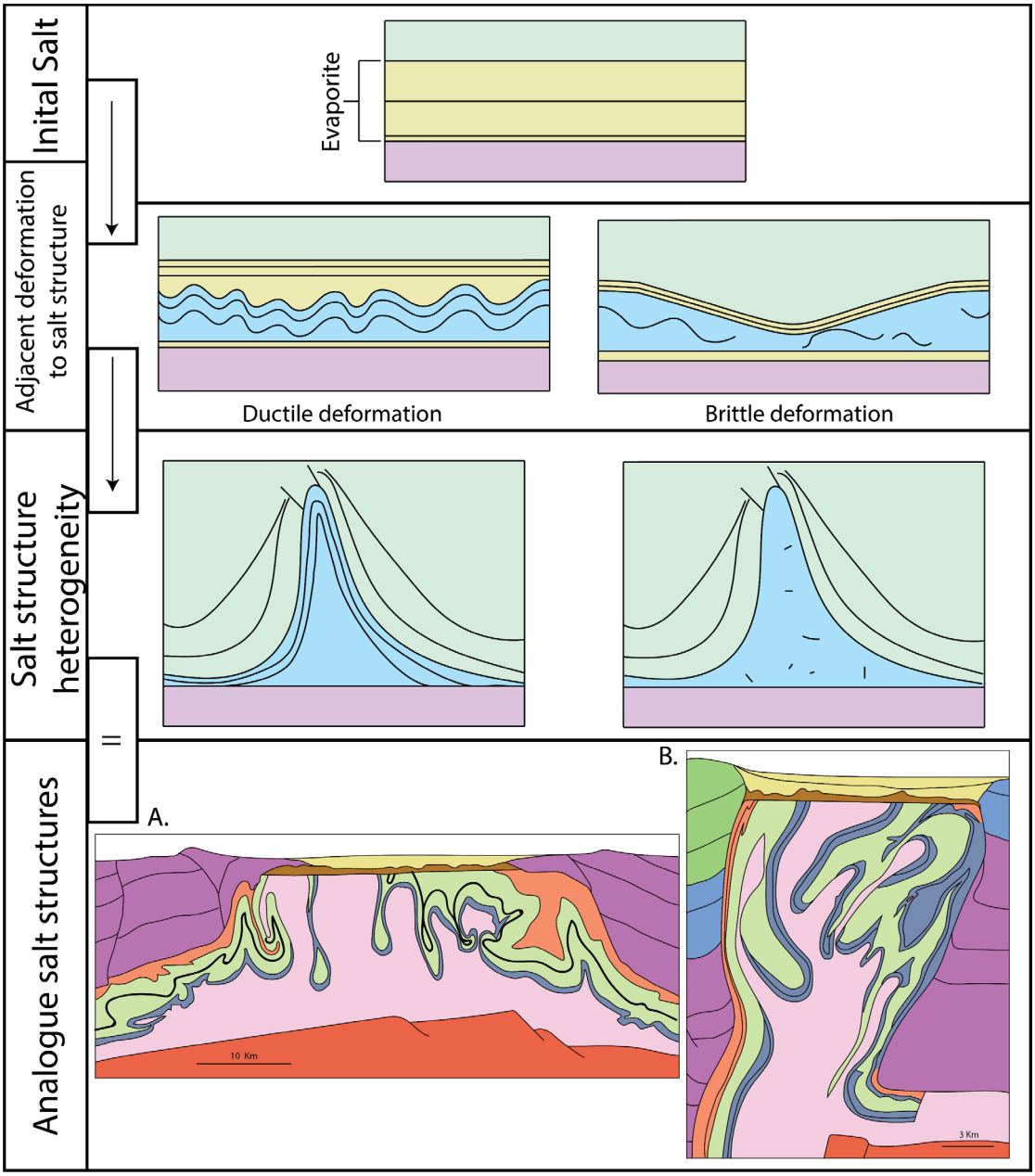

FIGURE 3-14 PROPOSED MODEL FOR INTERPRETING THE INTERNAL HETEROGENEITY OF SALT STRUCTURES WERE POORLY IMAGED BY SEISMIC DATA. THE INITIAL STAGES OF THE EVAPORITE FORMATION ARE BEDDED AND UNDEFORMED. WHEN SALT MOBILISATION OCCURS, THE COMPETENT LAYERS UNDERGO EITHER BRITTLE OR DUCTILE DEFORMATION. WHICH TYPE OF DEFORMATION IT UNDERGOES DETERMINES THE INTERNAL HETEROGENEITY OF THE SURROUNDING SALT

STRUCTURE AS THE COMPETENT LAYERS WILL BE MOBILISED INTO THE STRUCTURE. CROSS-SECTION OF THE BENTHE SALT DOME, A CROSS-SECTION OF AN UNNAMED SALT DIAPIR REDRAWN AFTER PICHAT (2022)

3.7.5 Other North Sea intra-Zechstein models

There are several mechanisms behind the origin of intra-Zechstein internal structural complexity suggested within the literature;

1.) Moneron (2025) suggests multi-layered evaporite flow within the Zechstein was induced by sub-salt thick skinned tectonics, acting to decouple the Zechstein from pre and post salt sediments. Late-Cretaceous inversion induced flow was portioned between the Z2+ and Z3- units, with elements of decoupling between both occurring (Figure 3-15).

2.) Strozyk *et al.* (2014) suggests that a combination of syn-depsoitonal gravity gliding within the Zechstein, differential loading of post salt sediments and reginal extension in the Triassic – Early Cretaceous caused the complex geometries that are observed today.

Regardless of flow mechanics and mechanisms behind the internal structural deformation of the Zechstein stratigraphy. The most probable and simple interpretation of structural deformation within the Zechstein supergroup is the occurrence of folding within the Z2+ Zechstein stratigraphy.

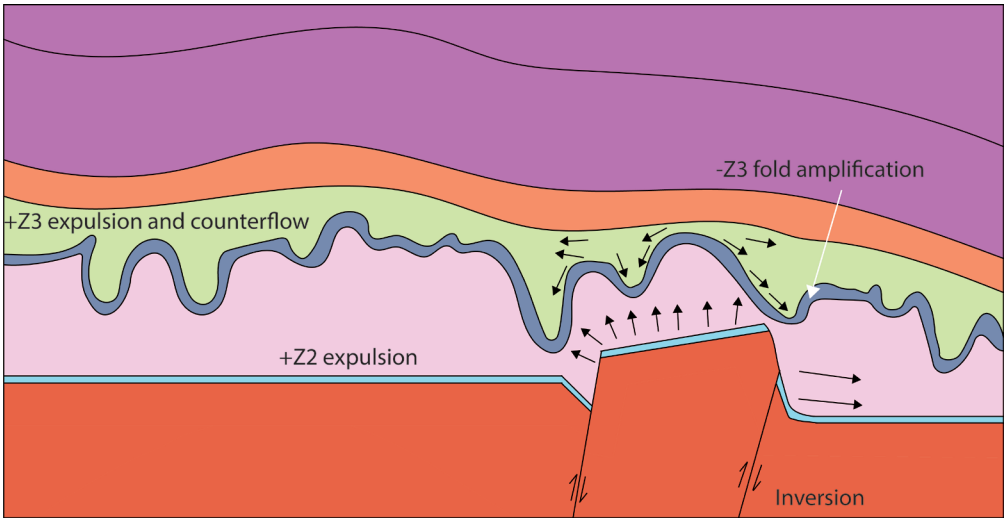

FIGURE 3-15 INVERSION INDUCED DEFORMATION MODEL FOR INTRA ZECHSTEIN STRATIGRAPHY WITHIN THE SOUTHERN NORTH SEA. MODIFIED FROM (MONERON, 2025)

3.8 Conclusions

The Zechstein of the South Permian Basin can be characterised by six distinct internal deformation styles. Each deformation style represents a type of internal deformation or unique salt deformation. Four of these deformation styles represent a continuum in the increase in the magnitude of strain increasing basinward, due to the structures observed. We propose this is due to salt flow towards the basin depocenter. These internal deformation styles of the Zechstein can be further grouped into three distinct broader domains throughout the basin. Observations indicate that a combination of the type of internal salt flow and the variation in vertical mechanical stratigraphy control the deformation style and the internal geometries that form within the Zechstein.

We suggest an alternative interpretation for the lack of continuity in the seismic imaging of the Zechstein's Hauptanhydrit and Plattendolomit (-Z3), which are often interpreted as stringers formed via brittle deformation. Our observations suggest that the lack of continuity with the seismic reflections are from the limbs of fold structures with dips steeper than can be imaged or thinned beyond seismic resolution, having undergone ductile deformation from salt flow, rather than the Zechstein no longer being competent, having undergone brittle deformation in these areas. This does not exclude the possibility that brittle deformation has occurred at sub seismic resolution within the -Z3.

A model-driven approach for deriving the possible structures and heterogeneities has been conceived for the internal heterogenity of salt structures or areas where the seismic imagining of salt bodies is too poor to be interpretable. This model relies on observations of the internals of the surrounding salt, which has fed these structures. If heterogeneities such as stringers are present, we suggest they will have been expulsed into the salt structures; if not we suggest that the layers within the evaporite sequence will remain competent.

Chapter 4. Capturing geological uncertainty in salt cavern developments for hydrogen storage

4.1 Abstract

Future energy systems with greater contributions from renewable energy will require long duration energy storage to optimise integration of renewable sources. Hydrogen is viable energy vector that could be utilised for energy storage. Grid-scale underground natural gas storage (methane) is already in operation in solution-mined salt caverns, where individual cavern capacities are ~0.025 - 0.275 TWh. While traditionally salt caverns have been restricted to being developed onshore, in some offshore locations, such as the UK Continental Shelf, there are extensive evaporites that have potential for storage development. Capacity estimates for offshore areas typically rely upon generalised regional geological interpretations, frequently do not incorporate site specific structural and lithological heterogeneities, use static cavern geometries, and can use methodologies that are deterministic and not repeatable.

We developed a stochastic method for identifying potential salt cavern locations and estimating conceptual clusters' storage capacity. The workflow incorporates principal geomechanical constraints on cavern development, captures limitations from internal evaporite heterogeneities, and uses the ideal gas law to calculate the volumetric capacity. The workflow accommodates either fixed cavern geometries or geometries that vary depending on the thickness of salt. By using a stochastic method, we quantify uncertainties for storage capacity estimates and cavern placement across defined regions of interest. The workflow is easily adaptable allowing users to consider multiple geological models or evaluate the impact of interpretations of varying resolutions.

We illustrate the workflow for four areas and geological models in the UK's Southern North Sea:

Basin Scale (58,900 km^2) - >48,800 TWh's of hydrogen storage with >199,000 potential cavern locations.

Sub-Regional Scale (24,800 km^2) - >9,600 TWh's of hydrogen storage with >36,000 potential cavern locations.

Block Specific – Salt Wall (79.8km^2) - >580 TWh's of hydrogen storage with >400 cavern potential locations.

Block Specific – Layered Evaporite (225 km^2) - >263 TWh's of hydrogen storage with >500 potential cavern locations.

Our workflow enables reproducible and replicable assessments of site screening and storage capacity estimates. A workflow built around these ideals allows for fully transparent results. We compare our results against other similar studies in literature and find that often highly cited papers have inappropriate methodologies and hence capacities.

4.2 Introduction

Long-duration energy storage (LDES) will be a vital feature in future energy systems (McNamara *et al.*, 2022; Smdani *et al.*, 2022). As renewable and low-carbon energy aims to displace fossil fuels there will be a requirement to accommodate the increased variability in supply that comes with this transition (Dowling *et al.*, 2020). LDES allows for the management of grid imbalances that arise from both the variable supply of renewable energy and the variability on the demand side, while improving the overall flexibility and reliability of the energy system (Kueppers *et al.*, 2021; Sepulveda *et al.*, 2021). There are three principal mechanisms for geological LDES: mechanical (compressed air or solid weight), thermal, and chemical energy storage (e.g. hydrogen, ammonia, methane) (Bauer *et al.*, 2013; Shan *et al.*, 2022). Chemical storage is often considered the most versatile option of these three, as the energy storage medium can also be transported via pipelines or tanks and used with relative ease and with a lower energy loss (<0.1%) than when energy is transported for high voltage energy cables (5%), over long distances, adding to the flexibility of the energy system as a whole (Calado and Castro, 2021).

Subsurface formations have proven to be suitable storage volumes for geological scales of time, as evidenced by the occurrence of natural hydrocarbon accumulations (Lokhorst and Wildenborg, 2006). The subsurface has already been utilized since 1915 for the storage of natural gas, with the first site in operation in Ontario, Canada (Lord, 2009). More modern examples include the Rough gas storage field, located offshore UK, that has been in operation since 1985 (with a 5-year hiatus from 2017 - 2022) with the capacity to store 54 BCF of natural gas (Centrica, 2023), in Cheshire, UK, Storengy operates a salt cavern cluster consisting of 28 caverns with the ability to store 14 BCF of gas (≈ 4.1 TWh) (Eising, Brouwer and Bernd, 2021). Hydrogen has also been stored within the subsurface, the Spindletop salt caverns cluster in Texas, USA, for example, which stored 5 BCF (≈ 1.45 TWh) of natural gas, was converted to store .274 TWh of hydrogen (Bérest *et al.*, 2021). Compared with other methods of LDES such as Li-Po batteries and pumped-hydro, subsurface geological storage, also known as Underground Energy Storage (UES), provides several advantages including greater capacities, small surface footprint, low operating costs, operational timespans for over 30 years, and increased security (Crotogino, Schneider and Evans, 2017). There are two differing storage methods within the subsurface, porous media (e.g. saline aquifers and abandoned

hydrocarbon fields) and salt caverns (Evans, 2007; Bauer *et al.*, 2013). Salt caverns for hydrogen storage are the option investigated within this study. While research has been undertaken on hydrogen storage in porous media such as Heinemann *et al.* (2018),Heinemann *et al.* (2021) and Hassanpouryouzband *et al.* (2022), storage of hydrogen in porous media is in its infancy with only demonstrations being in operating having first injection in the early 2020s. Whereas there are several salt cavern clusters storing hydrogen currently in operation, with the first beginning operation in the 1960s (Underground Sun Storage EN, 2023; Evans, 2007).

Salt caverns are solution mined voids within an evaporitic (salt) layer (Warren, 2006; Tarkowski and Czapowski, 2018). They range volumetrically from 70,000 m^3 (e.g Teesside, UK (HyUnder, 2013)) to 17,000,000 m^3 (Texas) (Leith, 2000). Salt caverns are an established technology having been in use since 1960's for storing gas (Allen, Doherty and Thorns, 1982; Allen, 1971). Hydrogen has been stored within salt caverns since the early 1970's for use in the chemical industry, with the first site located in Teesside, UK (Landinger and Crotogino, 2007; Caglayan *et al.*, 2020; François, 2021) and Texas. Although recent published work on salt cavern volumetrics has mostly focused on onshore areas, there are few which focus in the offshore, these works frequently investigate country-wide scale analysis for capacity estimates and cavern placement (e.g. Caglayan *et al.* (2020), Williams *et al.* (2022) and, Allsop *et al.* (2023)). The modelled capacity estimates across the whole basin greatly exceeds the estimated requirements for LDES for the UK's energy transition requirements (Ofgem, 2021; Cárdenas *et al.*, 2021). The current estimates rely on geological models with limited resolutions and are not able to capture the geological complexity of both the salt layers, and the overburden. Simplified, or basic geological models may not reliably estimate cavern placement options, and their storage capacity. While there have been assessments of the geological constraints on offshore developments for salt caverns in the UK, notably Allsop *et al.* (2023) and Caglayan *et al.* (2020), they have not utilised a systematic approach. Offshore salt caverns are not outside technological feasibility (Costa *et al.*, 2017). One of the possible benefits from offshore storage is the co-location of storage next to offshore windfarms or pre-existing pipelines (which will require modification or replacement to be hydrogen compliant), developing both a hub of energy production and storage. Salt caverns are typically developed

in clusters (Gillhaus, 2007) and the work here could be considered as the basis for pre-feasibility studies of cavern placement options.

We demonstrate the robustness and flexibility of our methodology for the offshore of the UK. The UK is currently undergoing a shift in the supply of energy to meet its 2050 net-zero obligations, with installed wind power capacity in 2023 reaching 27.9 GW (Staffell *et al.*, 2023). For 100% renewable penetration by 2035 in the UK, Cárdenas *et al.* (2021) found that with the optimum mix of renewable technologies and allowing for over-generation, the UK would require ~43 TWh of LDES, far lower than the suggested 115 TWh needed if no over generation is allowed. Over generation within Cárdenas *et al.* (2021)'s energy system models is used to avoid curtailment of renewable technologies and allows for a more efficient energy system, and hence require less storage. The UK's Electricity System Operator (2023) states that a whole energy system transformation by 2050 would require the UK to have 56 TWh of hydrogen storage by 2050, where the hydrogen is utilised for both heat and energy. Without the utilisation of LDES within the energy mix it will be difficult for the UK to achieve its legislated net-zero carbon goals (King *et al.*, 2021). Geological storage is currently the most viable option for LDES within the UK as: 1) there are a number of possible location options distributed across the UK, and the location of storage is an important consideration in the whole system (Sunny, Mac Dowell and Shah, 2020); 2) pre-existing oil and gas infrastructure could be repurposed to reduce capital expenditure associated with LDES scale up (Oil and Gas Authority, 2021); 3) Geological storage is estimated to currently be one of the lowest cost LDES options available (Hunter *et al.*, 2021; The Royal Society, 2023).

We focus on the Southern North Sea area of the UKCS due to the data availability, geological suitability, and possible future demand for hydrogen storage within the area. Four areas of interest (AoIs) are defined within our study (Figure 4-1) to consider the potential locations and capacity for salt caverns for hydrogen storage within Zechstein Supergroup. The Zechstein Supergroup is a Late Permian-aged layered evaporite sequence deposited during the Lopingian (Peryt *et al.*, 2010), it is laterally extensive, and, across large areas exceeds 750 m in thickness, of which only a portion is pure halite that can be utilised for cavern emplacement (≈40% in layered sequences and ≈80% in structured areas). It is located within both the North Permian and South Permian Basins of Europe, where it extends from onshore the eastern coast of the UK, across to western Poland (Glennie, 1998; Fyfe and Underhill, 2023). The

Zechstein Supergroup is found as both layered and structured salt throughout both basins. Current understanding of the Zechstein Supergroup comes from both the hydrocarbon exploration industry, where it is important for trapping mechanisms and sealing reservoir intervals, and the onshore mining industry (notably from Europe), where further understanding of the internal composition and structuring originates (Glennie, 1998; Strozyk, 2017; Doornenbal *et al.*, 2019; Grant *et al.*, 2019; Pichat, 2022; Raith *et al.*, 2016). The Zechstein's deposition as a layered evaporite sequence is typically divided into five cycles. However, the nomenclature used frequently varies depending on regional location and environment of deposition (Johnson, Warrington and Stoker, 1993; Fyfe and Underhill, 2023). The internal heterogeneity of the Zechstein also varies in complexity across the Southern North Sea due to the Zechstein's mobility from halokinesis (Barnett, Ireland and van der Land, 2023).

Within this chapter 'salt' is used as a general term to refer to a vertical and lateral extent of evaporites, which typically comprise mostly of halite, however, have non-halite heterogeneities present. A salt unit refers to a stratigraphically recognised vertical section of salt which is part of a larger evaporite group.

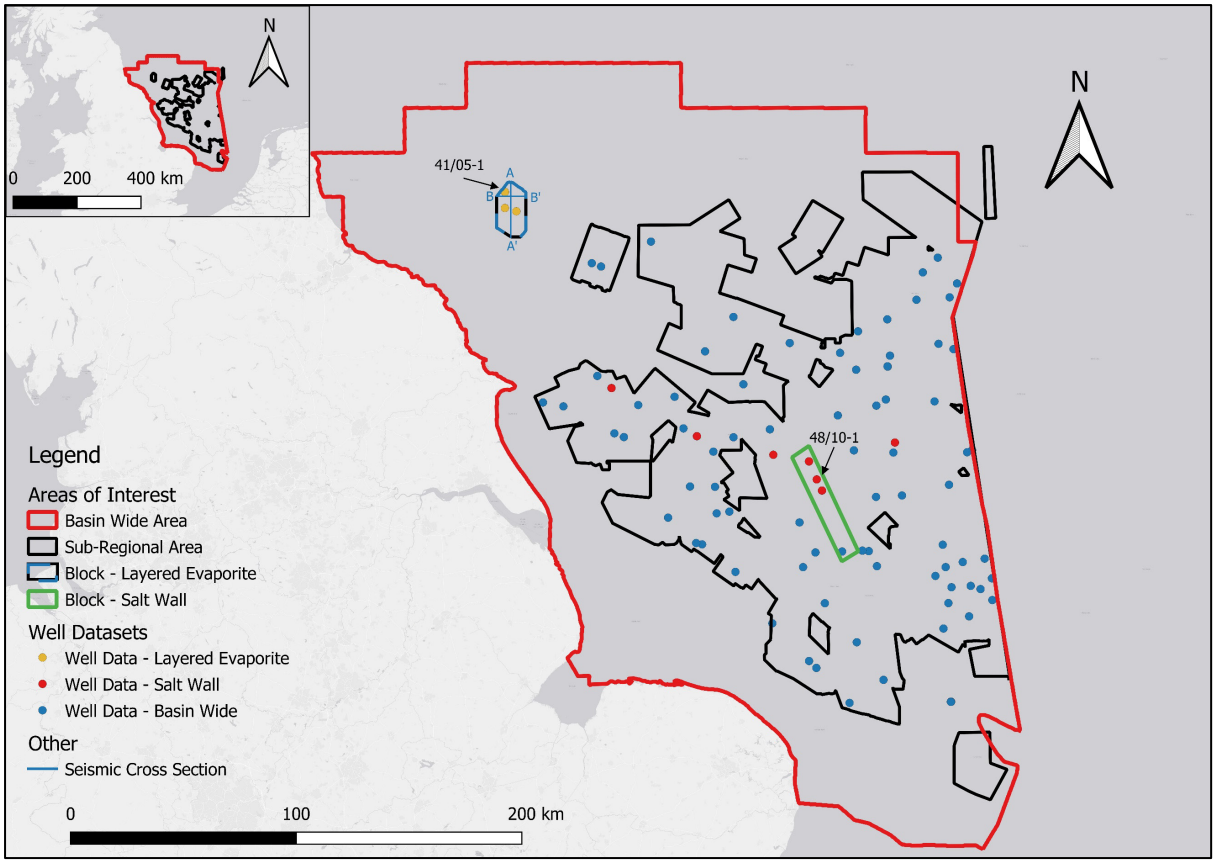

FIGURE 4-1 LOCATION MAP OF AREAS OF INTEREST (AOIS), OFFSHORE EAST COAST OF THE UK. AOI LOCATIONS ARE LABELLED AND SHOWN ON THE MAP. WELL DATA USED IN THE 'BLOCK – LAYERED EVAPORITE' AREA IS MARKED ON, AS WELL AS SEISMIC CROSS SECTIONS (FIGURE 4-3). MAP 2, (TOP LEFT) DETAILS THE EXTENT OF THE STUDY AREAS IN RESPECT TO THE WHOLE OF THE UK AND NORTHERN EUROPE. WELL DATA USED TO DERIVE INSOLUBILITY CONTENT FOR EACH AREA PRESENT (NOTE, ALL SALT WALL WELLS ARE LOCATED WITHIN DIAPIRIC STRUCTURES).

4.3 Methodology

4.3.1 Workflow

The workflow developed uses a geological model as the input, determines an idealised cavern layout and calculates the potential working hydrogen storage capacity (Figure 4-2). Due to the inherent uncertainty associated with geological models, the method can accommodate both single values and distributions. The workflow is agnostic to the resolution of the input geological model, recognising that the availability of data varies by area, allowing for site to basin scale investigations. The method can incorporate distribution-based inputs in which case the workflow is run as a Montecarlo simulation, capturing the inherent uncertainty of

the geological model. The workflow is a reproducible and reliable method to determine the placement of salt caverns and calculate the hydrogen storage capacity. The workflow can be set to optimise for either cavern number or capacity, allowing for idealised utilisation of the area of interest.

The workflow initially removes areas of the geological model that have been determined as unsuitable based on the set parameters (Figure 4-2). The suitability of these areas for cavern placement is treated as binary condition, being either more or less suitable. It is possible to incorporate both geological and surface constraints, such as faults and heterogenous areas of salt mapped from seismic, or roads and densely populated areas onshore. Buffers can be applied to these features, which then determine a set distance for caverns to be placed.

The depth to geological formations can be constrained using seismic and well data, where seismic is used to interpret between the depth-calibrated measurements from wells. As a result, depths in geological models have an inherent level of uncertainty. We accounted for this by using a uniform distribution calculated from the residual depth values calculated during the depth conversion process. The largest residual value from the depth conversion process was calculated as a percentage and set both the positive and negative limits of the uniform distribution. As depth uncertainty can be either positive or negative, setting the maximum residual to limit the uniform distribution (E.g., -10% and +10%) allows the workflow to account for depth uncertainty.

The workflow assumes that every grid cell within the geological model which has not been removed is a potential location for cavern placement. The height-to-diameter ratio at each potential location is determined by using the salt thickness at that location (Figure 4-2, Appendix 2). From the salt thickness and height-to-cavern ratio, a cavern geometry is determined (Figure 4-2, Appendix - Equation Sheets A – E (Caglayan *et al.*, 2020)), a maximum limit on cavern height is imposed at 750 m, however this is adjustable as required. If a fixed cavern geometry is used, then the pre-set cavern height and cavern diameters are used instead. These cavern geometry calculations also account for the required thickness of footwall and hanging wall within the salt unit of choice per cavern to allow for geomechanical stability (Figure 4-2).

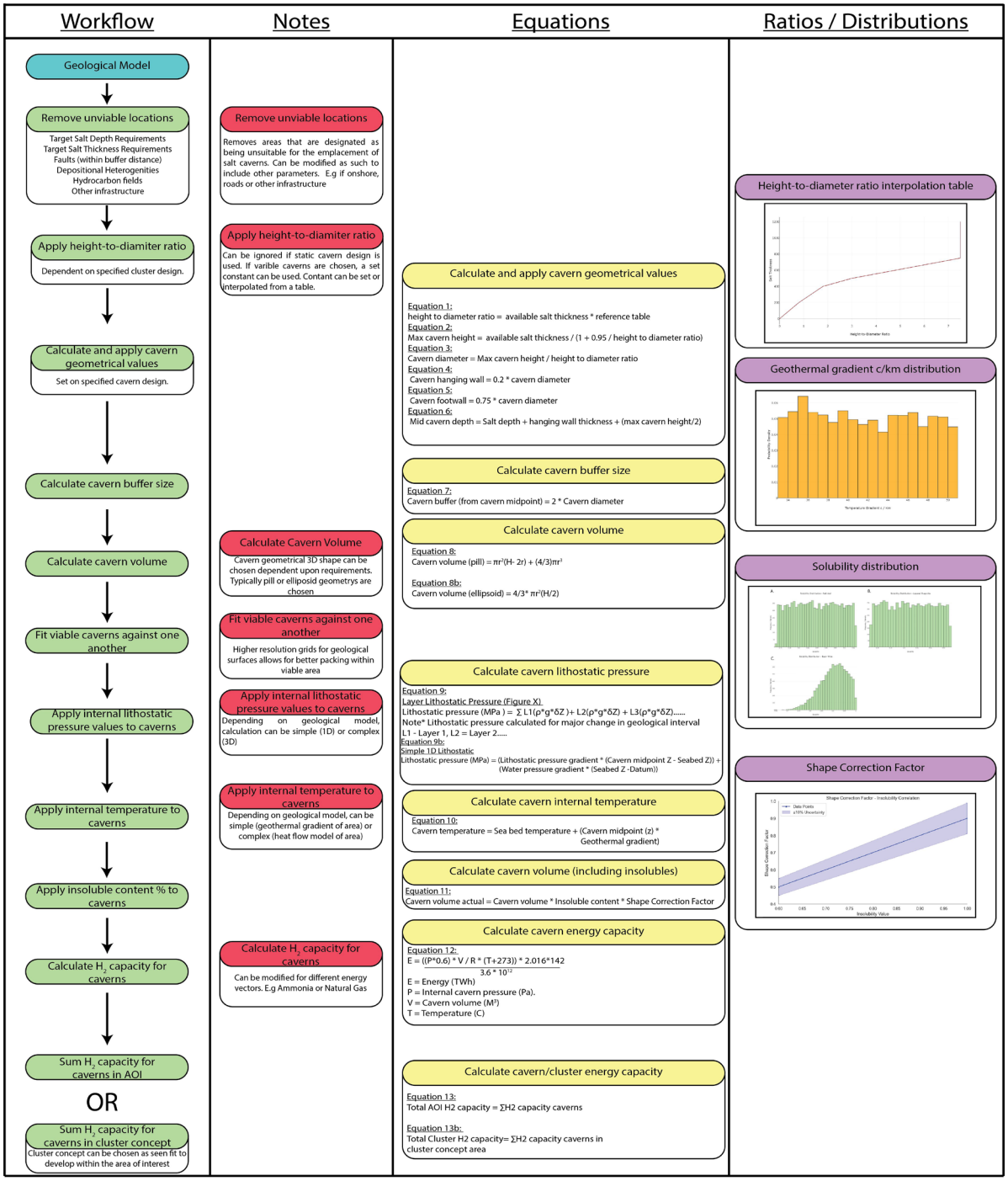

FIGURE 4-2 WORKFLOW, EQUATIONS, AND RATIOS/DISTRIBUTION USED FOR THE WORKFLOW DESCRIBED IN SECTION 4.3 (LARGER RATIOS AND DISTRIBUTION FIGURES ARE PRESENT IN APPENDIX 2-4)

Typically a cavern will aim to be emplaced in salt below a depth of 500 m, as deeper emplacement allow larger working gas capacities and increased quantities of hydrogen storage due to the increased operating pressure requirements (Warren, 2006; Caglayan *et al.*, 2020; Tan *et al.*, 2021). However, it is worth noting that onshore caverns within the UK have been emplaced at depths as shallow as 300 m, shallow caverns can have advantages due to less drilling required, the location of salt may be optimal for storage requirements, and required volumes may be adequate (Parkes *et al.*, 2018). We optimise cavern storage capacity in this workflow by emplacing caverns at a minimum depth of 500 m if possible. To accomplish this, if a possible cavern location is in a location where the topsalt is <500 m, it is checked to see if the salt interval extends deeper than 500 m and has sufficient thickness beyond 500 m depth than the minimum cavern geometrical requirements. If so, a cavern is placed 500 m. This optimisation allows for higher operating pressures, and hence higher hydrogen capacities in areas of shallow but thick salt (Figure 4-2, Equation. 1 (Fanchi and Christiansen, 2016)). These optimisations of depth windows within the workflow are modifiable such that if shallower cavern emplacement is required it can be adjusted as needed.

$$E = \frac{\left(\frac{(P * 0.6) * V}{R * (T + 273)}\right) * 2.016 * 142}{3.6 * 10^{12}} \qquad \textit{EQUATION 21}$$

E = Energy Hydrogen (TWh)

P = $Pressure\ (Pa)$

R = $Gas\ Constant$

V = $Volume\ (m^3)$

T = $Temperature$ (°C)

The minimum distance between cavern mid points (buffer distance, Figure 4-3) is then determined to establish a feasible combination of adjacent cavern locations (Figure 4-2, Appendix - Equation Sheet– Equation G) and is a simplified approach to account for the geomechanical requirements for stability between adjacent caverns (Caglayan *et al.*, 2020; Ma *et al.*, 2022). Where the grid cell spacing is greater than the buffer distance between caverns then there will be overlap between buffers. To determine a layout where there is no overlap of buffers the workflow iterates in the x coordinate through the array of potential cavern locations starting at 0,0 (top left), plots a cavern, checks to see if the buffer overlaps

with another caverns' buffer, and if it does not, keeps it, if it does, it is deemed unsuitable and removed. Further details of this method can be found in 'Appendix - Further Info - Best fit algorithm'. This methodology optimally packs the caverns within the areas with potential for cavern placement.

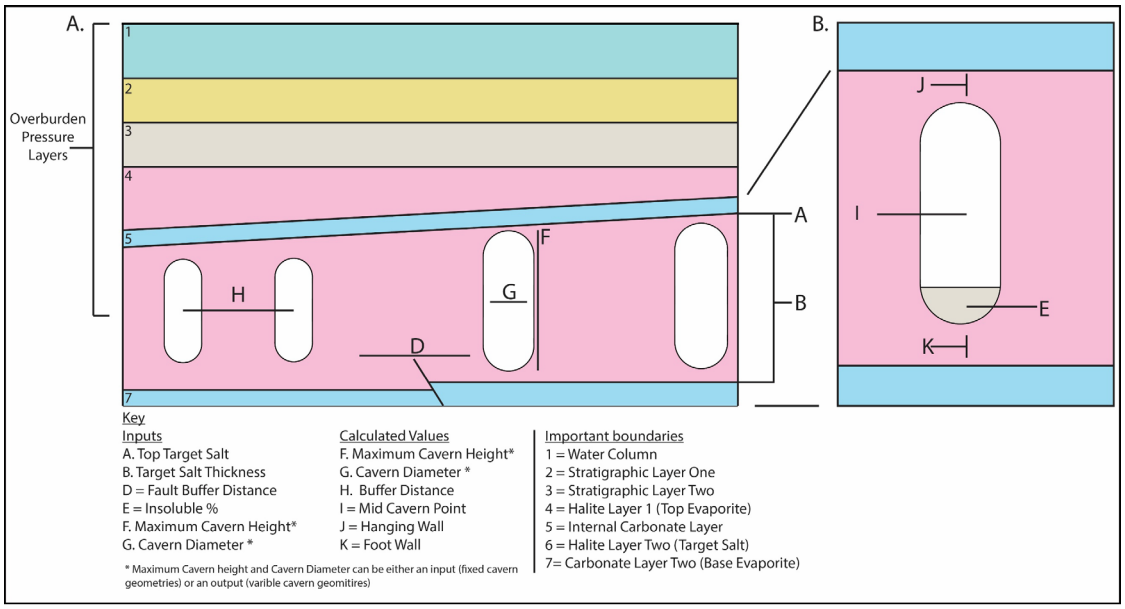

FIGURE 4-3 A) CARTOON SCHEMATIC GEOLOGICAL CROSS-SECTION OF EMPLACED SALT CAVERNS (NOT-TO-SCALE). IMPORTANT PARAMETERS (BOTH INPUTS AND CALCULATIONS) FOR CHARACTERIZING A SALT CAVERN SITE HAVE BEEN LABELLED A – K, AND OVERBURDEN CHARACTERIZATION 1 - 7. B) DIAGRAM SHOWS AN INDIVIDUAL CAVERN AND THE PARAMETERS CONSIDERED FOR INDIVIDUAL CAVERN PLACEMENT.

The volume for each cavern is then calculated, (Figure 4-2, Equation 22). For caverns with a height-to-diameter ratio of < 1, an ellipsoid shape was assumed for the volume (Figure 4-2, Appendix - Equation Sheet H), as capsule geometries become ellipsoids with a height-to-diameter of <1. The volume for the cavern will depend on its planned geometrical shape. Our workflow uses capsule geometries for the 3D cavern shape (Figure 4-3), as these are the most stable and have the lowest stress risk (Ozarslan, 2012).

$$V = \pi r^2(H - 2r) + (4/3)\pi r^3 \qquad \textit{EQUATION 22}$$

$V = Cavern\ Volume\ (Pill)(m^3)$

$H = Cavern\ Height\ (m)$

$r = Cavern\ Radius\ (m)$

Remaining are all potential cavern locations within the area with suitable spacing and geometries for the salt layer in the geological model. Lithostatic pressure for the mid cavern depth are calculated as they determine the cavern operating pressure. A simple 1D layer cake approach can be taken for calculating lithostatic pressure (Equation. 23 (Zoback, 2010) or a simple gradient approach depending on data available (Section 4.3.2.1). For layer cake models, the same depth uncertainty is applied to that of the salt depth and thickness surfaces. An uncertainty can also be applied to the density of the overburden layers. Internal cavern temperatures are then calculated using the geothermal gradient and mid cavern depth (Equation. 24, Section 4.3.2.2). The geothermal gradient used can either be a set value or be derived from a distribution (Appendix 3).

The cavern volume is then adjusted to account for the insoluble content that is present within the salt (Figure 4-2, Appendix - Equation Sheet J, Section 4.3.2.3), a simple % may be used, a distribution derived from well data, or a map (Appendix 4). Geomechanical instability is not accounted for with raised levels of insoluble content within this workflow. A shape correction factor is incorporated to account for change in the planned cavern geometry from non-halite content (Williams *et al.*, 2022). As insoluble content will modify the shape of the emplaced cavern, the value of the shape correction factor was correlated to the insoluble content % (Warren, 2016). A linear relationship between insoluble content and shape correction factor was assumed, after a shape correction factor had been calculated (Appendix 5).

Individual cavern hydrogen capacity is then calculated using the ideal gas law Equation. 21 (Fanchi and Christiansen, 2016). The working capacity is calculated based on 60% of the lithostatic pressure at mid cavern depth, with a cushion gas of 20% to maintain cavern integrity and a maximum pressure inside caverns of 80% to avoid exceeding the fracture gradient (Ozarslan, 2012; Caglayan *et al.*, 2020; Muhammed *et al.*, 2022). Once the individual capacity of each cavern is calculated, the energy capacity for the whole area or a cavern

cluster can be determined (Appendix - Equation Sheet K,L). The energy capacity calculations are modifiable to allow for different energy vectors, such as natural gas, ammonia, or other gases or fluids.

From the Montecarlo simulation, p10, p50 and p90 values can be calculated. The outputs from this workflow allow not only for numerical capacity and cavern number but also the geospatial data.

4.3.2 Model Parameters

The geological model requires the parametrisation of the following, insoluble content, geothermal gradient, and pressure. These can be determined from both well and seismic data.

4.3.2.1 Overburden Pressure

Two separate approaches can be taken dependent on data available. 1) For areas where data for the above layers of the overburden were available as well as density data, a layer cake approach was used in Equation. 23 (Zoback, 2010). Due to the geological surfaces being used for thickness calculations and affected by the uncertainty in the depth conversion, these values were modified to the same uncertainty distribution that had been applied to the geological surfaces. Bulk density well logs were used to calculate the average densities for each of the geological layers in Figure 4-2 - Equation 9. These values were also subject to a certain level of uncertainty, so to account for this it was decided that a uniform distribution of +-10% was applied to the densities on each model run. This was not applied for the water column layer, instead, a constant value of 1024 Kg/m^3 was applied.

$$\sigma_{lith} = \sum L1(\rho * g * \delta Z) + L2(\rho * g * \delta Z) + L3(\rho * g * \delta Z).. \qquad \textit{EQUATION 23}$$

σ_{lith} = $Lithostatic\ Pressure\ (Pa)$

Ln = $Geological\ Layer$

ρ = $Density\ of\ geological\ layer\ (Kg/m^3)$

g = $gravitational\ constant$

δZ = $thickness\ of\ geological\ layer\ (m)$

2) For areas where the data were not available to make a layer cake model, a simple 2-layer depth/gradient approach was used which accounted for both the water column and rock overburden separately. The gradient of the rock overburden was calculated from the average overburden density, a value of 1024 kg/m^3 assumed for the water column and the depth taken from the cavern mid-point (Appendix - Equation Sheet - I). Regional stresses were not considered when creating the over burden pressure models.

4.3.2.2 Temperature

Geothermal gradient was calculated using Allen and Allen (2013)s principle for determining geothermal gradient. Bottom well temperatures were examined from wells within the AOI to calculate the geothermal gradients. From these calculated gradients, minimum and maximum gradients were extracted. The minimum maximum values set the bounds of a uniform distribution for geothermal gradients to use in the calculation of mid-cavern temperature (Appendix 3). The geothermal gradient was then used in Equation 24 to calculate cavern temperature.

$$T_{mc} = T_{sb} + (Z_{mc} * \nabla T) \qquad \textit{EQUATION 24}$$

T_{mc} = $Mid\ Cavern\ Temperature$ (°C)
T_{sb} = $Seabed\ temperature$ (°C)
Z_{mc} = $Mid\ Cavern\ depth\ below\ sea\ floor$ *(Km)*
∇T = $Geothermal\ gradient$ *(*°C$/km$*)*

4.3.2.3 Insoluble Content

Insoluble content of the AOI is calculated from available well logs within the area. Insoluble content was identified as any siliciclastic and carbonate lithologies present within the well, the evaporitic minerals anhydrite and polyhalite were also included within the insoluble content criteria, due to their high level of insolubility compared with halite (Warren, 2016). From the calculated insoluble content values, a distribution was created to be used within the workflow.

$$Ic = \frac{\Delta Z_{IC}}{\Delta Z_{TES}} * 100$$

EQUATION 25 EQUATION 5 MODIFIED EQUATION FOR NET TO GROSS FROM (ALYAFEI, 2021).

$Ic = Insoluble\ content\ (\%)$

$\Delta Z_{IC} = Length\ insoluble\ lithology\ in\ target\ evaporite\ stratigraphy$

$\Delta Z_{TES} = Total\ length\ of\ target\ evaporite\ stratigraphy$

4.3.3 Sensitivity Analysis

A sensitivity analysis was undertaken for two separate AOI's and geological models, the layered evaporite block and the salt wall block (Section 4.3.2.1 and 4.3.1). A Sobol sensitivity analysis used 1000 iterations and was implemented with the use of the SALib python module (Sobol', 2001; Herman and Usher, 2017; Iwanaga, Usher and Herman, 2022). For the sensitivity analysis, four parameters were included: depth uncertainty, geothermal gradient, insolubility, and overburden gradient.

4.4 3. Geological Model Building

4.4.1 Geological model methodology

4.4.1.1 Well data interpretation.

Petrophysical logs were interpreted to distinguish different lithologies and different stratigraphic intervals. A combination of gamma-ray, sonic, and density logs were used alongside the well site geological descriptions from cuttings. For the Zechstein Supergroup stratigraphy, however, lithologies were applied to the highest resolution allowed by the petrophysical logging tools. This resolution varies depending on the type of logging tool used; however, it typically ranges from 1 – 5 m (Bourke *et al.*, 1989). Following this, well-tops were applied for the intra Zechstein stratigraphy, using the same QC as used for the non-Zechstein stratigraphy. This well interpretation allowed for the interpretation of the key geological horizons within the seismic data.

4.4.1.2 Seismic Well Tie

Synthetic-seismic well ties were generated to correlate the interpreted stratigraphic boundaries from the well data that were in the depth domain (m) to the seismic data that were in the time domain (ms). Synthetic traces were generated using a 35hz ricker wavelet and extracted wavelets. These were compared with the original seismic data and the best match selected to be used. The wells were bulk shifted vertically to assure the most suitable time-depth match between well and seismic data, the top Zechstein seismic reflection was aimed to be matched by the bulk shifting process.

4.4.1.3 Seismic Data Interpretation

The reflections identified as key stratigraphic boundaries were interpreted on the seismic data. Reflections of stratigraphic boundaries were initially mapped at intervals of 25 m on both crosslines and inlines. 3D auto tracking was used to complete the horizon interpretation. If areas were not sufficiently mapped by the auto-tracking process, they were manually remapped in smaller increments and then re-autotracked. This process was repeated until suitable interpretations of each key reflection had been achieved. From these reflection interpretation horizons, surfaces were generated, the surfaces had a grid spacing of 50 x 50 m and used a convergent gridding algorithm. This process produced seamless surfaces.

Geological faults were mapped from the seismic data. To accomplish this, the seismic data were viewed perpendicular to the strike of the fault,. Intersection intervals of 25 m were used, with the view of the seismic data being re-orientated if the fault orientation changed. Faults were mapped until they could not be perceived anymore within the seismic data.

4.4.1.4 Seismic Depth Conversion

Depth conversion is required where seismic data are in the time domain since all calculations used to determine cavern placement and geometry require depth as a constraint. To depth convert we follow a standard approach of using geophysical logs to determine the velocity structure in the subsurface (Al-Chalabi, 2014). This is subsequently used to determine interval velocities for the layers within the geological model. Time-depth relationship data were extracted from wells within the area and generated time surfaces used at the identified velocity interval. The model build aimed for residuals <10 %. For a complete description of the depth conversion method please see the data repository.

4.4.2 Geological Models

In the sections below we describe the different geological models, and their parametrisations used as case studies for the workflow described. Three discrete sets of depth surfaces were used for the four areas of investigation, these depth surface datasets have different resolutions and different associated depth uncertainties. The basin wide, sub regional and salt wall depth surfaces are from existing available interpretations, while the layered evaporite model had surfaces interpreted for this study using the methodology described in section 3.1.1 – 3.1.4. Data from different sources was used to investigate the response of the proposed workflow at different data scales, resolutions, and uncertainties.

4.4.2.1 Basin Wide Salt Depth Model

The basin wide depth model covers an area of 58,904 km^2 (Figure 4-1). The surfaces used in the model have a grid cell size of 250 m x 250 m (the lowest resolution of depth models used) and bounded the top and base Zechstein Supergroup. The surfaces are from the 'NSTA and Lloyd's Register SNS Regional Geological Maps (Open Source)' dataset and available from the NSTA public open data repository (https://opendata-nstauthority.hub.arcgis.com/explore). No information was supplied regarding depth uncertainty. We assume a 10% depth uncertainty to account for this unknown.

4.4.2.2 Sub-Regional Salt Depth Model

The depth surfaces for the sub regional salt depth model are from Barnett, Ireland and van der Land (2023) and cover 25,000 km^2 (Figure 4-1). The surfaces are from the interpretation of a regionally extensive 3D merge seismic volume of the Southern North Sea (OA__2019seis0001a), with the top and base surfaces uses bounding top and base Zechstein, the surfaces having already been converted from the time to depth domain. The grid cell size is 50 m x 50 m. The depth surfaces have a 5% uncertainty associated with them (Barnett, Ireland and van der Land, 2023).

4.4.2.3 Block Specific

Blocks, when referring to the offshore energy industry, define set areas in which licences have been granted for specific activities, such as oil and gas exploration, or more recently, carbon capture and storage. Gas storage licences are also awarded as blocks from the UK's North Sea Transition Authority, with Centrica being awarded a licence for the Rough Gas storage site in

2022 (North Sea Transition Authority, 2022). Exploration blocks in the Southern North Sea are on average 115 km^2, with the largest being 250 km^2. We aimed to mimic these spatial constraints when applying our workflow, as it is likely that licences and areas for gas storage in salt caverns will be granted in a similar manner by the North Sea Transition Authority.

4.4.2.3.1 Salt Wall Salt Depth Model

The depth surfaces from the salt wall cover an area of 420 km^2 (Figure 4-1). It is located on a structure often referred to as the Audrey salt wall (Elam, 2007; Allsop *et al.*, 2023), which trends NNW – SSW in the UK sector of the South Permian Basin. The depth surfaces were extracted from the Sub regional depth model, and thus the grid cell sizing of 50 m x 50 m and depth uncertainty of 5% remain the same.

4.4.2.3.2 Layered Evaporite Salt Depth Model

The layered evaporite salt depth model covered an area of 225 km^2 (Figure 4-1). It is located at the northern edges of the South Permian Basin, just south of the Mid-North Sea High (Figure 4-1). Seismic survey MA933F0002 was used to interpret top and base target salt, and other major stratigraphic reflections for the area (Table 4-1). The reflection chosen as top target salt was the top of the Stassfurt Halite and base target salt was Basel Polyhalite of Stassfurt Halite because the thickest and most homogenous section of halite was at this section in the interpreted well data (Figure 4-4,Figure 4-5). Seismic reflections in layered evaporite sequences can be difficult to interpret. Fortunately, the targeted reflections within the seismic data set were mostly continuous and able to be interpreted. However, in areas where seismically resolvable high internal structural heterogeneity and deformation was present, the targeted reflection could not be interpreted with a high degree of confidence. As these areas contained seismic heterogeneities that deemed the area to have no potential for cavern emplacement, a best effort was made to map the targeted reflections, and the area of internal structural heterogeneities was mapped in a timeslice view to be used as an input within the geological model as an area not to emplace caverns. Two-way time surfaces were created as described in section 4.4.1.3 from the interpreted seismic reflections. As the surfaces were in two-way time, they had to be depth converted. The depth conversion model used 5 layers (Table 4-1) and time-depth relationship data were taken from two wells within the area (See Data Repository). The final depth surfaces had a grid cell size of 50 m x 50 m,

and a residual uncertainty of 7%. Within the Stassfurt Halite there were heterogeneities observed that were interpreted to be non-halite (insoluble) lithologies. These heterogeneities cannot always be interpreted on seismic data due to the seismic reflections within the area abruptly terminating and being discontinuous (Barnett, Ireland and van der Land, 2023). The area in which these heterogeneities were observed was instead mapped using seismic time slice views within the Stassfurt Halite (Appendix 6). These mapped heterogeneities were included within the geological model as areas incompatible with salt cavern placement.

Geological Horizon - Mapped
Seabed
Top Bunter Sandstone
Base Bunter Sandstone
Top Zechstein (Base bunter Shale)
Top Stassfurt Halite
Base Stassfurt Halite (above basal polyhalite reflection)
Base Zechstein

TABLE 4-1 KEY STRATIGRAPHIC SURFACES USED FOR THE LAYERED EVAPORITE GEOLOGICAL MODEL.

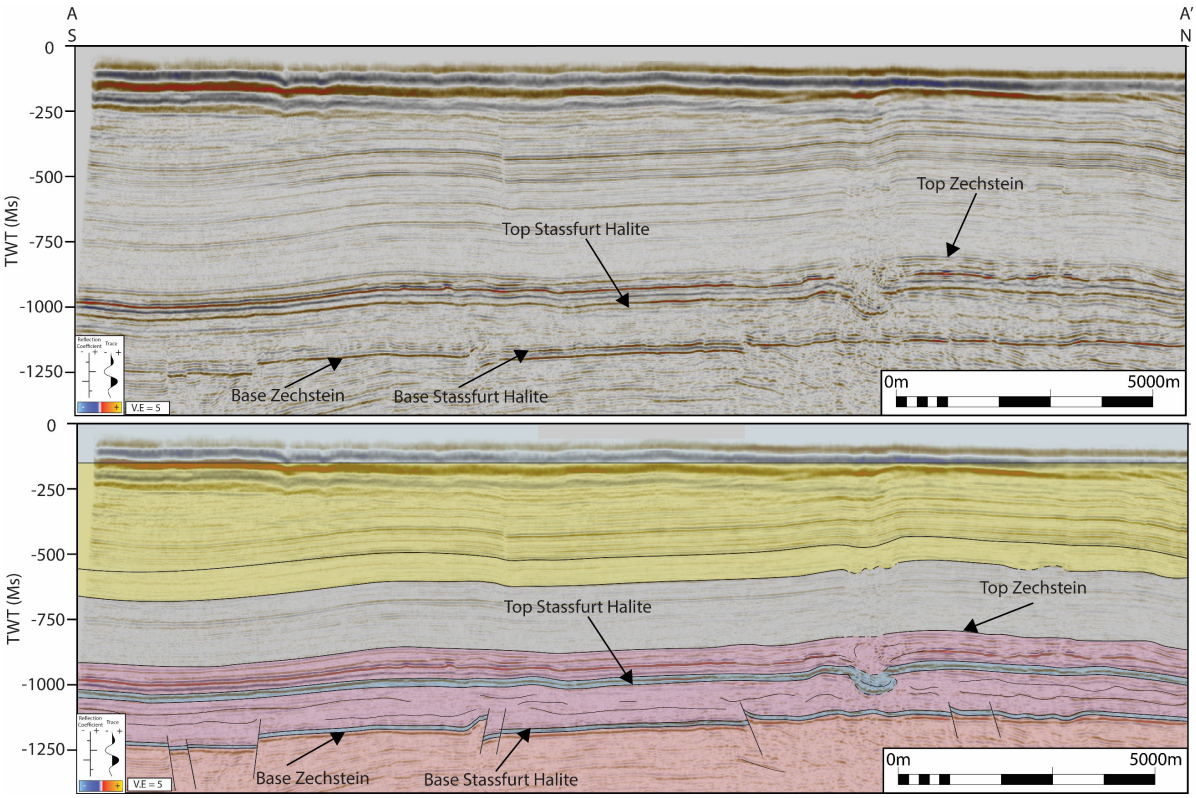

FIGURE 4-4 A) EXAMPLE SEISMIC CROSS SECTION FROM THE 'BLOCK – LAYERED EVAPORITE' AOI (SEISMIC SURVEY MA933F0002), RUNNING NORTH TO SOUTH, A – A' (FIGURE 4-1), IN TWT, KEY REFLECTIONS HAVE BEEN MARKED ON.

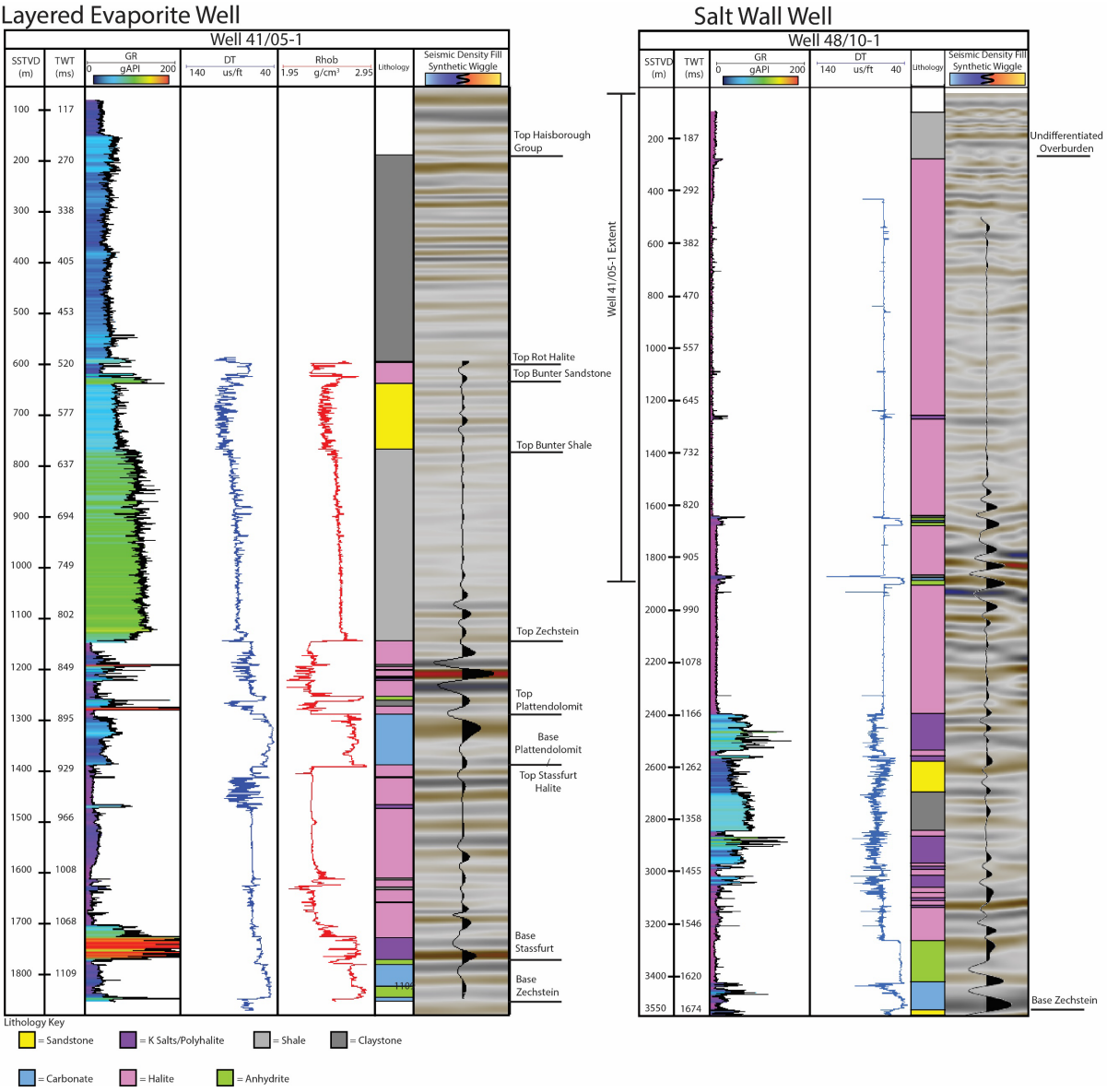

FIGURE 4-5 PETROPHYSICAL LOGS OF WELL 41/05-1 AND 48/10-1 (FIGURE 4-1), GR (GAMMA-RAY), DT (SONIC), RHOB (DENSITY), INTERPRETED LITHOLOGY LOG IS PRESENT. CALCULATED SYNTHETIC SEISMIC TRACE OVERLYING SEISMIC TRACE FROM SEISMIC SURVEY MA933F002 AND INTERPRETED KEY STRATIGRAPHIC BOUNDARIES.

4.4.3 Geological Model Parameter Setup

Seven separate geological models were devised using the five depth models in section 3.2. The models were devised to investigate different scales, cavern design, data quality and salt type on the effect on cavern placement. Parameters for the workflow, such as minimum salt thickness and maximum depth were taken from literature and can be found in Table 4-2.Each AOI had a distribution of insoluble content calculated from wells within the area to account

for non-halite lithologies present within the cavern column (Figure 4-1, Same distribution applied to basin wide and sub-regional). Each geological model (Table 4-3) was ran as a Montecarlo simulation for a total of 2500 iterations.

Parameter	Value
Depth to target salt	500 – 2000 m (Warren, 2006; Caglayan *et al.*, 2020; Tan *et al.*, 2021)
Target salt thickness	>200m (Smith, Evans and Andrews, 2005; Wang *et al.*, 2015; Caglayan *et al.*, 2020).
Structural heterogeneities	Mapped parameter, buffer set at 250m (Yang *et al.*, 2013; Chen *et al.*, 2022)
Height – to – diameter ratio	0.5 minimum (Wang *et al.*, 2015; Caglayan *et al.*, 2020) Typical no greater than 7.5
Fixed Cavern Size	300 m tall 58.5 m Diameter
Variable Cavern Size	Maximum Cavern Height: 750 m Minimum cavern height: 91.5 m (based on minimum salt thickness 200 m) Maximum height-to-diameter ratio: 7.5 Minimum height-to-diameter ratio: 0.8
Cavern spacing	2 * Cavern diameter taken from (Caglayan *et al.*, 2020). Can be modified to different value if required
Target salt Solubility	No value requirements, needed for hydrogen capacity calculation. Ideally as high as possible.
Energy system integration	Mapped parameter

TABLE 4-2 SALT CAVERN PARAMETERS WITHIN WORKFLOW

4.5 Results

4.5.1 Basin Wide – Fixed caverns

The p50 cumulative storage capacity from the basin wide geological model is 48,875 TWh (Figure 4-6). The p90 and p10 capacities are 39,570 and 64,438 TWh. This is based on total cavern number of 195,563 for the p50, 161,876 for the p90 and 252,614 for the p10. The average cavern capacity for the Montecarlo iteration closest to the p50 value (iteration 149) is 245 TWh. Iteration 1808 of the Montecarlo is the geospatial representative of the p50 capacity and can be seen in Figure 4-6A. Individual cavern capacity is typically lower towards the edges of the basin and placement in the basin depocenter is typically restricted to salt structures (Figure 4-6).

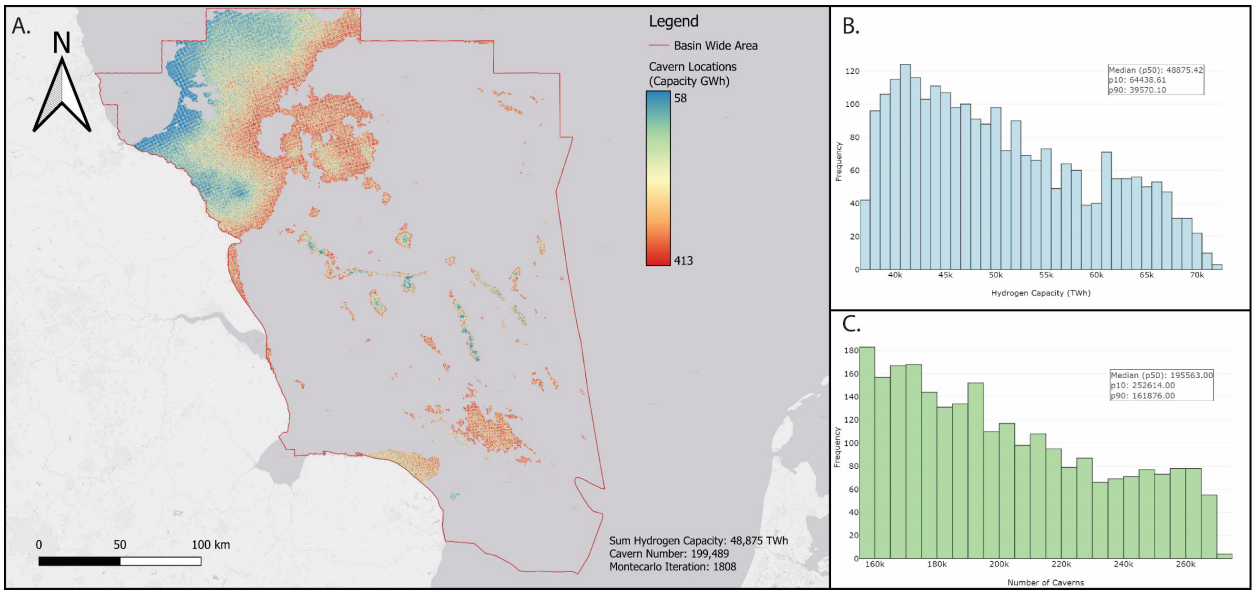

FIGURE 4-6 A) CAVERN PLACEMENT MAP 'BASIN WIDE' AOI, FIXED CAVERN GEOMETRIES. GEOSPATIAL PLACEMENT REPRESENTS THE OUTPUT MODEL FROM THE WORKFLOW WITH THE CLOSEST TOTAL HYDROGEN CAPACITY TO THE CALCULATED P50 (ITERATION 1808/2500). A TOTAL OF 199,489 CAVERNS ARE PLACED, WITH A P50 SUM OF 48,875 TWH OF HYDROGEN STORAGE CAPACITY. B) HISTOGRAM OF TOTAL HYDROGEN CAPACITIES FOR EACH ITERATION OF THE MONTECARLO SIMULATION (2500 ITERATIONS). C) HISTOGRAM OF TOTAL CAVERN NUMBER FOR EACH ITERATION OF THE MONTECARLO SIMULATION (2500 ITERATIONS).

Model	Max Salt Depth (m)	Minimum Salt Depth (m)	Min Salt thickness (m)	Top Salt Surface	Base Salt Surface	Depth Model	Grid Cell Resolution (m)	Temperature (°c)	Overburden Pressure Model	Insoluble Content (%)	Cavern Geometry	Depth Uncertainty (%)	Exclusion Zones	Area Km²
Basin Wide – Fixed Caverns	1700	500	358.5	Top Zechstein (Stochastic)	Base Zechstein (Stochastic)	Basin Wide Salt Depth Model (Section 3.1)	250	Distribution, see Appendix 4 (Stochastic)	Gradient – 0.02354 MPa/m (2400kg/m3 equivalent) (Deterministic) (Williams *et al.*, 2022)	Distribution (Regional), see Data repository (Stochastic)	Height: 300 Diameter: 58	10	None	58,904
Sub-Regional - Fixed Caverns	1700	500	358.5	Top Zechstein (Stochastic)	Base Zechstein (Stochastic)	Sub Regional Salt Depth Model (Section 3.2)	50	Distribution, see Appendix 4 (Stochastic)	Gradient – 0.02354 MPa/m (2400kg/m3 equivalent) (Deterministic, but linked to depth uncertainty) (Williams *et al.*, 2022)	Distribution (Regional), see Data repository (Stochastic)	Height: 300 Diameter: 58	5	None	25,000
Layered Evaporite – Variable Caverns	1700	500	200	Top Stassfurt Halite (Stochastic)	Base Stassfurt Halite (Stochastic)	Layered Evaporite Salt Depth Model (Section 3.3.2)	50	Distribution, see Appendix 4 (Stochastic)	Layer cake model (Stochastic)	Distribution (Layered Evaporite), see Data repository (Stochastic)	Variable, Set from height-to-diameter ratio, See Appendix 2. Maximum height 750 m	7	Interpreted heterogeneity in seismic, Faults (250 m buffer)	238.5
Layered Evaporite – Fixed Caverns	1700	500	358.5	Top Stassfurt Halite (Stochastic)	Base Stassfurt Halite (Stochastic)	Layered Evaporite Salt Depth Model (Section 3.3.2)	50	Distribution, see Appendix 4 (Stochastic)	Layer cake model (Stochastic)	Distribution (Layered Evaporite), see Data repository (Stochastic))	Height: 300 Diameter: 58	7	Interpreted heterogeneity in seismic, Faults (250 m buffer)	238.5
Layered Evaporite - Basin Wide Data - Variable Caverns	1700	500	200	Top Zechstein (Stochastic)	Base Zechstein (Stochastic)	Basin Wide Salt Depth Model (Section 3.1)	50	Distribution, see Appendix 4 (Stochastic)	Layer cake model (Stochastic)	Distribution (Layered Evaporite), see Data repository (Stochastic)	Variable, Set from height-to-diameter ratio, See Appendix 2. Maximum height 750 m	10	Interpreted heterogeneity in seismic, Faults (250 m buffer)	238.5
Salt Wall – Variable Caverns	1700	500	200	Top Zechstein (Stochastic)	Base Zechstein (Stochastic)	Sub Regional Salt Depth Model (Section 3.2, cut for Salt – Wall Block)	50	Distribution, see Appendix 4 (Stochastic)	Gradient – 0.2305 MPa/m (2040kg/m3 equivalent) (Deterministic, but linked to depth uncertainty) (Williams *et al.*, 2022)	Distribution (Salt Wall), see Data repository (Stochastic)	Variable, Set from height-to-diameter ratio, See Appendix 2. Maximum height 750 m	5	500m buffer away from salt wall edges	420
Salt Wall – Fixed Caverns	1700	500	358.5	Top Zechstein (Stochastic)	Base Zechstein (Stochastic)	Sub Regional Salt Depth Model (Section 3.2, cut for Salt Wall -Block)	50	Distribution, see Appendix 4 (Stochastic)	Gradient – 0.2305 MPa/m (2040kg/m3 equivalent) (Deterministic, but linked to depth uncertainty) (Williams *et al.*, 2022)	Distribution (Salt Wall), see Data repository (Stochastic)	Height: 300 Diameter: 58	5	500m buffer away from salt wall edges	420

TABLE 4-3 GEOLOGICAL MODELS RUN THROUGH PROPOSED WORKFLOW WITH IDENTIFIED GEOLOGICAL PARAMETRISATIONS.

4.5.2 Sub-Regional – Fixed caverns

The p50 capacity of the sub-regional basin scale geological model is 9,685 TWh, the p90 and p10 are 8,045 and 12,579 TWh. This is based on a total cavern number of 35,873 for the p50, 30,086 for the p90 and 46,230 for the p10. Iteration 2011 of the Montecarlo simulation is the geospatial representative of the p50 result and can be seen in Figure 4-7A. The locations identified for the development of caverns predominantly show that cavern placement in the mid basin follows the orientation of the major salt structures. 27.4% of caverns of the p50 model are plotted in salt walls and diapirs, despite walls and diapirs only accounting for 5.6% of the total area of the sub-regional basin area (1,400 km^2). The remaining 72.6 % of caverns are plotted at the basin edges to the north-west towards the Mid-North sea high, where the cavern placement occurs within areas of layered evaporite and hence cavern placement is more ordered (Figure 4-7).

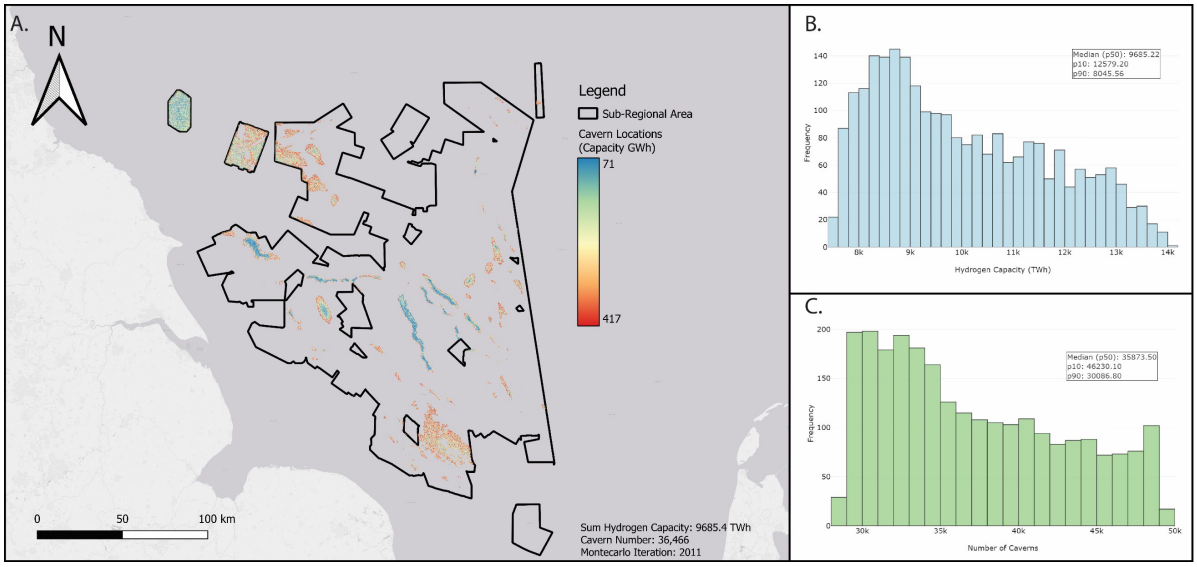

FIGURE 4-7 A) CAVERN PLACEMENT MAP 'SUB-REGIONAL' AOI, FIXED CAVERN GEOMETRIES. GEOSPATIAL PLACEMENT REPRESENTS THE OUTPUT MODEL FROM THE WORKFLOW WITH THE CLOSEST TOTAL HYDROGEN CAPACITY TO THE CALCULATED P50 (ITERATION 2011/2500). A TOTAL OF 36,466 CAVERNS ARE PLACED, WITH A SUM OF 9,685 TWH OF HYDROGEN STORAGE CAPACITY. B) HISTOGRAM OF TOTAL HYDROGEN CAPACITIES FOR EACH ITERATION OF THE MONTECARLO SIMULATION (2500 ITERATIONS). C) HISTOGRAM OF TOTAL CAVERN NUMBER FOR EACH ITERATION OF THE MONTECARLO SIMULATION (2500 ITERATIONS).

4.5.3 Block Specific

4.5.3.1 Salt Wall

4.5.3.1.1 Salt Wall - Variable Cavern

The p50 capacity of the salt wall – with variable cavern sizes, is 580 TWh, p90 and p10 capacities are 562 and 580 respectively (Figure 4-8A, B). We identify 409 potential cavern locations in the salt wall (Figure 4-8,A). Despite the stochastic approach applied to the salt surfaces to account for depth uncertainty, as the interpreted salt thickness is typically greater than 2500 m the 5% depth uncertainty does not affect how many caverns can be placed. As such all caverns were determined to have the maximum hight possible, 750m (Table 4-3,Table 4-4) and hence had the same height-to-diameter ratio applied to them. This resulted in all caverns before being adjusted for both insoluble content and shape correction factor to having the same volume at 5,628,686 m^3.

Parameter	Value
Depth to target salt	500 – 2000 m (Warren, 2006; Caglayan *et al.*, 2020; Tan *et al.*, 2021)
Target salt thickness	>200m (Smith, Evans and Andrews, 2005; Wang *et al.*, 2015; Caglayan *et al.*, 2020).
Structural heterogeneities	Mapped parameter, buffer set at 250m (Yang *et al.*, 2013; Chen *et al.*, 2022)
Height – to – diameter ratio	0.5 minimum (Wang *et al.*, 2015; Caglayan *et al.*, 2020) Typical no greater than 7.5
Fixed Cavern Size	300 m tall 58.5 m Diameter
Variable Cavern Size	Maximum Cavern Height: 750 m Minimum cavern height: 91.5 m (based on minimum salt thickness 200 m) Maximum height-to-diameter ratio: 7.5 Minimum height-to-diameter ratio: 0.8
Target salt Solubility	No value requirements, needed for hydrogen capacity calculation. Ideally as high as possible.
Energy system integration	Mapped parameter

TABLE 4-4 SALT CAVERN PARAMETERS WITHIN ALL WORKFLOWS

4.5.3.1.2 Salt Wall - Fixed Cavern

The p50 capacity of the salt wall geological model with caverns of fixed geometry (Table 4-2) was 178 TWh, the p90 and p10 results are 174 and 183 TWh (Figure 4-8C, D). The total number of potential cavern locations within the area ranges between 1154 and 1151, depending on the depth uncertainty applied (Figure 4-8C, D). Small edge case variations between the Montecarlo iterations caused by the associated depth uncertainty %, cause small areas to become theoretically viable or unviable, causing the small change in cavern number, similar to that of the salt wall variable cavern number.

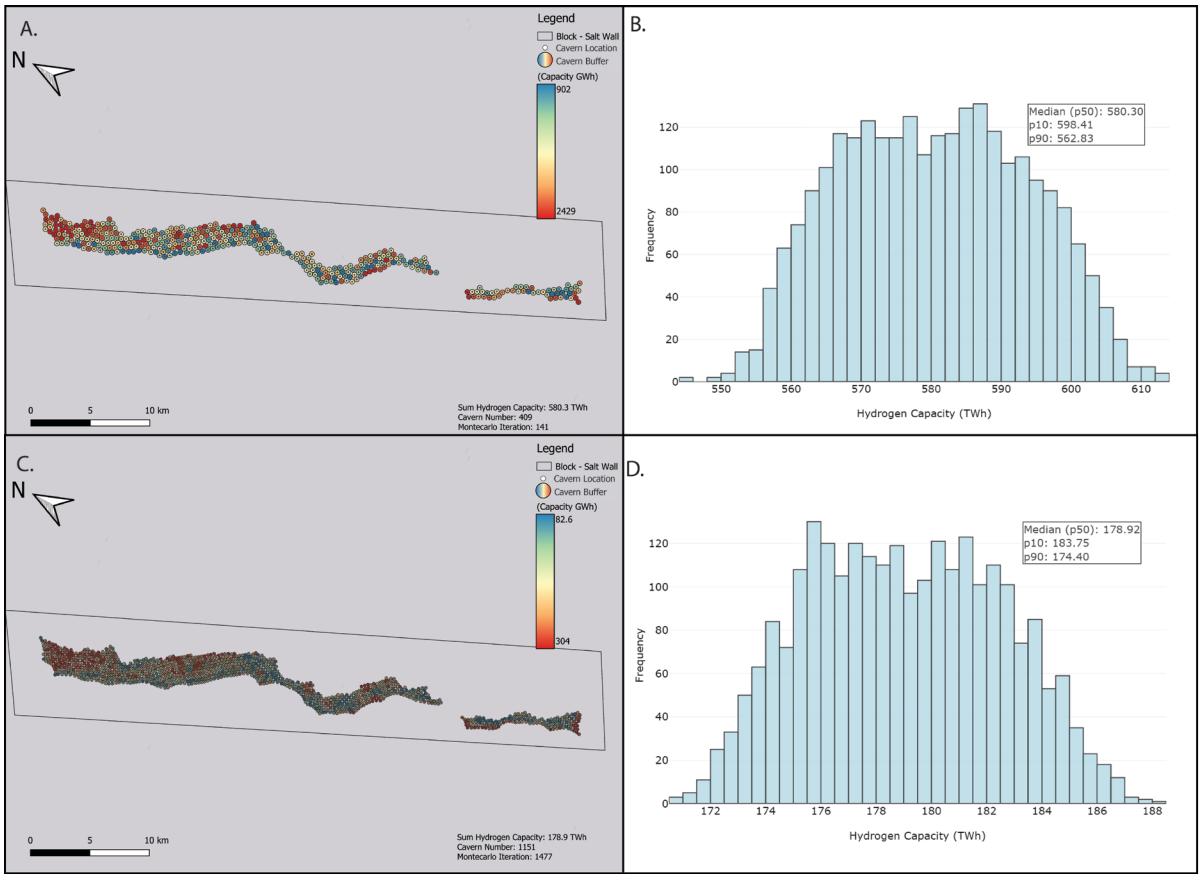

FIGURE 4-8 CAVERN PLACEMENT MAP 'BLOCK SPECIFIC – SALT WALL' AOI, VARIABLE CAVERN GEOMETRIES. GEOSPATIAL PLACEMENT REPRESENTS THE OUTPUT MODEL FROM THE WORKFLOW WITH THE CLOSEST TOTAL HYDROGEN CAPACITY TO THE CALCULATED P50 (ITERATION 141/2500). A TOTAL OF 409 CAVERNS ARE PLACED, WITH A SUM OF 580.3 TWH OF HYDROGEN STORAGE CAPACITY. B) HISTOGRAM OF TOTAL HYDROGEN CAPACITIES FOR EACH ITERATION OF THE MONTECARLO SIMULATION (2500 ITERATIONS). C) CAVERN PLACEMENT MAP 'BLOCK SPECIFIC – SALT WALL' AOI, FIXED CAVERN GEOMETRIES. GEOSPATIAL PLACEMENT REPRESENTS THE OUTPUT MODEL FROM THE WORKFLOW

WITH THE CLOSEST TOTAL HYDROGEN CAPACITY TO THE CALCULATED P50 (ITERATION 1477/2500). A TOTAL OF 1151 CAVERNS ARE PLACED, WITH A SUM OF 178.9 TWH OF HYDROGEN STORAGE CAPACITY. D) HISTOGRAM OF TOTAL HYDROGEN CAPACITIES FOR EACH ITERATION OF THE MONTECARLO SIMULATION (2500 ITERATIONS).

4.5.3.2 Layered Evaporite

4.5.3.2.1 Layered Evaporite - Variable Cavern

The p50 capacity of the layered evaporite – variable caverns geological model is 263.1 TWh, p90 and p10 are 242.2 and 283.0 TWh. For the p50 the number of potential cavern locations is 440 (Figure 4-9, Table 4-5) with 358 and 495 for the p90 and p10 respectively (Figure 4-9, Table 4-5). Table 4-5 has the closest model iterations output to the p10, p50 and p90 capacity values (Figure 4-9). The iteration closest to the p50 has the largest number of caverns present, however it has the smallest working average cavern working capacity with .524 TWh compared with .596 TWh of the p90 and .198 TWh of the p10. The iterations closest to the p10 and p90 capacity values have a similar number of caverns placed (408 and 406), however the P10's greater average working capacity gives the model greater total working capacity.

4.5.3.2.2 Layered Evaporite - Fixed Cavern

The p50 capacity of the layered evaporite – fixed caverns geological model is 161.9 TWh, 101.2 TWh less than that of the variable cavern model for same AoI (Figure 4-10). The p90 and p10 capacity values are 106.6 and 178.8 TWh respectively. The p50 for cavern placement is 780, p90 and p10 for cavern number are 519 and 820 potential locations. The iteration from the Montecarlo simulation with the closet hydrogen value to the p50 capacity has a total of 806 potential cavern locations, 304 more caverns than the equivalent variable cavern p50 iteration. The fixed caverns however have a much lower average capacity, with value of .208 TWh, compared with .524 TWh of the variable caverns.

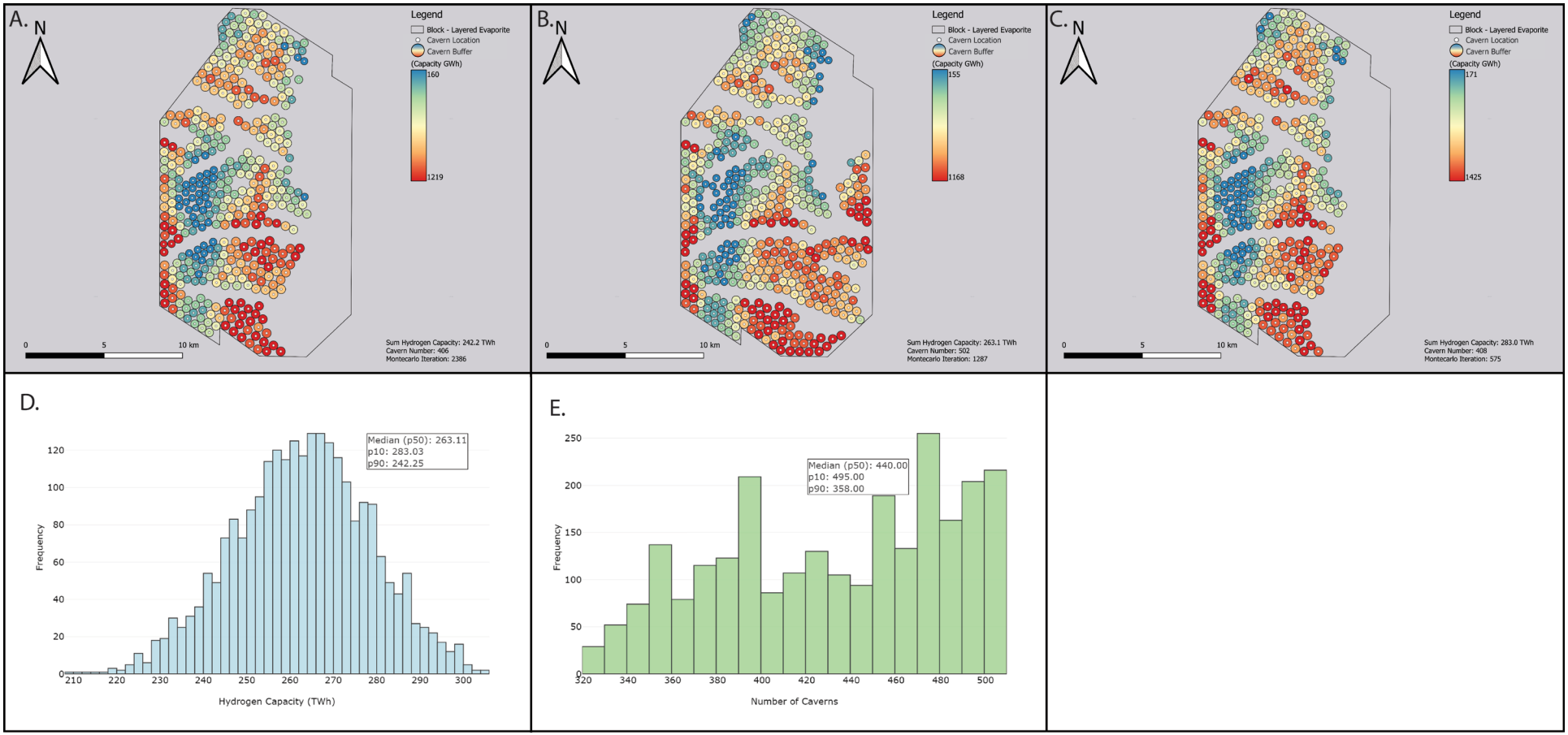

FIGURE 4-9 CAVERN PLACEMENT MAP 'BLOCK SPECIFIC – LAYERED EVAPORITE' AOI, VARIABLE CAVERN GEOMETRIES. GEOSPATIAL PLACEMENT REPRESENTS THE OUTPUT MODEL FROM THE WORKFLOW WITH THE CLOSEST TOTAL HYDROGEN CAPACITY TO THE CALCULATED P90 (A, ITERATION: 2386), P50(B, ITERATION: 1287), AND P10 (C, ITERATION: 575). D) HISTOGRAM OF TOTAL HYDROGEN CAPACITIES FOR EACH ITERATION OF THE MONTECARLO SIMULATION (2500 ITERATIONS). E) HISTOGRAM OF TOTAL CAVERN NUMBER FOR EACH ITERATION OF THE MONTECARLO SIMULATION (2500 ITERATIONS).

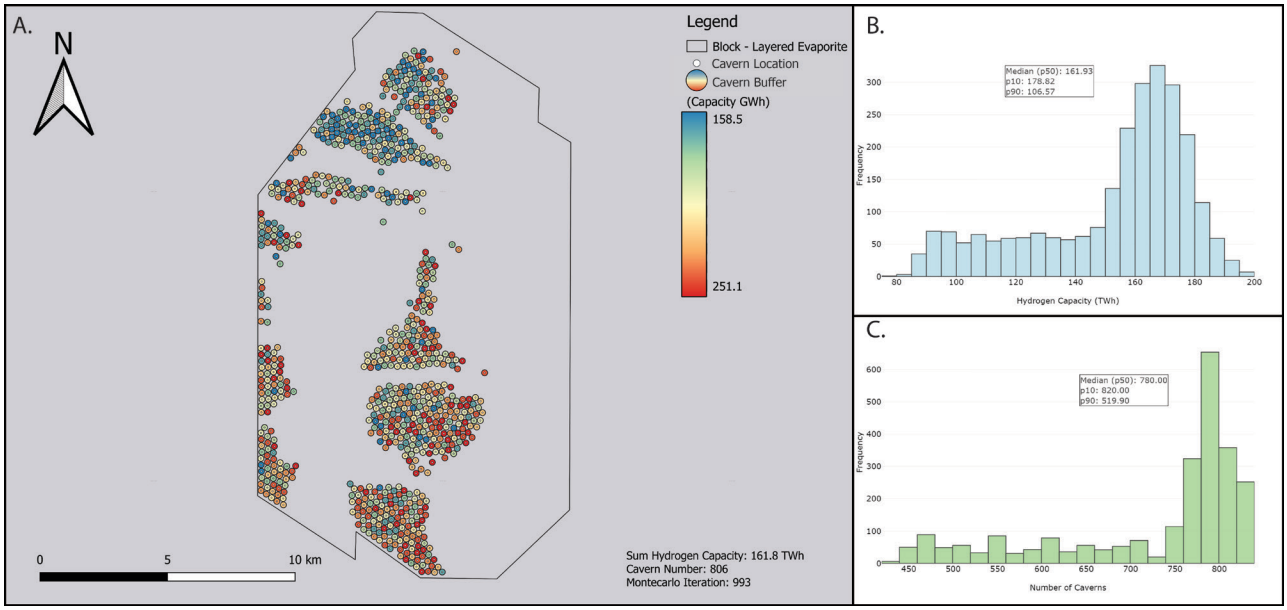

FIGURE 4-10 A) CAVERN PLACEMENT MAP 'BLOCK SPECIFIC – LAYERED EVAPORITE' AOI WITH FIXED GEOMETRIES. GEOSPATIAL PLACEMENT REPRESENTS THE OUTPUT MODEL FROM THE WORKFLOW WITH THE CLOSEST TOTAL HYDROGEN CAPACITY TO THE CALCULATED P50 (ITERATION 993/2500). A TOTAL OF 806 CAVERNS ARE PLACED, WITH A P50 SUM OF 161.8 TWH OF HYDROGEN STORAGE CAPACITY. B) HISTOGRAM OF TOTAL HYDROGEN CAPACITIES FOR EACH ITERATION OF THE MONTECARLO SIMULATION (2500 ITERATIONS). C) HISTOGRAM OF TOTAL CAVERN NUMBER FOR EACH ITERATION OF THE MONTECARLO SIMULATION (2500 ITERATIONS).

4.5.3.2.3 Layered Evaporite - Basin Wide Depth Model – Variable Cavern

The p50 capacity of the layered evaporite – basin wide depth model - variable caverns was 683 TWh (Figure 4-11), the p90 and p10 capacities are 624.4 and 746 TWh. The p50 for cavern placement is 579, p90 and p10 for cavern number are 564 and 587 potential locations. The resultant geospatial distribution of the caverns differs from the site-specific depth model (Section 4.5.3.2.1), as there are large gaps between placed caverns (Figure 4-11). The caverns placed have a higher average capacity than the site-specific geological model 1.183 TWh vs .524 TWh (closest iteration to the p50 capacity of both models).

4.5.4 Conceptual cavern cluster developments

While cumulative hydrogen capacity across large tracts of basins may be useful for initial comparison of storage potential, a more useful consideration is the capacity of a salt cavern cluster development. We therefore consider five conceptual salt cavern cluster developments as a demonstration of how the workflow could aid in early-stage planning for a possible

cavern site at the project pre-feasibility stage (Figure 4-12). The theoretical cluster concepts were developed using iteration 175 (Figure 4-9) from the Montecarlo simulation, the iteration where the cumulative hydrogen capacity was closest to the p50 of the block specific – layered evaporite – variable cavern model (Section 4.5.3.2.1). We determine the following scenarios: 1) Maximum hydrogen storage capacity within a 1.5 km radius of fixed point; 2) Maximum hydrogen storage capacity within a 3 km cluster radius of fixed point; 3) Maximum cavern number within a 1.5 km radius of fixed point; 4) Maximum cavern number within a 3 km radius of fixed point; 5) Storage capacity within 1.5 km radius of pre-existing infrastructure (wellbore 41/05-1) (Figure 4-1, 4-5). Radiuses of 1.5 – 3 km are considered viable step-out or deviation distances from a central facility point for development of individual caverns based on known developments. The geographic layout of the development concepts is shown in Figure 4-12, and a summary of results is in Table 4-6.

Model	Total Working hydrogen Capacity (TWh)	Total Cavern Number	Average Cavern Working Capacity (Cushion Gas) (TWh)	Smallest Cavern Working Capacity (Cushion Gas) (TWh)	Largest Cavern Working Capacity (Cushion Gas) (TWh)	Energy Density (TWh/Km^2)
P90 (Iteration: 1590)	242.2	406	0.596 (.198)	.160 (.053)	1.219 (.406)	1.07
P50 (Iteration: 175)	263.1	502	0.524 (.174)	.154 (.051)	1.167 (.389)	1.17
P10 (Iteration: 1128)	283.0	408	0.693 (.231)	.171 (.057)	1.424 (.474)	1.26

TABLE 4-5 RESULTS OF MONTECARLO SIMULATION, ITERATIONS CLOSEST TO P VALUES FROM LAYERED EVAPORITE – VARIABLE CAVERN GEOMETRIES

4.5.5 Sensitivity Analysis

The layered evaporite area cavern cluster's largest uncertainty was the overburden gradient (Figure 4-13,A), compared with insolubility content for the salt wall area (Figure 4-13,B). The layered evaporite area had a more constrained insolubility distribution (Figure 4-13A, B, Appendix 7) than that of a salt wall and is likely the cause of it being less sensitivity to the insoluble content. Overburden pressure gradient was the most sensitive parameter for the layered evaporite area and second for the salt wall, this suggests that more complex site-

specific geomechanical models should be incorporated to help reduce uncertainty from capacity estimates. The salt wall block was mostly insensitive to the depth uncertainty (Figure 4-13,B), as increasing or decreasing the salt geometries made no change to the suitability of an area for cavern emplacement, however, the layered evaporite area was sensitive (Figure 4-13,A) to the depth uncertainty, likely due to the top salt being close to the maximum salt depth (Table 4-2, Appendix 6). Sensitivities for salt cavern emplacement will vary on a per-site basis as shown in Williams *et al.* (2022), our findings agree with this and site-specific models for both insolubility and overburden pressures should be modelled to help constrain capacity estimates.

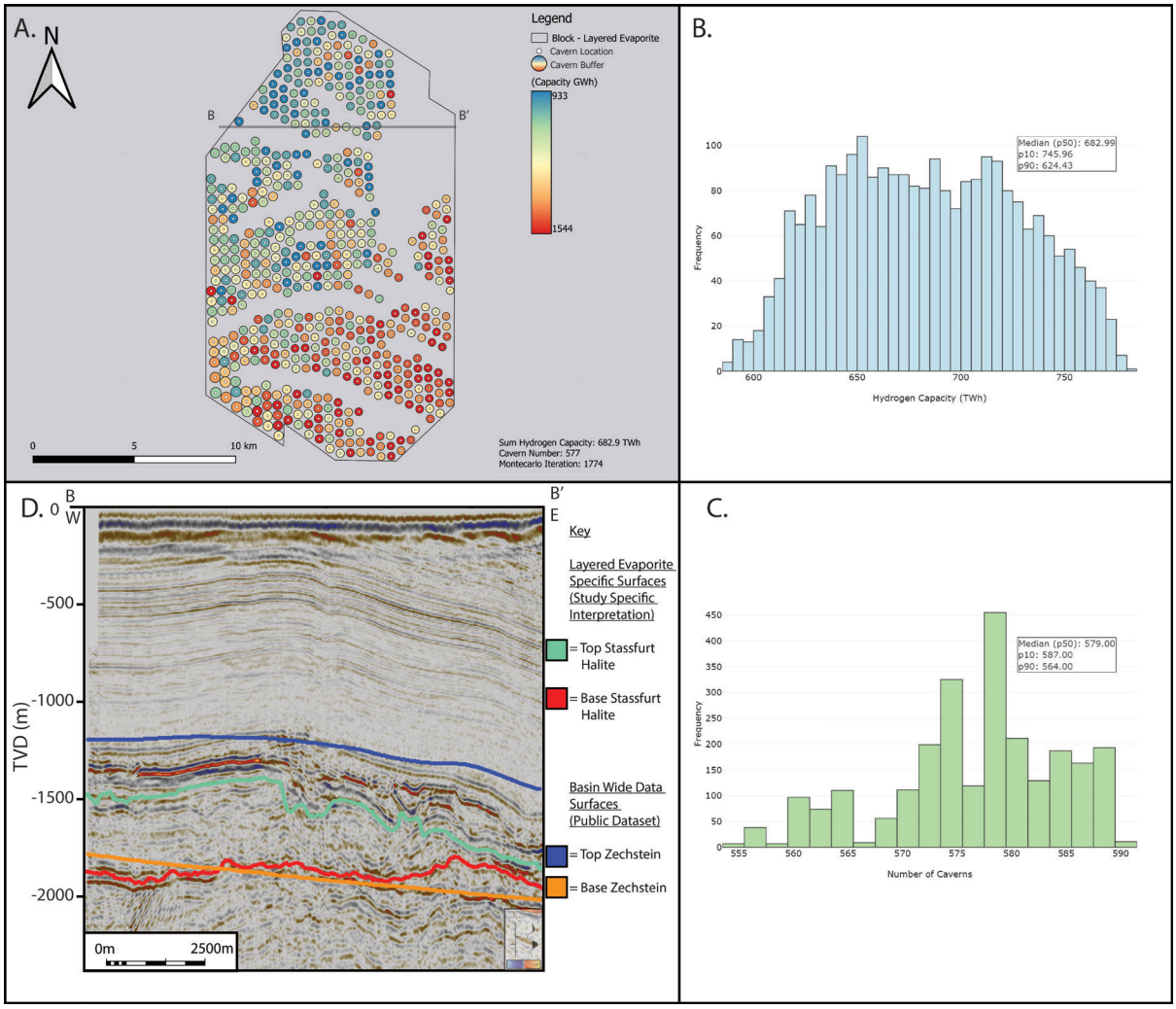

FIGURE 4-11 A) CAVERN PLACEMENT MAP 'BLOCK SPECIFIC – LAYERED EVAPORITE' AOI, VARIABLE CAVERN GEOMETRIES USING 'BASIN WIDE' AOI DEPTH SURFACES. GEOSPATIAL PLACEMENT REPRESENTS THE OUTPUT MODEL FROM THE WORKFLOW WITH THE CLOSEST TOTAL HYDROGEN CAPACITY TO THE CALCULATED P50 (ITERATION

1774/2500). A total of 577 caverns are placed, with a sum of 682.9 TWh of hydrogen storage capacity. B) Histogram of total hydrogen capacities for each iteration of the Montecarlo simulation (2500 iterations). C) Histogram of total cavern number for each iteration of the Montecarlo simulation (2500 iterations). D) Seismic cross section running West to East, B – B' (Figure 4-1Figure 4-12), in TVD (m). Stassfurt Halite surfaces interpreted from seismic survey MA933F002 and depth converted are present, Green (Top Stassfurt Halite) and Red (Base Stassfurt Halite / Top Basal Polyhalite). Blue and orange lines represent publicly available depth surfaces acquired from the NSTA of the top and base Zechstein, used for the 'Basin Wide' AOI geological model.

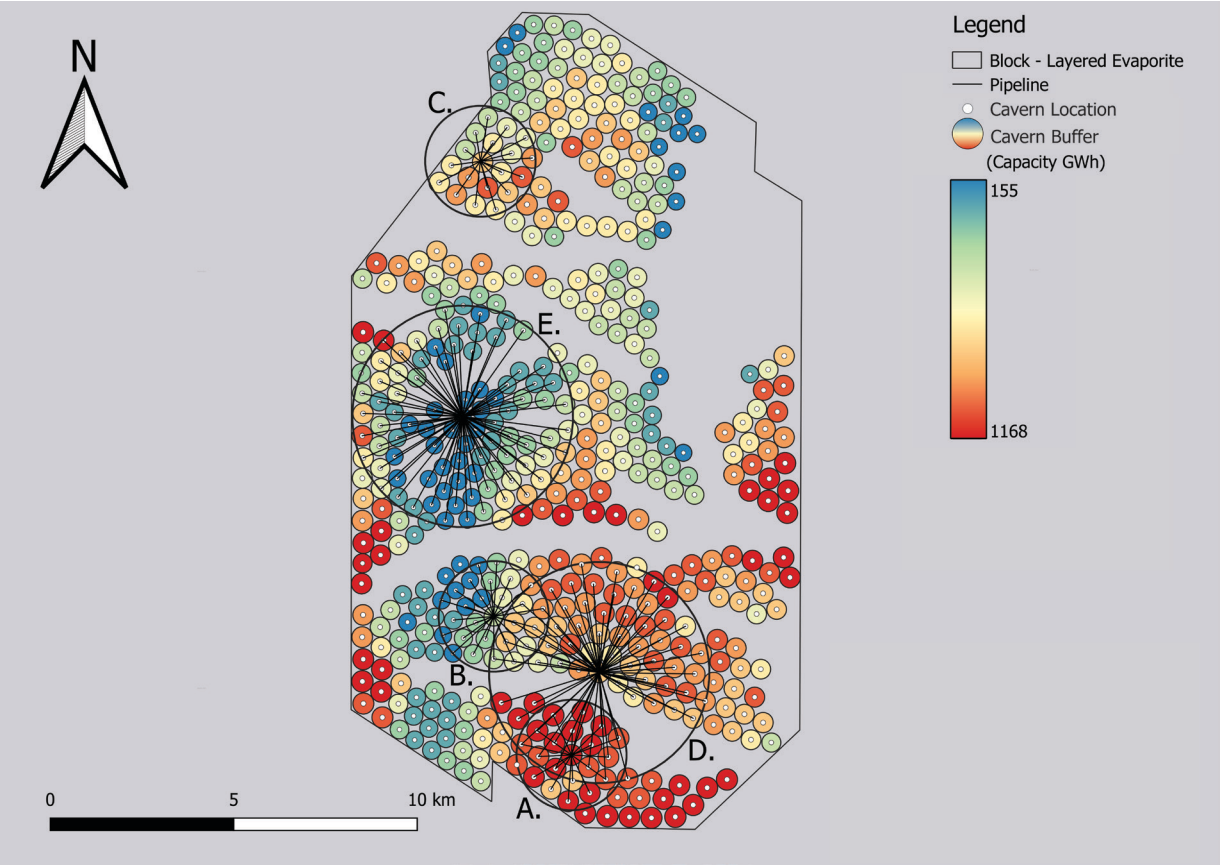

Figure 4-12 Salt cavern cluster concept play map. Base salt cavern map is the representative p50 of the 'Block - Layered Evaporite' AOI variable cavern model (Figure 4-9,B). 5 possible cavern cluster concepts are described A) Maximum hydrogen capacity within a 1.5 km radius. B) Maximum cavern number within a 1.5 km radius. C) 1.5km radius placed upon existing infrastructure (wellbore 41/05-1, Figure

4-1,FIGURE 4-5). D) MAXIMUM HYDROGEN CAPACITY WITHIN A 3 KM RADIUS. E) MAXIMUM CAVERN NUMBER WITHIN A 3 KM RADIUS. RADIUSES WERE CHOSEN AS SUCH TO MIMIC OFFSHORE INFRASTRUCTURE.

Cluster Concept	Total Hydrogen Capacity (Cushion Gas) (TWh)	Cavern Number	Pipeline / Deviation length (km)
A – Maximum Hydrogen Capacity 1.5km radius	16.7 (5.5)	20	18.7
B – Maximum Caverns (1.5km radius)	10.4 (3.5)	27	27.9
C – On existing well	10.8 (3.5)	19	17.9
D – Maximum Hydrogen Capacity (3 km radius)	51.7 (17.2)	73	147.9
E – Maximum Caverns (3km radius)	28.5 (9.4)	86	174.5

TABLE 4-6 THEORETICAL SALT CAVERN CLUSTER INFORMATION (FIGURE 4-12)

4.6 Discussion

4.6.1 Capacities, volumetrics and cavern placement

The results described demonstrate the value in stochastic approaches to evaluating geological energy storage. The case studies demonstrate the importance of high-veracity geological models as inputs for such analysis. The results presented indicate that theoretically salt cavern capacity offshore could meet all existing scenarios for the UK's required hydrogen storage, 40 – 115 TWh as suggested by Electricity System Operator (2023) and Cárdenas *et al.* (2021).

The basin wide and sub-regional investigations demonstrate there are up to 10,000s of TWh of potential storage within the Southern North Sea for hydrogen (Figure 4-6, 4-7), an order of magnitude greater than is required, and several times larger than the estimated working capacity of depleted gas fields and aquifers in the same location (2661 TWh) (Jahanbakhsh *et al.*, 2024). The p50 of possible cavern locations estimated is 195,563 (Basin Wide geological model) and 35,873 (Sub-Regional geological model), clearly providing extensive possible sites for consideration for development in the future. When the total number of caverns is so high, the total capacity across is largely irrelevant. Value from our Basin wide and Sub-Regional results hence does not come from the capacity of hydrogen storage, but rather the cavern

number and placement, both factors being required for energy systems planning (Samsatli and Samsatli, 2019). At a block scale the results from using higher resolution geological models (Figure 4-8, 4-12) demonstrate that areas equivalent to individual exploration and production licence areas (average 115 km^2, largest 250 km^2) the number of feasible cavern locations, and the total capacity are far greater than current scenarios for the UK's required hydrogen storage (Cárdenas *et al.*, 2021; Electricity System Operator, 2023).

By considering clusters of caverns (e.g. Figure 4-12) we make use of the spatial outputs of the model to compare the merits of different cluster development locations. We examine conceptual salt cavern cluster developments in the layered evaporite area, using the variable cavern Montecarlo iteration closest to the p50 capacity value (Figure 4-9, 4-12) as the base case. The development concepts, although lacking integral detailed engineering constraints built in, are limited to spatial extents that are feasible with existing technologies (Energy Technologies Institute, 2013). The principal consideration is the step out distance from a fixed offshore infrastructure point, for which we have considered distances of 1.5km and 3km. The distance from the fixed centre point to the centre of each theoretical cavern location is considered a viable representation of either a) a seabed pipeline distance to tie back individual caverns, or b) the drilling of a deviated well with a step out. The examples shown are to demonstrate the value of the outputs from the workflow we have developed. Cavern cluster concept E (maximising for hydrogen capacity in 3 km radius of set infrastructure) had sufficient capacity to match the minimum required energy storage set by Cárdenas *et al.* (2021), however this required a large number of caverns present >50. Cluster A, however, with 16.9 TWh potential makes up 42% of the 42 TWh requirement, with only 20 caverns and 22.3km of pipeline, a typical salt cavern cluster development consists of up to 35 caverns (Gillhaus, 2007).

4.6.2 Comparison to other studies

Previous studies have evaluated the offshore storage capacities for salt caverns in the Southern North Sea. We compare our results to these (Table 4-7). Previous studies e.g. Caglayan *et al.*, 2020; Allsop *et al.*, 2023 suggest there is also greater than required energy storage capacity within the both the onshore and offshore salt basins domains (43 TWh for 100% renewable penetration into the UK energy grid (Cárdenas *et al.*, 2021)).

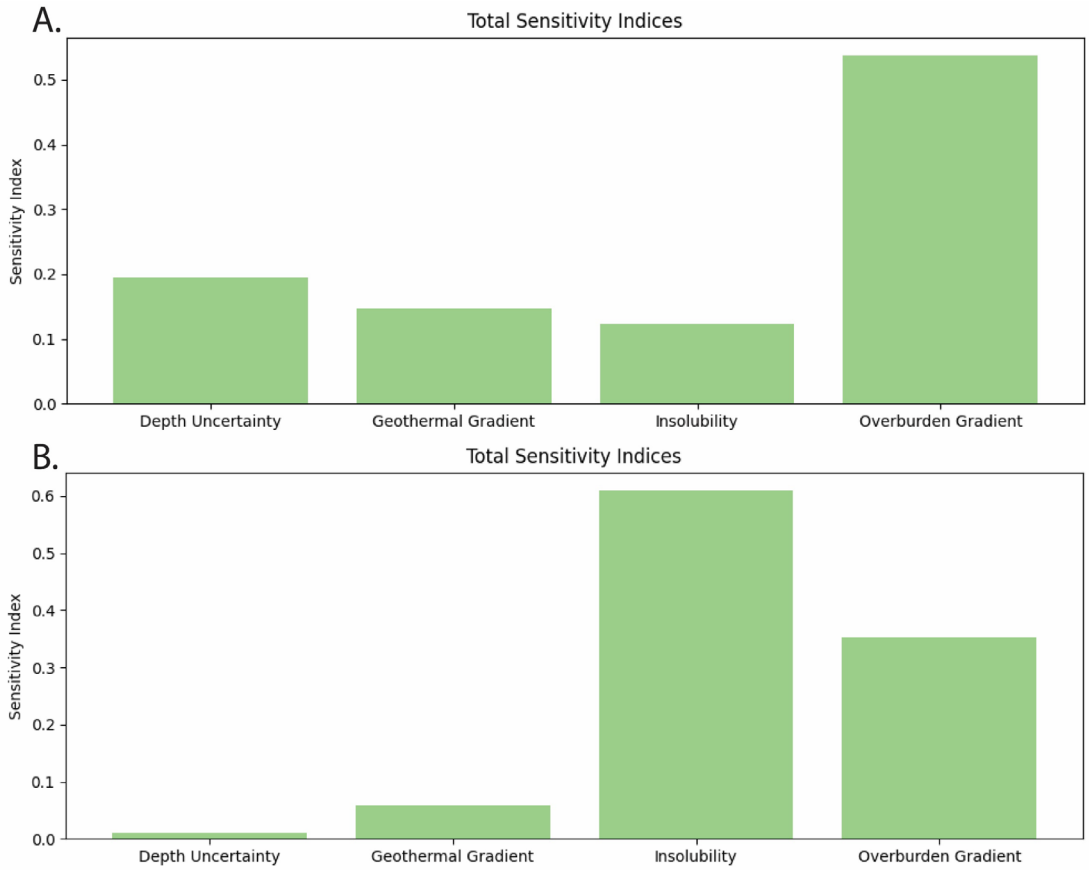

FIGURE 4-13 SOBOL SENSITIVITY RESULTS OF INPUT PARAMETERS FOR A) LAYERED EVAPORITE WITH VARIABLE CAVERNS (4.5.3.2.1); AND B) THE SALT WALL WITH VARIABLE CAVERNS (4.5.3.1.1)

The results of our study are in line with Caglayan *et al.* (2020) indicating there are 1000's of TWh of potential storage within the offshore of the UK in the Southern North Sea, with the results of both studies differing by only 6.7% in total hydrogen capacity (Table 4-7). Caglayan *et al.* (2020) only places cavern locations within 47 salt structures within the Southern North Sea, whereas our salt structure maps have 42 unique structures within our sub-regional depth model, which may account for the differences. These values suggest the Southern North Sea's capacity for LDES in salt caverns far exceeds any onshore basin within the UK (Table 4-7) not considering the economic feasibility of offshore development.

Whilst basin wide capacity may be useful to benchmark one basin against another, all the estimates demonstrate that the total of all possible cavern locations far exceeds the UK storage requirements (Table 4-7), this is unsurprising as basin wide estimations usually do not

fully account for the one of the most important factors, localised salt heterogeneities present within salt. For geographic areas with laterally extensive salt, the issues that are most pertinent are not related to total capacity, but rather to identifying the optimum geographic location of development clusters relative to other infrastructure (Sunny, Mac Dowell and Shah, 2020). Our workflow allows for this geospatial investigation. This has implications for the development of energy production infrastructure, such as industrial clusters, marine renewable infrastructure and hydrogen production facilities, because the proximity of energy storage, production and usage are important factors in considering whether sites next to each other can be advantageous (Walsh *et al.*, 2023). It can also aid with identifying, for example, how many caverns can be emplaced in a suitable shallow offshore setting or within a set buffer distance of previously mentioned infrastructure.

Study	Basin/Area	Working Hydrogen Capacity (TWh)	Number of Caverns	Average Cavern Working Capacity (GWh)	Cavern dimensions
Williams *et al.* (2022)	Cheshire Basin	129	1297	99.4	Height: 20 -262 Diameter: 100 m
Williams *et al.* (2022)	Wessex Basin	557	3378	164.8	Height: Variable Diameter: 100 m
Williams *et al.* (2022)	East Yorkshire	1465	8425	173.9	Height: Variable Diameter: 100 m
The Royal Society (2023)	East Yorkshire	≈100	3000	33.3 (Estimates of 120 in chosen locations)	Height 100m Diameter 31m Raw Volume: 300,000
Caglayan *et al.* (2020)	Offshore UK (Southern North Sea, Salt structures only)	9,000	NA	NA	Height 300 Diameter 58 Raw Volume: 750,000
***Basin Wide – Fixed Caverns – p50 (Iteration: 1808)**	Offshore UK (Southern North Sea, 58,904 km ^{2})	48,875	199,489	245	Height 300 Diameter 58 Raw Volume: 750,000
Allsop *et al.* (2023)	Offshore UK – (Mega Merge Area - Southern North Sea)	53 - 292	1485	35.6 / 196.6	Height 300 Diameter 58 Raw Volume 750,000
***Sub-Regional – Fixed Caverns – p50 (Iteration: 2011)**	Offshore UK – (Mega Merge Area – Southern North Sea, 25,000 km^2)	9685	36,466	265	Height 300 Diameter 58 Raw Volume: 750,000
Allsop *et al.* (2023)	Audrey Salt Wall	23 - 105	105	219 / 1005	Height 300 Diameter 58 Raw Volume: 750,000
***Salt Wall - Fixed Caverns - p50 (Iteration: 1477)**	Audrey Salt Wall	178	1151	154	Height 300 Diameter 58 Raw Volume: 750,000
***Salt Wall – Variable Caverns - p50 (Iteration: 141)**	Audrey Salt Wall	580	409	1418	Variable
***Layered Evaporite - Variable Caverns - p50 (Iteration: 1287)**	Seismic Survey MA933F002	263	502	524	Variable
***Layered Evaporite – Basin Wide Depth Model Data - Variable Caverns p50 (Iteration: 1085)**	Seismic Survey MA933F002	682	577	1182	Variable
***Layered Evaporite – Fixed Caverns p50 (Iteration: 1537)**	Seismic Survey MA933F002	161	806	199	Height 300 Diameter 58 Raw Volume: 750,000

*TABLE 4-7 COMPARISON OF RESULTS TO OTHER STUDIES. *NOTE RESULTS FROM THIS STUDY REGARDING CAVERN NUMBER ARE OBTAINED FROM THE MONTECARLO ITERATION (ITERATION NUMBER IN BRACKETS, SEE DATA FOR*

*MONTECARLO ITERATION LIST) WITH THE CLOSEST TOTAL HYDROGEN CAPACITY TO THE CALCULATED P50 FOR THAT MODEL RUN. * = MODELS FROM THIS STUDY.*

4.6.3 Sensitivity analysis of salt cavern site capacity

The layered evaporite model was most sensitive to overburden pressure gradient, while it was second most sensitive parameter for the salt wall (Figure 4-13). This high level of sensitivity suggests that more complex site-specific geomechanical models should be incorporated to help reduce uncertainty from capacity estimates at sites. The layered salt was less sensitive to insolubility then the salt wall, this is likely as the layered salts insoluble distribution was constrained better from the available data (Appendix 5) than the insoluble distribution for the salt wall. The salt wall also had larger caverns placed due to the greater thickness available and as such, will be more negatively influenced by increased insoluble content. To reduce sensitivity to insoluble content refining the distribution with more data points or using seismic data for 3D quantitative interpretation of solubility content is mandatory to reducing uncertainty as the input distribution can change it substantially. The salt wall block was not sensitive to the depth uncertainty and hence bounding top and base salt depths (Figure 4-13B), as increasing or decreasing the salt geometries made no change to the suitability of an area for cavern emplacement, however, the layered evaporite area was sensitive (Figure 4-13A) to the depth uncertainty, likely due to the top salt being close to the maximum salt depth (Table 4-2, Appendix 8). Sensitivities for salt cavern emplacement will vary on a per-site basis as shown in Williams *et al.* (2022), our findings agree with this and site-specific models for both insolubility and overburden pressures should be modelled to help confine capacity results.

4.6.3.1 Limitations of workflow/approach

As with any subsurface modelling method, there are limitations. We use variable cavern geometries, and frequently the capacities are calculated to have volumes greater than those frequently stated in literature (Table 4-7). These volumes do not exceed the volume of the largest documented cavern, which has a total volume of 17,000,000 m^3 (670 m tall and 180 m diameter) (Leith, 2000). We compare the results of modifying cavern geometries while keeping every other parameter the same as seen in Table 4-7 (Layered evaporites – Variable

Caverns - p50 vs layered evaporite – Fixed Caverns - p50 Models). Allowing for larger and variable cavern geometries allows for higher storage capacities within an area. However, there are fewer caverns placed within these iterations (Table 4-7), if the placement of caverns was of important consideration, smaller caverns may be favoured as they allow for greater opportunities in their placement. Fewer, larger caverns would require less drilling in the development of a possible cluster, although larger caverns would take a longer time to develop. It is also important to mention that within our workflow cavern spacing remained static at twice the cavern diameter from the mid-point for all potential caverns, however with increased depth the caverns will encounter higher associated stresses, and to account for such, a greater buffer distance may need to be incorporated within the workflow, reducing potential cavern locations. As with this in consideration, is why the developed workflow can be modified to adapt cavern spacing for greater distances between cavern mid-point, allowing cluster developments to be planned in deeper salt formations with higher stresses. While our geological models capture the thickness changes and the 3D structures of the Zechstein of the Southern North Sea, the model used a simple percentage for the insoluble content and did not account for evaporite minerals which may be more soluble than halite (carnallite for example) which may affect cavern morphology, and also did not incorporate a 3D model of the internal heterogeneities. For the layered evaporite area, however, we chose to take a 2D approach by mapping areas of non-viability such as faults and generalised areas of insolubility and removing them as deterministic nonviable areas. However, within the salt structures, non-soluble stringers and complex geometries are typically associated with the internal structural heterogeneity (Pichat, 2022). Imaging in salt structures is typically poor both due to the complex ray paths in the crystalline structure of salt, and seismic surveys often being designed to image post and pre-salt (Jones and Davison, 2014). As such the 3D heterogeneity for the salt structures investigated was not incorporated within the workflow. Currently, internal heterogeneities of salt units are one of the most important parameters to consider when planning a cavern site (Ramesh Kumar *et al.*, 2021). Assuming pure halite rather than a heterogenous evaporite system means that physical and rock mechanical properties will be incorrectly calculated, compromising the longevity of the salt cavern within the salt body. Several new methods for seismic imagining and depth conversion can off substantially improved images of the internals of salt units (Multi-layer pre-stack depth migration (PDSM), Full waveform inversion (FWI)). It is imperative that future workflows, which concentrate on

a more potential site investigation scale, include estimation and 3D spatial understanding of intra-salt heterogeneities.

Evaporite units are known to cause thermal anomalies in subsurface heat flow due to their crystalline structure conducting heat energy more efficiently than the surrounding lithologies (Jackson and Hudec, 2017). This increased complexity makes using a geothermal gradient a simplification for basins with extensive salt (Williams *et al.*, 2022), and future work could investigate the value of incorporating 1D, 2D or 3D heat flow models to determine the influence of salt layers on thermal structure. The flexibility of our workflow means that the outputs from such modelling could be incorporated in the future.

The geomechanics of cavern emplacement were not considered in detail within our workflow. The distances used for geomechanical stability between caverns was taken from literature and determined as suitable for our workflow development (Allen, Doherty and Thorns, 1982; Caglayan *et al.*, 2020). It should be noted that caverns emplaced deeper may require larger separating buffer distances as there are higher stresses acting upon them, increased distances between caverns would reduce total cavern number and hence the total capacity within an area (Williams *et al.*, 2022). Area specific geomechanics models could be incorporated into our workflow for more suitable cavern placement, such as rheologic contrast between evaporitic and non-evaporitic units, however the development of such was outside the scope of our research.

Despite these limitations, it has been designed in such a way that it is easily modified for different geological models, parameters, or uncertainties. This is seen by the number of different cases and iterations we have run, where the inputs to the workflow have been modified to be more suitable with the input geological model. The outputs can even be modelled such that they are plotted against the initial 3D seismic data that the depth surfaces originate from, allowing for visualisation of true plotting location (Appendix 9)

4.6.3.2 Veracity of data

The necessity for geological models to be reliable and reproducible is essential where they underpin vital developments as part of sustainable pathways and in achieving Net Zero (Steventon *et al.*, 2022). We compare the layered evaporite salt model using seismic specific data (Sections 4.5.3.2.1,Figure 4-9) and using basin wide depth data (Section 4.5.3.2.3, Figure

4-11). Both models use the same parameters with only the surfaces and associated depth uncertainty changing (Appendix 8). The changing of surfaces causes several parameters to be affected: 1) the formation thickness changes because the basin wide data is from top to base Zechstein, whereas the site-specific surfaces are from top to base Stassfurt Halite (Figure 4-5). 2) The depth to the top salt is different, with the basin wide model being shallower, allowing for more potential locations. 3) The grid cell resolution is also different; Appendix 8 shows the differences in surfaces. The basin wide data results estimate 75 more caverns, 419 TWh higher capacity, and an average cavern working capacity of 0.658 TWh greater than the specific data geological model. These differences arise from the basin wide data use of the top and base Zechstein as input, rather than having the specified salt target, which in turn causes the salt to be thicker, allowing for larger caverns to be placed by the workflow. Using the top and base Zechstein also causes non-soluble stratigraphic layers within the Zechstein, such as the Plattendolomit (Figure 4-3, 4-5) to be within the area for cavern emplacement in the workflow. If a stratigraphic layer, such as the Plattendolomit, were to be encountered while attempting to solution mine a cavern it may cause many issues, such as cavern collapse, inability to continue solution mining, contamination, or act as a porous and permeable pathway for hydrogen to escape, and, as such should be avoided (Chen *et al.*, 2018; Zhang *et al.*, 2021; Zhu *et al.*, 2023; Jones and Blom, 2014).

The public surfaces are also lower resolution with a grid cell spacing of 250 m, as opposed to 50m. This lower resolution leads to ineffective packing of the caverns (Figure 4-11,A), as the grid cell size is greater than the typical buffer (~100 m) between adjacent caverns. A higher resolution model enables not only more potential cavern locations to be considered but also captures a higher resolution of structural variability in the geometry of the salt interval. The work presented here suggests that the minimum grid cell size of the input geological model is at most 4x the minimum cavern size diameter, as this will allow for every grid cell to have a point with minimum overlap. At lower resolutions the cavern packing is not efficiently modelled (Appendix 10). At higher grid cell resolution, it is possible to model more cavern locations and then determine the optimum cavern spacing and placement (Appendix 10).

4.6.3.3 Importance of reproducibility and replicability

Within subsurface geosciences, practical frameworks for reproducibility are in their infancy, particularly where there are significant uncertainties related to data (Steventon *et al.*, 2022). It has been identified that availability of data and software (including code), frequently limit the possibility of reproducing studies (Ireland *et al.*, 2023). Previous studies into geological energy storage estimates rarely provide all the required information to be reproduced. This study has made available the code through a CC BY-SA so that it can be used, revised, and modified, including for commercial purposes. This therefore allows others to reproduce of our work (same method, same data) and replicate our work (same method, different data). As well as the method, it is vital that the underlying data for studies are made available and easily accessible (Hardwicke *et al.*, 2018). Previous studies of geological energy storage have not always provided accessible data repositories with sufficient data to examine the reliability (different method, same data) of the capacity estimates. In this study we use data, and interpretations from existing open licence sources (NSTA), as well as our own interpretations, which we also make available through CC-Y licence. This approach allows for the evaluation of the reproducibility and reliability of our findings.

The comparison shown in Table 4-7 highlights the importance of reproducibility and reliability in studies where results may have implications for both the scientific community and policy makers. The results from Caglayan *et al.* (2020) and Allsop *et al.* (2023), for the same areas indicate differences of up to 685 TWh and 9393 TWh respectively (compared with sub-regional model). With such large differences in predictions, it is important to be able to understand where such differences arise from, however replicability is only viable when the input data to a model is made available and accessible. While our capacity calculations are larger than the those proposed in Caglayan *et al.* (2020), they are in general agreement (generalisable, different method, different data) that there is over 9000 TWh storage potential of hydrogen within the Southern North Sea, with our sub-regional model differing by 6.7%, while using different subsurface datasets (Caglayan *et al.* (2020) do not incorporate layered evaporite domains into their geological model). Allsop *et al.* (2023) estimated significantly different capacities in comparison to this study, for both the salt wall and the area of the sub-regional model (Table 4-2,Table 4-7) while using the same seismic data (2016 Southern North Sea Mega-merge). They estimate that there are only 1485 cavern locations

within the sub-regional area, in contrast to 36,466 in our study, and only 105 within the Audrey salt wall as opposed to the 1154 in our study (using the same cavern geometries) (Figure 4-7, 4-8). Unfortunately, due to the lack of detail in the methodology and results presented (no geospatial data regarding cavern placement) as well as no data being provided in the data repository by Allsop et al. (2023) we were unable to reproduce their results and make a detailed comparison between each workflow to understand where these differences originated. This example of researchers reaching different conclusions while utilising the same dataset emphasises both the importance of reproducibility and replicability in geoscience, adding to the many studies in the geoscience community, where the results are unable to be reproduced or replicated (Ireland *et al.*, 2023). The differences also emphasise the importance of using the same parameters within the methodology, as using or discarding of essential parameters such as intra-salt heterogeneities, may significantly alter the number of potential caverns. Another important aspect is the veracity of interpretation obtained from the same dataset as it will have a strong influence on the geological model and therefore the results. When all aspects of research are open this improves their trustworthiness (Rosman *et al.*, 2022), which is essential if findings are to inform policy or aspects of national planning, such as energy systems (UK Government, 2012). While much of the research in the field, particularly block/license-scale evaluation, may use proprietary data, technologies and interpretations, efforts should be made to make the data and information open where possible.

4.6.3.4 Energy system integration

The outputs generated from our workflow are such that they contain individual cavern locations, specification, and capacities. These outputs can be used as inputs into further energy systems modelling that include storage (e.g (Sunny, Mac Dowell and Shah, 2020)). Energy system models and energy value chain studies, while having offshore energy generation within their models, typically implement storage opportunities within the onshore domain, not offshore (mainly due to economic feasibility), limiting opportunity and limiting the exploration of possible solutions (Samsatli and Samsatli, 2019). Our outputs can aid in the design of energy systems at all scales (national grid level planning to local energy storage requirements) because of the different scales of geological models ran through our workflow (broad whole basin geological models to site specific models). While we are not suggesting

the integration of every potential cavern location generated into an energy system, the outputs allow for areas with high hydrogen supply potential and LDES demand to be located and utilised.

The geographic results, both individual caverns and conceptual clusters can be reviewed with respect to important energy infrastructure. For example, Figure 4-14 shows the number of caverns and capacity within 20km radius of existing and planned offshore wind developments in the Southern North Sea. Of the 32 developments, 15 have > 1000 potential cavern locations and 13 have over 500 TWh of potential hydrogen capacity (Figure 4-14). We can also examine the setting of cavern locations, such as water depth or distance from the coastline, both which could impact the development cost (Energy Technologies Institute, 2013). All cavern locations are situated in under 100 m water depth, which would mean they could be accessed by a jack-up rig (limits are typically 120m). There are 22,000 possible cavern locations within 10 km and 37,000 within 20 km of the east coast (Basin wide model).

These are some possible examples as to how the output from this study and our workflow could be integrated into energy systems design. While our brief overview of this is simplistic, our data could be used for much more complex analysis because of the level of information associated with each cavern generated.

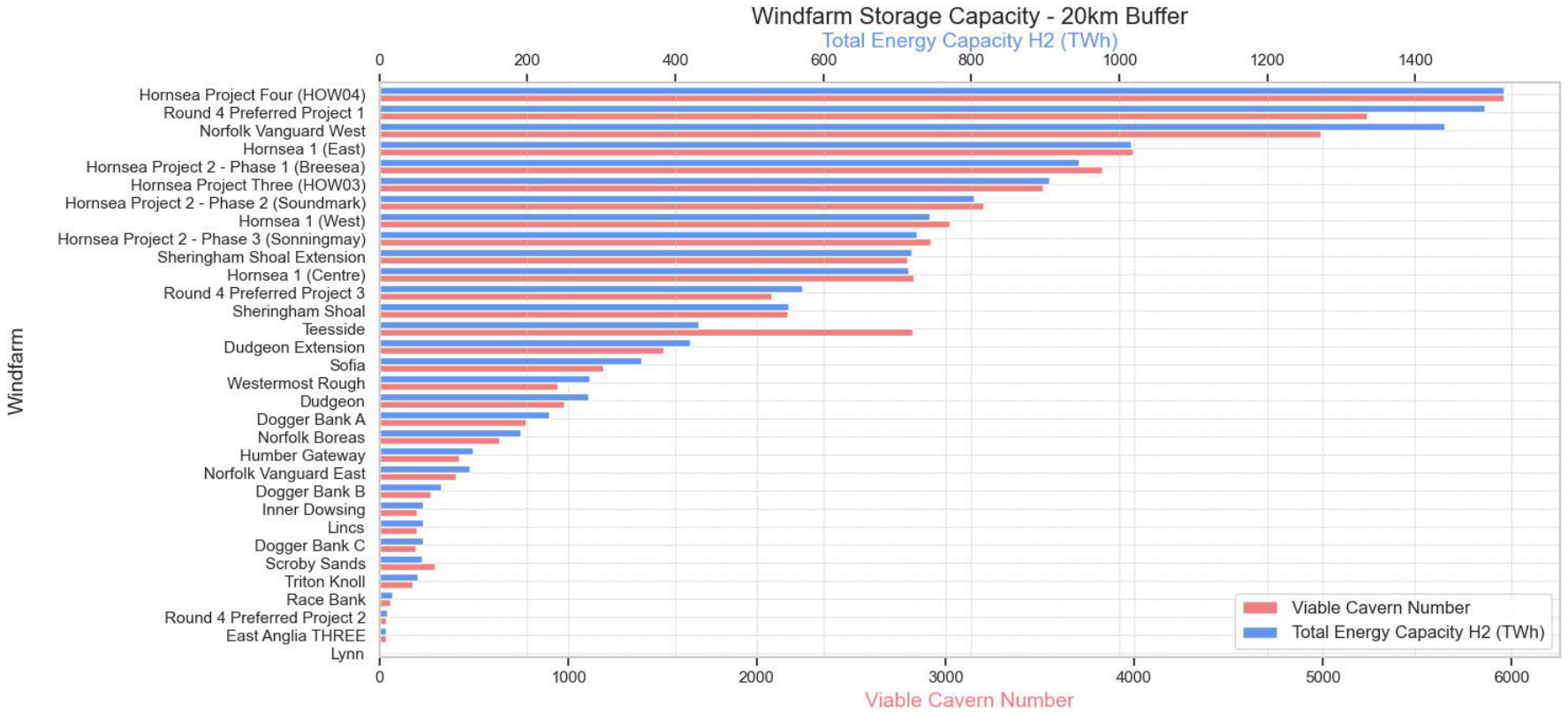

FIGURE 4-14 WINDFARMS LOCATED WITHIN THE 'BASIN WIDE' AOI (FIGURE 4-6), PLOTTED AGAINST POTENTIAL CAVERN NUMBER AND TOTAL HYDROGEN STORAGE CAPACITY WITHIN A 20KM BUFFER OF THE WINDFARM SITE (BASIN WIDE RESULTS USED (BASIN WIDE – FIXED CAVERNS - 4.5.1)).

4.6.3.5 Offshore salt caverns for LDES

To date, all salt caverns have been emplaced onshore, however offshore salt cavern projects have been proposed before (Evans and Holloway, 2009). We have demonstrated that not only does the estimated total capacity available exceed current estimates for storage, but that the number of potential geographic locations offshore have the potential to provide effective integration with current and future marine renewable infrastructure (Figure 4-6, 4-7, 4-14) and reach the calculated demand (43 TWh) (Cárdenas *et al.*, 2021).

The integration of salt cavern clusters for LDES could provide greater flexibility and variability in the generation of energy from offshore renewables (Arellano-Prieto *et al.*, 2022). However, the offshore development costs such as, drilling, tie-in and pipeline costs, of such infrastructure need to be considered as to if they are economically viable for these areas, specifically the idealised locations for caverns, which is next to hydrogen production hubs (generating either blue or green hydrogen). Integrating all aspects of hydrogen production allows for optimising the integration, flexibility and transport of hydrogen from production to storage (Walsh *et al.*, 2023).

Energy infrastructure offshore has costs associated with it that are higher than those that occur onshore, for example wind turbines are 50% more expensive offshore than onshore (Bilgili, Yasar and Simsek, 2011). Savings might be possible regarding salt caverns, as the brine produced by the creation of the salt caverns may be sold to reduce costs or if not possible to be sold to be diluted and disposed of in the sea, which will be more cost effective than the cost of transporting the brine onshore (Ahmad and Baddour, 2014) . The cost of pipelines, drilling and tie-in costs will be a key aspect of site consideration as they will be a significant component of the CAPEX costs. Throughout our theoretical salt cavern sites, we have modelled the possible distances of pipeline for a single cluster to get reasonable estimates as to what may be required (Table 4-6), however a more thorough specific investigation into this will be needed.

Conflict of spatial interest remains a factor that needs to be considered when planning any offshore infrastructure, especially for a basin with high renewable potential, such as the North Sea (Guşatu *et al.*, 2024). All infrastructure, such as windfarms, LDES, or CCS require space with suitable buffers around it to ensure safe operation without causing interference with the

operations of other offshore projects. As such, areas that have we have described as having potential for salt cavern emplacement may no longer be suitable for cavern emplacement due to areas being prioritised for other technologies. However, the large number of potential cavern sites 199,489 (Figure 4-6) and the relatively small number needed to meet the storage requirements (Table 4-6) suggest that this issue may not affect cavern placement locations.

Alternate energy vectors could be stored within salt caverns to alleviate carbon emissions in other industries. Global shipping accounts for 2% of global carbon dioxide emissions, both ammonia and methanol have been suggested as replacement zero emission fuel sources (Svanberg *et al.*, 2018; Gallucci, 2021). Ammonia is a possible energy vector alternative (Patonia and Poudineh, 2020). At the average internal pressure/temperature conditions of the salt caverns from our basin wide study (64 °c and 36.2 MPa), ammonia would be in its super critical phase and methanol would be in its liquid phase (National Institute of Standards and Technology, 2023). Ammonia has previously been suggested as storable within salt caverns (Adams and Cottle, 1954). Combining storage and offshore production of these low emission fuels would allow for an fully integrated green ship refuelling ecosystem.

4.7 Conclusion

Within this chapter we have demonstrated our proposed workflow using several geological models and parameters. We position this workflow at the pre-feasibility stage of an area for the investigation placement of salt caverns. The workflow takes a geological model as an input and outputs valid salt cavern locations alongside capacity estimates. The workflow has been designed that such that any parameter and variables can be changed to suit the geological model and area of interest, even allowing the chosen energy vector to be altered. The workflow allows for the input of not only deterministic values but stochastic values, allowing to compensate for the uncertainty typically associated with geological models of the subsurface.

From our workflow we produce realistic theoretical salt cavern clusters that help to show how the results from our model could be used to develop such a cluster. The capacity results show that a single large offshore cavern cluster (with a 3km diameter AOI) may have enough hydrogen storage capacity to meet the UK's long duration energy storage requirements in full. The workflow and associated data should be used to aid site planners or policy setters to making further decisions regarding hydrogen storage offshore using salt caverns.

The offshore domain is often not considered when deciding where LDES should be placed. We have demonstrated that the offshore of the UK is a suitable location, with over 199,000 locations of caverns and +10,000 TWh scale capacity for hydrogen. This viability of the offshore domains opens possible co-location with offshore energy production hubs, allowing for the UK to have a full green energy production hub operating offshore.

We also compare our results against other studies to emphasise how important it is to have a reproducible and replicable methodology. All code, data and interpretations used within this study are supplied within the data repository.

The workflow presented deals with some of the main parameters that need to be assessed and considered during basin screening and initial planning of UES in salt basins and areas of interest. However, more detailed geological information obtained from well data combined with high resolution seismic data derived from PSDM models, such as salt heterogeneities and internal structing and composition, need to be incorporated in detail when passing from the conceptual stage to the effective planning of salt cavern infrastructure.

Chapter 5. Gassmann fluid substitution and seismic response of hydrogen and carbon dioxide in clastic storage reservoirs

5.1 Abstract

The ability to safely store non-hydrocarbon fluids in the subsurface, such as carbon dioxide or hydrogen, will be pivotal for the energy transition. Storage of these fluids will require monitoring programmes (such as with seismic monitoring) to understand dynamic changes in storage and to identify unintended migration. We investigate the changes in seismic response for different non-hydrocarbon fluids and different saturations.

The bulk elastic properties of subsurface rocks are influenced by the fluids present within the pore space and impact the seismic response of the rock. We undertake fluid substitution modelling, calculating new rheological properties of reservoir intervals after substituting brine for either hydrogen or carbon dioxide. We vary the water saturation from 100% to 0% to determine the new elastic properties of the fluid-substituted rocks. We investigate three proposed reservoirs for carbon dioxide storage in the UKCS, the Endurance closure (Bunter Sandstone), the Viking field (Rotliegend Sandstone) and the Hamilton field (Ormskirk Sandstone). The workflow is stochastic and as such allows for the investigation of the impact of geological uncertainty on the results. The newly determined elastic properties are then used for modelling different types of geophysical responses such as, acoustic impedance modelling, wedge model analysis (both seal-reservoir and reservoir-reservoir interfaces), amplitude vs offset modelling, and 4D time-shift analysis.

Our results show that both hydrogen and carbon dioxide cause a change in acoustic impedance values, with hydrogen having more of an impact than carbon dioxide. For brine to carbon dioxide fluid substitutions, these values are typically lower than a 10% change in acoustic impedance at 20% water saturation, Bunter (6.5%), Rotliegend (9%), and Ormskirk (7%), whereas for hydrogen these are Bunter (10%), Rotliegend (12%), and Ormskirk (11%). We show that amplitude versus offset analysis will be sufficient as a monitoring technique, depending on the initial properties of the reservoir rock. However, time shift analysis shows that relatively thin reservoir intervals (< 35 m) with 20% carbon dioxide, could be detected by 4D time shifts between baseline and monitoring surveys.

5.2 Introduction

Pore-filling fluids within a rock modify the bulk elastic properties and consequently impact the seismic response (Mavko, Mukerji and Dvorkin, 2009). Forward modelling of the seismic response of porous reservoirs with different pore-filling fluids is commonplace within hydrocarbon exploration and production workflows where it is used to understand the expected seismic response of the subsurface (Avseth, Mukerji and Mavko, 2005). In recent years these methods have used to model carbon dioxide in the subsurface (Dupuy *et al.*, 2017; Carpentier, Boullenger and Barros, 2021; Harvey *et al.*, 2022a), however it is just as applicable to hydrogen.

The seismic response of a geological boundary can be described by the reflection coefficient of the interface, which is determined by the acoustic impedance of the two layers, defined as: (Bacon, Simm and Redshaw, 2003);

$$Rc = \frac{Ai_2 - Ai_1}{Ai_2 + Ai_1} \qquad \textit{EQUATION 26}$$

$$Ai = \rho_{bulk} * v_p \qquad \textit{EQUATION 27}$$

Where Ai_1 and Ai_2 are the acoustic impedance values for the rock layers above and below the geological boundary, and where ρbulk is the bulk density of the rock layer and V_p is the compressional velocity. The bulk density and compressional velocity of a geological layer are both modified by the pore-filling fluid within. As different fluids have different properties, the extent to which the bulk density and compressional velocity of a rock are modified depends on the constituent properties of the filling liquid (Batzle and Wang, 1992). The ability to forward model the seismic response quantitively and compare it with the actual seismic response allows for the prediction of the fluid or fluid mixture present within the pore space at the time of acquisition (Ahmed *et al.*, 2015). Change in pore filling fluid can also impact the amplitude of seismic response at different seismic wave offsets and can also modify the velocity at which a seismic wave propagates through a rock. Changes in elastic properties hence modify the reflection response in different ways, which can be interpreted to identify changes in fluid saturation (Wandler, Evans and Link, 2007). These approaches are used for

both hydrocarbon exploration and production, where changes in fluid distribution as a result of production can be detected, and for subsurface storage, where, changes in fluid distribution due to injection can be detected(Chadwick, Arts and Eiken, 2005; Singer, Byerley and Rose, 2018)

In this chapter, we use the Gassmann equations to undertake fluid substitutions in three porous stratigraphic intervals on the United Kingdom Continental Shelf (UKCS). We forward model both carbon dioxide and hydrogen to determine the new elastic properties and model the expected seismic responses at different areas of the subsurface plume Figure 5-1.

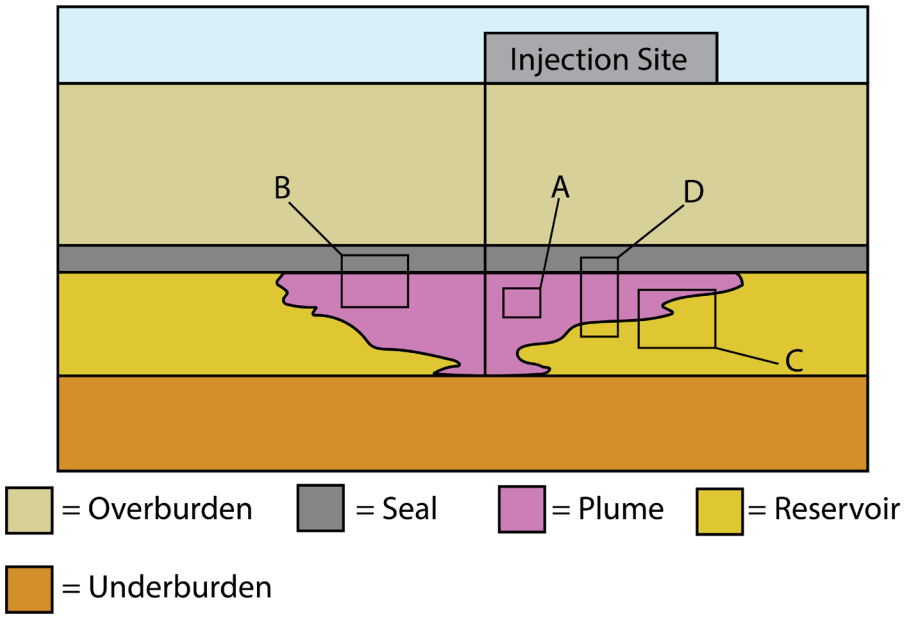

FIGURE 5-1 SCHEMATIC SUBSURFACE DIAGRAM OF A FLUID STORAGE SITE IN A POROUS RESERVOIR (NOT TO SCALE). BLACK BOXES REPRESENT AREAS WHICH ARE FORWARD MODELLED, A) RESERVOIR PROPERTIES B) SEAL - RESERVOIR INTERFACE, C) RESERVOIR (INJECTED FLUID SATURATED) – RESERVOIR (BRINE SATURATED) INTERFACE, D) WHOLE RESERVOIR COLUMN. PLUME FROM QUEST CCS FACILITY 2050 MODEL (HARVEY ET AL., 2022B).

5.3 Geological Setting

We undertake seismic modelling of three discrete reservoir – seal pairs from the UKCS. The chosen reservoir-seal pairs are located within two separate basins. The pairs from the Southern North Sea, the Bunter and Rotliegend, are located within the UK sector of the South

Permian Basin, while the Ormskirk is located within the Foryd-Gograth sub-basin of the East Irish Sea Basin (Jack *et al.*, 1995; Ziegler, 1990). The South Permian Basin is an east-west trending basin, stretching from the eastern coast of the United Kingdom across Northern Europe to western Poland. Its formation is primarily attributed to mid-to-late Permian rifting events with modification from later phases of rifting and thermal subsidence. Its structural configuration was significantly influenced by the pre-existing tectonic framework established during the early Palaeozoic (Glennie, 1998; Glennie and Underhill, 1998; Ziegler, 1992a). The East Irish Sea Basin is part of a Permo-Triassic rift system, consisting of northwest-southeast trending normal faults which control the basin architecture. A east-west trending horst graben system is responsible for the many sub-basins within the area including the Foryd-Gograth sub basin (Jack *et al.*, 1995). The chosen stratigraphy was picked in part due to each stratigraphic interval having a planned CCS storage site (Pale Blue Dot Energy and Axis Well Technology, 2016).

The Bunter Sandstone was deposited during the Olenekian of the Lower Triassic (Figure 5-2)**.** (Bachmann *et al.*, 2010). It consists of coarse-grained sandstones deposited in alluvial fan and fluvial environments in arid and semi-arid environments (Brook *et al.*, 2003). It is overlain by the Haisborough group, which consists of a number of sealing formations, including claystone intervals and the Röt Halite (Bentham, Green and Gammer, 2013). The Zechstein supergroup, which overlies the Bunter Sandstone, has undergone significant halokinesis, forming numerous salt domes and diapirs (Peryt *et al.*, 2010). The mobilisation of the underlying Zechstein has caused several trap geometries to form within the Bunter Sandstone of the Southern Permian Basin, one of which, known as the Endurance structure, is likely to be the United Kingdom's first CCS site planned (James, Baines and McCollough, 2016a; Gibson-Poole *et al.*, 2024).

The Ormskirk sandstone formation is part of the Sherwood sandstone group (Figure 5-2). It is located on the west coast of the United Kingdom, and the offshore in the East Irish Sea (Kirk, 2005). It is early Triassic in age, having been deposited during the Anisian (Howard *et al.*, 2008). It was deposited in a fluvial environment setting with aeoline influences, with facies of aeolian dunes and sandsheets present (Yaliz and Taylor, 2003; Scorgie *et al.*, 2021). It is a reservoir rock for a number of gas fields within the East Irish Sea, with notable inclusions being the Hamilton field and Calder field (Yaliz and Taylor, 2003; Blow and Hardman, 2022).

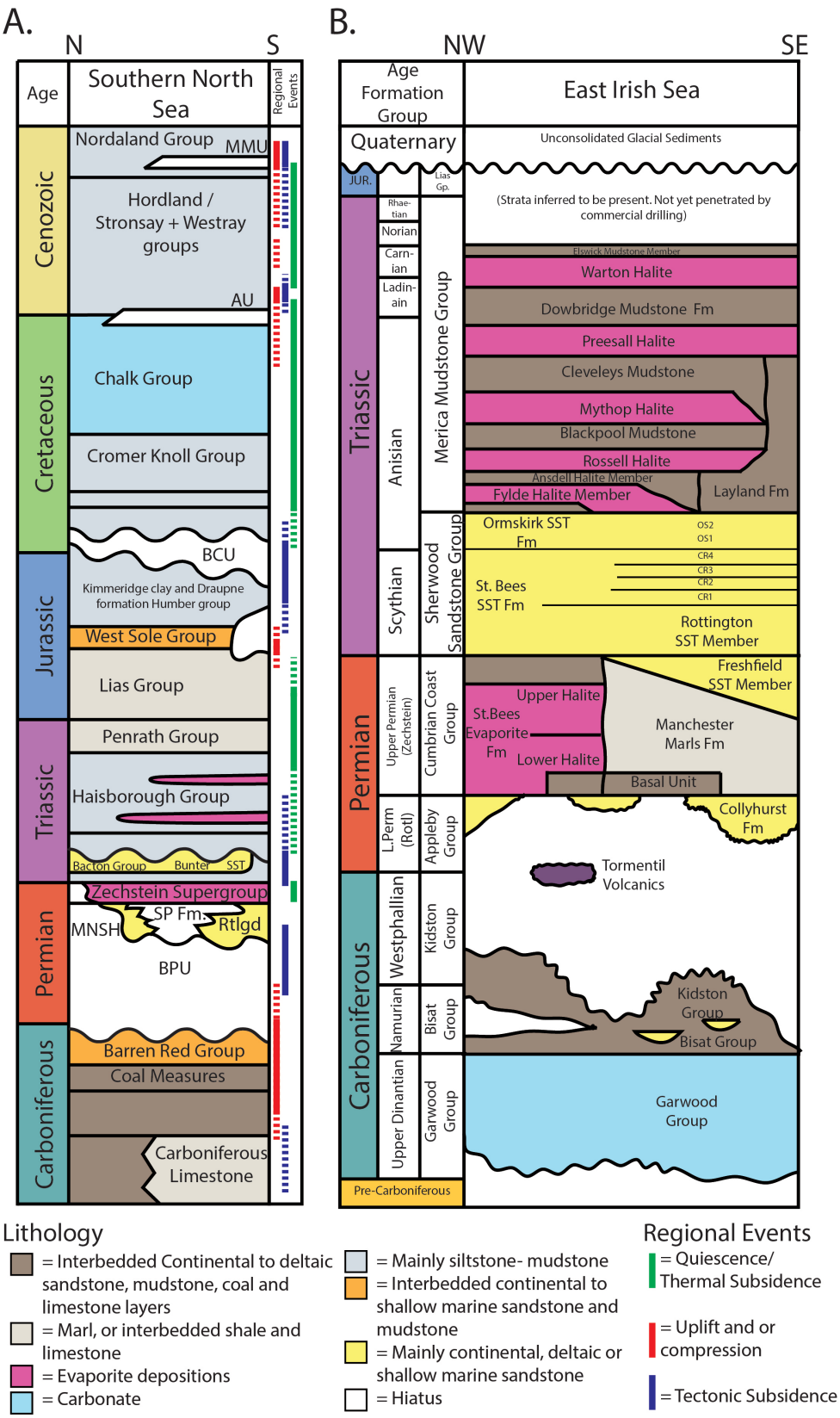

FIGURE 5-2 SOUTHERN NORTH SEA (A) AND EAST IRISH SEA (B) CHRONOSTRATIGRAPHIC DIAGRAM. A MODIFIED AFTER PATRUNO ET AL. (2022), B MODIFIED AFTER PATRONI ZAVALA ET AL. (2020)

The Rotliegend group is an Early Permian (Guadalupian - Lopingian) aged sedimentary succession consisting mainly of Aeolian sediments (Figure 5-2) (Gast *et al.*, 2010). The Rotliegend group is found extensively throughout the South Permian Basin of Northern Europe, stretching from the east coast of the United Kingdom to the eastern edges of the Polish trough in Ukraine (Gast *et al.*, 2010). It is the main gas-bearing reservoir within the UK sector of the South Permian Basin, where it is sealed by the Zechstein evaporite supergroup (Rouillard *et al.*, 2020). The Rotliegend is also the reservoir used for the Rough gas storage field, where 54 BCF of natural gas is stored (Stuart, 1991).

5.4 Methodology

5.4.1 Fluid substitutions

Fluid substitution is the property modelling of a rock, with the pore-filling fluid having been replaced by a new fluid or new ratios of two or more different fluids (Dvorkin, Mavko and Gurevich, 2007). Fluid substitution modelling is commonly used to understand how the constituent properties of the rock are modified when alternative fluids to the original fill the pore space (Nolen-Hoeksema, 2000). The Gassmann equations are the most commonly used methodology to undertake fluid substitution (Gassmann, 1951; Smith, Sondergeld and Rai, 2003). The equations relate the bulk modulus of the saturated rock, K_{sat}, the bulk modulus of the dry rock frame, K^*, the bulk modulus of the mineral matrix, K_o, the porosity of the rock, Φ, and pore filling fluids bulk modulus, K_{fl} (Smith, Sondergeld and Rai, 2003);

$$K_{sat} = K^* + \frac{(1 - \frac{K^*}{K_O})^2}{\frac{\Phi}{K_{fl}} + \frac{(1 - \Phi)}{K_O} - \frac{K^*}{K_O^2}}$$

EQUATION 28 – GASSMANN EQUATION

5.4.1.1 Bulk elastic rock properties

The bulk modulus of a rock can be calculated using the compressional velocity, V_p, the shear velocity, V_s and the bulk density, ρ_{bulk} as;

$$K_{sat} = \rho_{bulk}(Vp^2 - \frac{4}{3}Vs^2)$$ *EQUATION 29 – BULK MODULUS*

Compressional velocity and shear velocity data can be obtained from either wireline logging or core measurements for a specific formation. We use data derived from well logs. Where the data are recorded as slowness (us/ft) a conversion into velocity is required;

$$Vp\left(\frac{m}{sec}\right) = 10^6 * 0.3048 * Sonic\ Log(us/ft)$$ *EQUATION 30 – VELOCITY COMPRESSIONAL FROM SONIC COMPRESSIONAL LOG DATA*

$$Vs\left(\frac{m}{sec}\right) = 10^6 * 0.3048 * Shear\ Log(us/ft)$$ *EQUATION 31 – VELOCITY SHEAR FROM SONIC SHEAR LOG*

5.4.2 Fluid physical properties

Physical properties for pore filling fluids for substitution into the pore space may be determined from laboratory experiments (Salemi *et al.*, 2018) or calculated theoretically using equations of state (EoS) (Danesh, 1998). In this study, the fluid's physical properties were calculated using the EoS models in the NIST Chemistry WebBook (1997) (NIST used the following equations of state, carbon dioxide (Span and Wagner, 1996), hydrogen (Leachman *et al.*, 2009), methane (Setzmann and Wagner, 1991)). Reservoir conditions for the Ormskirk reservoir were taken from Yaliz and Taylor (2003), conditions for the Rotliegend were taken from Anston-Race and Ganesh (2020), and conditions for the Bunter formation were taken from Gluyas and Bagudu (2020).

We assume carbon dioxide and hydrogen are in the supercritical phase at the described reservoir conditions (NIST Chemistry WebBook, 1997; Okere, Sheng and Ejike, 2024) (Table 5-1), for methane we model a pure dry pure system.

The bulk modulus of a fluid was calculated using the bulk density and speed of sound through the medium as;

$$K_{fl} = \rho * v^2$$ *EQUATION 32 – BULK MODULUS OF FLUID*

Reservoir	Assumed depth (m)	Pressure (MPa)	Temperature (c)	Density (Kg/m^3)	Bulk modulus (Gpa)
Rotliegend	2447	30.4	72.5	173.6 (Methane) 18.3 (Hydrogen) 781 (Carbon dioxide)	0.068 (Methane) 0.050 (Hydrogen) 0.199 (Carbon dioxide)
Bunter	1406	15.2	57	100 (Methane) 10.3 (Hydrogen) 641 (Carbon dioxide)	.024 (Methane) .023 (Hydrogen) .068 (Carbon dioxide)
Ormskirk	792	9.68	30	71.2 (Methane) 7.3 (Hydrogen) 763 (Carbon dioxide)	.014 (Methane) .014 (Hydrogen) .105 (Carbon dioxide)

TABLE 5-1 –FLUID ELASTIC PROPERTIES AT RESERVOIR CONDITIONS FOR ROTLIEGEND, BUNTER AND ORMSKIRK FORMATIONS

5.4.2.1 The Gassmann Equations

For accurate modelling of the Gassmann equation, the bulk modulus of the dry rock frame is required to be calculated from the measured properties of rocks in situ,

$$K^* = \frac{K_{sat}\left(\frac{\Phi K_o}{K_{fl}} + 1 - \Phi\right) - K_o}{\frac{\Phi K_o}{K_{fl}} + \frac{K_{sat}}{K_o} - 1 - \Phi}$$

EQUATION 33 – GASSMANN - DRY ROCK FRAME BULK MODULUS CALCULATION

To calculate the dry rock frame's bulk modulus, the following parameters of the rock are required: the bulk modulus of the mineral matrix, porosity, and the bulk modulus of the pore filling fluid. To calculate the bulk modulus of the mineral matrix we can use the Voight-Reuss-Hill method (Smith, Sondergeld and Rai, 2003):

$$K_o = \frac{1}{2}((F_1K_1 + F_2K_2) + (\left(\frac{F_1}{K_1} + \frac{F_2}{K_2}\right)^{-1})$$

EQUATION 34 - VOIGHT-REUSS-HILL.

where F_n is the mineral fraction and K_n is mineral bulk modulus of the mineral. The above implementation accounts for a two mineral system. The gamma-ray log was used to calculate shale volume, and the inverse of this was used to calculate the quartz volume to assume a 2-mineral system of quartz and clay. While the investigated reservoirs are more complex than a 2-mineral system, the constitute minerals have a bulk moduli of similar orders of magnitude. The similarity allows the use of a mixing law means, which provides sufficient accuracy for the Gassmann equation. This is due to the bulk modulus of the mineral matrix only having a minor effect on the bulk modulus of the whole rock (Darling, 2005).

$$v_{sh} = \frac{GR - GR_{Matrix}}{GR_{Shale} - GR_{matrix}}$$

EQUATION 35 – VOLUME SHALE

Porosity can be derived from well-log data; in this study we use the neutron-density methodology (Kennedy, 2015);

$$\Phi_\rho = \frac{\rho_{matrix} - \rho_{Bulk}}{\rho_{matrix} - \rho_{fluid}}$$

EQUATION 36 – DENSITY POROSITY

$$\Phi = (\frac{\Phi_N^2 + \Phi_\rho^2}{2})^{1/2}$$

EQUATION 37 – POROSITY FROM NEUTRON POROSITY LOG AND DENSITY POROSITY

The bulk modulus of the fluid and ρ_{fl}, the bulk density of the fluid, can be derived for a single fluid or a fluid mixture. Either can be calculated via;

$$K_{fl} = [\frac{S_w}{K_w} + \frac{(1 - S_w)}{K_{fn}}]^{-1}$$

EQUATION 38 – BULK MODULUS OF FLUID MIXTURE

and;

$$\rho_{fl} = S_w * \rho_w + (1 - S_w)\rho_{fn}$$

EQUATION 39 – DENSITY OF FLUID MIXTURE

Once the bulk modulus of the pore filling fluid mixture is calculated, the bulk modulus of the mineral rock frame can be calculated. With all constituent parts of the Gassmann equation calculated, the new elastic properties of the fluid-substituted rock can be calculated.

Along with the new bulk modulus of the fluid-substituted rock having been calculated, the bulk density of the rock with the substituted fluids can be calculated with;

$$\rho_{new} = \rho_{matrix} * (1 - \Phi) + (\rho_{fl} * \Phi)$$

EQUATION 40 – DENSITY OF FLUID SUBSTITUTED ROCK

Once the new bulk modulus and bulk density of the rock have been calculated, the new compressional and shear velocities of the rock can be calculated by rearranging the equations for bulk modulus and G, the shear modulus. Note that the shear modulus of the rock remains unchanged despite fluid substitution;

$$Vp = \sqrt{\frac{K + \frac{4}{3}G}{\rho_{bulk}}}$$

EQUATION 41 – VELOCITY COMPRESSIONAL FROM BULK AND SHEAR MODULUS

$$G = \rho_{bulk} * Vs^2$$

EQUATION 42 – SHEAR MODULUS

The equations used do not account for the substituted fluids (carbon dioxide, hydrogen) having been absorbed by residual water at non-end member water saturations. Our methodology also does not account for pore pressure changes, which can have effects on seismic responses (Bahmaei and Hosseini, 2020). We assume a uniform heterogeneous matrix and uniform liquid pathways. We assume plume modelling, rather than precipitated carbon dioxide in pore space or carbon dioxide dissolved in brine.

5.4.3 Determining net reservoir

Reservoir cut-offs were used to define reservoir intervals within wells. Shale volume (Vshale), porosity and bulk density were the chosen factors in determining which areas of the reservoir were suitable (Table 5-2). A shale volume value of 30% was selected as the cutoff volume. The

bulk density values were chosen, as outside these ranges typically consisted of either A) interbeds of low-density evaporites such as halite or B) interbeds of high-density evaporites such as anhydrites or carbonates. A minimum porosity of 5% was chosen.

Cut off parameter	Minimum Value	Maximum Value
Volume Shale (Vshale)	0%	30%
Porosity (Φ)	5%	NaN
Bulk density (ρ_{bulk})	2.00 g/cm^3	2.67 g/cm^3

TABLE 5-2 – RESERVOIR CUTOFF VALUES FROM DIFFERENT ROCK PROPERTIES

5.4.4 Stochastic modelling

A stochastic approach to implementing the Gassmann equations was adopted to account for the irreducible uncertainty in reservoir properties. The elastic property inputs of the Gassmann equations are defined as distributions derived from well data. The elastic properties of porous material are in general correlatable (Figure 5-3); hence, a multi-variate distribution was derived from the properties (Castagna *et al.*, 1993). Distributions were determined for defined porosity intervals (Table 5-3). For a valid distribution to be defined, a minimum of 25 data points was required. This threshold allowed for the shape of the distribution to be suitably characterised, and for the avoidance of edge cases, which stopped poor-quality distributions being generated. The compressional velocity, shear velocity, porosity, bulk modulus and shale volume were the required parameters to be derived from porosity-separated distributions for the Gassmann equations. For each porosity of each formation investigated (Table 5-3) there were 1,500 iterations of the model run. Multi-variate distributions were also created for the seal paired with the reservoir intervals. The distribution for these was used within the AVO analysis, so the well data was used to derive distributions for shear/compressional velocity and bulk density of the seals.

Formation	Stochastic Porosity (Φ) Groups
Rotliegend	7, 9, 11, 13, 15, 17, 19
Ormskirk	14, 16, 18, 20, 22, 24, 26
Bunter	19, 21, 23, 25, 27

TABLE 5-3 – POROSITY GROUPS OF CHOSEN STRATIGRAPHY FOR STOCHASTIC ANALYSIS

Alongside stochastic modelling we use the UQ(Py)Lab package for Python to undertake a sensitivity analysis using the Solbol methods on the Gassmann equation (Soboĺ, 1993; Marelli and Sudret, 2014). The output chosen to investigate the sensitivity of the Gassmann equation was the new acoustic impedance of the fluid-substituted rock. The use of sensitivity modelling allows for understanding which parameters within the Gassmann equation have the most significant effect on the resultant acoustic impedance.

5.4.4.1 Validation of parameters from stochastic modelling

While compressional and shear velocity and, bulk density, can be directly derived from the data taken from the well logs, other parameters, notably porosity and bulk modulus of the mineral matrix, must be calculated using transforms that relate to theoretical relationships. Our calculated values of porosity were checked against those from measured core plug values (Appendix 11), a difference between the measured values and calculated values was found to be 11% (e.g. 20% vs 22.2% porosity), which was determined to be reasonable.

The validation of calculated values for the mineral matrix bulk modulus was more difficult to establish, as there were two issues: 1) Validating mineral matrix components and inputs into Equation 34 . 2) validating the output of Equation 34. For issue 1, literature was used to determine typical mineral percentages for the matrix and check against our shale volume and quartz volume estimates. We assume a 2-mineral system, as the only other main mineral within the system (apart from clays) is likely to be feldspar. The average value for feldspars' bulk modulus is similar to that of quartz (37.5 vs 37), thus for this use it was deemed suitable (Smith, Sondergeld and Rai, 2003). For issue 2, even if exact values for the mineral matrix components were available, there are high levels of variability between the two parameters, as shown by Qin, Han and Zhao (2022).

5.4.5 Seismic responses

Once the new elastic properties are calculated, the seismic response can be calculated. The new reservoir elastic properties and associated seismic response of the fluid-substituted reservoirs were calculated for water saturations from 100% to 0% in 10% increments. Three different fluids were investigated: methane, carbon dioxide, and hydrogen.

5.4.5.1 Wedge modelling

Wedge models were created to model the seismic response at geological interfaces. The wedge models were produced in Python using parts of the PySeisTuned 2.0 code base (Dowdell, 2020). Two wedge models were created for the Bunter Sandstone Formation: reservoir-reservoir interfaces and seal–reservoir interfaces. The wedge models used simple three-layer geological models, which included an overburden, the reservoir wedge and the underburden. The rock properties used in the wedge models were derived from the deterministic fluid substitution scenarios for the reservoir, and well logs for the original reservoir and seal properties. The acoustic impedance was calculated for each wedge section and, subsequently, the reflection coefficient at the wedge interfaces. A ricker wavelet with a frequency analogous to the seismic data that covers the area of the well data was used (see appendix for full details). The wavelet was convolved with the reflection coefficient model to create a synthetic wedge model. The wedge models use the American standard polarity, where a negative reflection co-efficient event shows a negative reflection event.

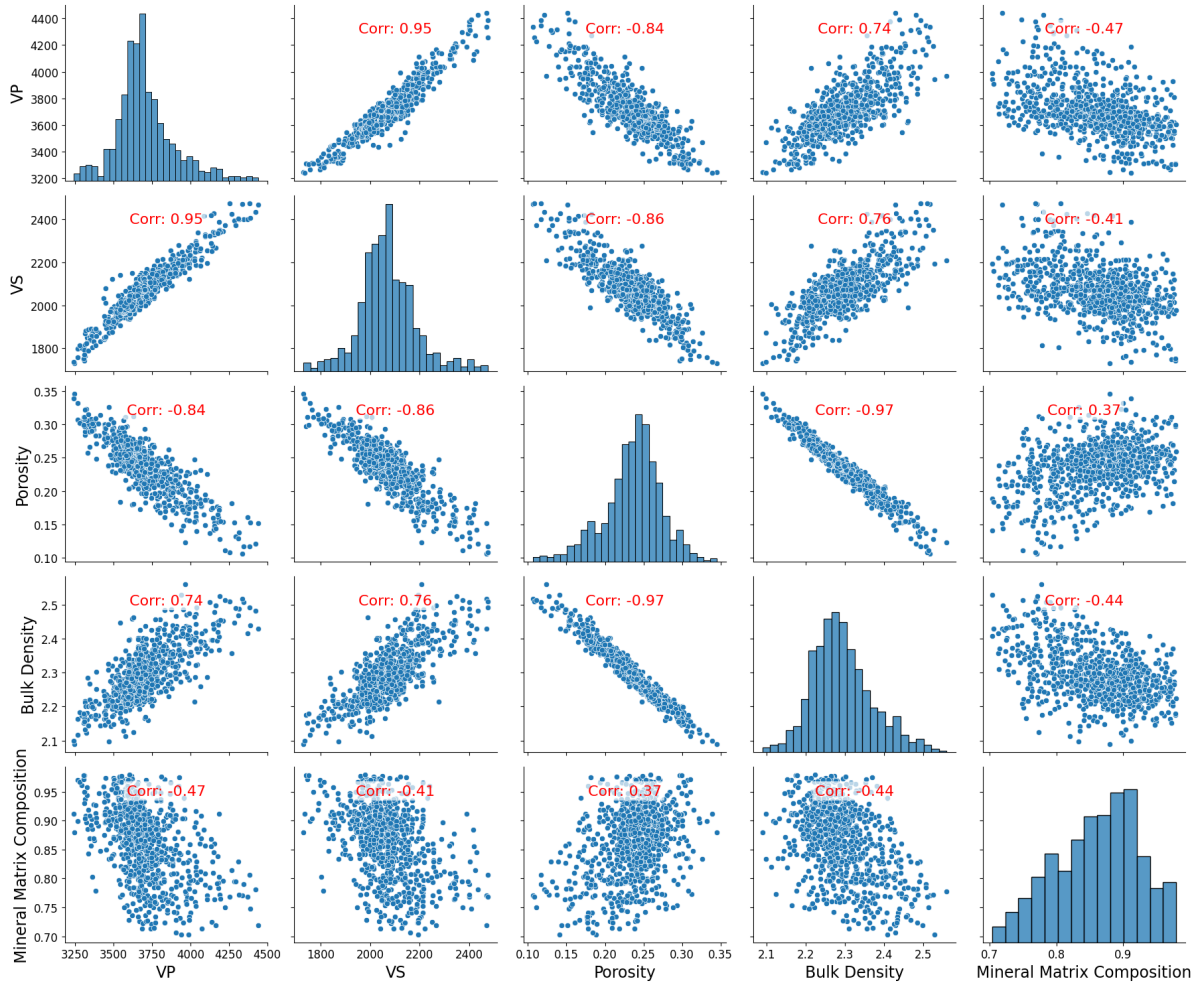

FIGURE 5-3 CROSSPLOT OF ELASTIC PROPERTIES FOR BUNTER RESERVOIR INTERVAL FROM WELL 42/25-D3. PEARSON CORRELATION VALUES HAVE ALSO BEEN PLOTTED.

5.4.5.2 *AVO Responses*

Amplitude versus offset (AVO) analysis examines the change in reflection and transmission coefficient of an incident P-wave (compressional wave, V_p) as a function of the angle of incidence (Chopra and Castagna, 2014). For interface modelling and calculating the expected amplitude versus the offset of the seismic wave (AVO), the Zoeppritz's equations was used (Zoeppritz, 1919);

$$\begin{bmatrix} cos\theta_{p1} & -sin\theta_{s1} & cos\theta_{p2} & sin\theta_{s2} \\ sin\theta_{p1} & cos\theta_{s1} & -sin\theta_{p2} & cos\theta_{s2} \\ Z_1 cos2\theta_{s1} & -W_1 sin2\theta_{s1} & -Z_2 cos2\theta_{s2} & -W_2 sin2\theta_{s2} \\ \frac{V_{s1}}{V_{p1}} W_1 sin2\theta_{p1} & W_1 cos2\theta_{s1} & \frac{V_{s2}}{V_{p2}} W_2 sin2\theta_{p2} & -W_2 cos2\theta_{s2} \end{bmatrix} \begin{bmatrix} R_p \\ R_s \\ T_p \\ T_s \end{bmatrix} = \begin{bmatrix} cos\theta_{p1} \\ -sin\theta_{p1} \\ -Z_1 cos2\theta_{s1} \\ \frac{V_{s1}}{V_{p1}} W_1 sin2\theta_{p1} \end{bmatrix}$$

EQUATION 43 – THE ZOEPPRITZ (1919) EQUATIONS

The Zoeppritzs equations allow for the calculation of the reflected p-wave response at a geological interface with a set angle of incidence. For the application of the AVO equations to our data, we used the Python module Bruges by Agile-Scientific (2022) which is based on the methodology described by Dvorkin, Gutierrez and Grana (2014). We used the stochastic outputs from our reservoir response analysis as inputs into the Zoeppritz equations and looked at two separate responses, reservoir – reservoir contacts (water saturation 100% and water saturation 0%) and seal – reservoir contacts. The seal parameters were stochastically generated from the previously mentioned distributions.

5.4.5.3 Timeshift analysis

As fluids within the pore-space affect the compressional and shear velocity properties of a rock, they affect the travel time of seismic waves through the media and modify the recorded responses in the seismic surveys (Dvorkin, Gutierrez and Grana, 2014). Time-shift analysis involves identifying the time variation between two seismic traces in the same location from different acquisitions. These are typically taken pre-fluid injection/withdrawal (baseline) and after fluid injection or withdrawal (monitor) (MacBeth, Amini and Izadian, 2020). Two methods were used to investigate the time shifts caused by fluid substitution, 1) Using a baseline and monitor seismic trace generated from well data to measure the timeshift on actual geological data and, 2) From stochastically generated compressional velocities for baseline and monitor reservoir values to calculate Δt over various distances and water saturations.

$$\Delta t = z\left(\frac{1}{v'} - \frac{1}{v}\right)$$

EQUATION 44 TIME-SHIFT ESTIMATION, FROM MACBETH, MANGRIOTIS AND AMINI (2018)

5.5 Data

From the three chosen reservoir-seal pairs, the wells were selected based on the availability of data. We prioritised wells that had bulk density, shear slowness, compressional slowness,

gamma ray and neutron porosity logs across reservoir intervals. This requirement for shear slowness data limited well selection as it is not commonly acquired. The stratigraphic intervals within the well logs were determined using the completion logs, which were available for each well through the North Sea Transition Authority's National Data Repository (https://ndr.nstauthority.co.uk/). For the wells used within this study, please view the appendix.

Due to limited shear sonic data availability in wells from the Ormskirk and Bunter formations, the parameter distributions are derived from a single well, whereas, for the Rotliegend, more wells had the required logs available, which allowed for distributions to be derived from multiple wells. As the modelling of the Bunter Sandstone used a single well it effectively investigates the vertical heterogeneity and uncertainty, while for the Rotliegend that availability of data means the modelling effectively investigates the lateral and vertical heterogeneity.

5.6 Results

5.6.1 Reservoir Responses

5.6.1.1 Response to different fluids

The change in water saturation from 100% – 80% for all fluids and reservoirs shows a sharp initial drop in compressional velocity, however, after this initial drop, compressional velocity begins to increase (Figure 5-4). Hydrogen and methane in all reservoirs increase the compressional velocity beyond the initial value at between 40% - 20% water saturation. However, after the initial drop the compressional velocity of carbon dioxide increases at a proportionally slower rate than that of hydrogen and methane, in each scenario. The compressional velocity for each reservoir never increases over the initial value for carbon dioxide.

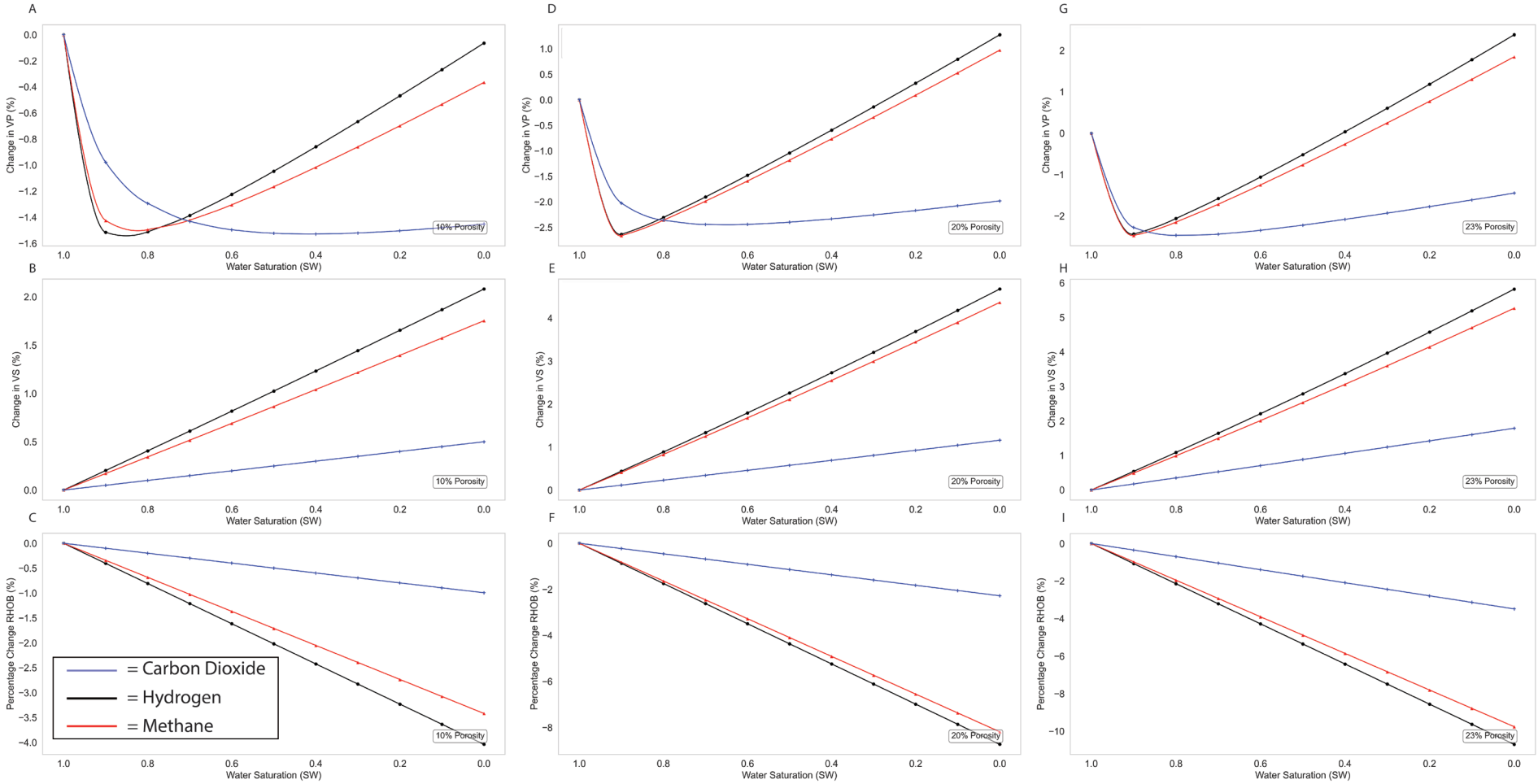

FIGURE 5-4 DETERMINISTIC ELASTIC RESPONSES OF THE A-C) ROTLIEGEND, D-F) BUNTER, G-I) ORMSKIRK. A,D,G) % CHANGE IN COMPRESSION VELOCITY. B,E,H) % CHANGE IN SHEAR VELOCITY. C,F,H) % CHANGE IN BULK DENSITY

The change in shear velocity for all reservoir fluid combinations is a positive linear increase (Figure 5-4). There are differences amongst the fluids however. Hydrogen in all scenarios has the greatest increase, with methane showing similar increases. Carbon dioxide has the lowest increase in shear velocity overall for all scenarios. As the porosity of the reservoir has increased so has the % increase of shear velocity (Figure 5-4).

Change in bulk density is a negative linear trend for all scenarios. This occurs as the substituted fluids all have densities lower than water Figure 5-4). Because carbon dioxide is the densest of the fluids substituted, it shows the least decrease to % change of bulk density, with hydrogen showing the most. The higher porosity reservoir undergoes the highest % change to bulk density, because there is more pore space for the less dense fluids into which they can be substituted.

The sensitivity analysis of the Gassmann equation for calculating acoustic impedance shows that it is most sensitive to a change in compressional velocity, with a first-order index value of 78% and a total Sobol index of 53% (Figure 5-5). Moderate sensitivity to both porosity and density is indicated, with first order results being 20.7 % and 20.4 % and total order indexes being 4.9 % and 5.5 % respectively. The equation is not sensitive to shear velocity or the mineral matrix composition.

5.6.1.2 Stochastic analysis of geophysical responses

We concentrate on describing the results of the fluid substitution at 20% water saturation, as this is likely the near maximum value possible for subsurface storage sites (Yan *et al.*, 2018). The Rotliegend data set was split into seven porosity groups with a 2% porosity interval increase from 7% to 19% (Table 5-3). Increasing proportions of hydrogen results in a greater acoustic impedance change than for the equivalent carbon dioxide at each porosity interval. The largest change in acoustic impedance for 20% water saturation for both hydrogen and carbon dioxide occurred at 19% porosity, being -12.7% and -9.2% respectively (Figure 5-6). Hydrogen has a much sharper initial decrease in acoustic impedance, whereas while carbon dioxide also shows an initial drop in acoustic impedance, its response curve is more gradual (Figure 5-6).

For the Bunter Sandstone, the p50 results, hydrogen is shown to modify the acoustic impedance a greater amount than carbon dioxide, at 27% porosity and 20% water saturation.

The effect change on acoustic impedance for hydrogen is -9.8% and for carbon dioxide it is -6.7%. The trend is the same as those in the deterministic reservoir responses (Figure 5-7) with hydrogen having a sudden drop at 90% water saturation and then a relatively continuous linear decrease, whereas carbon dioxide has a more pronounced curve to its trend in decreasing acoustic impedance (Figure 5-7). The minimum response for hydrogen and carbon dioxide in the p50 values is both at the lowest porosity, 19%, where at 20% water saturation, hydrogen has an acoustic impedance change of -6.2% and carbon dioxide has a negative change of -4.2%.

The results for the Ormskirk follow the same trends as the Bunter data, with higher porosities having a larger effect on acoustic impedance and hydrogen also having a larger effect. At 26% porosity and 20% water saturation, hydrogen fluid substituted sample showed a change in acoustic impedance of -10.4%, while carbon dioxide was -6.5%. At the lowest porosity, 14%, the change in acoustic impendence at 20% water saturation was -2.8% for hydrogen and -1% for carbon dioxide.

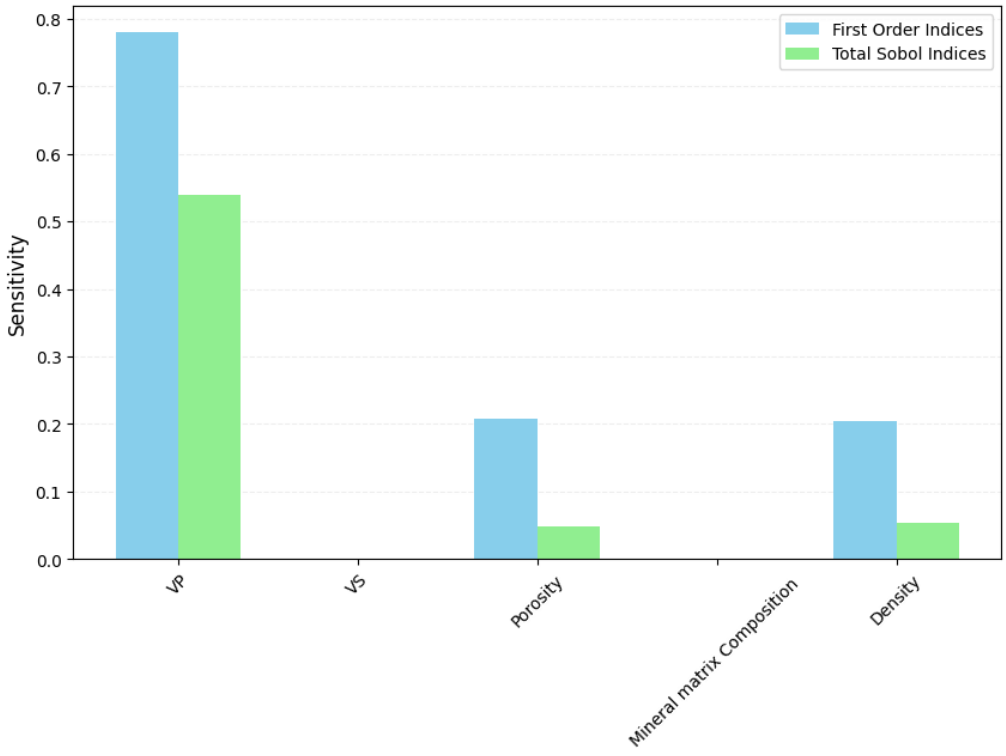

FIGURE 5-5 SOBOL SENSITIVITY ANALYSIS RESULTS FOR THE PARAMETER INPUTS DERIVED FROM WELL LOG DATA ON THE GASSMANN EQUATION FOR THE COMPUTATION OF THE ACOUSTIC IMPEDANCE.

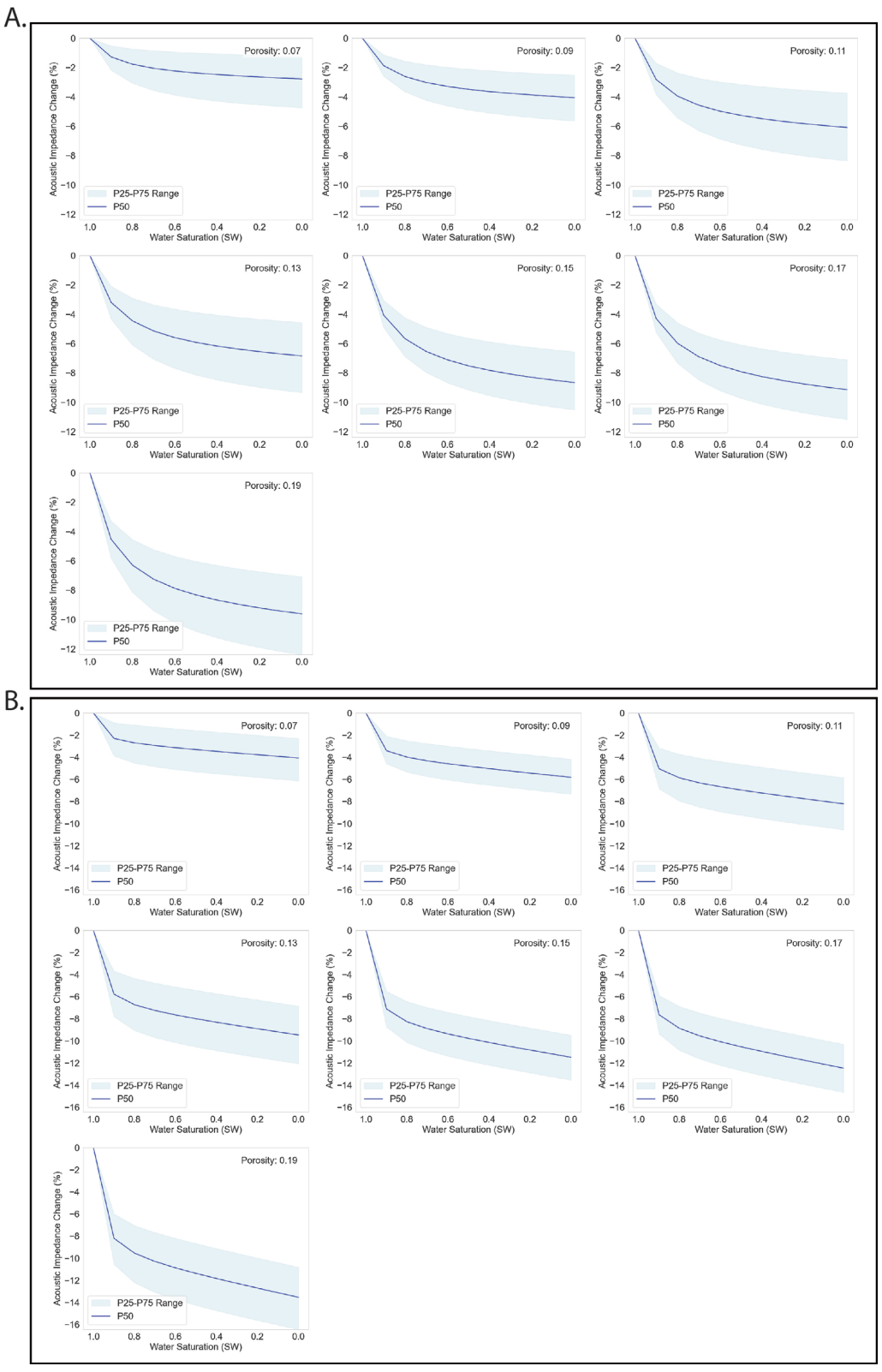

FIGURE 5-6 ROTLIEGEND STOCHASTIC ACOUSTIC IMPEDANCE MODELS FOR VARYING POROSITY VALUES AFTER FLUID SUBSTITUTION FOR FLUIDS. A) CARBON DIOXIDE, B) HYDROGEN

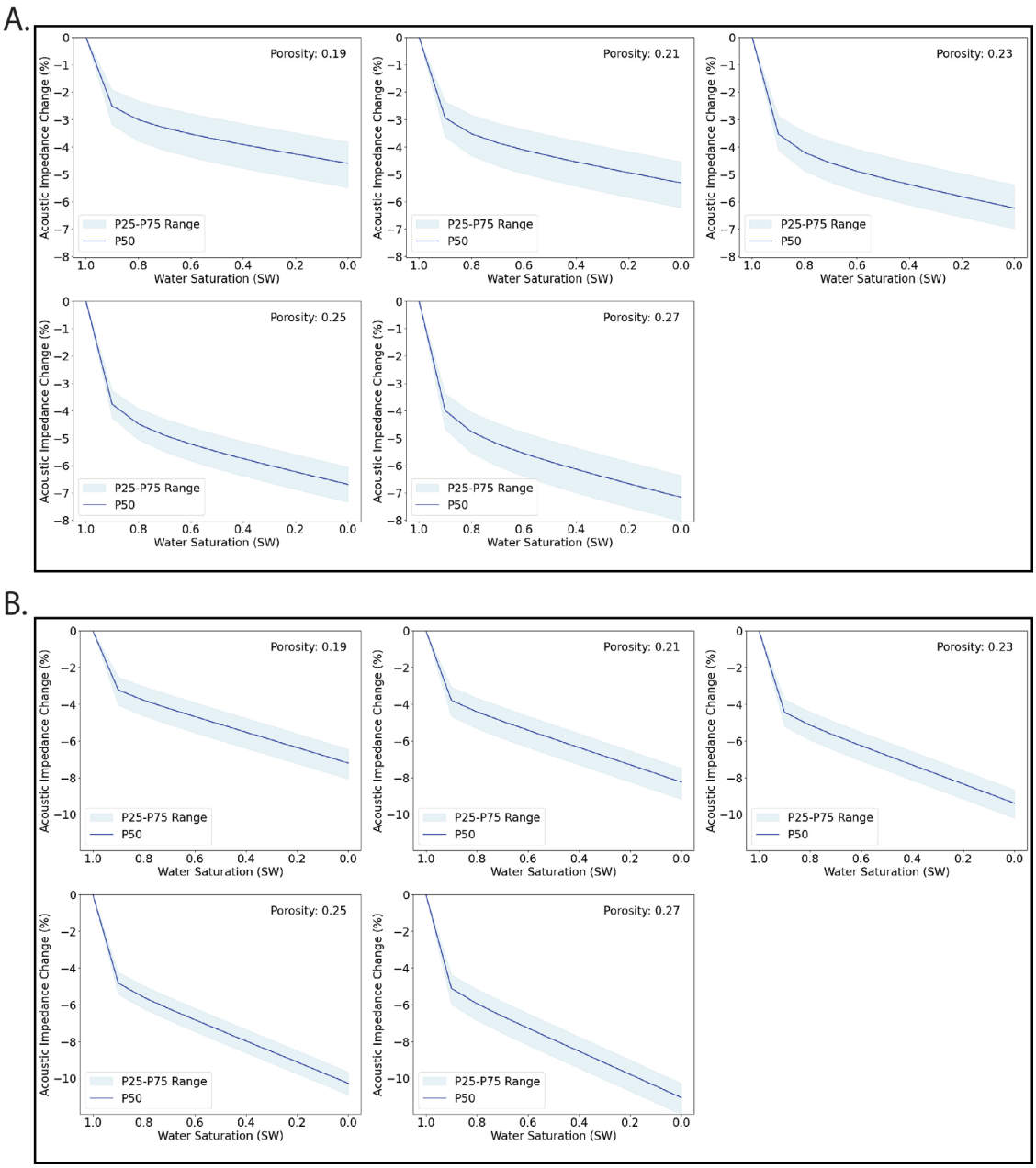

FIGURE 5-7 BUNTER STOCHASTIC ACOUSTIC IMPEDANCE MODELS FOR VARYING POROSITY VALUES AFTER FLUID SUBSTITUTION FOR FLUIDS. A) CARBON DIOXIDE, B) HYDROGEN

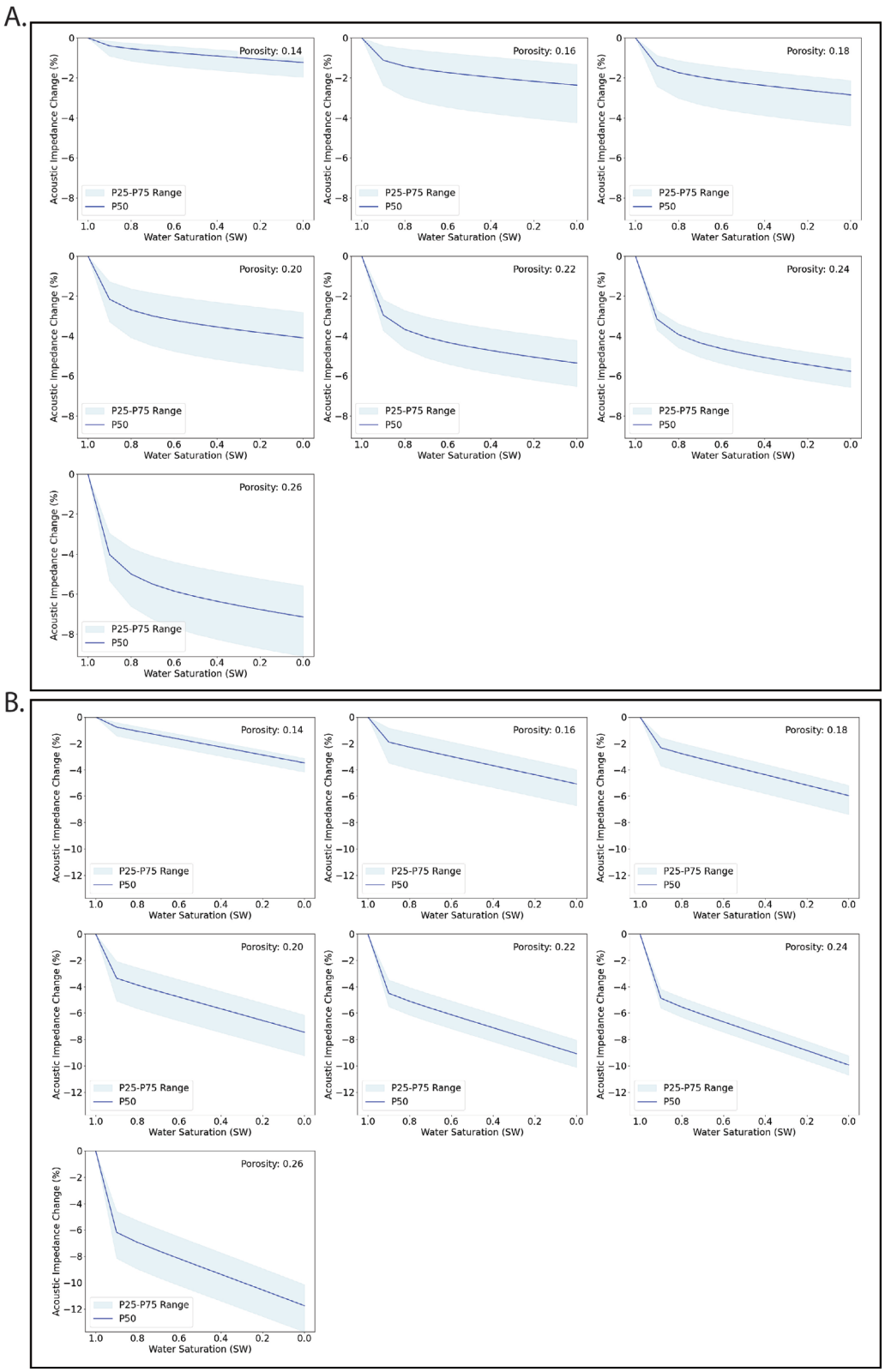

FIGURE 5-8 ORMSKIRK STOCHASTIC ACOUSTIC IMPEDANCE MODELS FOR VARYING POROSITY VALUES AFTER FLUID SUBSTITUTION FOR FLUIDS. A) CARBON DIOXIDE, B) HYDROGEN

5.6.2 AVO responses

Figure 5-9 shows the modelled AVO responses for the reservoir–reservoir and reservoir–seal interface for the Rotliegend data set (all porosities are present within Appendix 12 - 17). The reservoir-reservoir interface shows little difference in the amplitude for typical changes in the recorded reflection offsets from seismic data. Notable differences in amplitude occur at offset angles which are greater than that which would typically be recorded with a seismic survey (45°+), and this is common for all porosities. However, for the reservoir–seal interface there are differences to the amplitude at typical survey offsets for all porosities. The largest change as offset increased was for the 19% porosity seal-reservoir interface, where from 5° (near stack) to 45° (ultra far stack) there was a relative amplitude change of +0.14.

As the Bunter sandstone has two possible seals within the Southern North Sea, halite, and claystone, and both interface lithologies were modelled for their AVO response (Figure 5-10). For the reservoir-reservoir interface AVO analysis, both carbon dioxide and hydrogen results show moderate to minor differences in amplitude with an increase in offset from the near stack to the ultra-far stack with a difference of 17 - 18.7% and 5.9 – 4.7% (7 – 19% porosities) respectively. The amplitude difference for the carbon dioxide filled reservoir is smaller with an increasing offset, with the most noticeable change occurring at offsets of +50° where amplitudes decrease rapidly. The inverse is true for hydrogen, where there is a minor increase in amplitude for all porosities throughout increasing offset, with the most notable changes being large increases again after +50°. The evaporite seal–reservoir interface shows very similar results for both hydrogen and carbon dioxide (Figure 5-7). Minor amplitude differences are apparent, however these do not impact the trend of the amplitude differences. The claystone seal model again has similar results for both carbon dioxide and hydrogen, with only minor amplitude differences up until reaching the ultra-far offset values. At the ultra-far offset values, the lower porosities amplitude falls, whereas the higher porosity values increase slightly.

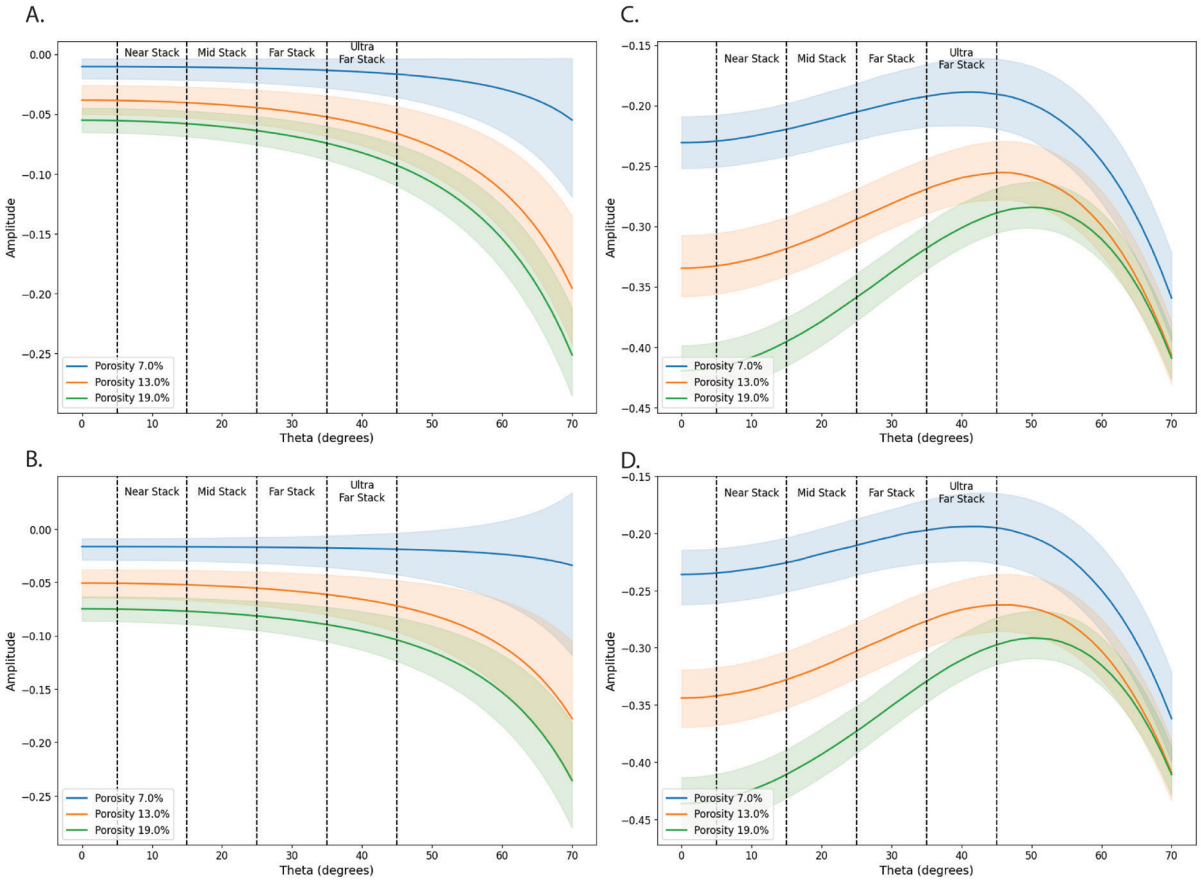

FIGURE 5-9 ROTLIEGEND AMPLITUDE VERSUS OFFSET FOR RESERVOIR-RESERVOIR INTERFACE FOR (A) CARBON DIOXIDE AND (B) HYDROGEN. SEAL-RESERVOIR INTERFACE FOR (C) CARBON DIOXIDE AND (D) HYDROGEN

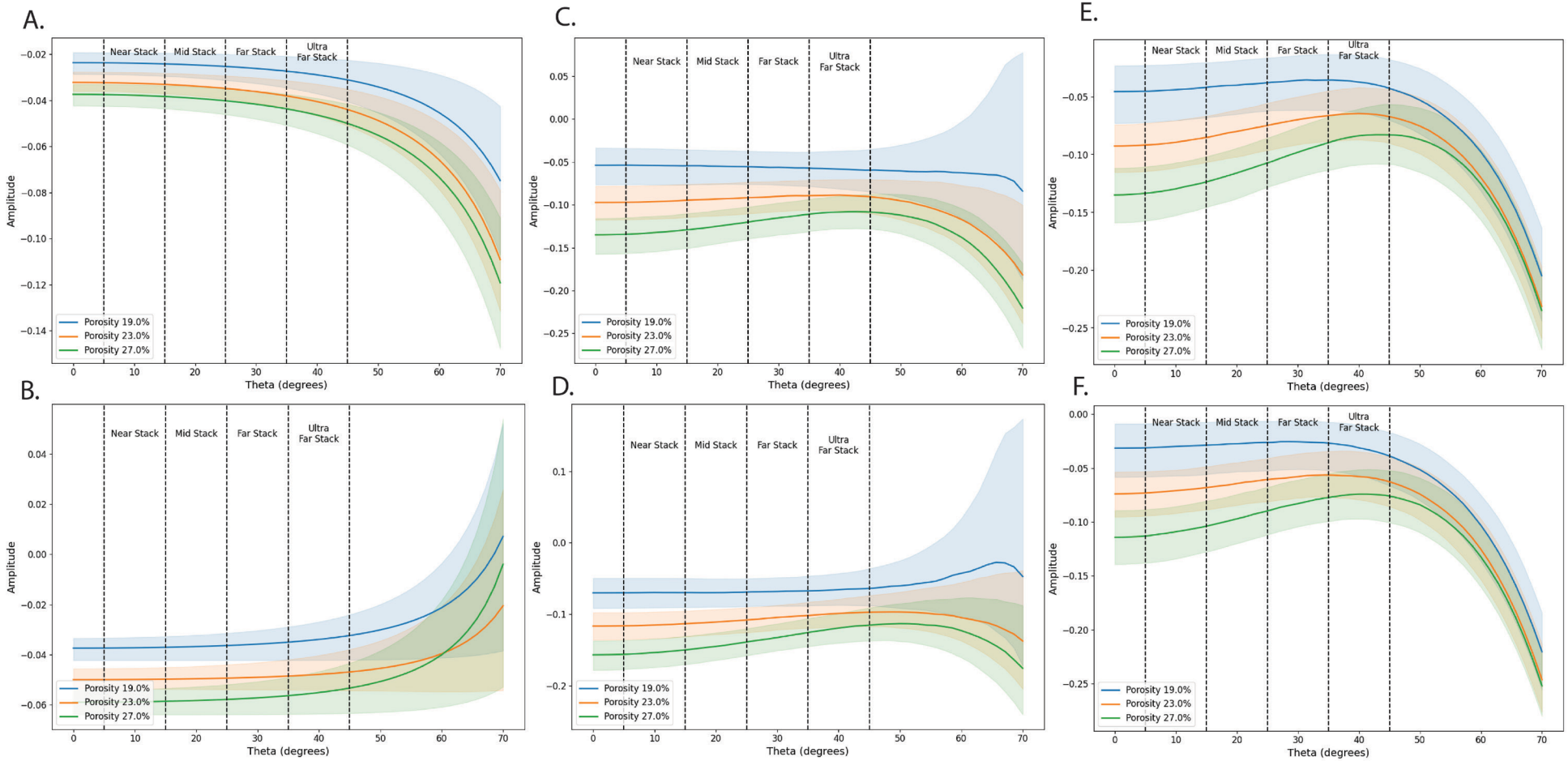

FIGURE 5-10 BUNTER AMPLITUDE VERSUS OFFSET FOR RESERVOIR-RESERVOIR INTERFACE FOR (A) CARBON DIOXIDE AND (B) HYDROGEN. SEAL-RESERVOIR (EVAPORITE) INTERFACE FOR (C) CARBON DIOXIDE AND(D) HYDROGEN. SEAL-RESERVOIR - (CLAYSTONE) INTERFACE FOR (E) CARBON DIOXIDE AND (F) HYDROGEN.

The results for the Ormskirk Sandstone show a minor difference of decreased amplitude for the reservoir–reservoir interface for carbon dioxide and a minor increase for hydrogen in the typically recorded offset ranges (Figure 5-11). At large offsets (+45°), the carbon dioxide reservoir – reservoir interface shows a decreased value for amplitude for every porosity except for the 14% porosity values, which increase. Hydrogen results show all amplitudes increase at these offsets at greater than 45°, with the lowest porosity, 14%, showing the greatest increase. For the carbon dioxide seal-reservoir interface, an increase in amplitude from low to high offsets is observed for all porosities. This increase in relative amplitude peaks in the range of 50°- 60°, after which it falls rapidly. For hydrogen the results for higher porosities are like that of the carbon dioxide, however, for the lower porosities, notably 14%, a gradual decrease in relative amplitude occurs, with a greater drop off offsets of 65°+ (Figure. 8).

5.6.3 Interface modelling

Reservoir-seal and reservoir-reservoir interfaces were modelled for the Bunter sandstone for hydrogen and carbon dioxide (Figure 5-12). All models show initial constructive interference at wedge thicknesses <10 ms. All models show the onset tuning to occur at a wedge thickness of 14 ms, after which constructive interference occurs. The reservoir-seal interfaces both have onset tuning thickness of 28 ms, while the reservoir-reservoir interfaces onset tuning thickness is 29 ms. The interface wedges for hydrogen (Figure 5-12 E,F) show higher amplitude values than those for carbon dioxide (Figure 5-12 C,D).

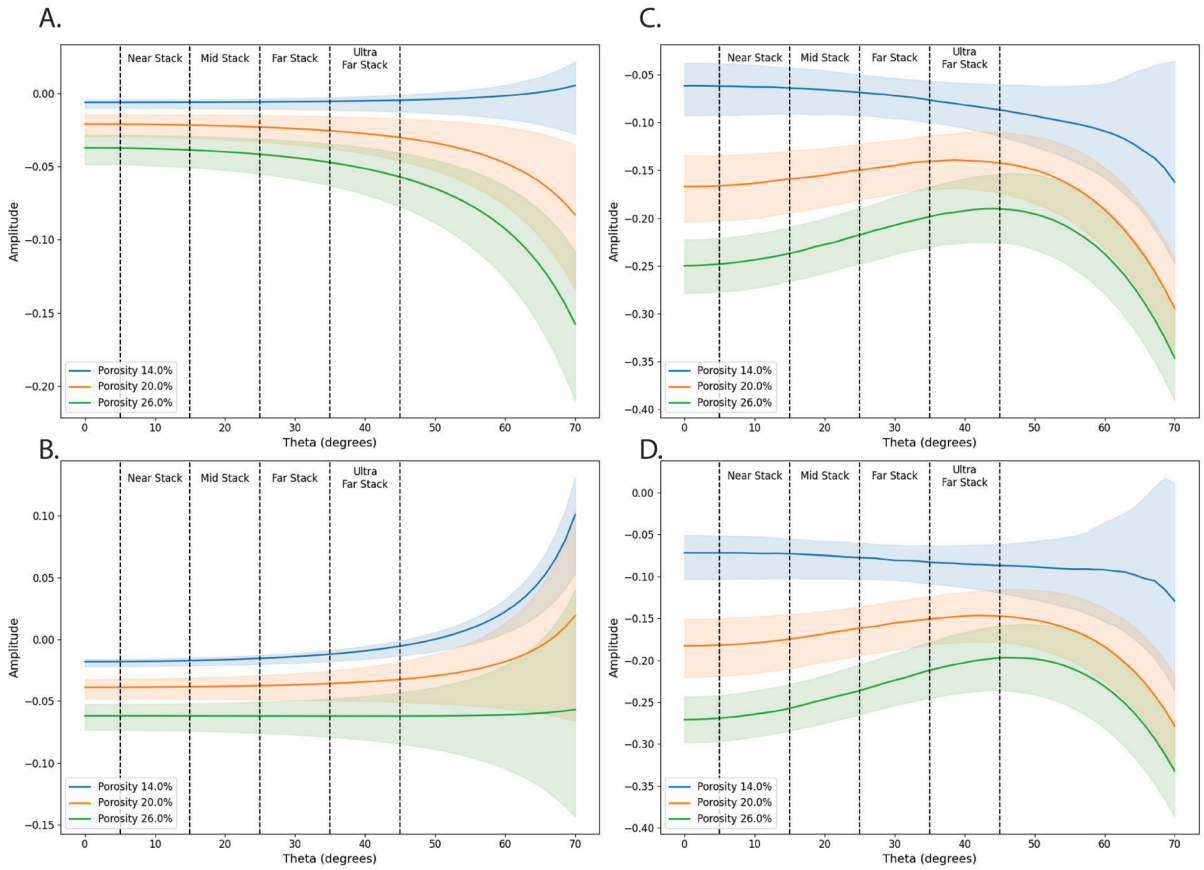

FIGURE 5-11 ORMSKIRK AMPLITUDE VERSUS OFFSET FOR INTERFACE FOR (A) CARBON DIOXIDE AND (B) HYDROGEN . SEAL-RESERVOIR INTERFACE FOR (C) CARBON DIOXIDE AND (D) HYDROGEN

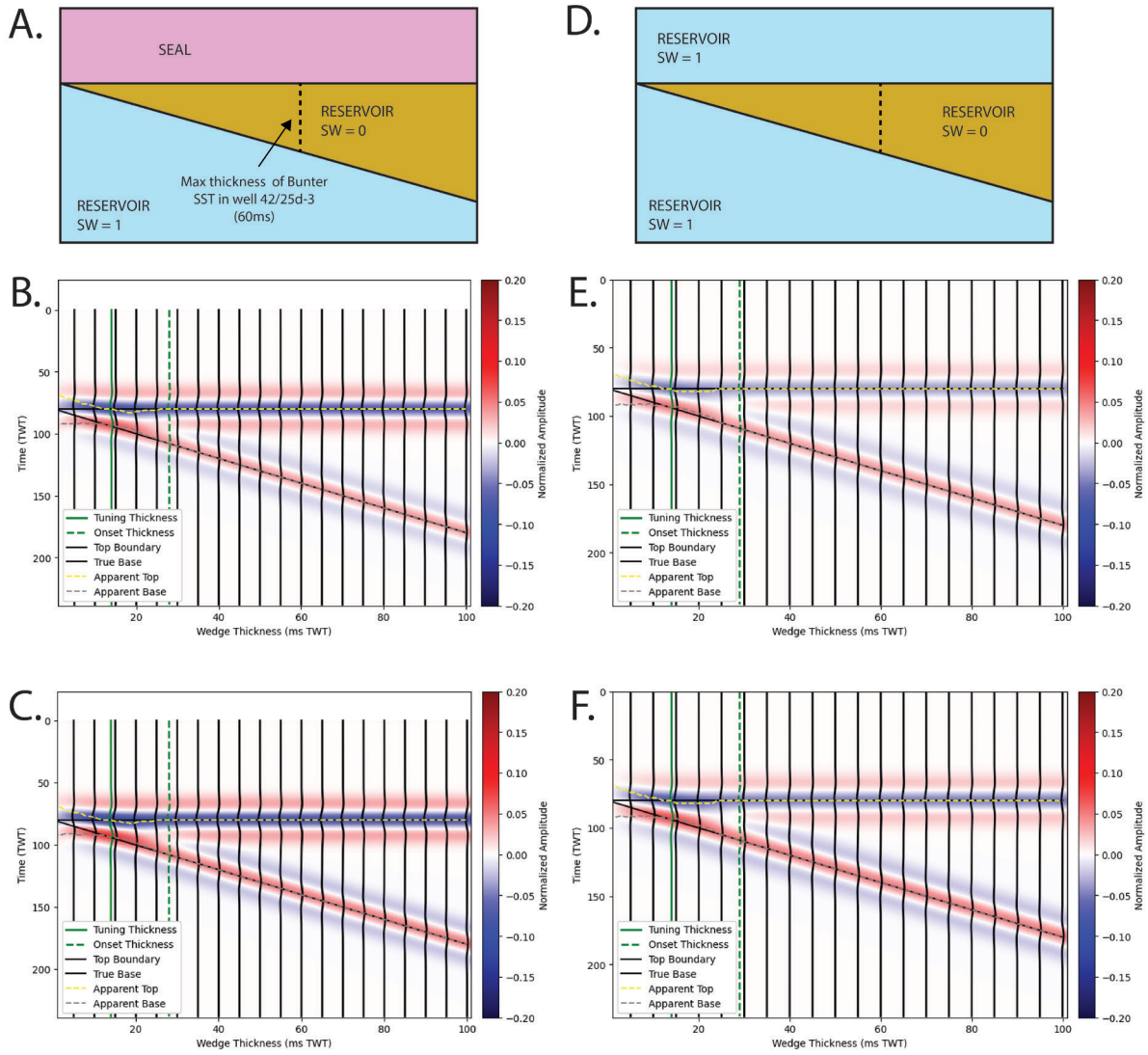

FIGURE 5-12 INTERFACE SEISMIC WEDGE MODELS FOR THE BUNTER SANDSTONE. A) 2D BLOCK DIAGRAM OF GEOLOGY SIMULATED FOR B AND C. B) RESERVOIR SATURATED WITH CARBON DIOXIDE (C) HYDROGEN. D) BLOCK DIAGRAM OF SIMULATED GEOLOGY FOR E AND F. E) RESERVOIR SATURATED WITH CARBON DIOXIDE, (F) HYDROGEN. FREQUENCY USED FOR WAVELET IS 35HZ

5.6.4 Time Shift

Synthetic seismic traces were calculated for the Bunter Sandstone from well log data (well 42/25-d3, 130 m section of reservoir). Traces were made for pre and post-fluid-substitution (20% water saturation) of carbon dioxide to act as baseline and monitor seismic traces. Figure 5-13 shows the monitor, baseline, and an overlay for the synthetic seismic well traces from the Bunter Sandstone well for carbon dioxide. A positive timeshift for the monitor initiates at the top of the reservoir when brine is replaced with carbon dioxide, with a shift in seismic traces (Figure 5-13). The difference in TWT at the bottom of the reservoir is 0.877 ms over the reservoir interval of 130 m .

Time shifts for the Bunter sandstone were calculated using the velocity values from the stochastic fluid substitution analysis section 5.1.2. Initial low water saturations (0.7,0.8) show the greatest timeshift over any set unit thickness, with the p50 value at 0.7 having a timeshift of 2.46 ms for 250 m (Figure 5-13). This aligns with the values seen in section 4.1.2 where large decreases in Vp are initially observed at relatively high-water saturation values (Figure 5-4). Extrapolating values to match the reservoir thickness in Figure 5-13, at 0% water saturation and a 130 m reservoir, the calculated timeshifts are 0.93 ms for the p50, 0.64 ms for the p25 and 1.11 ms for the p75. This locates the calculated value from the log derived timeshift (0.72 ms) within the range of provided values.

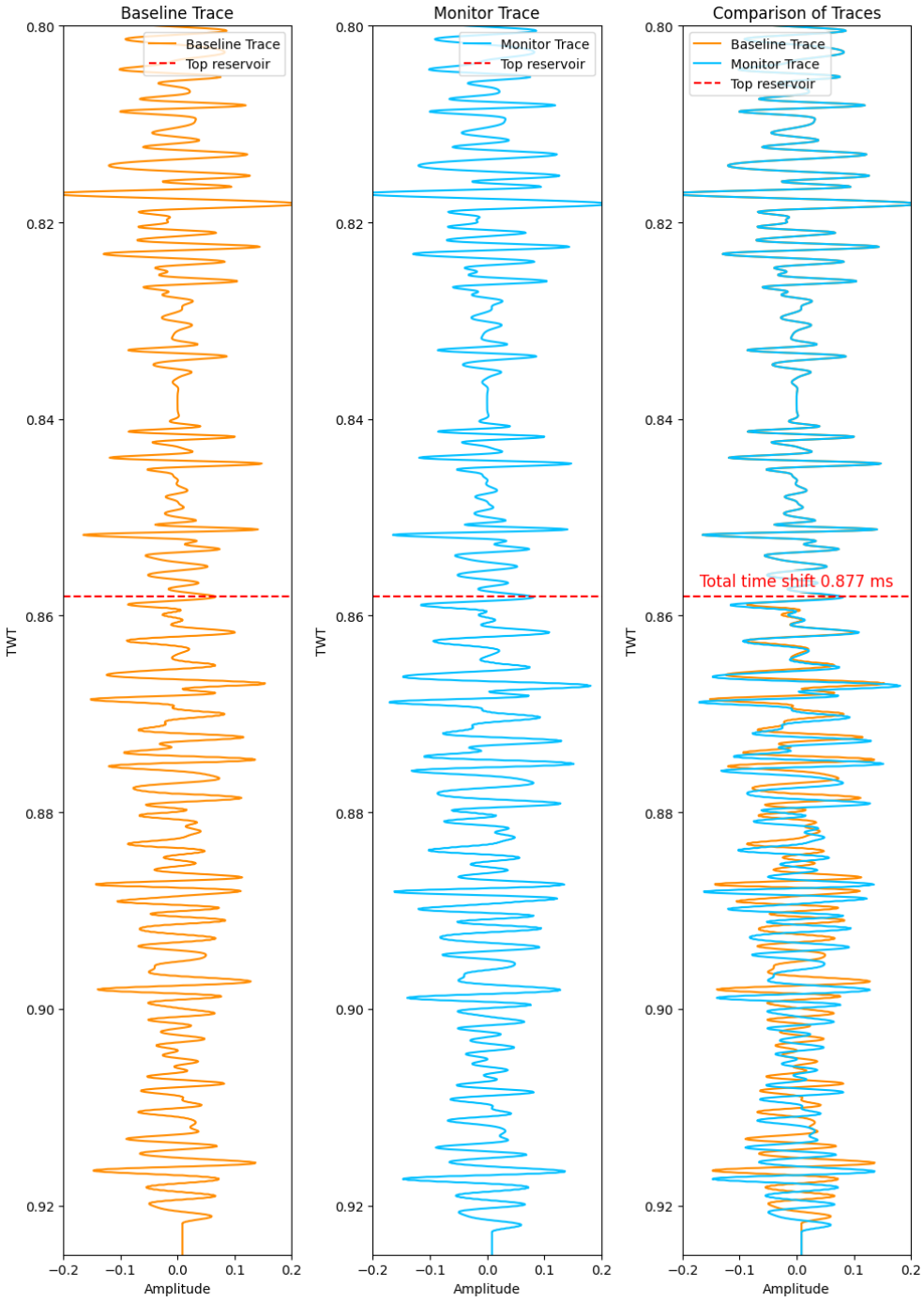

FIGURE 5-13 BUNTER RESERVOIR INTERVAL FROM WELL 42/25-D3 (RED LINE = TOP OF RESERVOIR). (A) BASELINE SYNTHETIC SEISMIC LOG, (B) MONITOR SYNTHETIC SEISMIC LOG AFTER GASSMANN FLUID SUBSTITUTION 100% CARBON DIOXIDE SATURATION. (C) A + B OVERLAIN ONE ANOTHER FOR VISIBLE TIMESHIFT COMPARISON

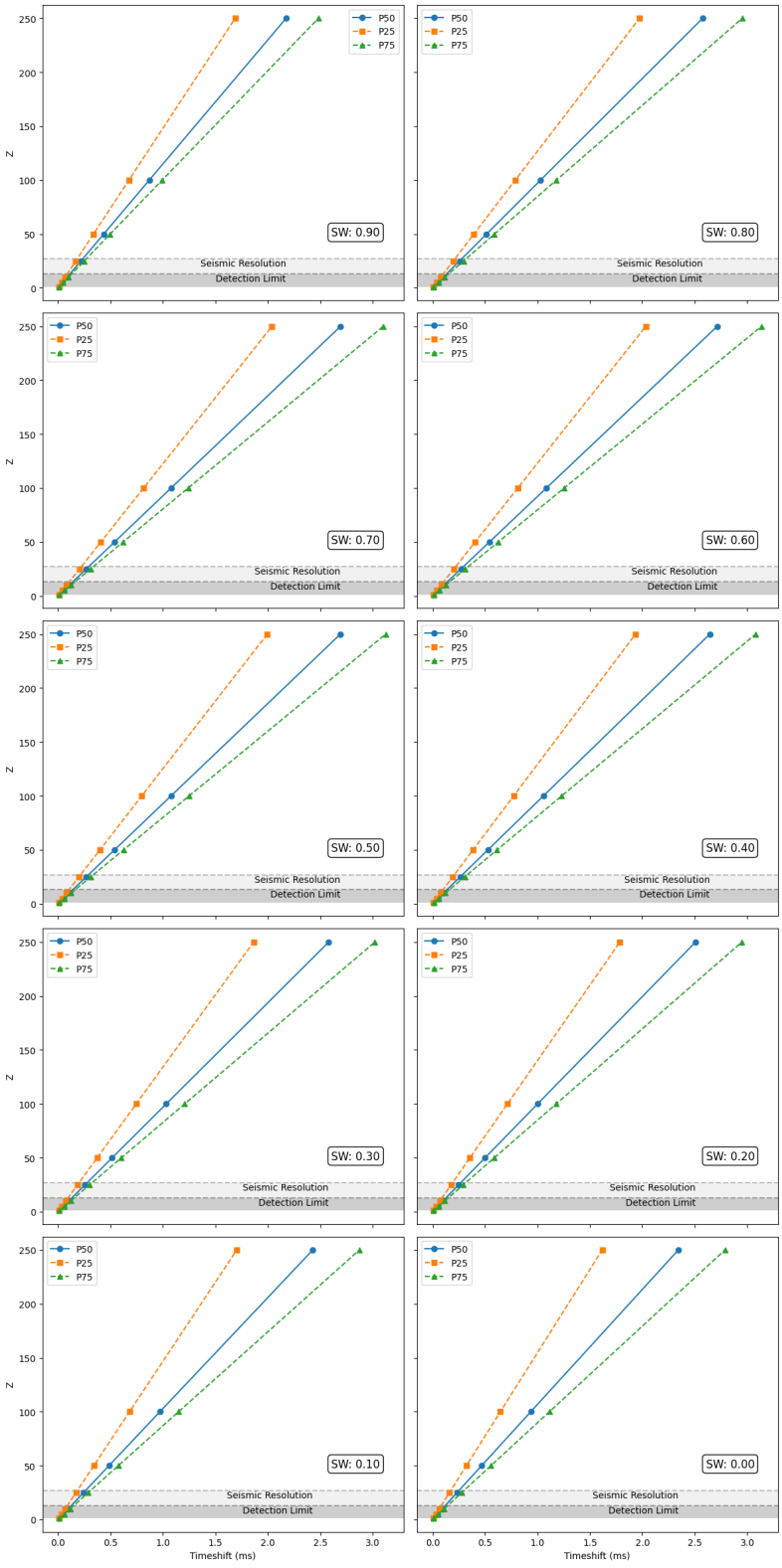

FIGURE 5-14 SYNTHETIC TIMESHIFT MODELS FOR THE BUNTER SANDSTONE. 90% – 0% WATER SATURATION IS MODELLED FOR A THICKNESS OF 0 – 250. P25,P50 AND P75 VALUES ARE INCLUDED. THE RESOLUTION (27 M) AND DETECTION LIMIT (13 M) OF THE SEISMIC FOR THIS WELL AND DEPTH ARE INCLUDED.

5.7 Discussion

5.7.1 Results

The results from all formations investigated show a decrease in acoustic impedance when brine is replaced by either carbon dioxide or hydrogen (Figure 5-6, 5-8). For all formations, higher porosities result in a greater change to acoustic impedance. When the same porosity was investigated for different formations, 19% porosity for the Rotliegend and Bunter formations for example, there were large differences to the change in acoustic impedance values, for the Rotliegend, a p50 of 9.2% and for the Bunter a p50 of 4.2% at 20% water saturation (Figure 5-6, 5-7).

The acoustic impedance results for the Bunter sandstone has a narrower range for the p25 and p75 results compared with both the Rotliegend and Ormskirk examples (Figure 5-7, 5-8, 5-9). The difference in ranges for outputs is likely the result of two factors. Firstly, the input data for both the Rotliegend and Ormskirk multivariate distributions shows a much larger ranges of values, and a higher quantity of outliers present than compared with the Bunter values (Figure 5-15). The wider ranges of generated values from the multivariate distributions coincide with formation and porosity intervals with large p25 – 75 ranges for acoustic impedance results, for example the Rotliegend 13% porosity and Ormskirk 22% porosity interval (Figure 5-6, 5-8, 5-15). Secondly, the increase in pore-fluid being substituted led to large ranges within the output results. Every output result for change in acoustic impedance shows a significantly lower range in output values for the initial 100% – 70 % water saturation, with saturations from 70% – 0% showing increased ranges for the p25 – p75 values. It is likely the increased variation in ranges for results shown for acoustic impedance is from a combination of these effects.

5.7.2 Comparison with published results

We discuss the results of our modelling with other published results for the same reservoir storage formations. Our results (Table 5-4) show different values to those given in reports on monitoring of the stratigraphy we investigated, notably to James, Baines and McCollough (2016b) for the Rotliegend, to Green and Grammer (2016) for the Ormskirk and to BEIS (2021) for the Bunter Sandstone. Seismic monitoring is a valid technique to monitor migration pathways for carbon dioxide using change of acoustic impedance. However, the properties unique to the rock being monitored may mean that the change in elastic properties is below

that of the detection limit of the seismic data. As a rule of thumb, an acoustic impedance contrast of 4% is required for a 4D seismic survey to detect the change in a feature (Lumley and Behrens, 1998). Table 5-4 shows that the predicted acoustic response from the Rotliegend is well above this 4% boundary, however the Bunter is only just above this boundary and the Ormskirk is < 4% boundary. As the cited sources did not provide the parameters used within their workflow or the output models, direct comparisons with the results presented in this study are difficult. Had such data been given in a readily accessible data base more in-depth comparisons could have been concluded.

While changes in acoustic impedance values in seismic data can aid in the monitoring of subsurface fluid migration, utilising the changes to seismic amplitude with different seismic reflection offsets, utilising different qualities within the same dataset, may aid in further detecting the change in acoustic impedance and provide more informative results for carbon dioxide plume monitoring. For example, both the Rotliegend and the Bunter Sandstone (Table 5-3, Figure 5-9, 5-10) show larger % changes for the reflection coefficient and hence amplitude at the interface of reservoir – reservoir and seal – reservoir than the % increase when calculating just acoustic impedance change (Table 5-3).

The results of timeshift analysis also indicate notable variations in reflection two-way-time because of changes in fluid saturations (Figure 5-14). The plotted detection limit (13 m) and seismic resolution (27 m) show that at the detection limit, the resolvable timeshift values range from 0.09 ms to 0.11 ms, and for the seismic resolution, the timeshift values vary from 0.22 ms to 0.27 ms. Typical detection limits for timeshift values reported from separate monitor seismic surveys range from 0.1 ms – 2 ms in literature (MacBeth and Izadian, 2023). The calculated timeshift of 0.8.77 ms for the Bunter sandstone from well 42/25d-2 (Figure 5-13), is therefore likely detectable on a monitor seismic survey. However, this timeshift occurs from a 130 m reservoir thickness interval, as such reservoir thickness below the suggested timeshift detection limit (13 m) may not be detectable in a monitor survey.

The relatively positive findings from our study, however, do not excuse the literature sources for failing to give quantifiable inputs and results for their fluid substitution modelling and analysis. If the cited sources are supportive of seismic monitoring and such methods are proposed for large-scale infrastructure projects, there should be stringent evidence supplied in a repeatable and reliable manner, as shown in this study.

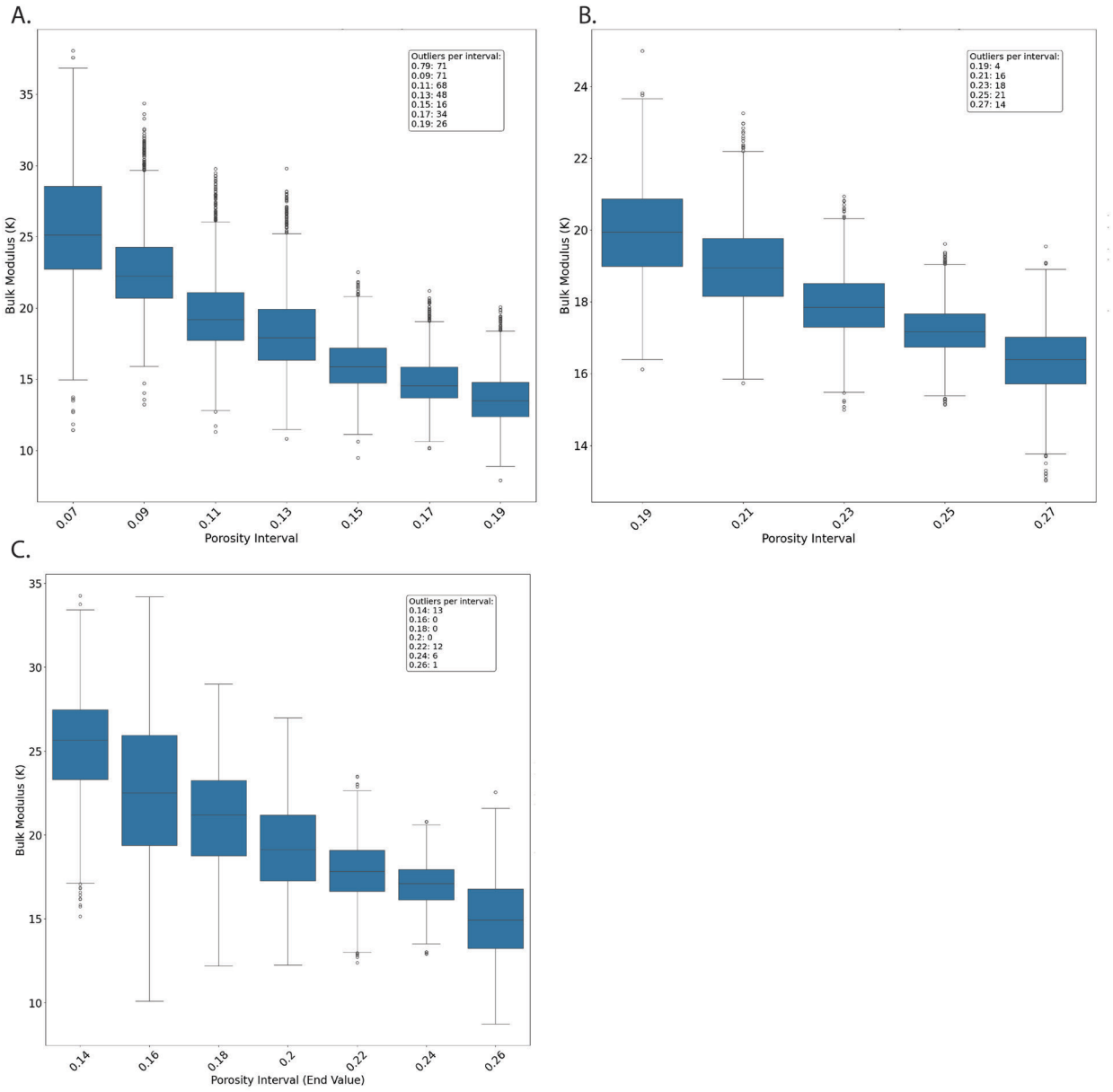

FIGURE 5-15 BOX PLOTS BULK MODULUS FOR POROSITY INTERVALS GENERATED FROM MULTIVARIATE DISTRIBUTIONS FOR A) ROTLIEGEND, B) BUNTER, C) ORMSKIRK

The reproducibility and reliability of methods for subsurface monitoring is important for subsurface infrastructure projects, as it allows for evaluation of results to be more efficient and undertaken reliably, strengthening evidence for proposed projects (Steventon *et al.*, 2022). However, a common theme regarding site specific subsurface storage, is the lack of data supplied to allow for results to be seen as both reproducible (same data same methodology), or reliable (same data different methodology). While best efforts were made

to replicate the results of those published in literature (Table 5-4), this was not possible (James, Baines and McCollough, 2016a; James, Baines and McCollough, 2016b; Green and Grammer, 2016; BEIS, 2021). While we cannot comment on which results are more accurate, we can provide all data and the methodologies we use so that the results shown are reproducible and method replicable.

5.7.3 Stochastic simulations

The approach of our methodology allowed for the usage of datasets from individual wells (Ormskirk and Bunter Sandstone) and to consider a greater range of reservoir properties from multiple wells (Rotliegend). While this approach was taken for reasons of practicality and data availability, the two types of data set used have differing implications for the results from one another. For a dataset that contains more than one well, the results will be more representative of the target stratigraphy throughout the whole area. As the multi-variate distributions are derived from several wells within the same area, the variance in elastic properties of the target stratigraphy, and different logging tools are accounted for and incorporated within the model. For single-well datasets, while the results are not as applicable to a regional area, the stochastic approach taken does provide valuable insights into the uncertainty prediction for a highly localised area in and around the wellbore. Value is also gained when comparing the two datasets, using a wider range of data from which to generate distributions from allows for an indication of how reservoir heterogeneity may impact fluid substitution and hence seismic response.

5.7.4 Implications for hydrogen exploration and storage

While proposed native hydrogen source rock settings typically involve basement rocks and non-sedimentary basin-based processes, these generation pathways do not exclude the possibility of a sedimentary reservoir overlaying potential generation processes, and hence acting as a reservoir for the migration of native hydrogen into them (Jackson *et al.*, 2024). Understanding the potential seismic response of hydrogen in porous materials can have applications in exploration in sedimentary sequences.

Our work shows that through forward modelling hydrogen, the elastic properties of a rock saturated with hydrogen are affected in a similar context as a rock fully saturated with methane (natural gas) (Figure 5-4). Thus typical industry exploration methodologies used for

determining natural gas within the subsurface, are likely to be applicable to native hydrogen within the subsurface.

Stratigraphy	Calculated AI Change p50 (Water saturation 20 %)	Literature Ai change	Calculated AVO (Rc) % Change Difference Near stack – Far stack offsets	Timeshift	Notes
Rotliegend (Φ 15)	-8 (Figure 5-6)	Not quantified but 'Very poor' (James, Baines and McCollough, 2016b)	Res – Res: 38.2 Seal – Res: 22.2	Nan	Seal (Zechstein) may cause an issue
Bunter (Φ 23)	-6 (Figure 5-7)	12 – 20% (BEIS, 2021)	Res – Res: 25.4 Seal – Res (Claystone): 4.48 Seal – Res (Evaporite):-23.5	0.877ms (Figure 5-13)	No data given by (BEIS, 2021) on how value calculated,
Ormskirk (Φ 16)	-2 (Figure 5-8)	Not quantified, but 'Maybe detectable' at 60% carbon dioxide saturation (Green and Grammer, 2016)	Res – Res: -3.32 Seal – Res:0.91	Nan	

TABLE 5-4 INVESTIGATED STRATIGRAPHY WITH RESULTS FOR SELECT POROSITY. RESULTS FROM THE LITERATURE ARE ALSO PRESENT

Extra to this hydrogen in pore space gives a larger acoustic impedance change than that of carbon dioxide (Figure 5-6). This has implications for storage and management of hydrogen within the subsurface, as is proposed for areas of the UKCS or in salt caverns (Jahanbakhsh *et al.*, 2024). Storage complexes ideally should be modelled and chosen, such that hydrogen within the pore space enables the 4% change in acoustic impedance required for 4D seismic detection. Hydrogen also shows stronger responses than carbon dioxide when the reflection offset of a seismic wave is increased, suggesting that these methods may be suitable for monitoring potential storage sites or detecting natural accumulations. We did not examine possible time shifts from hydrogen substituted into a sandstone reservoir. However as

hydrogen causes compressional velocity increases at relatively high water saturations (+80%) (Figure 5-4), we would expect a similar timeshift to that shown in (Figure 5-13, 5-14).

5.7.5 Future work and limitations

While the injection phase of carbon capture sites is typically expected to last decades, the migration and chemical reactions of carbon dioxide in the subsurface will continue for far longer (Metz *et al.*, 2005). While most modelling scenarios consider carbon dioxide in the super critical phase just after injection, longer time scales (>50 years) considerations need to be given to carbon dioxide dissolved within brine and any mineral precipitation. While these chemical reactions will take significant time, >10 years to dissolve into water, and >100 for the precipitation of carbonate minerals, an understanding of whether seismic methods could offer effective monitoring of these subsurface changes is essential. The modelling approach here could be extended to investigate different scenarios and the resulting elastic properties. Such models would investigate the elastic properties of brine with significant carbon dioxide dissolved within, and the host reservoir with carbonates precipitated within the pore space, both of which are likely to modify the elastic properties.

Current monitoring methods using seismic data require baseline and monitor seismic surveys to map plume migration. Acquisition of monitor seismic surveys is a large expenditure for carbon capture sites, with typical individual survey costs being in the 10's of millions (Waal and Calvert, 2003). Other seismic monitoring methods that do not rely on follow up surveys may prove more cost-effective than these traditional techniques.

Passive seismic methods use a permanent array of receiver nodes and natural or anthropogenic seismic signals as the source signal for seismic monitoring. Passive arrays collect both compressional and shear velocity data of the subsurface rather than seismic travel time of active seismic surveys. Vp/Vs ratios can be used to identify pore-filling fluid and as such, changes to the Vp/Vs ratio would allow for identification of change in pore-fluid (Hamada, 2006). Trials have already been undertaken for the usage of passive seismic for carbon capture monitoring which showed promising results in the detection, however, none have occurred in an offshore setting (Payre *et al.*, 2014).

Point-to-point VSP (vertical seismic profiling), may prove another alternative low-cost method for monitoring of carbon storage sites. This technology utilises a permanent seismic receiver

array and source to constantly monitor the seismic response and hence elastic properties of the storage reservoir. As the elastic properties of the rock are modified by the fluid filling the pore space, the temporal and spatial changes of elastic properties are recorded. So long as such a technology can detect these changes at an acceptable resolution, this could allow for constant monitoring without the need of acquisition for monitor seismic surveys.

Our work on timeshifts does not account for the affects that heterogeneities such as thin beds may have. Thin beds and low frequencies can both cause tuning effects to occur within 4D seismic data sets (MacBeth, Amini and Izadian, 2020), and if a thin bed is < tuning thickness can be assumed that the timeshift signal drops to 0 (MacBeth and Izadian, 2023). Characterisation of the heterogeneities within a storage complex and inclusion within the forward modelling workflow would allow for more accurate timeshift results.

The Q factor is the measure of attenuation observed within seismic waves (Jyothi *et al.*, 2017). Changes in reservoir fluids have been shown to modify the value of Q (Joel *et al.*, 2003). Measuring the Q factor within a 4D seismic dataset could provide viable ways to monitor change in carbon dioxide saturation within reservoirs.

5.8 Conclusions

We have undertaken Gassmann fluid substitution on key stratigraphic intervals of offshore interest for geostorage of the United Kingdom in a stochastic, repeatable manner with all data and methodology being open and available. We examine datasets derived from both multi-well and single-well scenarios to determine the implications of carbon dioxide and hydrogen on the elastic properties and hence geophysical responses.

Our results show that a combination of seismic techniques will likely be required for monitoring carbon dioxide plume migration in the subsurface for UK stratigraphy, as typically changes to acoustic impedance are lower than that reported in public documents. Extra to relaying on 4D seismic and amplitude comparison, AVO and timeshift analysis will also be required to understand plume migration for geology where its acoustic impedance responses are calculated to be low (<4%).

We also calculate the results for hydrogen in the subsurface to understand responses of possible native hydrogen reservoirs or for hydrogen storage sites. Results for hydrogen show that it affects the elastic properties in a similar way to natural gas (from 100 to 0 % water

saturation), and thus we can expect typical industry quantitative seismic techniques to be applicable for both the exploration of native hydrogen reserves and for the monitoring of hydrogen in storage.

We also discuss the difference in our results from published literature for the UKCS. While we cannot comment on the rightness of our results compared with those in published reports for target CCS sites, we can be open and transparent with our scientific practices, making all our code and input data available at the time of publication. We suggest that this should be the case for subsurface infrastructure of national importance, especially when CCS sites are government-funded and not-for-profit activities, as it allows for proper scrutiny and scientific process to be undertaken.

Chapter 6. Discussion and conclusions

This chapter concludes the thesis by summarising the key findings from Chapters 3,4 and 5. The overarching ideas, themes, and implications for geological storage site characterisation are discussed.

6.1 Principal Findings

Chapter 3 characterises the internal structural heterogeneity of the of the Zechstein Supergroup within the South Permian Basin. Intra-Zechstein deformation styles were characterised and mapped across the basin, identifying the changing trends from the basin edges towards the basin depo-centre. Models are proposed for the internal heterogeneity of the chaotic reflection's structural deformation style and associated areas of withdrawal, where the currently available seismic data does not resolve the internal structure. The common interpretation that high amplitude discontinuous reflections are stringers within the Zechstein of the South Permian Basin (Strozyk *et al.*, 2014; Zijp *et al.*, 2018), is challenged with an alternative interpretation that non-continuous high amplitude reflections are continuous geological layers that in places dip too steeply to be resolved correctly by the seismic data, indicating ductile deformation rather brittle deformation.

Chapter 4 demonstrates a stochastic workflow for determining viable location and capacity of salt caverns for storing hydrogen. The developed workflow is agnostic to geological model resolution. Key input parameters are defined by distributions such that the impact of subsurface uncertainties can be captured. Sensitivity analysis demonstrates that salt structures and layered salt are sensitive to different inputs, with layered salts being most sensitive to overburden gradient and then depth uncertainty, however salt structures were most sensitive to insolubility content within the salt and secondly, to overburden gradient. Using the South Permian Basin as a case study, the results show that the energy requirements for the United Kingdom's energy transition (43 – 115 TWh (Cárdenas *et al.*, 2021)) can easily be met by as few as 73 potential salt cavern locations in the offshore domain.

Within Chapter 5 stochastic fluid substitution modelling is used to investigate the effect that carbon dioxide and hydrogen have on the elastic properties and the subsequent seismic response. A stochastic approach to the workflow was adopted to account for uncertainties

regarding the initial reservoir parameters and capture these uncertainties within the results. The change in elastic properties and geophysical responses are quantified. The change in amplitude of seismic reflections for changes in the incident seismic wave offset at geological interfaces are also quantified. Timeshift analysis is undertaken to quantify the affect carbon dioxide has on the response of reflections for monitor seismic surveys.

6.2 Uncertainty in site characterisation

There are several types of uncertainty which may affect the characterisation of a subsurface site: measurement uncertainty, conceptual uncertainty, ambiguous information, lack of information, statistical uncertainty, model uncertainty (Mann, Davis and Herzfeld, 1993; Benson and Yuhrm, 2015; Hasan and Shang, 2022; Schweizer, Blum and Butscher, 2017). Uncertainty is present for measurable features of the subsurface and associated data and, as such, any parameter associated with a geological process, phenomenon or object can be a source of uncertainty (Bárdossy and Fodor, 2001).

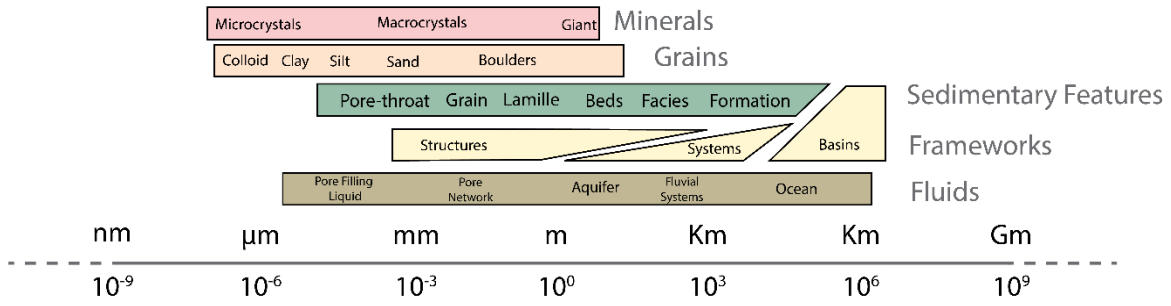

FIGURE 6-1 SCALES OF GEOSCIENCE, MODIFIED FROM. HALL (2011)

The natural variability of the subsurface combined with the scales of geoscience (Figure 6-1), human effort, financial cost and the impossible task of understanding and capturing all heterogeneities leads to a level of imperfect knowledge of the subsurface (Figure 6-2). When relating uncertainty to imperfect knowledge there will always be an inherent level of irreducible uncertainty associated with geology and hence present within derived models.

Subsurface data acquisition methods and tools introduce measurement uncertainties agnostic to the geological variation already present. Seismic data, for example, has a resolution which is frequency dependent, and limits its ability to image features within the subsurface (Section 2.1.1). The design of a seismic survey determines the resolution, and

hence constrains the size of detectable features. Features below the detection limit of a seismic survey will be an irreducible uncertainty within the dataset. For petrophysical and core data, a well drilled within a formation gives in-depth information about that exact point within the subsurface; however, as rocks are heterogeneous, parameters and values within the subsurface can be different, just meters away from the data collection location.

For the interpretation of data, it is essential to understand how the data is gathered and what features it represents within the subsurface so that the known uncertainties can be managed appropriately. Interpretation of the data, however, can also be subject to conceptual uncertainties, whether that be from the individuals' previous experiences, the tools used to interpret the data or the motivation to interpret the data (Bond *et al.*, 2007). Much like acknowledging the inherent uncertainties within the observations and data, these pre-existing and individual conceptual uncertainties must also be understood and recognised so that the models developed from these interpretations are able to either better manage these uncertainties, limiting the uncertainty passed into the model, or make those deriving predictions from the model aware of the conceptual uncertainties that may be associated with interpretations (Bond *et al.*, 2007).

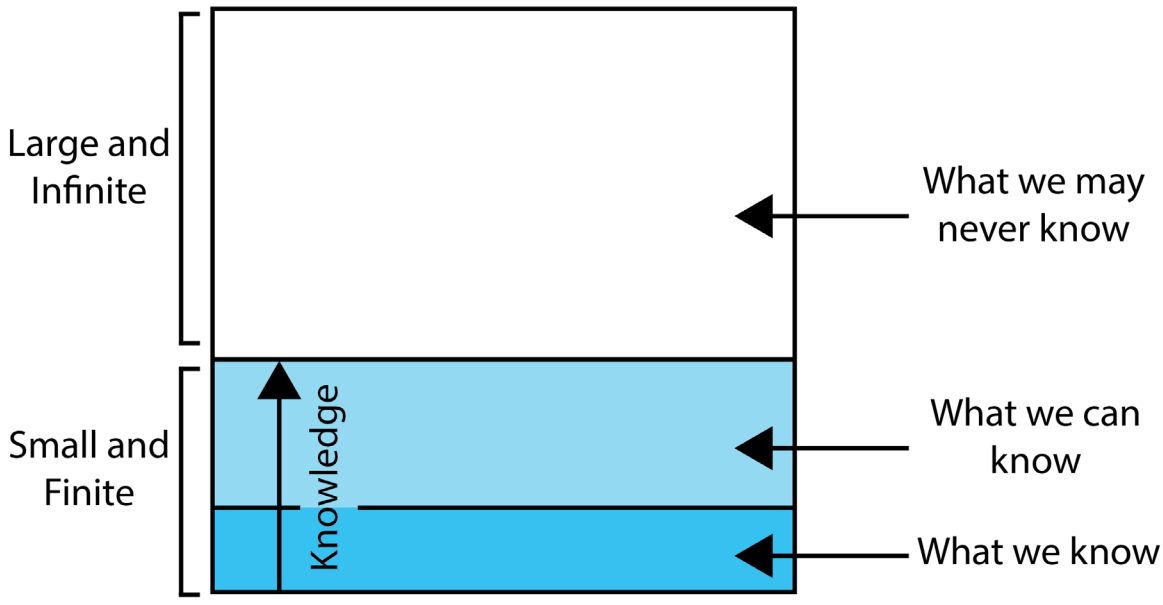

FIGURE 6-2 THE LIMITATIONS OF KNOWLEDGE INVOLVED IN SITE CHARACTERISATION, AFTER BENSON AND YUHRM (2015)

For a site characterisation to be representative of the geology of the subsurface and the data acquired, the uncertainties associated with each parameter must attempt to accurately and precisely constrain the true values as best as the data allows. Without the correct understandings of the uncertainties present, the resultant models and hence predictions derived from the models are likely to be unreliable, unrepresentative, and not capture the possible variations of the site being characterised.

6.3 Managing uncertainties and mitigating risk

A risk is defined by Sheriff (2002) as the 'probability of undesirable consequences arising from possible events'. Risks are known and can be mitigated, whereas uncertainties can only be managed and confined (due to irreducible uncertainty). It is important to note that while uncertainties in site characterisation aid in identifying key risks associated with development of the site, not all uncertainties contribute to the risk and hence matter. For mitigation of risks, the uncertainties that do affect the results need to be ascertained, and the ways in which they may interact with the possible desired outputs understood.

Throughout this thesis uncertainties within the subsurface have been captured in several ways. A stochastic approach to modelling enables the uncertainties in parametrising the geology to be captured and incorporated into the resultant predictions generated. The usage of sensitivity analyses also aided in capturing which uncertainties most significantly influence the outputs. The outputs from both these methods allow for understanding which uncertainties need to be correctly managed to reduce risk.

Quantifying the extent to which an uncertainty influences the outputs derived from models enables a value to be placed on reducing these uncertainties (Scott, Dimitrakopoulos and Brown, 2002). Placing a value on the ability to reduce uncertainty allows for a value to be placed on the information required and hence the data which can reduce this uncertainty. When there is a focus on the value of information, it allows for more efficient planning of data acquisition, as there is a known quantitative value to the resultant data being acquired.

Reducing uncertainties as described above allows for the generation of more accurate modelling and hence improved forecasting and predictions to be derived from these models.

Improved model forecasts will reduce the range in predicted value, allowing for the associated risk to be reduced.

6.4 Reproducibility, Replicability and Reliability

The reproducibility, replicability, and reliability of science has been a research philosophy embedded within the work undertaken in this thesis (Figure 6-3). As such, all initial data, interpretations, methodologies, code, models produced, and output results have been made available in the linked data repositories (Data availability). The approach of making all research undertaken reproducible, replicable, and reliable at each stage allows for researchers in the future to re-use, re-run and learn from successes and failures of those before them. This approach also enables more in-depth accountability and verification of predictions within geoscience allowing for 'better' and more robust science (Steventon *et al.*, 2022).

With the aim of making sure all research was reproducible, replicable, and reliable at the start of the thesis, there was a raised awareness for literature and project reports within the geophysical and geoscientific community not meeting acceptable standards. All too often geo-scientific literature results are presented without details of the input data that has been used or excluding detailed enough methodology to repeat the study (Ireland *et al.*, 2023). Without both input and output data being provided or suitable methodologies given, it is impossible to reproduce the results shown or allow for quantitative comparisons with other studies. Quantitative comparisons between studies that have used different data sets allows for the validation of results and shows that each study is both generalisable or replicable (The Turing Way, 2022). If the outputs are such that the results between two studies are not agreeable, the use of both input data and a comprehensive methodology allows for ease in locating the source of the differences. This allows for further understanding and learning from the each study.

However, there are areas within geoscience in which reproducibility, replicability, and reliability can be difficult to implement, for example, interpretation of data for inclusion within geological models. Within this thesis discrete features within seismic and well data are the most relevant example. While providing interpretations of discrete features for input into geological models (such as a river channel or faults) allows for subsequent analysis to be undertaken in a reproducible manner, it does not account for the uncertainty within the

interpretation (Alcalde and Bond, 2022). The inherent subjective nature of seismic interpretation, in that no pick is necessarily the correct one, leads to further uncertainty within the final interpretation datasets (Alcalde and Bond, 2022). While the exact interpretation of the feature may differ, interpretations can agree on the underlying geological features that are present and still increase uncertainty. However, disagreements can occur when the interpretations of identified discrete features differ. Such disagreements can occur in all environments, however, can be especially prevalent where pre-existing and or long-standing interpretations may be challenged, or in environments in which pre-existing literature does not exist, and existing biases are used (Alcalde, Bond and Randle, 2017; Alcalde and Bond, 2022). This difficulty in reproducibility, replicability, and reliability of discrete features from seismic data is countered by the relative ease in the incorporation of property-based features in geological models where a range of values can be implemented within a geological model and be accounted for stochastically. Property based interpretations allow for a direct way to incorporate uncertainty within a model and hence prediction, whereas the discrete nature of geological features makes it more difficult to implement the implication of a range of interpretations. The issues relating to reproducibility, replicability, and reliability in interpretation is further evidence as to why the methodology behind the interpretations and interpretations themselves should be supplied with scientific literature.

Within this thesis commercially licensed software packages such as SLB's Petrel and Techlog were used for both data interpretation, manipulation and analysis. Unfortunately, commercial software packages often have several negatives associated with their use, such as not detailing the exact methodology used in data processing or analysis, impeding reproducibility, replicability, and reliability, or, the lack of flexibility within the workflows for use in new research areas. Not knowing exactly how the data has been manipulated by the software package, means that it cannot fully be reported in literature, apart from stating what process was used within that specific licensed software package. This lack of transparency can also cause issues for governmental operations, where transparency is key and commercial software packages are the only viable method to undertake certain analysis. The lack of flexibility from such packages originates from the need for well-established workflows within industry and relative lack of demand for flexibility or need to deviate and research new workflows. A possible way to alleviate the understanding behind processes within these

software packages would be to standardize common processes or workflows undertaken within geoscience, however, this would rely upon the collaboration from within industry, which, when little monetary incentive is given, is unlikely. Another alternative maybe to promote the use of opensource software alternatives, such as QGIS instead of the ESRI suite of software, however changing software packages within industry can be slow and costly.

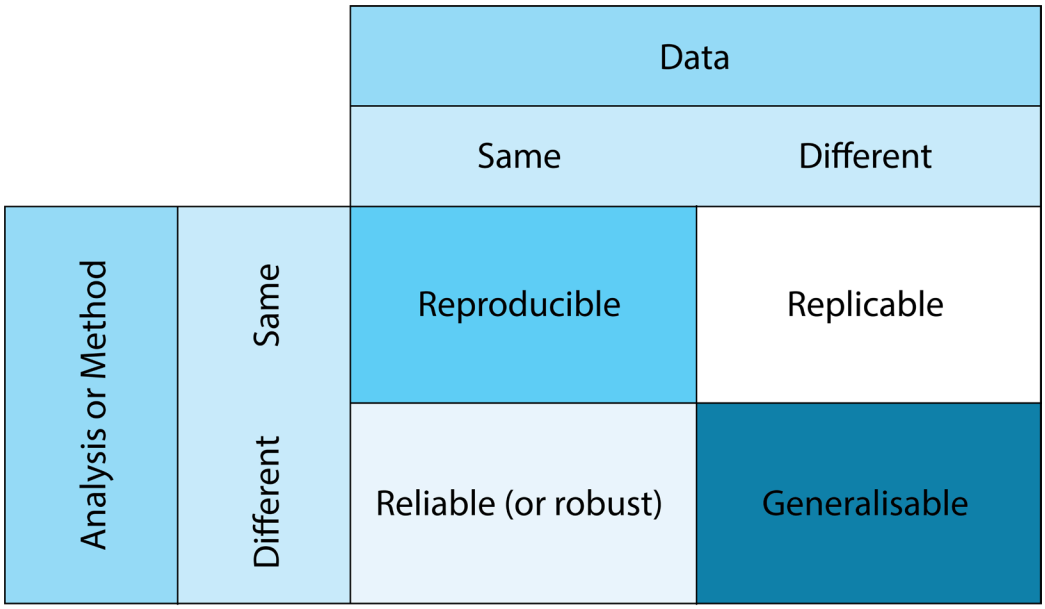

FIGURE 6-3 REPRODUCIBILITY, REPLICABILITY RELIABILITY, AND GENERALISABLE DEFINITION MATRIX CONSIDERING DATA AND METHOD USED (IRELAND ET AL., 2023)

Making all data used and generated within a study accessible is as important as providing a comprehensive methodology. Often when initial data and results are provided in literature the interpretations of the data and models used to derive the predictions and results are not given. Providing both the interpretations of the data and models is as important as providing the initial data, as these allow for a more comprehensive understanding of how a study reaches its conclusions, helping to understanding the conceptual bias present. Interpretations of data, especially in geoscience are subject to large levels of variability dependent on the individual undertaking the interpretation and the software package used for interpretation (Bond *et al.*, 2007). Models built around this interpretation data will hence inherit the unique attributes gained from data interpretation. Providing both interpretations and models allows

for every stage of the research (Figure 6-4) to be understood and a clear pathway of how the results were manipulated to compute the final outputs. Without supplying the models and predictions, providing both the initial data inputs and outputs becomes redundant.

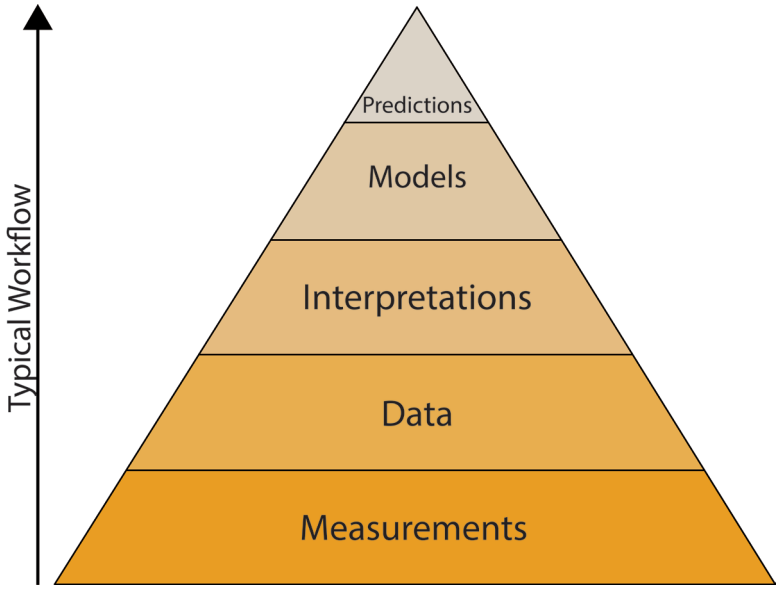

FIGURE 6-4 PYRAMID OF KNOWLEDGE, MODIFIED FROM JENNEX (2017)

6.5 Future Work

Building upon the findings in this thesis future work should focus on the following areas: 3D seismic inversion for rock properties, integration of techno-economic data for viable salt cavern placement, exploration of further monitoring techniques for carbon capture sites, and developing a framework for capturing uncertainty for subsurface energy projects. Below are further details of how this would expand on the findings presented within this thesis;

Inversion of 3D seismic datasets for rock properties. The process of seismic inversion aims to reconstruct a quantitative rock properties model from seismic measurements. The model will quantitively represent the property inverted for in a spatially variable way (Pendrel, 2001; Teixeira, Lupinacci and Maul, 2020; Wang, 2016). For salt layers and bodies the possibility to invert 3D seismic data to solubility or lithology properties would allow for more robust interpretation on internal structural heterogeneity mapping (Chapter 3) or greater control on

viable salt cavern location placement (Chapter 4). Similar techniques have previously been used on evaporite formations, for example inverting of seismic data for evaporite lithology in Teixeira, Lupinacci and Maul (2020). Inverting a 3D volume for each of the elastic properties used within the Gassmann equations would allow for full in situ 3D modelling of the change in seismic responses from fluid substitution. Previous studies have successfully undertaken the inverting of seismic data for elastic properties, for example, Teixeira and Lupinacci (2019), Cyz and Azevedo (2020), and He *et al.* (2020).

The developed workflow for hydrogen capacity and salt cavern placement locations within the Southern North Sea (Chapter 4) concentrated on constraining geological uncertainty, however, it did not incorporate any techno-economic aspects within the tool. Further work could help in incorporating the techno-economic aspects within the workflow, such that it can act as a more in-depth decision support tool for cavern cluster developments. Literature that models energy storage and energy systems, such as Sunny, Mac Dowell and Shah (2020) and Samsatli and Samsatli (2019) could incorporate the developed workflow and tools or outputs provided for better and more integrated energy systems modelling. Integration of the workflow would also allow for CAPEX and OPEX data to be calculated and incorporated into larger energy system design models. This would prove valuable for policy holders, stakeholders and those responsible for planning large-scale energy systems which require storage.

I discuss alternatives for the monitoring techniques and the requirements of a subsurface gas storage site in Chapter 5. There remains a gap within the literature about what methodologies or techniques are the most cost-effective and reliable for monitoring subsurface plume migration. While 4D seismic is a valid methodology which has proven to be able to monitor plume migration (elastic properties dependent (Chapter 5), the cost and deployment issues (other surface infrastructure e.g. windfarms) may make this method non-viable for monitoring or require new methodologies of 4D seismic to be implemented . Further studies for other seismic techniques on subsurface monitoring may prove to be beneficial. Methodologies such as VP/VS monitoring through passive seismic, point-to-point seismic, or 4D gravity subsidence are still within their infancy and receive little attention compared with 4D seismic methodologies (Payre *et al.*, 2014; Goertz-Allmann *et al.*, 2024; Lescanne *et al.*,

2011; Ruiz, Lien and Lindgard, 2020). If matured through further scientific research, they could prove to be more economically viable than the typically suggested 4D seismic approach.

Throughout this thesis several different methods have been utilised to capture uncertainties within the subsurface (Chapter 4, Chapter 5). Many different tools and methodologies utilised to capture and ascertain uncertainties within the subsurface are present and available to use from the literature. However, there is no defined framework for capturing each of the conceptual, property, and data uncertainties that are associated with a subsurface site. A framework for site characterisation would allow for a systematic and reproducible way to capture all important uncertainties within a subsurface site irrespective of the geology and data available. Creating a framework in place would be advantageous to academia, industry, and regulators.

Chapter 7. Bibliography

A

Adams, L. and Cottle, J. (1954) *Underground storage of ammonia and its recovery*. [Online].
Adamuszek, M., Tămaş, D. M., Barabasch, J. and Urai, J. L. (2021) 'Rheological stratification in impure rock salt during long-term creep: morphology, microstructure, and numerical models of multilayer folds in the Ocnele Mari salt mine, Romania', *Solid Earth,* 12(9), pp. 2041-2065.
Agile-Scientific (2012) *Polarity Cartoon*. Available at: https://subsurfwiki.org/wiki/Polarity_cartoon (Accessed: 16/02/2023.
Author (2022) *bruges 0.5.4*. Available at: https://pypi.org/project/bruges/ (Accessed: 01/06/2024).
Ahmad, N. and Baddour, R. E. (2014) 'A review of sources, effects, disposal methods, and regulations of brine into marine environments', *Ocean & Coastal Management,* 87, pp. 1-7.
Ahmed, N., Khalid, P., Ghazi, S. and Anwar, A. W. (2015) 'AVO forward modeling and attributes analysis for fluid's identification: a case study', *Acta Geodaetica et Geophysica,* 50(4), pp. 377-390.
Al-Chalabi, M. (2014) *Principles of seismic velocities and time-to-depth conversion.* Houten : EAGE Publications.
Al-Siyabi, H. A. (2005) 'Exploration history of the Ara intrasalt carbonate stringers in the South Oman Salt Basin', *GeoArabia,* 10(4), pp. 39-72.
Alcalde, J. and Bond, C. E. (2022) 'Chapter 5 - Subjective uncertainty and biases: The impact on seismic data interpretation', in Bell, R., Iacopini, D. and Vardy, M. (eds.) *Interpreting Subsurface Seismic Data*: Elsevier, pp. 103-123.
Alcalde, J., Bond, C. E. and Randle, C. H. (2017) 'Framing bias: The effect of figure presentation on seismic interpretation', *Interpretation,* 5(4), pp. T591-T605.
Allen, K. (1971) 'Eminence Dome - Natural-Gas Storage In Salt Comes of Age', *Journal of Petroleum Technology,* 24(11), pp. 1299-1301.
Allen, P. A. and Allen, J. R. (2013) *Basin Analysis: Principles and Application to Petroleum Play Assessment.* Wiley-Blackwell.
Allen, R. D., Doherty, T. J. and Thorns, R. L., Energy, U.S.D.o. (1982) *Geotechnical Factors and Guidelines for Storage of Compressed Air in Solution Mined Salt Cavities*.
Allsop, C., Yfantis, G., Passaris, E. and Edlmann, K. (2023) 'Utilizing publicly available datasets for identifying offshore salt strata and developing salt caverns for hydrogen storage', *Geological Society, London, Special Publications,* 528(1), pp. 139-169.
Alsadi, H. N. (2017) *Seismic Hydrocarbon Exploration - 2D and 3D Techniques. Advances in Oil and Gas Exploration & Production* 1 edn.: Springer Cham.
Alyafei, N. (2021) *Fundamentals of Reservoir Rock Properties - 2nd edition.* Hamad bin Khalifa University Press (HBKU Press).
Amthor, J. E., Ramseyer, K., Faulkner, T. and Lucas, P. (2005) 'Stratigraphy and sedimentology of a chert reservoir at the Precambrian-Cambrian Boundary: the Al Shomou Silicilyte, South Oman Salt Basin', *GeoArabia,* 10(2), pp. 89-122.

Anderson, W. G. (1987) 'Wettability Literature Survey Part 5: The Effects of Wettability on Relative Permeability', *Journal of Petroleum Technology,* 39(11), pp. 1453-1468.
Anston-Race, S. E. and Ganesh, D. (2020) 'The Viking Fields, Blocks 49/11d, 49/12a, 49/16a, 49/16c, 49/17a, UK North Sea', *Geological Society, London, Memoirs,* 52(1), pp. 273-287.
Archer, S. G., Alsop, G. I., Hartley, A. J., Grant, N. T. and Hodgkinson, R. (2012) 'Salt tectonics, sediments and prospectivity: an introduction', *Geological Society, London, Special Publications,* 363(1), pp. 1-6.
Arellano-Prieto, Y., Chavez-Panduro, E., Salvo Rossi, P. and Finotti, F. (2022) 'Energy Storage Solutions for Offshore Applications', *Energies,* 15(17).
Artiola, J. F., Pepper, I. L. and Brusseau, M. L. (2004) *Environmental Monitoring and Characterization.* Elsevier.
Avseth, P., Mukerji, T. and Mavko, G. (2005) *Quantitative Seismic Interpretation: Applying Rock Physics Tools to Reduce Interpretation Risk.* Cambridge University Press.

B

Bachmann, Geluk, M., Warrington, Becker-Roman, Beutler, Hagdorn, Hounslow, Nitsch, Rohling, Simon and Szulc (2010) 'Chapter 9: Triassic', in Doornenbal, H. and Stevenson, A. (eds.) *Petroleum Geological Atlas of the Southern Permian Basin Area*.
Bachu, A., Hawkes, C., Lawton, D., Pooladi-Darvish, M. and Perkins, E. (2010) *CCS SITE CHARACTERISATION CRITERIA*: IEA GREENHOUSE GAS R and D Program.
Bachu, S. (2000) 'Sequestration of CO2 in geological media: criteria and approach for site selection in response to climate change', *Energy Conversion and Management,* 41(9), pp. 953-970.
Bachu, S. (2008) 'CO2 storage in geological media: Role, means, status and barriers to deployment', *Progress in Energy and Combustion Science,* 34(2), pp. 254-273.
Bacon, M., Simm, R. and Redshaw, T. (2003) '3-D Seismic Interpretation': Cambridge University Press.
Bahmaei, Z. and Hosseini, E. (2020) 'Pore pressure prediction using seismic velocity modeling: case study, Sefid-Zakhor gas field in Southern Iran', *Exploration Geophysics*.
Bailey, J. B., Arbin, P., Daffinoti, O., Gibson, P. and Ritchie, J. S. (1993) 'Permo-Carboniferous Plays of the Silver Pit Basin', *Petroleum Geology of Northwest Europe: Proceedings of the 4th Conference*, pp. 707-715.
Baniak, G. M., Sayer, Z., Patterson, H., Gooder, R., Laing, N. and Love, A. (2020) 'The Mungo Field, Blocks 22/20a and 23/16a, UK North Sea', *Geological Society, London, Memoirs,* 52(1), pp. 537-549.
Bárdossy, G. and Fodor, J. (2001) 'Traditional and New Ways to Handle Uncertainty in Geology', *Natural Resources Research,* 10(3), pp. 179-187.
Barkved, O., Bartman, B., Compani, B. and Gaiser, J. (2004) 'The many facets of multicomponent seismic data'.
Barnes, A. E. 'Handbook of Poststack Seismic Attributes': Society of Exploration Geophysicists (SEG).
Barnes, A. E. (2016) *HANDBOOK OF POSTSTACK SEISMIC ATTRIBUTES.* Society of Exploration Geophysicists.

Barnett, H. G., Ireland, M. T. and van der Land, C. (2023) 'Characterising the internal structural complexity of the Southern North Sea Zechstein Supergroup Evaporites', *Basin Research,* 35(5), pp. 1651-1673.
Batzle, M., Hofmann, R., Prasad, M., Kumar, G., Duranti, L. and Han, D. h. (2005) 'Seismic attenuation: observations and mechanisms', *SEG Technical Program Expanded Abstracts 2005 SEG Technical Program Expanded Abstracts*: Society of Exploration Geophysicists, pp. 1565-1568.
Batzle, M. and Wang, Z. (1992) 'Seismic properties of pore fluids', *GEOPHYSICS,* 57(11), pp. 1396-1408.
Bauer, S., Beyer, C., Dethlefsen, F., Dietrich, P., Duttmann, R., Ebert, M., Feeser, V., Görke, U., Köber, R., Kolditz, O., Rabbel, W., Schanz, T., Schäfer, D., Würdemann, H. and Dahmke, A. (2013) 'Impacts of the use of the geological subsurface for energy storage: an investigation concept', *Environmental Earth Sciences,* 70(8), pp. 3935-3943.
BEIS, D. o. B. E. a. I. S. (2021) *Measurement Monitoring and Verification (MMV) Plan for Endurance*
Benson, R. C. and Yuhrm, L. B. (2015) *Site Characterization in Karst and Pseudokarst Terraines: Practical Strategies and Technology for Practicing Engineers, Hydrologists and Geologists.* Springer.
Bentham, M. S., Green, A. and Gammer, D. (2013) 'The Occurrence of Faults in the Bunter Sandstone Formation of the UK Sector of the Southern North Sea and the Potential Impact on Storage Capacity', *Energy Procedia,* 37, pp. 5101-5109.
Bérest, P., Brouard, B., Hévin, G. and Réveillère, A. 'Tightness of Salt Caverns Used for Hydrogen Storage'. *55th U.S. Rock Mechanics/Geomechanics Symposium*. ARMA-2021-1616.
Bilgili, M., Yasar, A. and Simsek, E. (2011) 'Offshore wind power development in Europe and its comparison with onshore counterpart', *Renewable and Sustainable Energy Reviews,* 15(2), pp. 905-915.
Blaich, O. A., Tsikalas, F. and Faleide, J. I. (2008) 'Northeastern Brazilian margin: Regional tectonic evolution based on integrated analysis of seismic reflection and potential field data and modelling', *Tectonophysics,* 458(1-4), pp. 51-67.
Blow, R. A. and Hardman, M. (2022) 'Calder Field appraisal well 110/7a-8, East Irish Sea Basin', *Geological Society, London, Special Publications,* 124(1), pp. 387-397.
Boggs, S. (2011) *Principles of Sedimentology and Stratigraphy,.* 5 edn.
Bokulich, A. (2021) 'Taming the tyranny of scales: models and scale in the geosciences', *Synthese,* 199(5), pp. 14167-14199.
Bond, C. E., Gibbs, A. D., Shipton, Z. K. and Jones, S. (2007) 'What do you think this is?``Conceptual uncertainty''in geoscience interpretation', *GSA today,* 17(11), pp. 4.
Bordenave, M. L. and Hegre, J. A. (2010) 'Current distribution of oil and gas fields in the Zagros Fold Belt of Iran and contiguous offshore as the result of the petroleum systems', *Geological Society, London, Special Publications,* 330(1), pp. 291-353.
Bourke, L., Delfiner, P., Felt, T., Grace, M., Luthi, S., Serra, O. and Standen, E. 1989. Using formation Microscanner images: The (Schlumberger) Technical Review.
Box, G. E. P. (1976) 'Science and Statistics', *Journal of the American Statistical Association,* 71(356), pp. 791-799.
Brook, M., Shaw, K., Vincent, C. and Holloway, S. (2003) *Gestco case study 2a-1: Storage Potential of the Bunter Sandstone in the UK sector of the southern North Sea and the adjacent onshore area of Eastern England*: British Geological Survey.

Burliga, S. (1996) 'Kinematics within the Kłodawa salt diapir, central Poland', *Geological Society, London, Special Publications,* 100(1), pp. 11-21.
Butler, R. W. H., Maniscalco, R., Sturiale, G. and Grasso, M. (2015) 'Stratigraphic variations control deformation patterns in evaporite basins: Messinian examples, onshore and offshore Sicily (Italy)', *Journal of the Geological Society,* 172(1), pp. 113-124.

C

Caglayan, D. G., Weber, N., Heinrichs, H. U., Linßen, J., Robinius, M., Kukla, P. A. and Stolten, D. (2020) 'Technical potential of salt caverns for hydrogen storage in Europe', *International Journal of Hydrogen Energy,* 45(11), pp. 6793-6805.
Calado, G. and Castro, R. (2021) 'Hydrogen Production from Offshore Wind Parks: Current Situation and Future Perspectives', *Applied Sciences,* 11(12).
Cameron, T. D. J. (1992) *Geology of the southern North Sea (POD).* BGS.
Cárdenas, B., Swinfen-Styles, L., Rouse, J., Hoskin, A., Xu, W. and Garvey, S. D. (2021) 'Energy storage capacity vs. renewable penetration: A study for the UK', *Renewable Energy,* 171, pp. 849-867.
Carneiro, J. F., Matos, C. R. and van Gessel, S. (2019) 'Opportunities for large-scale energy storage in geological formations in mainland Portugal', *Renewable and Sustainable Energy Reviews,* 99, pp. 201-211.
Carpentier, S., Boullenger, B. and Barros, E. (2021) 'CCS Monitoring by Inversion of Reservoir Pressure and Saturation Changes from Timelapse AVO Differences and Time-Shifts', *82nd EAGE Annual Conference & Exhibition*.
Cartwright, J., Jackson, M., Dooley, T. and Higgins, S. (2012) 'Strain partitioning in gravity-driven shortening of a thick, multilayered evaporite sequence', *Geological Society, London, Special Publications,* 363(1), pp. 449-470.
Cartwright, J., Stewart, S. and Clark, J. (2001) 'Salt dissolution and salt-related deformation of the Forth Approaches Basin, UK North Sea', *Marine and Petroleum Geology,* 18(6), pp. 757-778.
Castagna, J., Batzle, M., Kan, T. and Backus, M. (1993) 'Rock physics—The link between rock properties and AVO response', *Offset-dependent reflectivity—Theory and practice of AVO analysis: SEG,* 8, pp. 135-171.
Centrica (2023) *Centrica bolsters UK's energy security by doubling Rough storage capacity*. Available at: https://www.centrica.com/media-centre/news/2023/centrica-bolsters-uk-s-energy-security-by-doubling-rough-storage-capacity/ (Accessed: 27/09/2023 2023).
Chadwick, R. A., Arts, R. and Eiken, O. (2005) '4D seismic quantification of a growing CO2 plume at Sleipner, North Sea', *Geological Society, London, Petroleum Geology Conference Series,* 6(1), pp. 1385-1399.
Chadwick, R. A., Kirby, G. A. and Baily, H. E. (1994) 'The post-Triassic structural evolution of north-west England and adjacent parts of the East Irish Sea', *Proceedings of the Yorkshire Geological Society,* 50(1), pp. 91-102.
Chen, X.-S., Li, Y.-P., Jiang, Y.-L., Liu, Y.-X. and Zhang, T. (2022) 'Theoretical research on gas seepage in the formations surrounding bedded gas storage salt cavern', *Petroleum Science,* 19(4), pp. 1766-1778.

Chen, X., Li, Y., Liu, W., Ma, H., Ma, J., Shi, X. and Yang, C. (2018) 'Study on Sealing Failure of Wellbore in Bedded Salt Cavern Gas Storage', *Rock Mechanics and Rock Engineering,* 52(1), pp. 215-228.
Chopra, S. and Castagna, J. (2014) 'Chapter 4: Zoeppritz Equations and their Approximations', *AVO*: Tulsa, Oklahoma : Society of Exploration Geophysicists.
Chopra, S., Castagna, J., Xu, Y. and Tonn, R. (2007) 'Thin‐bed reflectivity inversion and seismic interpretation', *SEG Technical Program Expanded Abstracts 2014*.
Chopra, S. and Marfurt, K. (2005) 'Seismic attributes — A historical perspective', *Geophysics*.
Clark, J. A., Stewart, S. A. and Cartwright, J. A. (1998) 'Evolution of the NW margin of the North Permian Basin, UK North Sea', *Journal of the Geological Society,* 155, pp. 663-676.
United Kingdom, *The Continental Shelf (Designation of Areas) Order* (2013).
Costa, P. V. M., Costa, A. M., Szklo, A., Branco, D. C., Freitas, M. and Rosa, L. P. (2017) 'UGS in giant offshore salt caverns to substitute the actual Brazilian NG storage in LNG vessels', *Journal of Natural Gas Science and Engineering,* 46, pp. 451-476.
Crotogino, F., Schneider, G.-S. and Evans, D. J. (2017) 'Renewable energy storage in geological formations', *Proceedings of the Institution of Mechanical Engineers, Part A: Journal of Power and Energy,* 232(1), pp. 100-114.
Cyz, M. and Azevedo, L. (2020) 'Direct Geostatistical Seismic Amplitude Versus Angle Inversion for Shale Rock Properties', *IEEE Transactions on Geoscience and Remote Sensing,* PP, pp. 1-10.

D

Dale, M. S., Marín‐Moreno, H., Falcon‐Suarez, I. H., Grattoni, C., Bull, J. M. and McNeill, L. C. (2021) 'The Messinian Salinity Crisis as a trigger for high pore pressure development in the Western Mediterranean', *Basin Research,* 33(4), pp. 2202-2228.
Danesh, A. 1998. PVT and Phase Behaviour Of Petroleum Reservoir Fluids. Elsevier.
Darling, T. (2005) *Well Logging and Formation Evaluation.* Gulf Professional Publishing.
Davies, R., Stewart, S. A., Cartwright, J. A., Lappin, M., Johnston, R., Fraser, S. and Brown, A. (2004a) '3D Seismic Technology: Are We Realising Its Full Potential?', *Geological Society, London, Memoirs*, pp. 1 - 10.
Davies, R. J., Stewart, S. A., Cartwright, J. A., Lappin, M., Johnston, R., Fraser, S. I. and Brown, A. R. (2004b) '3D Seismic Technology: Are We Realising Its Full Potential?', *Geological Society, London, Memoirs,* 29(1), pp. 1-10.
Davison, I., Alsop, I. and Blundell, D. (1996) 'Salt tectonics: some aspects of deformation mechanics', *Geological Society, London, Special Publications,* 100(1), pp. 1-10.
Deepa, Goel, Saxena and Varadarajan 'Challenges in Merging Seismic Data (Six Vintage) at Pre-Stack Level & Time Migration of Offshore 3-D Seismic Data, Western Offshore, India: A Case Study', *Society of Petroleum Geophysicists: 9th Biennial International Confrence And Exposition on Petroleum Geophysics*.
Doornenbal, J. C., Kombrink, H., Bouroullec, R., Dalman, R. A. F., De Bruin, G., Geel, C. R., Houben, A. J. P., Jaarsma, B., Juez-Larré, J., Kortekaas, M., Mijnlieff, H. F., Nelskamp, S., Pharaoh, T. C., Ten Veen, J. H., Ter Borgh, M., Van Ojik, K., Verreussel, R. M. C. H., Verweij, J. M. and Vis, G. J. (2019) 'New insights on subsurface energy resources in the Southern North Sea Basin area', *Geological Society, London, Special Publications*.

Author (2020) *PySeisTuned2.0*. Available at: https://www.pyseistuned.com/ (Accessed: 01/06/2024).
Dowling, J. A., Rinaldi, K. Z., Ruggles, T. H., Davis, S. J., Yuan, M., Tong, F., Lewis, N. S. and Caldeira, K. (2020) 'Role of Long-Duration Energy Storage in Variable Renewable Electricity Systems', *Joule,* 4(9), pp. 1907-1928.
Dragoset, B. (2005) 'A historical reflection on reflections', *The Leading Edge,* 24(s1), pp. s46-s70.
Duffy, O., Hudec, M., Peel, F., Apps, G., Bump, A., Moscardelli, L., Dooley, T., Bhattacharya, S., Wisian, K. and Shuster, M. (2022) 'The Role of Salt Tectonics in the Energy Transition: An Overview and Future Challenges'.
Dupuy, B., C, V. A. T., Ghaderi, A., Querendez, E. and Mezyk, M. (2017) 'Constrained AVO for CO2 Storage Monitoring at Sleipner', *Energy Procedia,* 114, pp. 3927-3936.
Dvorkin, J., Gutierrez, M. and Grana, D. (2014) *Seismic Reflections of Rock Properties.* Cambridge University Press.
Dvorkin, J., Mavko, G. and Gurevich, B. (2007) 'Fluid substitution in shaley sediment using effective porosity', *Geophysics,* 72(3), pp. O1-O8.

E

Ebrom, D., Li, X., McDonald, J. and Lu, L. (1995) 'Bin spacing in land 3-D seismic surveys and horizontal resolution in time slices', *The Leading Edge,* 14(1), pp. 37-40.
Edgell, H. S. (1996) 'Salt tectonism in the Persian Gulf Basin', *Geological Society, London, Special Publications,* 100(1), pp. 129-151.
Eising, J., Brouwer, F. and Bernd, A. (2021) *Appendix: Risk analysis of worldwide salt cavern storage.* Vrije Universiteit Amsterdam.
Elam, S. D. 'First Gas after 40 Years – The Geophysical Challenges of the Saturn Gas Complex', *AAPG Annual Convention 2007*, Long Beach, Claifornia.
Electricity System Operator, Grid, N. (2023) *Future Energy Scenarios*.
Energy Technologies Institute (2013) *Hydrogen Storage and Flexible Turbine Systems WP2 Report – Hydrogen Storage*.
Erratt, D., Thomas, G. M. and Wall, G. R. T. (1999) 'The evolution of the Central North Sea Rift', *Geological Society, London, Petroleum Geology Conference series,* 5(1), pp. 63-82.
Evans, A., Strezov, V. and Evans, T. J. (2012) 'Assessment of utility energy storage options for increased renewable energy penetration', *Renewable and Sustainable Energy Reviews,* 16(6), pp. 4141-4147.
Evans, D. J. (2007) *An appraisal of Underground Gas Storage technologies and incidents, for the development of risk assessment methodology*.

Evans, D. J. and Holloway, S. (2009) 'A review of onshore UK salt deposits and their potential for underground gas storage', *Geological Society, London, Special Publications,* 313(1), pp. 39-80.

Evans, N., MacLeod, J. A., Macmillan, N., Rorison, P. and Salvador, P. (2004) 'The Banff Field, Blocks 22/27a, 29/2a, UK North Sea', *Geological Society, London, Memoirs,* 20(1), pp. 497-507.

Evans, S. L. and Jackson, C. A. L. (2021) 'Intra-salt structure and strain partitioning in layered evaporites: implications for drilling through Messinian salt in the eastern Mediterranean', *Petroleum Geoscience,* 27(4).

F

Fanchi, J. R. and Christiansen, R. L. (2016) 'PROPERTIES OF RESERVOIR FLUIDS', *Introduction to Petroleum Engineering*, pp. 45-66.
Fitch, P. J. R., Lovell, M. A., Davies, S. J., Pritchard, T. and Harvey, P. K. (2015) 'An integrated and quantitative approach to petrophysical heterogeneity', *Marine and Petroleum Geology,* 63, pp. 82-96.
François, L. L. 'Four Ways to Store Large Quantities of Hydrogen', *Abu Dhabi International Petroleum Exhibition & Conference*, Abu Dhabi, UAE, November 2021.
Fraser, S., Robinson, A., Johnson, H., Underhill, J. R. and Kadolsky, D. (2002) 'Upper Jurassic:' in Evans, D., Graham, C. and Bathurst, P. (eds.) *The Millenium Atlas: petroleum geology of the central and northern North Sea*. London: The Geological Society of London, pp. 157 - 189.
Fyfe, L.-J. C. and Underhill, J. R. (2023) 'A REGIONAL GEOLOGICAL OVERVIEW OF THE UPPER PERMIAN ZECHSTEIN SUPERGROUP (Z1 TO Z3) IN THE SW MARGIN OF THE SOUTHERN NORTH SEA AND ONSHORE EASTERN ENGLAND', *Journal of Petroleum Geology,* 46(3), pp. 223-256.

G

Gallucci, M. (2021) *The Ammonia Solution: Ammonia engines and fuel cells in cargo ships could slash their carbon emissions*: Institute of Electrical and Electronics Engineers.
Gassmann, F. (1951) 'Uber die Elastizitat Poroser Medien', *Veirteljahrsschrift der Naturforschenden Gesellschaft in Zzirich*, pp. 1 - 23.
Gast, R., Dusar, M., Breitkreuz, C., Gaupp, R., Schneider, J. W., Stemmerik, L., Geluk, M., Geißler, M., Glennie, K., Kabel, S. and Jones, N. (2010) 'Chapter 7 Rotliegend', in Doornenbal, H. and Stevenson, A. (eds.) *Petroleum Geological Atlas of the South Permian Basin Area*.
Geluk, M. (2007) 'Permian', in Wong, Batjes and Jager, d. (eds.) *Geology of the Netherlands*: Royal Netherlands Academy of Arts and Sciences, pp. 63 - 83.
Gibson-Poole, C. M., Taplin, M., Bouffin, N., Duffy, L., Sutherland, F., Cabral, A. and Ashby, D. (2024) 'Site Characterization of the Endurance CO2 Store, Southern North Sea, UK', *Geoenergy,* 0(ja), pp. geoenergy2024-012.
Giles, K. A. and Rowan, M. G. (2012) 'Concepts in halokinetic-sequence deformation and stratigraphy', *Geological Society, London, Special Publications,* 363(1), pp. 7-31.
Gillhaus, A. (2007) *Natural gas storage in salt caverns present trends in Europe* Solution Mining Research Institute.
Glennie, Higham and Stemmerik (2003) 'Chaper 8 Permian', in Evans, D., Graham, C., Armour, A. and Bathurst, P. (eds.) *The Millenium Atlas*: The Geological Society of London.
Glennie, K. W. (1998) *Petroleum Geology of the North Sea: Basic Concepts and Recent Advances.* 4 edn.: Blackwell Scoence.

Glennie, K. W. and Underhill, J. R. (1998) 'Origin, Development and Evolution of Structural Styles', *Petroleum Geology of the North Sea*, pp. 42-84.
Gluyas, J. G. and Bagudu, U. (2020) 'The Endurance CO2 storage site, Blocks 42/25 and 43/21, UK North Sea', *Geological Society, London, Memoirs,* 52(1), pp. 163-171.
Goertz-Allmann, B. P., Langet, N., Iranpour, K., Kühn, D., Baird, A., Oates, S., Rowe, C., Harvey, S., Oye, V. and Nakstad, H. (2024) 'Effective microseismic monitoring of the Quest CCS site, Alberta, Canada', *International Journal of Greenhouse Gas Control,* 133, pp. 104100.
Gough, C. and Mander, S. (2022) 'CCS industrial clusters: Building a social license to operate', *International Journal of Greenhouse Gas Control,* 119, pp. 103713.
Grant, R. J., Underhill, J. R., Hernández-Casado, J., Barker, S. M. and Jamieson, R. J. (2019) 'Upper Permian Zechstein Supergroup carbonate-evaporite platform palaeomorphology in the UK Southern North Sea', *Marine and Petroleum Geology,* 100, pp. 484-518.
Green, A. and Grammer, D. (2016) *Strategic UK CCS Storage Appraisal - WP5C - Hamilton Storage Development Plan*, ETI.
Groshong, R. H. (1999) 'Mapping Faults and Faulted Surfaces', *3-D Structural Geology: A Practical Guide to Surface and Subsurface Map Interpretation*. Berlin, Heidelberg: Springer Berlin Heidelberg, pp. 197-244.
Gunter, W. D., Bachu, S. and Benson, S. (2004) 'The role of hydrogeological and geochemical trapping in sedimentary basins for secure geological storage of carbon dioxide', *Geological Society, London, Special Publications,* 233(1), pp. 129-145.
Guşatu, L. F., Zuidema, C., Faaij, A., Martínez-Gordón, R. and Santhakumar, S. (2024) 'A framework to identify offshore spatial trade-offs in different space allocation options for Offshore Wind Farms, as part of the North Sea Offshore Grid', *Energy Reports,* 11, pp. 5874-5893.

H

Häggquist, E. and Söderholm, P. (2015) 'The economic value of geological information: Synthesis and directions for future research', *Resources Policy,* 43, pp. 91-100.
Hall, M. (2011) *The scales of geoscience*. Available at: https://agilescientific.com/blog/2011/4/7/the-scales-of-geoscience.html.
Hamada, G. M. (2006) 'Reservoir Fluids Identification Using Vp/Vs Ratio?', *Oil & Gas Science and Technology,* 59(6), pp. 649-654.
Han, C., Cader, A. and Brownless, M. (2021) 'Subsurface seismic interpretation technologies and workflows in the energy transition', *First Break,* 39(10), pp. 85-93.
Hanafi, B. R., Withjack, M. O., Durcanin, M. A. and Schlische, R. W. (2022) 'The development of the eastern Orpheus rift basin, offshore eastern Canada: A case study of the interplay between rift-related faulting and salt deposition and flow', *Marine and Petroleum Geology,* 139.
Hardwicke, T. E., Mathur, M. B., MacDonald, K., Nilsonne, G., Banks, G. C., Kidwell, M. C., Hofelich Mohr, A., Clayton, E., Yoon, E. J., Henry Tessler, M., Lenne, R. L., Altman, S., Long, B. and Frank, M. C. (2018) 'Data availability, reusability, and analytic reproducibility: evaluating the impact of a mandatory open data policy at the journal Cognition', *Royal Society Open Science,* 5(8).

Harvey, S., Hopkins, J., Kuehl, H., O'Brien, S. and Mateeva, A. (2022a) 'Quest CCS facility: Time-lapse seismic campaigns', *International Journal of Greenhouse Gas Control,* 117.
Harvey, S., Hopkins, J., Kuehl, H., O'Brien, S. and Mateeva, A. (2022b) 'Quest CCS facility: Time-lapse seismic campaigns', *International Journal of Greenhouse Gas Control,* 117, pp. 103665.
Hasan, M. and Shang, Y. (2022) 'Geophysical evaluation of geological model uncertainty for infrastructure design and groundwater assessments', *Engineering Geology,* 299, pp. 106560.
Hassanpouryouzband, A., Adie, K., Cowen, T., Thaysen, E. M., Heinemann, N., Butler, I. B., Wilkinson, M. and Edlmann, K. (2022) 'Geological Hydrogen Storage: Geochemical Reactivity of Hydrogen with Sandstone Reservoirs', *ACS Energy Letters,* 7(7), pp. 2203-2210.
He, F., Rao, Y., Wang, W. and Wang, Y. (2020) 'Prediction of hydrocarbon reservoirs within coal-bearing formations', *Journal of Geophysics and Engineering,* 17, pp. 484–492.
Heinemann, N., Alcalde, J., Miocic, J. M., Hangx, S. J. T., Kallmeyer, J., Ostertag-Henning, C., Hassanpouryouzband, A., Thaysen, E. M., Strobel, G. J., Schmidt-Hattenberger, C., Edlmann, K., Wilkinson, M., Bentham, M., Stuart Haszeldine, R., Carbonell, R. and Rudloff, A. (2021) 'Enabling large-scale hydrogen storage in porous media – the scientific challenges', *Energy & Environmental Science,* 14(2), pp. 853-864.
Heinemann, N., Booth, M. G., Haszeldine, R. S., Wilkinson, M., Scafidi, J. and Edlmann, K. (2018) 'Hydrogen storage in porous geological formations – onshore play opportunities in the midland valley (Scotland, UK)', *International Journal of Hydrogen Energy,* 43(45), pp. 20861-20874.
Herman, J. and Usher, W. (2017) 'SALib: An open-source Python library for Sensitivity Analysis', *The Journal of Open Source Software,* 2(9).
Hetényi, G., Balázs, L., Barcza, Z., Békési, E., Győri, E., Kern, A., Szabó, N. P. and Timár, G. (2022) 'The inherent uncertainty in geosciences', *Acta Geodaetica et Geophysica,* 57(3), pp. 411-418.
Hillis, R. R. and Nelson, E. J. (2005) 'In situ stresses in the North Sea and their applications: petroleum geomechanics from exploration to development', *Geological Society, London, Petroleum Geology Conference Series,* 6(1), pp. 551-564.
Hodgson, N. A., Farnsworth, J. and Fraser, A. J. (1992) 'Salt-related tectonics, sedimentation and hydrocarbon plays in the Central Graben, North Sea, UKCS', *Geological Society, London, Special Publications,* 67(1), pp. 31-63.
Holdaway, K. R. and Irving, D. H. B. (2017) *Enhance Oil and Gas Exploration with Data-Driven Geophysical and Petrophysical Models.* Wiley.
Horváth, P. L. and Schneider, G.-S. (2018) *Update of SMRI´s Compilation of Worldwide Salt Deposits and Salt Cavern Fields.*
Houlding, S., W (1994) '3D Geoscience Modeling': Springer Link.
Howard, A. S., Warrington, G., Ambrose, K. and Rees, J. G. (2008) *A formational framework for the Mercia Mudstone Group (Triassic) of England and Wales*, British Geological Survey.
Hudec, M. R. and Jackson, M. P. A. (2007) 'Terra infirma: Understanding salt tectonics', *Earth-Science Reviews,* 82(1-2), pp. 1-28.
Hunter, C. A., Penev, M. M., Reznicek, E. P., Eichman, J., Rustagi, N. and Baldwin, S. F. (2021) 'Techno-economic analysis of long-duration energy storage and flexible power generation technologies to support high-variable renewable energy grids', *Joule,* 5(8), pp. 2077-2101.
HyUnder (2013) *D3.1 - Assessment of the potential, the actors and relevant business cases for large*

scale and seasonal storage of renewable electricity by hydrogen underground storage in Europe.

I

Ireland, M., Algarabel, G., Steventon, M. and Munafò, M. (2023) 'How reproducible and reliable is geophysical research?', *Seismica,* 2(1).
Isah, A., Arif, M., Hassan, A., Mahmoud, M. and Iglauer, S. (2022) 'Fluid–rock interactions and its implications on EOR: Critical analysis, experimental techniques and knowledge gaps', *Energy Reports,* 8, pp. 6355-6395.
Iwanaga, T., Usher, W. and Herman, J. (2022) 'Toward SALib 2.0: Advancing the accessibility and interpretability of global sensitivity analyses', *Socio-Environmental Systems Modelling,* 4.

J

Jack, D. I., Jackson, A. A., Evans, D., Wingfield, R. T. R., Barnes, R. P. and Arthuer, M. J. (1995) *The geology of the Irish Sea.* London.
Jackson, C. A. L., Jackson, M. P. A., Hudec, M. R. and Rodriguez, C. (2014) 'Internal structure, kinematics, and growth of a salt wall: Insights from 3-D seismic data', *Geology,* 42(4), pp. 307-310.
Jackson, C. A. L., Jackson, M. P. A., Hudec, M. R. and Rodriguez, C. R. (2015) 'Enigmatic structures within salt walls of the Santos Basin—Part 1: Geometry and kinematics from 3D seismic reflection and well data', *Journal of Structural Geology,* 75, pp. 135-162.
Jackson, C. A. L. and Stewart, S. A. (2017) 'Composition, Tectonics, and Hydrocarbon Significance of Zechstein Supergroup Salt on the United Kingdom and Norwegian Continental Shelves: A Review', in Soto, Flinch and Tari (eds.) *Permo-Triassic Salt Provinces of Europe, North Africa and the Atlantic Margins*: Elsevier, pp. 175-201.
Jackson, D. I., Jackson, A. A., Evans, D., Wingfield, R. T. R., Barnes, R. P. and Arthuer, M. J. (1995) *The geology of the Irish Sea United Kingdom Offshore Regional Report.* British Geological Survey.
Jackson, M. P. A. and Hudec, M. R. (2017) *Salt Tectonics.* Cambridge University Press.
Jackson, O., Lawrence, S. R., Hutchinson, I. P., Stocks, A. E., Barnicoat, A. C. and Powney, M. (2024) 'Natural hydrogen: sources, systems and exploration plays', *Geoenergy,* 2(1).
Jahanbakhsh, A., Louis Potapov-Crighton, A., Mosallanezhad, A., Tohidi Kaloorazi, N. and Maroto-Valer, M. M. (2024) 'Underground hydrogen storage: A UK perspective', *Renewable and Sustainable Energy Reviews,* 189.
James, A., Baines, S. and McCollough, S. (2016a) *Strategic UK CCS Storage Appraisal - WP5A - Bunter Storage Development Plan*.
James, A., Baines, S. and McCollough, S. (2016b) *Strategic UK CCS Storage Appraisal - WP5E - Viking A Storage Development Plan*, EPI.
Jennex, M. (2017) 'Big Data, the Internet of Things, and the Revised Knowledge Pyramid', *ACM SIGMIS Database: the DATABASE for Advances in Information Systems,* 48, pp. 69-79.
Jenyon, M. K. (1989) 'Plastic Flow and Contraflow in Superposed Zechstein Salt Sequences', *Journal of Petroleum Geology,* 12(4), pp. 477-486.

Joel, W., Taner, M. T., Naum, D., Gary, M. and Jack, D. (2003) *SEISMIC ATTENUATION FOR RESERVOIR CHARACTERIZATION*. Available at: https://www.osti.gov/biblio/834365.
Johnson, Warrington and Stoker (1993) *Lithostratigraphic Nomenclature of the UK North Sea: Permian and Triassic of the Southern North Sea v. 6.* British Geological Survey.
Jones, C. E. and Blom, R. G. (2014) 'Bayou Corne, Louisiana, sinkhole: Precursory deformation measured by radar interferometry', *Geology,* 42(2), pp. 111-114.
Jones, I. F. and Davison, I. (2014) 'Seismic imaging in and around salt bodies', *Interpretation,* 2(4), pp. SL1-SL20.
Jyothi, V., Sain, K., Pandey, V. and Bhaumik, A. (2017) 'Seismic Attenuation for Characterization of Gas Hydrate Reservoir in Krishna-Godavari Basin, Eastern Indian Margin', *JOURNAL GEOLOGICAL SOCIETY OF INDIA,* 90, pp. 261-266.

K

Kaldi, J., Daniel, R., Tenthorey, E., Michael, K., Schacht, U., Nicol, A., Underschultz, J. and Backe, G. (2013) 'Containment of CO2 in CCS: Role of Caprocks and Faults', *Energy Procedia,* 37, pp. 5403-5410.
Kallweit, R. S. and Wood, L. C. (1982) 'The limits of resolution of zero-phase wavelets', *Geophysics*.
Kearey, P., Hill, I. and Brooks, M. (2013) *An Introduction to Geophysical Exploration.* 3rd edn.: Wiley-Blackwell.
Kennedy, M. (2015) *Practical petrophysics.* Amsterdam : Elsevier.
Kilkenny, M. F. and Robinson, K. M. 2018. Data quality:“Garbage in–garbage out”. SAGE Publications Sage UK: London, England.
Kim, K., Kim, D., Na, Y., Song, Y. and Wang, J. (2023) 'A review of carbon mineralization mechanism during geological CO2 storage', *Heliyon,* 9(12), pp. e23135.
King, M., Jain, A., Bhakar, R., Mathur, J. and Wang, J. (2021) 'Overview of current compressed air energy storage projects and analysis of the potential underground storage capacity in India and the UK', *Renewable and Sustainable Energy Reviews,* 139.
Kirk, K. L. (2005) *Potential for storage of carbon dioxide in the rocks beneath the East Irish Sea*: British Geological Survey (CR/05/127N.
Knipe, R. J., Cowan, G. and Balendran, V. S. (1993) 'The tectonic history of the East Irish Sea Basin with reference to the Morecambe Fields', *Geological Society, London, Petroleum Geology Conference Series,* 4(1), pp. 857-866.
Koson, S., Chenrai, P. and Choowong, M. (2021) 'Seismic Attributes and Their Applications in Seismic Geomorphology', *Bulletin of Earth Sciences of Thailand,* 6(1), pp. 1-9.
Krevor, S., de Coninck, H., Gasda, S. E., Ghaleigh, N. S., de Gooyert, V., Hajibeygi, H., Juanes, R., Neufeld, J., Roberts, J. J. and Swennenhuis, F. (2023) 'Subsurface carbon dioxide and hydrogen storage for a sustainable energy future', *Nature Reviews Earth & Environment,* 4(2), pp. 102-118.
Kueppers, M., Paredes Pineda, S. N., Metzger, M., Huber, M., Paulus, S., Heger, H. J. and Niessen, S. (2021) 'Decarbonization pathways of worldwide energy systems – Definition and modeling of archetypes', *Applied Energy,* 285.

L

Landinger, H. and Crotogino, F. 'The role of large-scale hydrogen storage for future renewable energy utilisation'. *Second International Renewable Energy Storage Conference (IRES II)*.
Leachman, J. W., Jacobsen, R. T., Penoncello, S. G. and Lemmon, E. W. (2009) 'Fundamental Equations of State for Parahydrogen, Normal Hydrogen, and Orthohydrogen', *Journal of Physical and Chemical Reference Data,* 38(3), pp. 721-748.
Leith, W. (2000) 'Geologic and engineering constraints on the feasibility of clandestine nuclear testing by decoupling in large underground cavities'.
Lescanne, M., Hy-Billiot, J., Aimard, N. and Prinet, C. (2011) 'The site monitoring of the Lacq industrial CCS reference project', *Energy Procedia,* 4, pp. 3518-3525.
Li, Z., Wang, X., Wang, H. and Liang, R. Y. (2016) 'Quantifying stratigraphic uncertainties by stochastic simulation techniques based on Markov random field', *Engineering Geology,* 201, pp. 106-122.
Lines, L. R. and Newrick, R. T. (2004) *Fundamentals of geophysical interpretation.* Tulsa, OK: Tulsa, OK: Society of Exploration Geophysicists.
Lippolt, Hautmann and Pilot (1993) '40 Ar/39 Ar-Dating of Zechstein Potash Salts: New Constraints on the Numerical Age of the Latest Permian and the P-Tr Boundary', *EUG (European Union of Geosciences) VII, Terra Abstract*, pp. 591.
Lokhorst, A. and Wildenborg, T. (2006) 'Introduction on CO2 Geological Storage - Classification of Storage Options', *Oil & Gas Science and Technology,* 60(3), pp. 513-515.
Lonergan, L. and White, N. (1999) 'Three-Dimensional Seismic Imaging of a Dynamic Earth', *Philosophical Transactions: Mathematical, Physical and Engineering Sciences*: Royal Society, pp. 3359 - 3375.
Lord, A. s. (2009) *Overview of Geologic Storage of Natural Gas with an Emphasis on Assessing the Feasibility of Storing Hydrogen*: Sandia National Labroatories.
Lumley, D. E. and Behrens, R. A. (1998) 'Practical Issues of 4D Seismic Reservoir Monitoring: What an Engineer Needs to Know', *SPE Reservoir Evaluation & Engineering,* 1(06), pp. 528-538.
Luo, J. (1996) 'Transition Probability Approach to Statistical Analysis of Spatial Qualitative Variables in Geology', in Förster, A. and Merriam, D.F. (eds.) *Geologic Modeling and Mapping*. Boston, MA: Springer US, pp. 281-299.
Lux, K. H. (2009) 'Design of salt caverns for the storage of natural gas, crude oil and compressed air: Geomechanical aspects of construction, operation and abandonment', *Geological Society, London, Special Publications,* 313(1), pp. 93-128.

M

Ma, H., Wei, X., Shi, X., Liang, X., Bai, W. and Ge, L. (2022) 'Evaluation Methods of Salt Pillar Stability of Salt Cavern Energy Storage', *Energies,* 15(20).
MacBeth, C., Amini, H. and Izadian, S. (2020) 'Review Paper: Methods of measurement for 4D seismic post‐stack time shifts', *Geophysical Prospecting,* 68(9), pp. 2637-2664.
MacBeth, C. and Izadian, S. (2023) 'A review and analysis of errors in post-stack time-shift interpretation', *Geophysical Prospecting,* 71(8), pp. 1497-1522.

MacBeth, C., Mangriotis, M. D. and Amini, H. (2018) 'Review Paper: Post‐stack 4D seismic time‐shifts: Interpretation and evaluation', *Geophysical Prospecting,* 67(1), pp. 3-31.
Mann, C. J., Davis, J. and Herzfeld, U. (1993) 'Uncertainty in geology', *Computers in geology—25 years of progress,* 20, pp. 241-254.
Marelli, S. and Sudret, B. (2014) 'UQLab: A Framework for Uncertainty Quantification in Matlab', *Vulnerability, Uncertainty, and Risk*, pp. 2554-2563.
Massarweh, O. and Abushaikha, A. S. (2024) 'CO2 sequestration in subsurface geological formations: A review of trapping mechanisms and monitoring techniques', *Earth-Science Reviews,* 253, pp. 104793.
Mavko, G., Mukerji, T. and Dvorkin, J. (2009) *The Rock Physics Handbook:Tools for Seismic Analysis of Porous Media.* Cambridge University Press.
Maynard, J. R. and Gibson, J. P. (2001) 'Potential for subtle traps in the Permian Rotliegend of the UK Southern North Sea', *Petroleum Geoscience,* 7(3), pp. 301-314.
McNamara, J. W., DeAngelis, V., Byrne, R. H., Benson, A., Chalamala, B. R. and Masiello, R. (2022) 'Long-duration energy storage in a decarbonized future: Policy gaps, needs, and opportunities', *MRS Energy & Sustainability,* 9(2), pp. 142-170.
Menning, M. (1995) 'A Numerical Time Scale for the Permian and Triassic Periods: An Integrated Time Analysis', *The Permian of Northern Pangea*, pp. 77-97.
Metz, B., Davidson, O., Coninck, H. d., Loos, M. and Meyer, L. (2005) *Carbon Dioxide Capture and Storage*, Cambridge University Press: IPCC.
Moneron, J. (2025) 'Major heterogeneity in evaporitic depositional systems: The genesis of kilometre-scale gypsum networks in the Zechstein Basin', *Global and Planetary Change,* 246, pp. 104710.
Morton-Thompson, D. and Woods, A., M (1992) *Development Geology Reference Manual.* American Association of Petroleum Geologists.
Mousa, W. A. and Al-Shuhail, A. A. (2011) 'Static Corrections', *Processing of Seismic Reflection Data Using MATLAB™*. Cham: Springer International Publishing, pp. 55-59.
Muhammed, N. S., Haq, B., Al Shehri, D., Al-Ahmed, A., Rahman, M. M. and Zaman, E. (2022) 'A review on underground hydrogen storage: Insight into geological sites, influencing factors and future outlook', *Energy Reports,* 8, pp. 461-499.

N

Nanda, N. c. (2021) *Seismic Data Interpretation and Evaluation for Hydrocarbon Exploration and Production.*
National Institute of Standards and Technology (2023): U.S Department of Commerce.
Nediljka, G.-M. and Karolina Novak, M. (2019) 'Carbon Capture and Storage (CCS): Geological Sequestration of CO2', in Leidivan Almeida, F., Adriana Marcela, S.-O. and Junio Cota, S. (eds.) *CO2 Sequestration*. Rijeka: IntechOpen, pp. Ch. 8.
NIST Chemistry WebBook (1997) *NIST Chemistry WebBook*. NIST Standard Reference Database 69. National Institute of Standards and Technology.
Nolen‐Hoeksema, R. C. (2000) 'Modulus—porosity relations, Gassmann's equations, and the low‐frequency elastic‐wave response to fluids', *GEOPHYSICS,* 65(5), pp. 1355-1363.

North Sea Transition Authority (2022) *Gas storage and unloading*. Available at: https://www.nstauthority.co.uk/regulatory-information/gas-storage-and-unloading/#:~:text=Award%20of%20Gas%20Storage%20Licence%20%2D%20July%202022,in%20the%20Southern%20North%20Sea.
Nüst, D. and Pebesma, E. (2020) 'Practical Reproducibility in Geography and Geosciences', *Annals of the American Association of Geographers,* 111(5), pp. 1300-1310.

O

Ofgem (2021) 'Future Energy Scenarios 2021'.
Oil and Gas Authority (2021) *OGA Stratergy*. Available at: https://www.nstauthority.co.uk/media/7105/the-oga-strategy.pdf.
Okere, C. J., Sheng, J. J. and Ejike, C. (2024) 'Evaluating reservoir suitability for large-scale hydrogen storage: A preliminary assessment considering reservoir properties', *Energy Geoscience,* 5(4), pp. 100318.
Ozarslan, A. (2012) 'Large-scale hydrogen energy storage in salt caverns', *International Journal of Hydrogen Energy,* 37(19), pp. 14265-14277.

P

Pale Blue Dot Energy and Axis Well Technology (2016) *Strategic UK CCS Storage Appraisal - Progressing Development of the UK's Strategic Carbon Dioxide Storage Resource - A Summary of Results from the Strategic UK CO*.
Pancost, R. D., Crawford, N. and Maxwell, J. R. (2002) 'Molecular evidence for basin-scale photic zone euxinia in the Permian Zechstein Sea', *Chemical Geology,* 188(3-4), pp. 217-227.
Parkes, D., Evans, D. J., Williamson, P. and Williams, J. D. O. (2018) 'Estimating available salt volume for potential CAES development: A case study using the Northwich Halite of the Cheshire Basin', *Journal of Energy Storage,* 18, pp. 50-61.
Pasten, C. and Santamarina, C. J. (2011) 'Energy geo-storage — analysis and geomechanical implications', *KSCE Journal of Civil Engineering,* 15(4), pp. 655-667.
Patonia, A. and Poudineh, R. (2020) *Ammonia as a storage solution for future decarbonized energy systems.* OIES Paper: EL.
Patruno, S., Kombrink, H. and Archer, S. G. (2022) 'Cross-border stratigraphy of the Northern, Central and Southern North Sea: a comparative tectono-stratigraphic megasequence synthesis', *Geological Society, London, Special Publications,* 494(1), pp. 13-83.
Payre, X., Maisons, C., Marblé, A. and Thibeau, S. (2014) 'Analysis of the Passive Seismic Monitoring Performance at the Rousse CO2 Storage Demonstration Pilot', *Energy Procedia,* 63, pp. 4339-4357.
Payton Ryan, L., Fellgett, M., Clark Brett, L., Chiarella, D., Kingdon, A. and Hier-Majumder, S. (2021) 'Pore-scale assessment of subsurface carbon storage potential: implications for the UK Geoenergy Observatories project', *Petroleum Geoscience,* 27(2), pp. petgeo2020-092.
Pendrel, J. (2001) 'Seismic Inversion – The Best Tool for Reservoir Characterization', *Recorder,* 26(1).

Peryt, T., Geluk, M., Mathiesen, M., Paul, J. and Smith, K. (2010) 'Chapter 8 Zechstein', in Doornenbal, H. and Stevenson, A. (eds.) *Petroleum Geological Atlas of the South Permian Basin Area*.
Pharaoh, T., Dusar, M., Geluk, M., Kockel, F., Krawczyk, C., Krzywiec, P., Scheck-Wenderoth, M., Thybo, H., Vejbaek, O. and Van Wees, J. (2010) 'Chapter 3: Tectonic Evolution', pp. 25-58.
Phillips, O. M. (2009) *Geological Fluid Dynamics: Sub-surface Flow and Reactions.* Cambridge: Cambridge University Press.
Pichat, A. (2022) 'Stratigraphy, Paleogeography and Depositional Setting of the K–Mg Salts in the Zechstein Group of Netherlands—Implications for the Development of Salt Caverns', *Minerals,* 12(4).

Q

Qin, X., Han, D. H. and Zhao, L. (2022) 'Measurement of Grain Bulk Modulus on Sandstone Samples From the Norwegian Continental Shelf', *Journal of Geophysical Research: Solid Earth,* 127(9).

R

Raith, A., Strozyk, F., Visser, J. and Urai, J. (2016) 'Evolution of rheologically heterogeneous salt structures: a case study from the NE Netherlands', *Solid Earth,* 7(1), pp. 67-82.
Ramesh Kumar, K., Makhmutov, A., Spiers, C. J. and Hajibeygi, H. (2021) 'Geomechanical simulation of energy storage in salt formations', *Scientific Reports,* 11(1), pp. 19640.
Randen, T. (1999) 'Automatic extraction of fault surfaces from three-dimensional seismic data', *Seg Technical Program Expanded Abstracts,* 20.
Rider, M. H. and Kennedy, M. (2011) *The Geological Interpretation of Well Logs.* Rider-French.
Rosman, T., Bosnjak, M., Silber, H., Koßmann, J. and Heycke, T. (2022) 'Open science and public trust in science: Results from two studies', *Public Understanding of Science,* 31(8), pp. 1046-1062.
Rouillard, P., Bagley, G., Moseley, D., Myers, K. and Harding, A. (2020) 'UKCS exploration: 50 years and counting', *Geological Society, London, Memoirs,* 52(1), pp. 32-42.
Rowan, M. G., Urai, J. L., Fiduk, J. C. and Kukla, P. A. (2019) 'Deformation of intrasalt competent layers in different modes of salt tectonics', *Solid Earth,* 10(3), pp. 987-1013.
Ruiz, H., Lien, M. and Lindgard, J. E. (2020) '4D gravity and subsidence monitoring as cost-effective alternatives to 4D seismic', *EAGE Seabed Seismic Today: from Acquisition to Application*.

S

Salemi, H., Iglauer, S., Rezagholilou, A. and Sarmadivaleh, M. (2018) 'Laboratory measurement of Biot's coefficient and pore pressure influence on poroelastic rock behaviour', *The APPEA Journal,* 58(1), pp. 182-189.

Samsatli, S. and Samsatli, N. J. (2019) 'The role of renewable hydrogen and inter-seasonal storage in decarbonising heat – Comprehensive optimisation of future renewable energy value chains', *Applied Energy,* 233-234, pp. 854-893.
Saraiva, M., Forechi, A., Neto, J. d. O., DelRey, A. and Rauber, T. 'Data-driven Full-waveform Inversion Surrogate using Conditional Generative Adversarial Networks', *IEEE International Joint Conference on Neural Network*.
Sarg, J. F. (2001) 'The sequence stratigraphy, sedimentology, and economic importance of evaporite–carbonate transitions: a review', *Sedimentary Geology,* 140(1-2), pp. 9-34.
Scheidt, C., Li, L. and Caers, J. (2018) *Quantifying Uncertainty in Subsurface Systems. Geophysical Monograph Series*.
Author (2019) *Petrel - Guru*.
Schön, J. H. (2011) *Physical Properties of Rocks.* Elsevier.
Schulmann, K., Catalán, J. R. M., Lardeaux, J. M., Janoušek, V. and Oggiano, G. (2014) 'The Variscan orogeny: extent, timescale and the formation of the European crust', *Geological Society, London, Special Publications,* 405(1), pp. 1-6.
Schweizer, D., Blum, P. and Butscher, C. (2017) 'Uncertainty assessment in 3-D geological models of increasing complexity', *Solid Earth,* 8(2), pp. 515-530.
Scorgie, J. C., Worden, R. H., Utley, J. E. P. and Roche, I. P. (2021) 'Reservoir quality and diagenesis of Triassic sandstones and siltstones from arid fluvial and playa margin environments: A study of one of the UK's earliest producing oilfields', *Marine and Petroleum Geology,* 131.
Scott, M., Dimitrakopoulos, R. and Brown, R. P. C. (2002) 'Valuing regional geoscientific data acquisition programmes: addressing issues of quantification,uncertainty and risk', *Natural Resources Forum,* 26(1), pp. 55-68.
Sepulveda, N. A., Jenkins, J. D., Edington, A., Mallapragada, D. S. and Lester, R. K. (2021) 'The design space for long-duration energy storage in decarbonized power systems', *Nature Energy,* 6(5), pp. 506-516.
Setzmann, U. and Wagner, W. (1991) 'A New Equation of State and Tables of Thermodynamic Properties for Methane Covering the Range from the Melting Line to 625 K at Pressures up to 1000 MPa', *Journal of Physical and Chemical Reference Data,* 20(6), pp. 1061-1155.
Shan, R., Reagan, J., Castellanos, S., Kurtz, S. and Kittner, N. (2022) 'Evaluating emerging long-duration energy storage technologies', *Renewable and Sustainable Energy Reviews,* 159.
Sheriff, R. E. (2002) *Encyclopedic Dictonary of Applied Geophysics.* Society of Exploration Geophysicists.
Sheriff, R. E. and Geldart, L. P. (1995) *Exploration Seismology.* 2nd edn.: University of Houston.
Singer, L., Byerley, G. and Rose, P. (2018) 'Re-saturation targets identified from 4D seismic softening responses in the Forties Field', *Geological Society, London, Petroleum Geology Conference Series,* 8(1), pp. 473-483.
Słowakiewicz, M., Blumenberg, M., Więcław, D., Röhling, H.-G., Scheeder, G., Hindenberg, K., Leśniak, A., Idiz, E. F., Tucker, M. E., Pancost, R. D., Kotarba, M. J. and Gerling, J. P. (2018) 'Zechstein Main Dolomite oil characteristics in the Southern Permian Basin: I. Polish and German sectors', *Marine and Petroleum Geology,* 93, pp. 356-375.

Smalley, C., England William, A., Muggeridge, A., Abacioglu, Y. and Cawley, S. (2004) 'Rates of reservoir fluid mixing: implications for interpretation of fluid data', *Geological Society, London, Special Publications,* 237(1), pp. 99-113.
Smdani, G., Islam, M. R., Ahmad Yahaya, A. N. and Bin Safie, S. I. (2022) 'Performance Evaluation of Advanced Energy Storage Systems: A Review', *Energy & Environment,* 34(4), pp. 1094-1141.
Smith, D. B. (1979) 'Rapid marine transgressions and regressions of the Upper Permian Zechstein Sea', *Journal of the Geological Society,* 136(2), pp. 155-156.
Smith, N. J. P., Evans, D. J. and Andrews, I. J. (2005) *The Geology of Gas Storage in Offshore Salt Caverns*: British Geological Survey. Available at: https://itportal.ogauthority.co.uk/information/papers/BGS_Report1.pdf.
Smith, T. M., Sondergeld, C. H. and Rai, C. S. (2003) 'Gassmann fluid substitutions: A tutorial', *Geophysics,* 68(2), pp. 430-440.
Snæbjörnsdóttir, S. Ó., Sigfússon, B., Marieni, C., Goldberg, D., Gislason, S. R. and Oelkers, E. H. (2020) 'Carbon dioxide storage through mineral carbonation', *Nature Reviews Earth & Environment,* 1(2), pp. 90-102.
Soboĺ, I. (1993) 'Sensitivity estimates for nonlinear mathematical models', *Math. Model. Comput. Exp.,* 1, pp. 407.
Sobol′ , I. M. (2001) 'Global sensitivity indices for nonlinear mathematical models and their Monte Carlo estimates', *Mathematics and Computers in Simulation,* 55(1-3), pp. 271-280.
Sollie, O. K., Bernstone, C., Carpenter, M. E. and Selmer-Olsen, S. (2011) 'An early phase risk and uncertainty assessment method for CO2 geological storage sites', *Energy Procedia,* 4, pp. 4132-4139.
Span, R. and Wagner, W. (1996) 'A New Equation of State for Carbon Dioxide Covering the Fluid Region from the Triple-Point Temperature to 1100 K at Pressures up to 800 MPa', *Journal of Physical and Chemical Reference Data,* 25(6), pp. 1509-1596.
Sprecher, C. (1997) 'Geological exploration strategies and site characterisation methodologies'.
Staffell, I., Green, R., Green, T., Johnson, N. and Jansen, M. (2023) *Electric Insights*.
Steventon, M. J., Jackson, C. A. L., Hall, M., Ireland, M. T., Munafo, M. and Roberts, K. J. (2022) 'Reproducibility in Subsurface Geoscience', *Earth Science, Systems and Society,* 2.
Stewart, S. A. and Coward, M. P. (1995) 'Synthesis of salt tectonics in the southern North Sea, UK', *Marine and Petroleum Geology,* 12(5), pp. 457-475.
Stewart, S. A. and Harvey, M. J. (1998) 'Influence of salt on the structural evolution of the Channel Basin', *Geological Society, London, Special Publications,* 133, pp. 241 - 266.
Stewart, S. A., Harvey, M. J., Otto, S. C. and Weston, P. J. (1996) 'Influence of salt on fault geometry: examples from the UK salt basins', *Geological Society, London, Special Publications,* 100, pp. 172-202.
Strozyk, F. (2017) 'The Internal Structure of the Zechstein Salt and Related Drilling Risks in the Northern Netherlands'.
Strozyk, F., Reuning, L., Schweck-Wenderoth, M. and Tanner, D. C. (2017) 'Chapter 10 - The Tectonic History of the Zechstein Basin in the Netherlands and Germany', in Soto, J., Flinch, J.F. and Tari, G. (eds.) *Permo-Triassic Salt Provinces of Europe, North Africa and the Atlantic Margins*: Elsevier, pp. 221-241.
Strozyk, F., Urai, J. L., van Gent, H., de Keijzer, M. and Kukla, P. A. (2014) 'Regional variations in the structure of the Permian Zechstein 3 intrasalt stringer in the northern Netherlands:

3D seismic interpretation and implications for salt tectonic evolution', *Interpretation,* 2(4), pp. SM101-SM117.
Strozyk, F., Van Gent, H., Urai, J. L. and Kukla, P. A. (2012) '3D seismic study of complex intra-salt deformation: An example from the Upper Permian Zechstein 3 stringer, western Dutch offshore', *Geological Society, London, Special Publications,* 363(1), pp. 489-501.
Stuart, I. A. (1991) 'The Rough Gas Storage Field, Blocks 47/3d, 47/8b, UK North Sea', *Geological Society, London, Memoirs,* 14(1), pp. 477-484.
Sunny, N., Mac Dowell, N. and Shah, N. (2020) 'What is needed to deliver carbon-neutral heat using hydrogen and CCS?', *Energy & Environmental Science,* 13(11), pp. 4204-4224.
Svanberg, M., Ellis, J., Lundgren, J. and Landälv, I. (2018) 'Renewable methanol as a fuel for the shipping industry', *Renewable and Sustainable Energy Reviews,* 94, pp. 1217-1228.

T

Tan, Z., Zhang, Y., Niu, J., Wenqi Ke, G. C., Zeng, H. and Liu, L. (2021) 'Construction Progress of Deep Underground Salt Cavern Gas Storage and Challenges of its Drilling and Completion Technology', *E3S Web of Conferences,* 329.
Taner, M. T., Schuelke, J. S., O'Doherty, R. and Baysal, E. (1994) 'Seismic attributes revisited', *SEG Technical Program Expanded Abstracts*.
Tarkowski, R. and Czapowski, G. (2018) 'Salt domes in Poland – Potential sites for hydrogen storage in caverns', *International Journal of Hydrogen Energy,* 43(46), pp. 21414-21427.
Teixeira, L. and Lupinacci, W. M. (2019) 'Elastic properties of rock salt in the Santos Basin: Relations and spatial predictions', *Journal of Petroleum Science and Engineering,* 180, pp. 215-230.
Teixeira, L., Lupinacci, W. M. and Maul, A. (2020) 'Quantitative seismic-stratigraphic interpretation of the evaporite sequence in the Santos Basin', *Marine and Petroleum Geology,* 122, pp. 104690.
The Royal Society (2023) *Large-scale electricity storage policy briefing* (978-1-78252-666-7.
The Turing Way (2022) 'The Turing Way: A handbook for reproducible, ethical and collaborative research'.
Thomas, D. W. and Coward, M. P. (1996) 'Mesozoic regional tectonics and South Viking Graben formation: evidence for localized thin-skinned detachments during rift development and inversion', *Marine and Petroleum Geology,* 13(2), pp. 149-177.

U

UK Government (2012) *Open Data White Paper Unleashing the Potential*.
UK Government (2016) *Composite log (Completion log)*.
Underground Sun Storage EN 2023. Underground Sun Storage: World's first geological hydrogen storage facility goes into operation.

V

Van Dalfsen, W., Doornenbal, J. C., Dortland, S. and Gunnink, J. L. (2016) 'A comprehensive seismic velocity model for the Netherlands based on lithostratigraphic layers', *Netherlands Journal of Geosciences - Geologie en Mijnbouw,* 85(4), pp. 277-292.
Van Gent, H., Urai, J. L. and de Keijzer, M. (2011) 'The internal geometry of salt structures – A first look using 3D seismic data from the Zechstein of the Netherlands', *Journal of Structural Geology,* 33(3), pp. 292-311.
Vernik, L. (2016) *Seismic petrophysics in quantitative interpretation.* Tulsa, Oklahoma : Society of Exploration Geophysicists.

W

Waal, H. d. and Calvert, R. (2003) 'Overview of global 4D seismic implementation strategy', *Petroleum Geoscience,* 9(1), pp. 1-6.
Walsh, S. D. C., Easton, L., Wang, C. and Feitz, A. J. (2023) 'Evaluating the Economic Potential for Geological Hydrogen Storage in Australia', *Earth Science, Systems and Society,* 3.
Wandler, A., Evans, B. and Link, C. (2007) 'AVO as a fluid indicator: A physical modeling study', *GEOPHYSICS,* 72(1), pp. C9-C17.
Wang, T., Yang, C., Ma, H., Daemen, J. J. K. and Wu, H. (2015) 'Safety evaluation of gas storage caverns located close to a tectonic fault', *Journal of Natural Gas Science and Engineering,* 23, pp. 281-293.
Wang, Y. (2016) *Seismic Inversion: Theory and Applications.*
Warren, J. K. (2006) 'Evaporites: Sediments, Resources and Hydrocarbons'.
Warren, J. K. (2016) *Evaporites - A Geological Compendium.* 2 edn.: Springer Cham.
Wen, Z., Jiang, S., Song, C., Wang, Z. and He, Z. (2019) 'Basin evolution, configuration styles, and hydrocarbon accumulation of the South Atlantic conjugate margins', *Energy Exploration & Exploitation,* 37(3), pp. 992-1008.
White, R. E. and Simm, R. (2003) 'Tutorial: good practice in well ties', *First Break,* 21(10).
Widess, M. B. (1973) 'How Thin Is a Thin Bed?', *Geophysics,* 38(6), pp. 1176-1180.
Williams, J. D. O., Fellgett, M. W., Kingdon, A. and Williamson, J. P. (2015) 'In-situ stress orientations in the UK Southern North Sea: Regional trends, deviations and detachment of the post-Zechstein stress field', *Marine and Petroleum Geology,* 67, pp. 769-784.
Williams, J. D. O., Gent, C. M. A., Fellgett, M. W. and Gamboa, D. (2018) 'Impact of in situ stress and fault reactivation on seal integrity in the East Irish Sea Basin, UK', *Marine and Petroleum Geology,* 92, pp. 685-696.
Williams, J. D. O., Williamson, J. P., Parkes, D., Evans, D. J., Kirk, K. L., Sunny, N., Hough, E., Vosper, H. and Akhurst, M. C. (2022) 'Does the United Kingdom have sufficient geological storage capacity to support a hydrogen economy? Estimating the salt cavern storage potential of bedded halite formations', *Journal of Energy Storage,* 53.
Wong, T. E., De Lugt, I. R., Kuhlmann, G. and Overeem, I. (2007) 'Tertiary', in Wong, Batjes and Jager, D. (eds.) *Geology of the Netherlands*: Royal Netherlands Academy of Arts and Sciences, pp. 151 - 172.

Y

Yaliz, A. and Taylor, P. (2003) 'The Hamilton and Hamilton North Gas Fields, Block 110/13a, East Irish Sea', *Geological Society, London, Memoirs,* 20.
Yan, H., Dupuy, B., Romdhane, A. and Arntsen, B. (2018) 'CO2 saturation estimates at Sleipner (North Sea) from seismic tomography and rock physics inversion', *Geophysical Prospecting,* 67(4), pp. 1055-1071.
Yang, C., Jing, W., Daemen, J. J. K., Zhang, G. and Du, C. (2013) 'Analysis of major risks associated with hydrocarbon storage caverns in bedded salt rock', *Reliability Engineering & System Safety,* 113, pp. 94-111.
Yu, M., Wang, K. and Vredenburg, H. (2021) 'Insights into low-carbon hydrogen production methods: Green, blue and aqua hydrogen', *International Journal of Hydrogen Energy,* 46(41), pp. 21261-21273.

Z

Zanella, E. and Coward, M. P. (2003a) 'Chapter 4 Structural Framework', *The Millennium Atlas: petroleum geology of the central and northern North Sea*: The Geological Society of London.
Zanella, E. and Coward, M. P. (2003b) 'Structural framework', pp. 45-59.
Zhang, G., Liu, Y., Wang, T., Zhang, H., Wang, Z., Zhao, C. and Chen, X. (2021) 'Pillar stability of salt caverns used for gas storage considering sedimentary rhythm of the interlayers', *Journal of Energy Storage,* 43.
Zhou, J., Sun, J. and Xuening, M. (2014) 'Application of Gabor transform to amplitude spectrum matching for merging seismic surveys', *SEG Technical Program Expanded Abstracts 2014*.
Zhu, S., Shi, X., Yang, C., Li, Y., Li, H., Yang, K., Wei, X., Bai, W. and Liu, X. (2023) 'Hydrogen loss of salt cavern hydrogen storage', *Renewable Energy,* 218.
Ziegler, P. A. (1990) *Geological Atlas of Central and Western Europe.* 2nd edn.: The Hague : Shell International Petroleum Maatschappij B.V.
Ziegler, P. A. (1992a) 'North Sea rift system', *Tectonophysics,* 208(1), pp. 55-75.
Ziegler, P. A. (1992b) 'North Sea rift system', *Tectonophysics,* 208(1-3), pp. 55-75.
Zijp, M. H. A. A., Huijgen, M. A., Wilpshaar, M., Bouroullec, R. and ter Heege, J. H. (2018) *Stringers in Salt as a Drilling Risk*: TNO. Available at: https://www.nlog.nl/sites/default/files/tno_stringers_in_salt.pdf.
Zoback, M. D. (2010) *Reservoir Geomechanics.* Cambridge University Press.
Zoeppritz, K. (1919) 'VIIb. Über Reflexion und Durchgang seismischer Wellen durch Unstetigkeitsflächen', *Nachrichten von der Königlichen Gesellschaft der Wissenschaften zu Göttingen*, pp. 66-84.
Zulauf, J. and Zulauf, G. (2005) 'Coeval folding and boudinage in four dimensions', *Journal of Structural Geology,* 27(6), pp. 1061-1068.
Zulauf, J., Zulauf, G., Hammer, J. and Zanella, F. (2011) 'Tablet boudinage of an anhydrite layer in rock-salt matrix: Results from thermomechanical experiments', *Journal of Structural Geology,* 33(12), pp. 1801-1815.

Chapter 8. Appendix

8.1 Appendix – Chapter 3

Well	Deformation style	-Z3 (m)	Thickness	Synthetic? Yes/No
41/5-1	Planar and continuous	103		Y
42/13-2	Area of withdrawal	NA		N
42/13-4	Gently folded and continuous	NA		N
42/15a-3	Open folded and continuous	Na		N
42/26-1	Area of 1withdrawal	92		Y
42/27a-1	Planar and continuous	98		Y
42/28a-6	Gently folded and continuous	102		Y
42/28b-5	Chaotic reflection	100		Y
42/29-2	Gently folded and continuous	38		Y
42/30-4A	Planar and continuous	NA		Y
43/10-1	Open folded and continuous	NA		N
43/17-2	Chaotic reflection	0		Y
43/21b-5Z	Open folded and continuous	NA		N
43/23-2	Closely folded and poorly imaged	53		N
43/24-2	Closely folded and poorly imaged	8		Y
43/28a-3	NA outside study area	Na		N
43/30-1	Chaotic reflection	NA		N
43/7-1	Open folded and continuous	NA		N
44/13-1	Open folded and continuous	NA		N
44/14-1	Open folded and continuous	61		Y
44/14-2	Open folded and continuous	NA		N
44/17-1	Closely folded and poorly imaged	NA		N
44/18-1	Area of withdrawal	9		Y

44/19-2	Open folded and continuous	NA	Y
44/19a-5	Open folded and continuous	NA	N
44/21-1	Closely folded and poorly imaged	37	Y
44/21a-5	Closely folded and poorly imaged	32	Y
44/21B-8	Closely folded and poorly imaged	NA	N
44/22-5	Closely folded and poorly imaged	9	Y
44/22b-8	Closely folded and poorly imaged	NA	Y
44/24-2	Closely folded and poorly imaged	NA	N
44/24a-5	Gently folded and continuous	NA	N
44/26c-6	Closely folded and poorly imaged	29	Y
44/27-1	Closely folded and poorly imaged	10	Y
44/27-2	Closely folded and poorly imaged	100	Y
44/28-3	Closely folded and poorly imaged	7	Y
44/29-2	Chaotic reflection	NA	N
47/15-1	Gently folded and continuous	74	Y
47/3-1	Closely folded and poorly imaged	5	Y
47/4a-7	Chaotic reflection	27	Y
48/03-1	NA outside study area	NA	N
48/10-1	Chaotic reflection	40	Y
48/10b-10	Chaotic reflection	NA	N
48/10c-11	Chaotic reflection	Undifferentiated	Y
48/11-1	Open folded and continuous	NA	Y
48/11-2	Planar and continuous	90	Y
48/11b-5	Planar and continuous	NA	N
48/1-2A	Chaotic reflection	132	N
48/12b-03	Planar and continuous	66	Y
48/12e-11	Gently folded and continuous	NA	N
48/14-2	Gently folded and continuous	10	Y
48/17-1	NA outside study area	64	N
48/17a-9	Planar and continuous	62	Y
48/19A- 4	Planar and continuous	101	N

48/1a-3	Chaotic reflection	NA	N
48/20-1	Gently folded and continuous	98	Y
48/23-2	Planar and continuous	55	Y
48/25-1	Planar and continuous	44	Y
48/2b-3	Area of withdrawal	Undifferentiated	Y
48/2c-5	Area of withdrawal	NA	N
48/30-1	Planar and continuous	NA	Y
48/30-6	Planar and continuous	43	Y
48/3-2	Chaotic reflection	NA	Y
48/3a-5	Chaotic reflection	NA	N
48/6-10	Gently folded and continuous	49	Y
48/7-1	Open folded and continuous	NA	Y
49/1-1	Chaotic reflection	69	Y
49/14a-2	Area of withdrawal	NA	Y
49/16-12	Chaotic reflection	0	N
49/16-5	Gently folded and continuous	NA	Y
49/16-6	Planar and continuous	107	Y
49/17-4	Planar and continuous	115	Y
49/17-9	Planar and continuous	102	N
49/19-1	Planar and continuous	NA	Y
49/19-3	Closely folded and poorly imaged	16	Y
49/19-7	Open folded and continuous	NA	Y
49/20-2	Open folded and continuous	NA	Y
49/20a-8	Open folded and continuous	NA	N
49/20b-3	Area of withdrawal	NA	Y
49/20b-4	Gently folded and continuous	NA	Y
49/2-2	Closely folded and poorly imaged	NA	N
49/2-3	Closely folded and poorly imaged	22	Y
49/24- 2	Planar and continuous	*	Y
49/24-12	Gently folded and continuous	91	Y
49/25a-5	Planar and continuous	NA	Y

49/26- 2	Planar and continuous	44	Y
49/5-2	Closely folded and poorly imaged	NA	N
49/5-5	Closely folded and poorly imaged	101	N
49/7a-1	Chaotic reflection	31	N
49/8-1	Chaotic reflection	NA	Y
49/9-1	Closely folded and poorly imaged	NA	Y
50/16-1	Gently folded and continuous	NA	N
50/21-1	Gently folded and continuous	32	Y
53/1b-12	Planar and continuous	NA	Y
53/2-2	Gently folded and continuous	57	Y

APPENDIX 1 TABLE OF WELLS USED WITHIN CHAPTER 3 ALONG WITH DEFORMATION STYLES AND THICKNESS OF -Z3 UNIT

Domain	Original Length (m)	Current Length (m)	Shortening %
CFPI	33198	24518	26.14615338
OFAC	10170	9856	3.087512291
GFAC	12434	12199	1.88997909
PAC	11985	11884	0.842720067

APPENDIX 2 SHORTENING % OCCURRING IN DIFFERENT STRUCTURAL DEFORMATION DOMAINS INVESTIGATED.

SHORTENING WAS CALCULATED FROM 1X VERTICAL EXAGGERATION FROM DEPTH CONVERTED SEISMIC LINES

Velocity Model information: present within data repository

8.2 Appendix – Chapter 4

8.2.1 Chapter 4 Appendix Figures

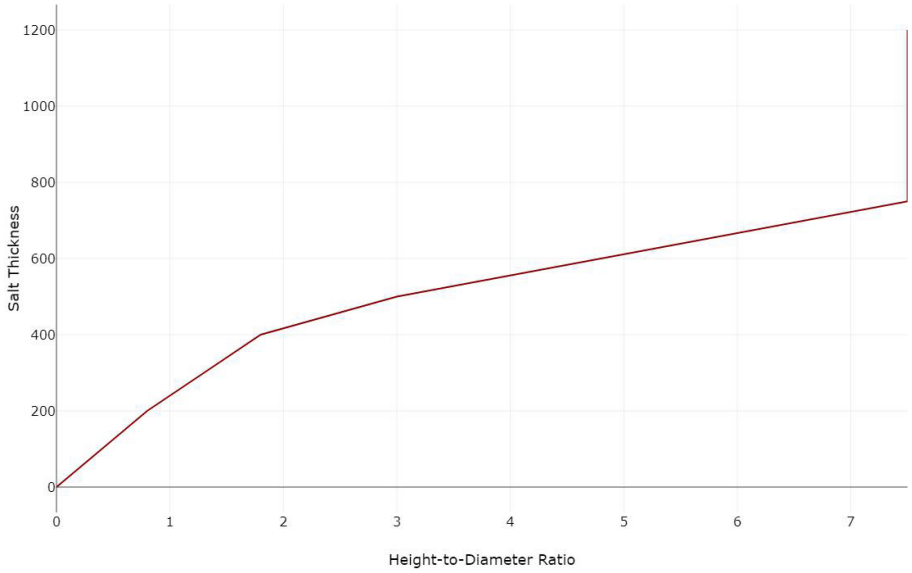

APPENDIX 3 HEIGHT-TO-DIAMETER RATIO PRE-SET RELATIONSHIP.

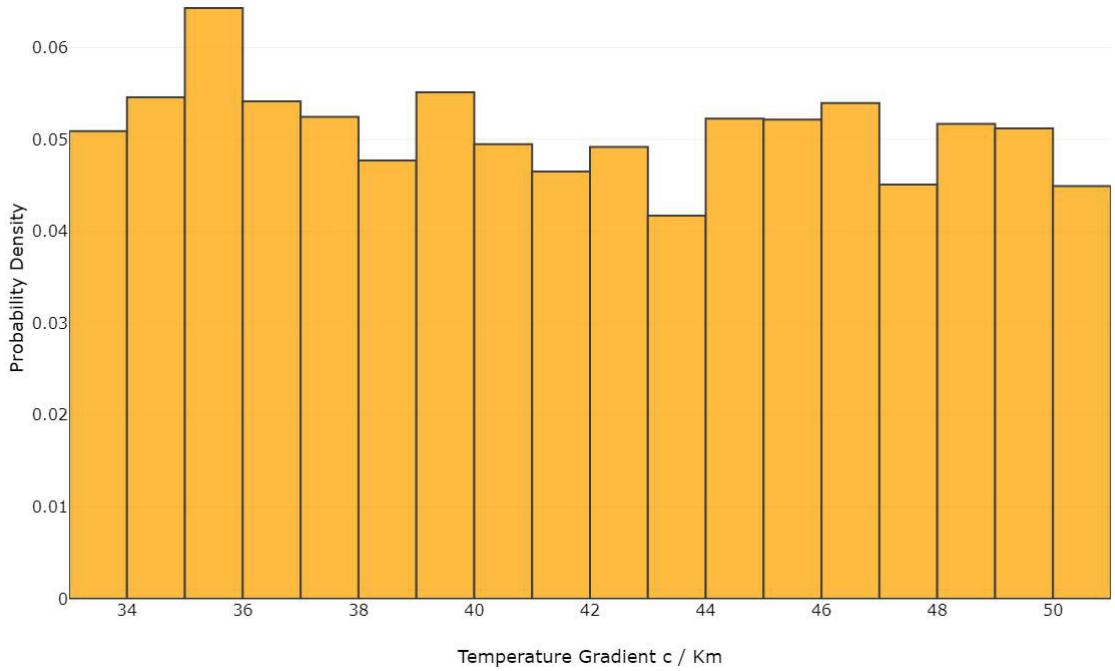

APPENDIX 4 GEOTHERMAL GRADIENT C / KM UNIFORM DISTRIBUTION FROM THE SOUTHERN NORTH SEA USED WITHIN WORKFLOW.

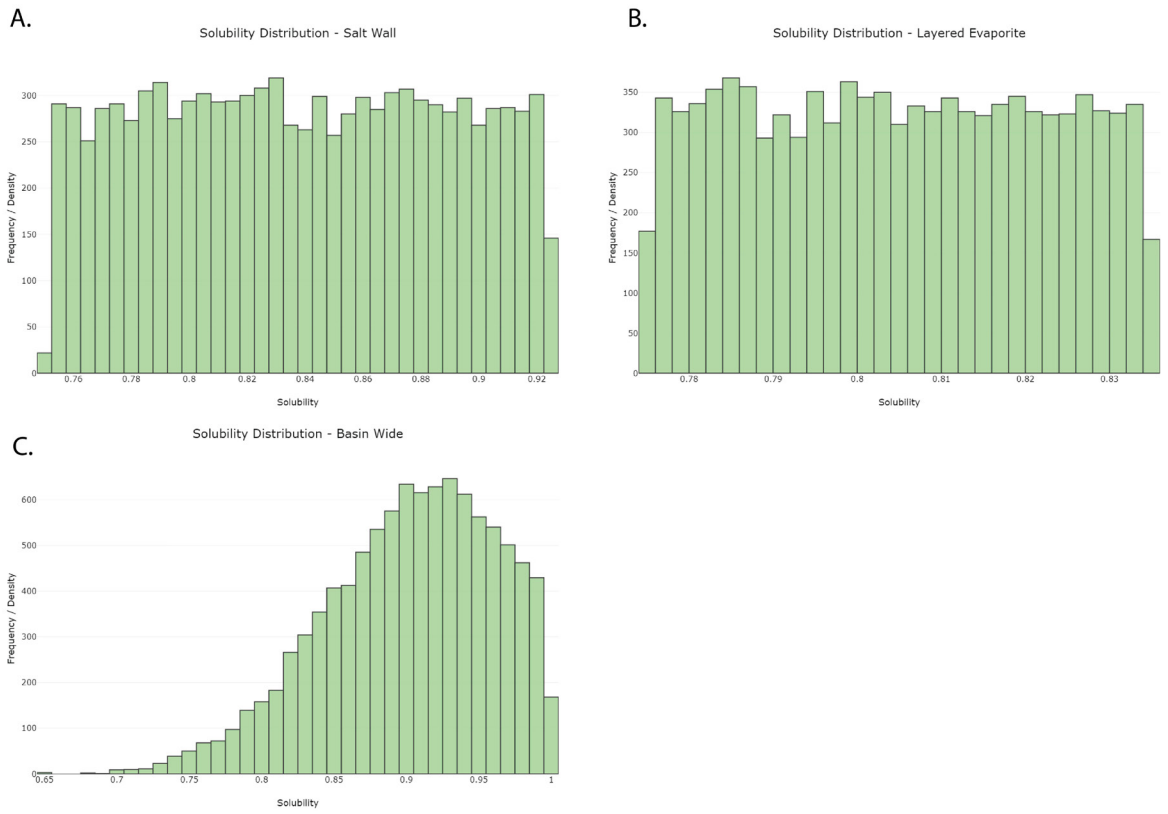

APPENDIX 5 ZECHSTEIN SOLUBILITY % DISTRIBUTION FOR THE AOI. A) DISTRIBUTION FOR UNDIFFERENTIATED SALT WITHIN THE SALT WALL AREA B) DISTRIBUTION FOR THE STASSFURT HALITE WITHIN THE LAYERED EVAPORITE AREA C) DISTRIBUTION FOR THE STASSFURT HALITE WITHIN THE BASIN WIDE AREA

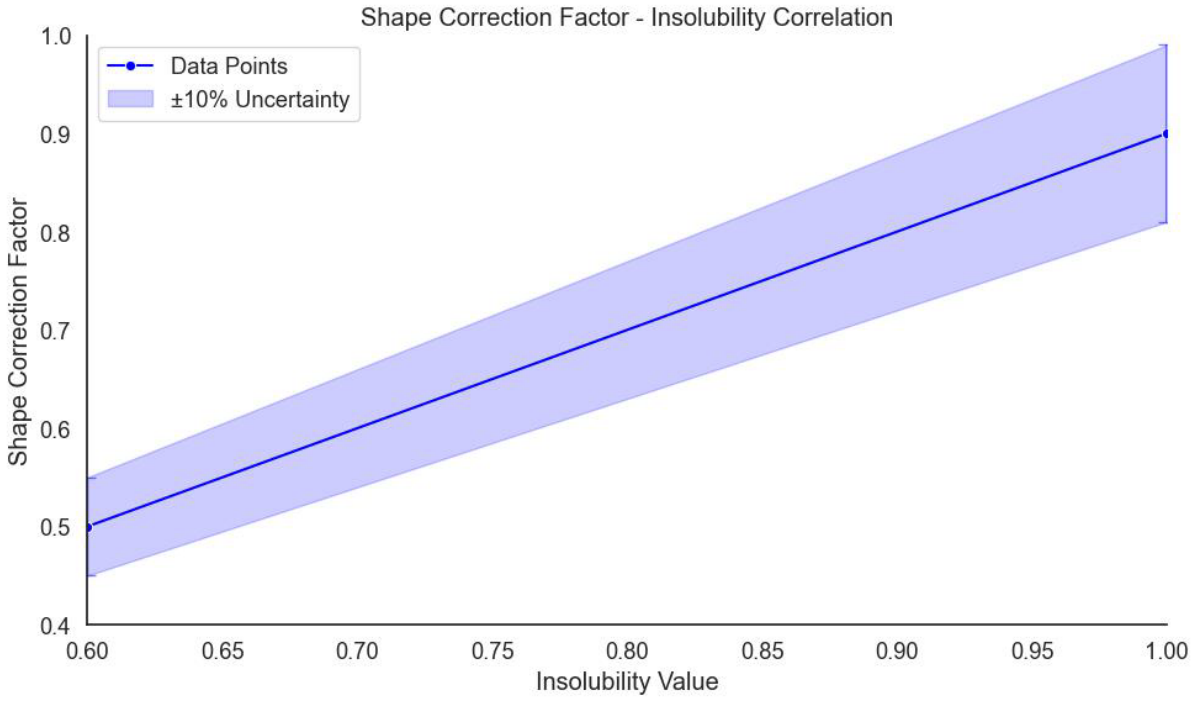

APPENDIX 6 SOLUBILITY % - SHAPE CORRECTION FACTOR RELATIONSHIP GRAPH.

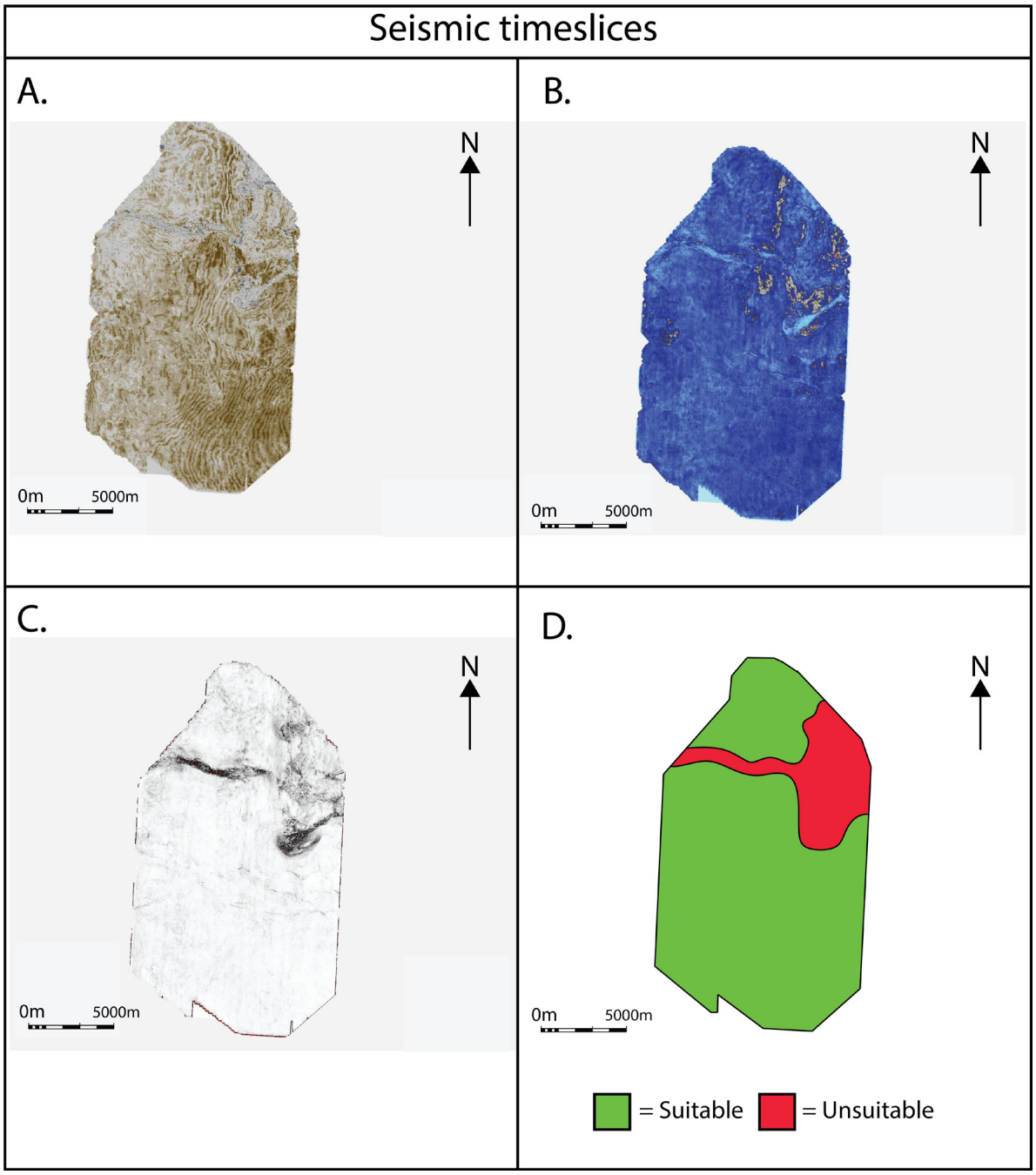

Appendix 7 Seismic attribute timeslices of the Stassfurt Halite from the Layered Evaporite area of interest for spatially mapping internal salt heterogeneities. Seismic attributes are as such A) Amplitude, B) RMS amplitude, C) Variance, D) Resultant suitability map

Variable	Value(s) Layered Evaporite / Salt Wall	Distribution type
Depth uncertainty (%)	+- 5 (SW) +- 7 (LE)	Uniform
Geothermal Gradient (°c)	32 – 52	Uniform
Insoluble Content (%)	77.5 – 83.5 (LE) 75.2 – 92.5 (SW)	Uniform
Overburden Pressure Gradient MPa/m	0.021 - 0.025	Uniform

APPENDIX 8 INPUTS FOR SOBOL SENSITIVITY ANALYSIS ON LAYERED EVAPORITE BLOCK AND SALT WALL BLOCK.

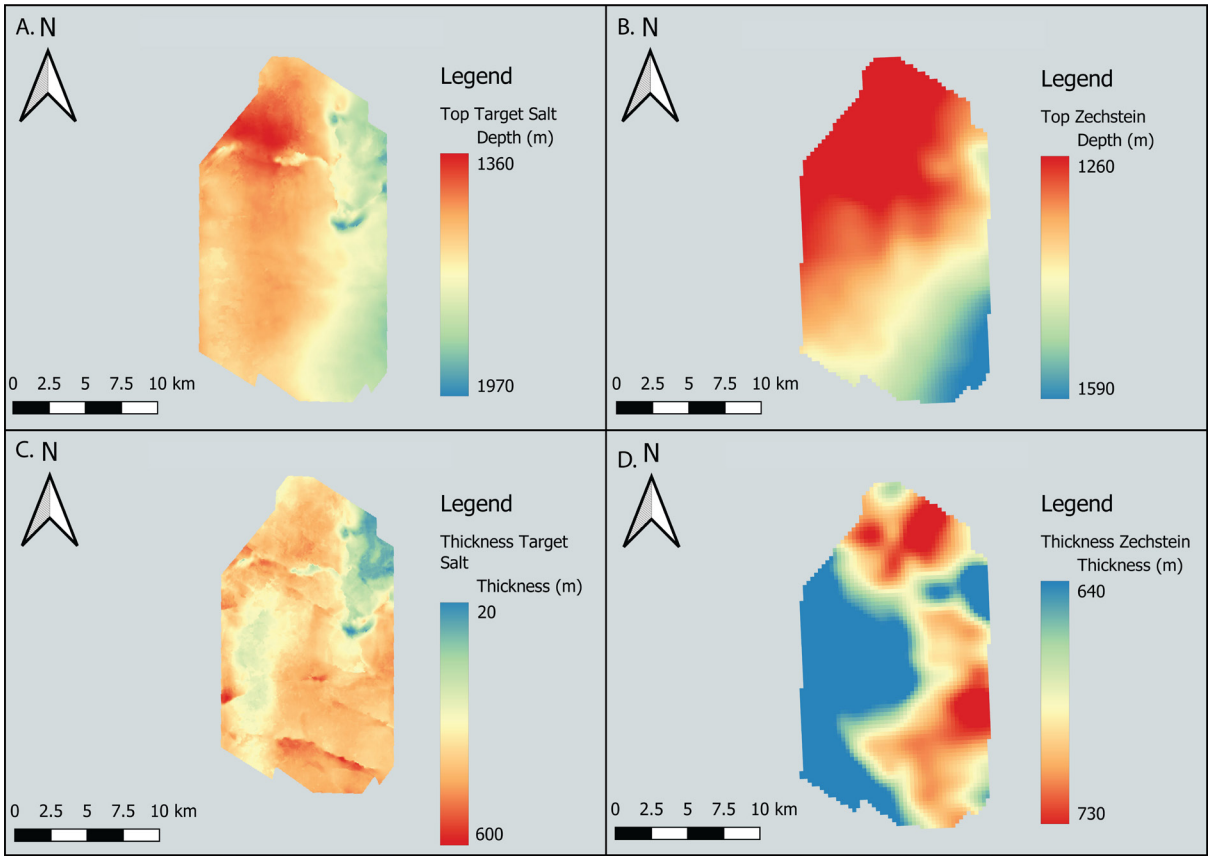

APPENDIX 9 DATA COMPARISONS BETWEEN SURFACES FROM 'BLOCK – LAYERED EVAPORITE' AOI SPECIFIC GEOLOGICAL MODELS (SECTION 4.4.1-2) BASIN WIDE DEPTH SURFACES (SECTION 4.4.3). A AND B ARE DEPTH SURFACES, A IS FOR THE TOP TARGET SALT THE TOP STASSFURT HALITE (FIGURE. 5), INTERPRETED FROM SEISMIC DATA SPECIFICALLY FOR THIS STUDY (USED IN SECTIONS 4.4.1-2), WHILE B IS THE TOP ZECHSTEIN FROM THE BASIN WIDE GEOLOGICAL MODEL CUT TO THE LAYERED EVAPORITE AREA (SECTION 4.4.3), CROSS SECTIONS ON SEISMIC DATA OF BOTH SURFACES CAN BE SEEN IN FIGURE. 11. C AND D ARE THICKNESS SURFACES, C WAS CALCULATED FROM TOP AND BASE STASSFURT HALITE INTERPRETED FROM SEISMIC DATA, D IS THE THICKNESS OF TOP AND BASE ZECHSTEIN FROM THE BASIN WIDE GEOLOGICAL MODEL.

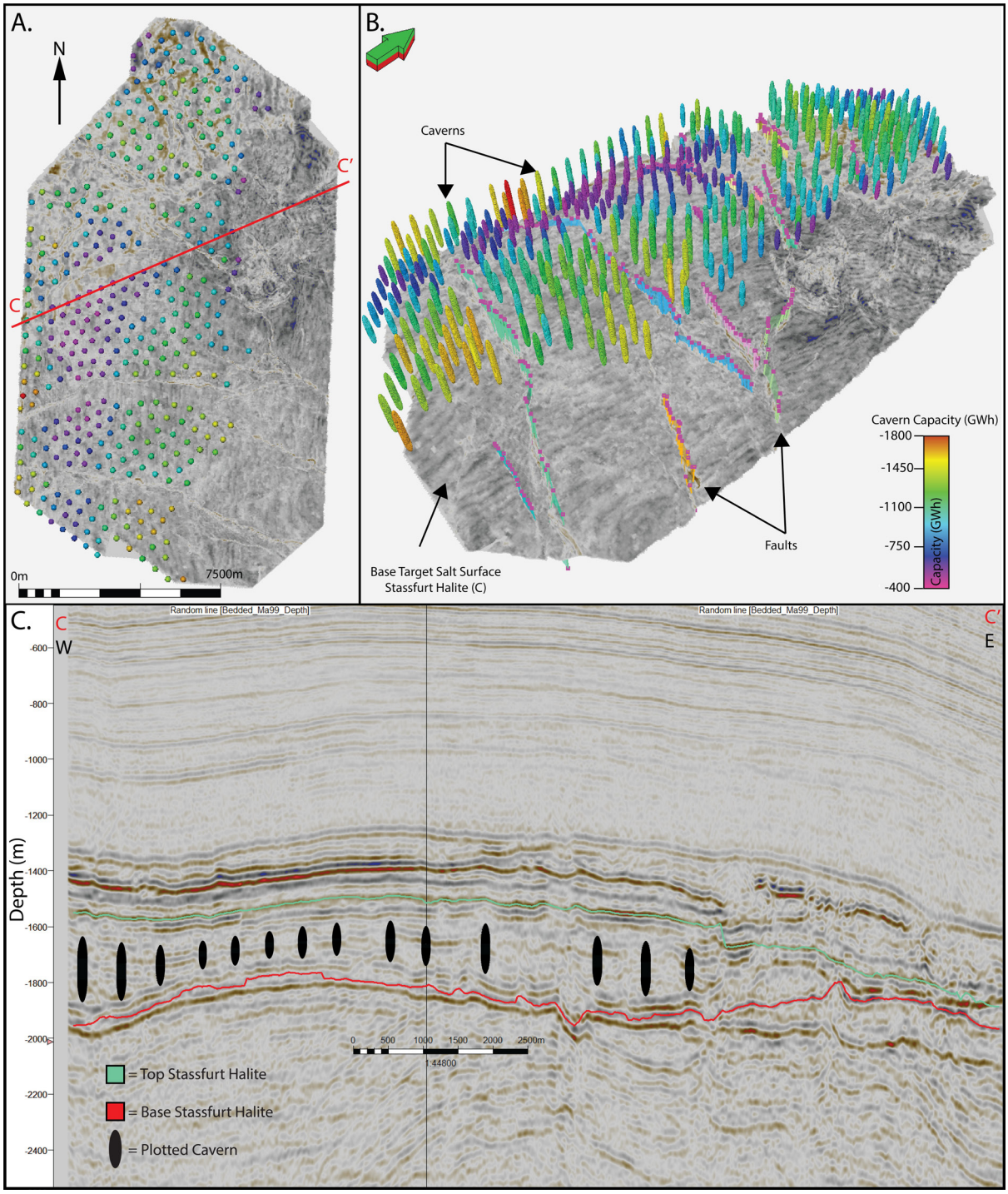

Appendix 10 Salt caverns within in 3D and 2D space plotted against seismic data (TVD). The salt caverns plotted are the 'Block - Layered Evaporite' AoI with variable caverns (Section 4.4.1). A) Shows caverns coloured for total hydrogen capacity, with the base Stassfurt halite seismic horizon probe surface. B) Shows the same as A, however the camera has been rotated to an angled view, and faults have been displayed on the 3D image, as sticks topped with pink dots. C) A 2d seismic cross-section in TVD (m), C – C' (Appendix 3, A), running west to east. Top and base Stassfurt halite reflections have been marked on in green and red respectively. Caverns have been plotted in their correct locations. Note how caverns avoid faults.

APPENDIX 9 – SYNTHETIC GRID DATA SURFACES OF VARYING DATA DENSITY (200 M – 33 M) WITH CIRCLES GENERATED USING THE SAME BUFFER PACKING FUNCTION THAT IS USED WITHIN THE CAVERN PLACEMENT WORKFLOW (SECTION. 2.1). THE DIFFERENT GRID DENSITIES AND GENERATED CIRCLES DEMONSTRATE HOW INPUT GRID DENSITY (GEOLOGICAL MODEL GRID CELL DENSITY) AFFECTS THE LOCATION AND PLACEMENT OF

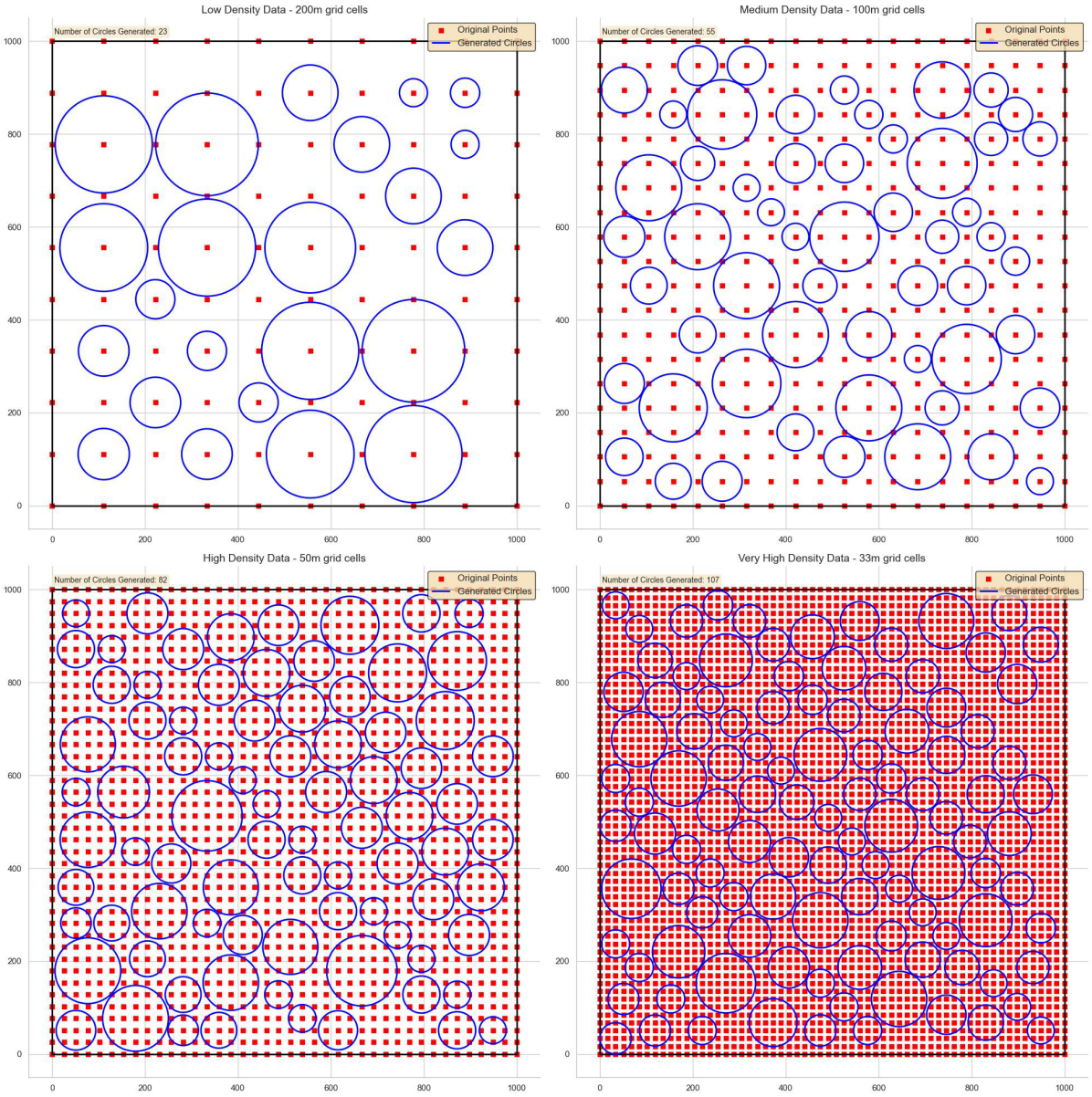

APPENDIX 11 SYNTHETIC GRID DATA SURFACES OF VARYING DATA DENSITY (200 M – 33 M) WITH CIRCLES GENERATED USING THE SAME BUFFER PACKING FUNCTION THAT IS USED WITHIN THE CAVERN PLACEMENT WORKFLOW (SECTION. 2.1). THE DIFFERENT GRID DENSITIES AND GENERATED CIRCLES DEMONSTRATE HOW INPUT GRID DENSITY (GEOLOGICAL MODEL GRID CELL DENSITY) AFFECTS THE LOCATION AND PLACEMENT OF CAVERNS.

8.2.2 Further Appendix Info

8.2.2.1 Appendix - Further Info - Best fit algorithm

The best fit algorithm initiates with the list of all viable cavern locations calculated previously in the workflow. Each viable grid cell has an associated cavern and cavern data. The algorithm iterates down the list of viable cavern locations (The spatial order being top left to top right then continuing from the row below again from left to right, finishing in the bottom right of the grid). From the viable caverns, it generates a polygon of equal radius to the required buffer radius depending on the size of the cavern. The buffer polygon is then plotted within the viable area polygon, and checks are made to see if it overlaps with another buffer polygon, if it does overlap, it is removed from the table of viable caverns and the algorithm continues onto the next cavern in the list. The algorithm iterates through every viable cavern location, discarding those that overlap with other caverns. The final product is caverns best fitting within the AOI.

8.2.2.2 Appendix - Further Info Depth Uncertainty

Depth conversion and uncertainty used the methodology laid out in (Barnett, Ireland and van der Land, 2023). See data repo for further information.

8.2.2.3 Appendix - Equation Sheet

Equation A: $Height - to - diameter\ ratio = Available\ Salt\ Thickness * Reference\ Table$

Equation B: $Max\ Cavern\ Height = \frac{Available\ Salt\ Thickness}{\frac{1.95}{Height-to-Diameter\ Ratio}}$

Equation C: $Cavern\ Diameter = \frac{Max\ Cavern\ height}{Height-to-Diameter\ Ratio}$

Equation D: $Cavern\ Hanging\ Wall = 0.2 * Cavern\ Diameter$ *(Caglayan et al., 2020)*

Equation E: $Cavern\ Footwall = 0.75 * Cavern\ Diameter$ *(Caglayan et al., 2020)*

Equation F: $Mid\ Cavern\ Depth = Salt\ Depth + Hanging\ Wall\ Thickness + \frac{Max\ Cavern\ Height}{2}$

Equation G: $Cavern\ Buffer\ (from\ cavern\ midpoint) = 2 * Cavern\ Diameter$ *(Caglayan et al., 2020)*

Equation H: $Cavern\ Volume\ (Ellipsoid) = \frac{4}{3} * \pi r^2 (Cavern\ Height/2)$

Equation I: $Lithostatic\ 1D = Lithostatic\ pressure\ gradient * (Cavern\ Mid\ point\ depth - Seabed\ Depth) + (Water\ Pressure\ Gradient * (Seabed\ Depth - Datum))$ *(Rider and Kennedy, 2011)*

*Equation J: Actual Cavern Volume = Cavern Volume * Insoluble Content * Shape Correction Factor*

Equation K: $Total\ AOI\ H_2\ Capacity = \sum H_2\ Capacity\ Caverns$

Equation L: $Total\ Cluster\ H_2\ Capacity = \sum H_2\ Capacity\ Caverns\ \ In\ Cluster\ Concept\ Area$

8.3 Appendix – Chapter 5

Depth	Core	Calculated	Difference	% Difference
4799	0.265	0.226	0.039	14.72
4712	0.199	0.271	-0.072	36.18
4898	0.262	0.242	0.02	7.63
5162	0.205	0.237	-0.032	15.61
5114	0.187	0.166	0.021	11.23
4864	0.27	0.276	-0.006	2.22
5030	0.26	0.249	0.011	4.23
4955	0.244	0.225	0.019	7.79
5108	0.234	0.245	-0.011	4.70
5045	0.256	0.223	0.033	12.89
		Average	0.0264	11.72

APPENDIX 12 POROSITY VALUES, CORE VS CALCULATED FOR WELL 42/25D-3

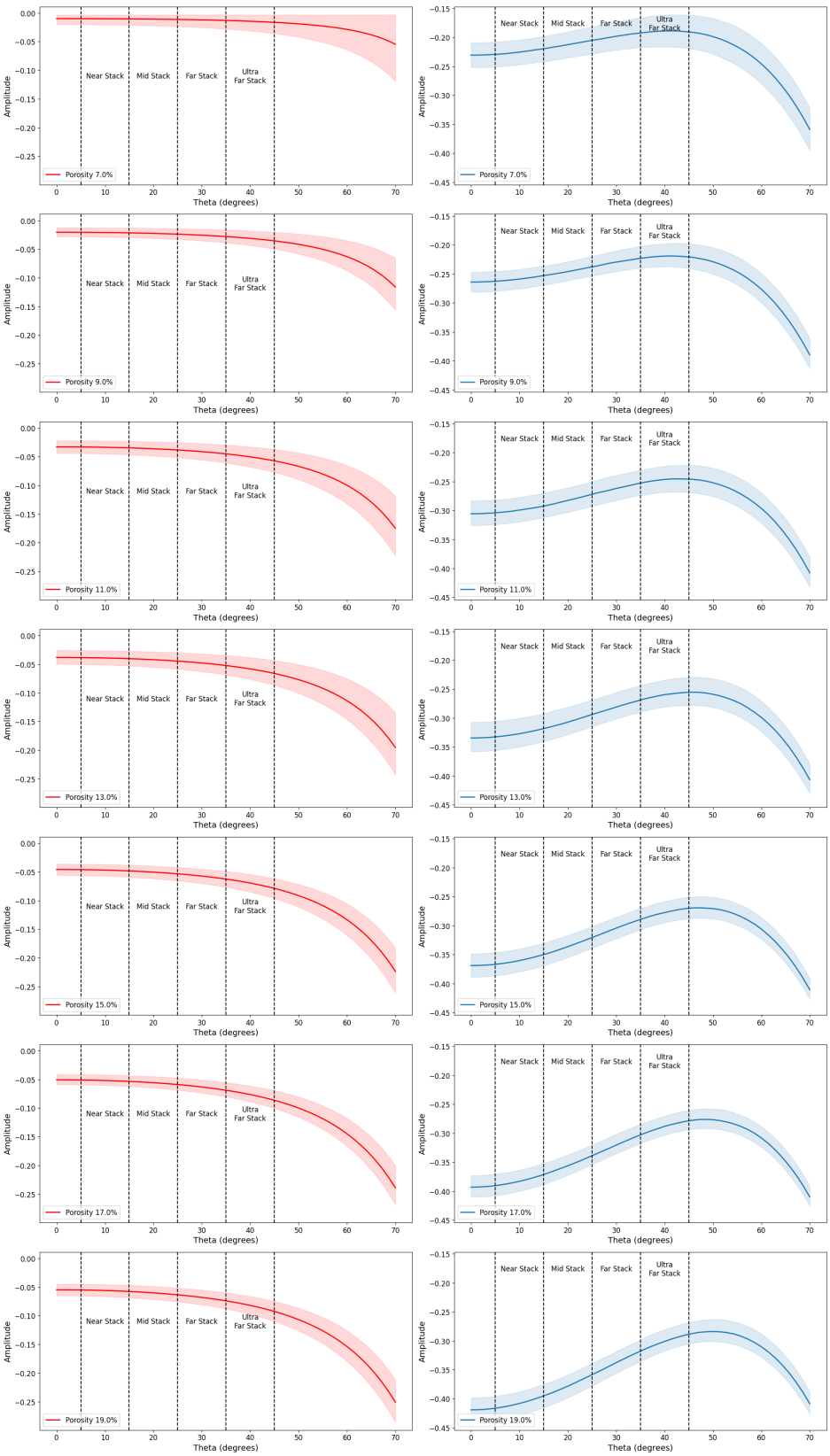

APPENDIX 13 ROTLIEGEND AMPLITUDE VERSUS OFFSET FOR CARBON DIOXIDE FLUID SUBSTITUTION. RED IS RESERVOIR – RESERVOIR CONTACT, BLUE IS SEAL – RESERVOIR CONTACT

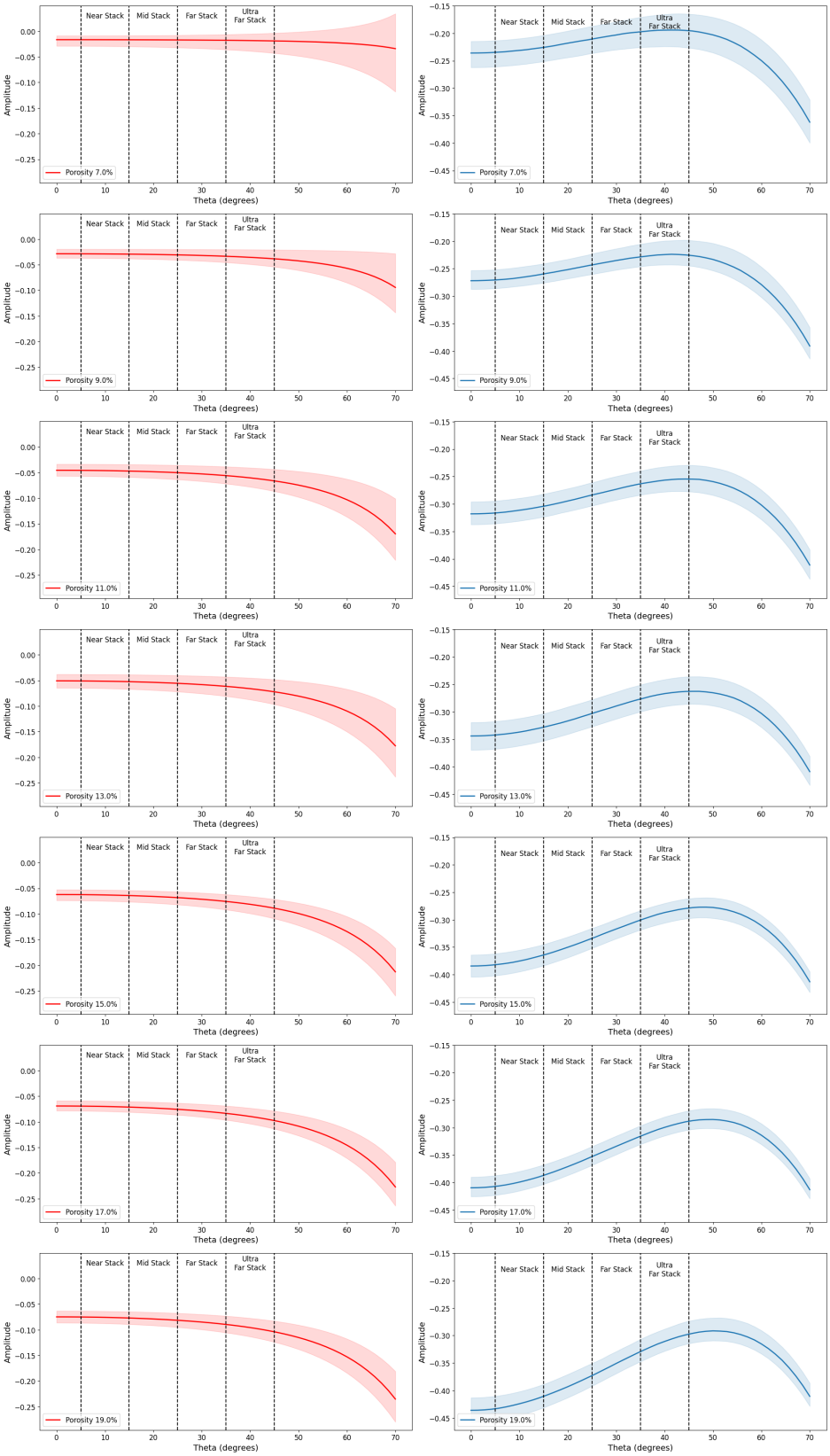

APPENDIX 14 ROTLIEGEND AMPLITUDE VERSUS OFFSET FOR HYDROGEN FLUID SUBSTITUTION. RED IS RESERVOIR – RESERVOIR CONTACT, BLUE IS SEAL – RESERVOIR CONTACT

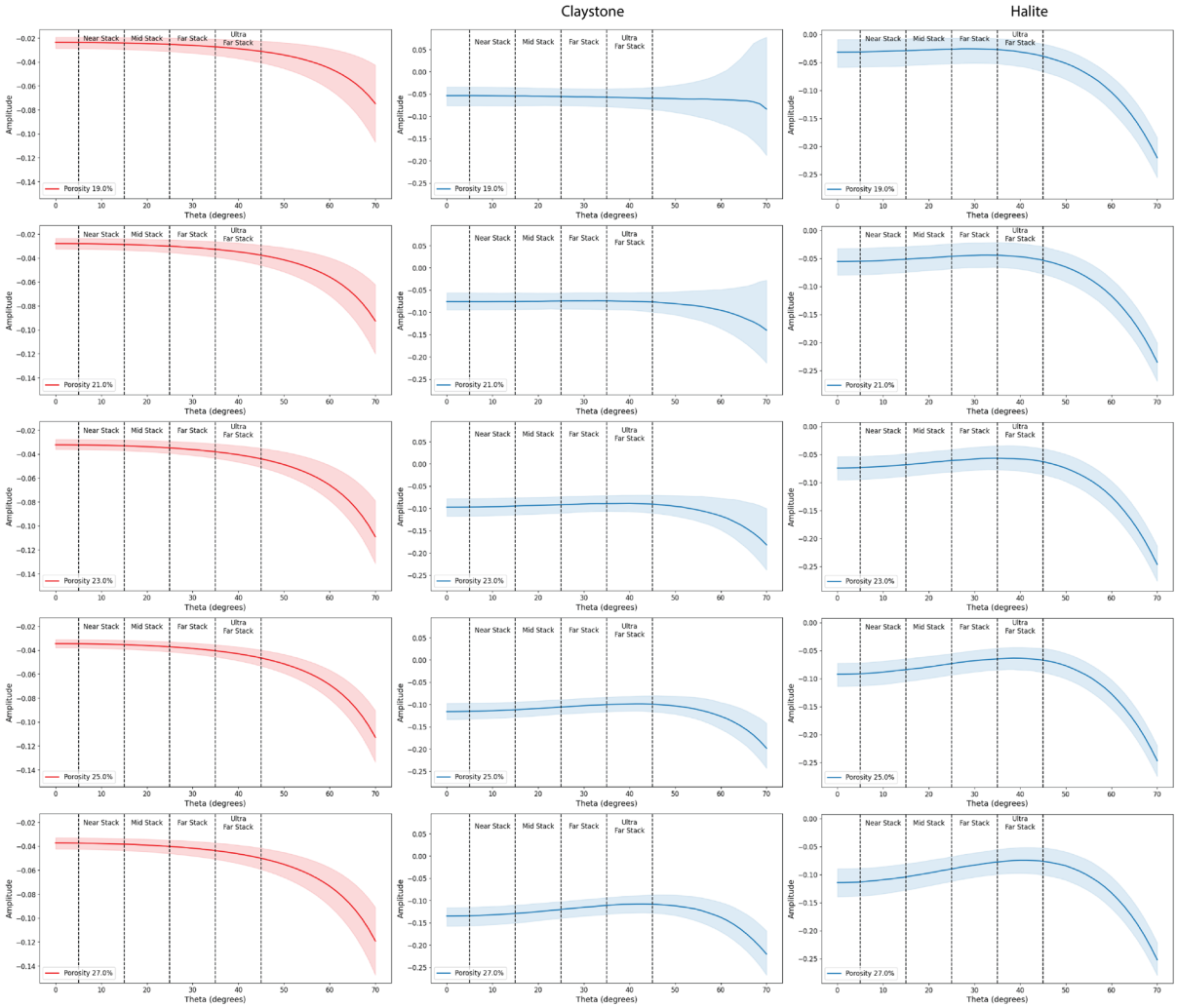

APPENDIX 15 BUNTER AMPLITUDE VERSUS OFFSET FOR CARBON DIOXIDE FLUID SUBSTITUTION. RED IS RESERVOIR – RESERVOIR CONTACT, BLUE IS SEAL – RESERVOIR CONTACT, CLAYSTONE AND HALITE CAPROCKS LABELLED

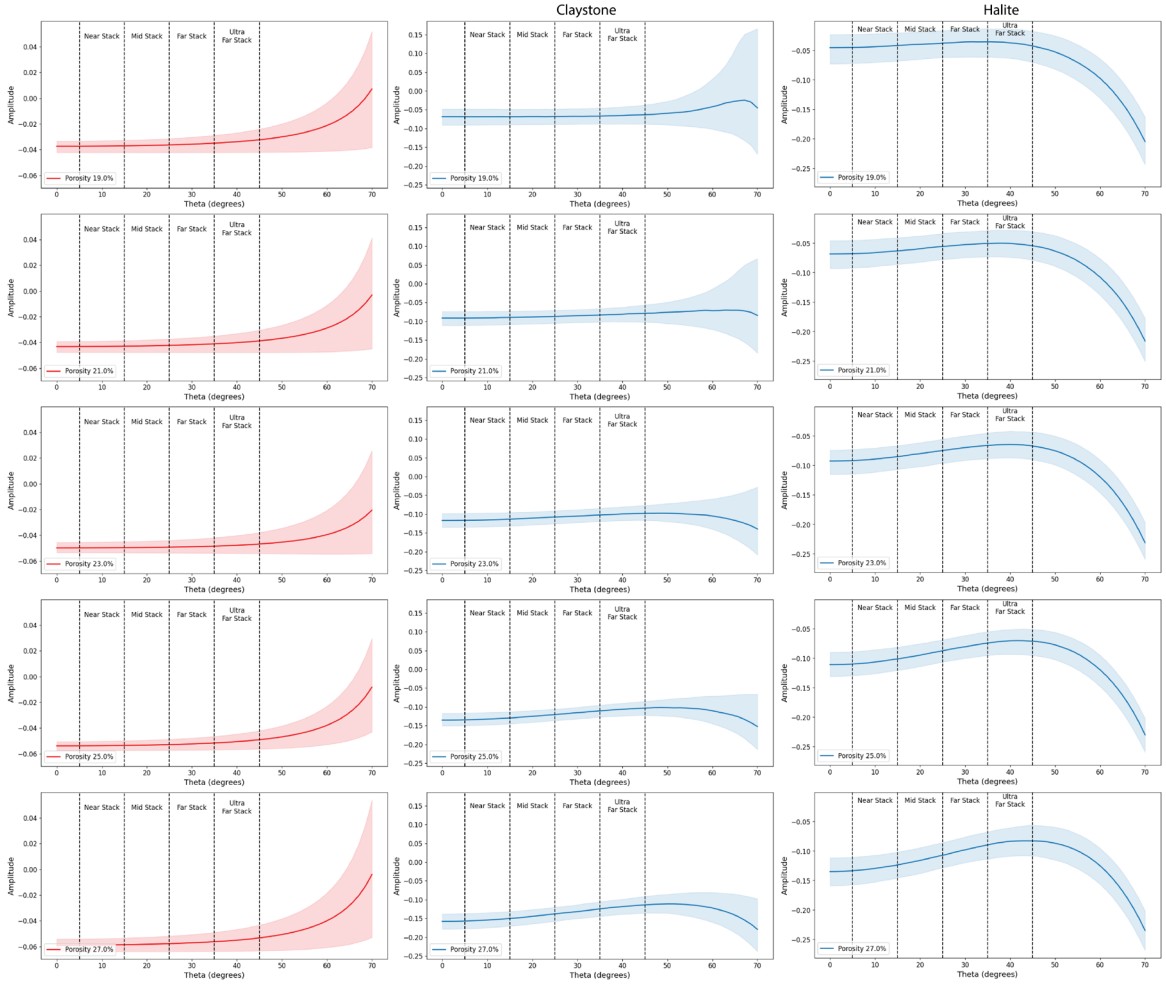

APPENDIX 16 BUNTER AMPLITUDE VERSUS OFFSET FOR HYDROGEN FLUID SUBSTITUTION. RED IS RESERVOIR – RESERVOIR CONTACT, BLUE IS SEAL – RESERVOIR CONTACT, CLAYSTONE AND HALITE CAPROCKS LABELLED

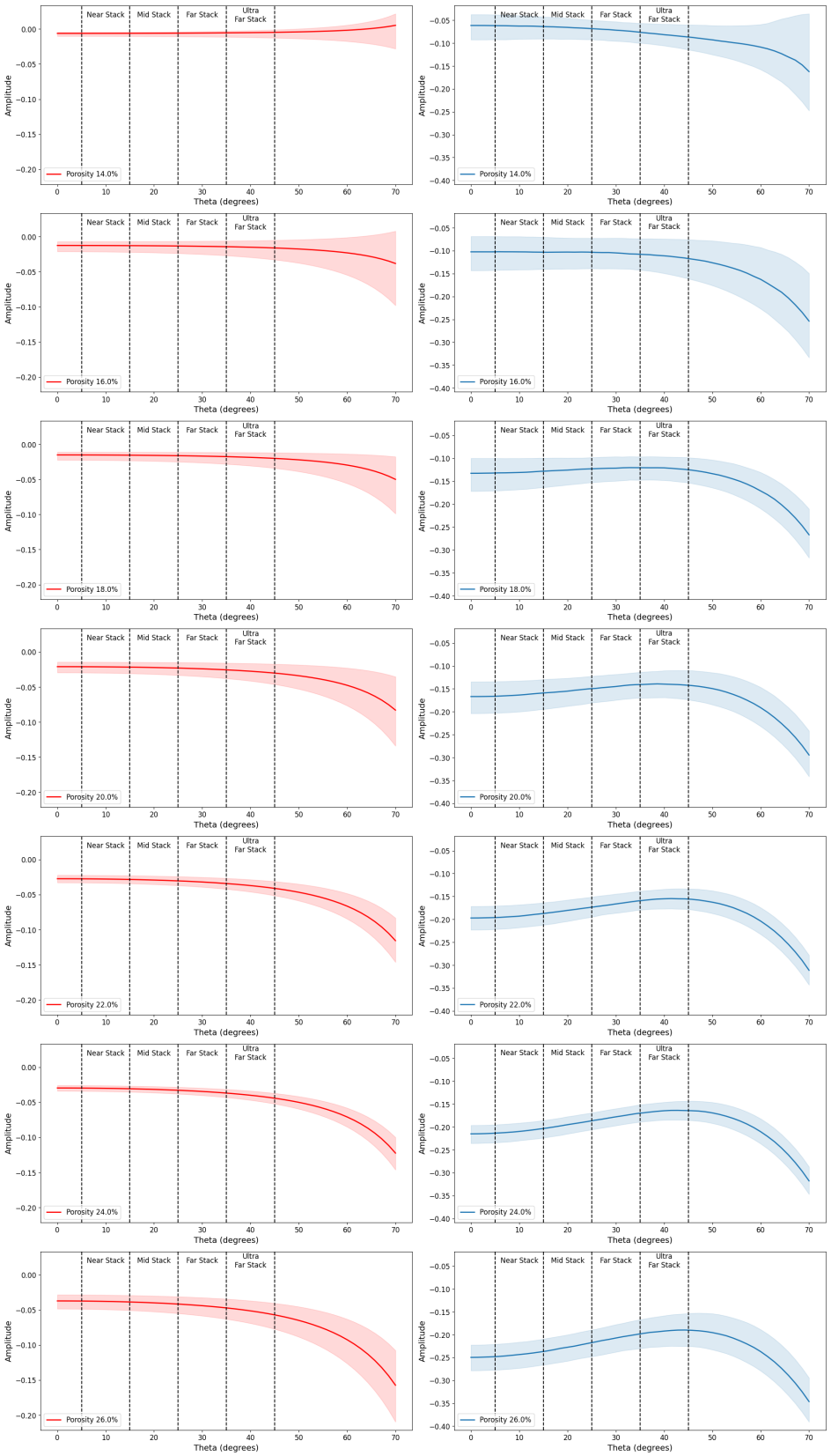

APPENDIX 17 ORMSKIRK AMPLITUDE VERSUS OFFSET FOR CARBON DIOXIDE FLUID SUBSTITUTION. RED IS RESERVOIR – RESERVOIR CONTACT, BLUE IS SEAL – RESERVOIR CONTACT

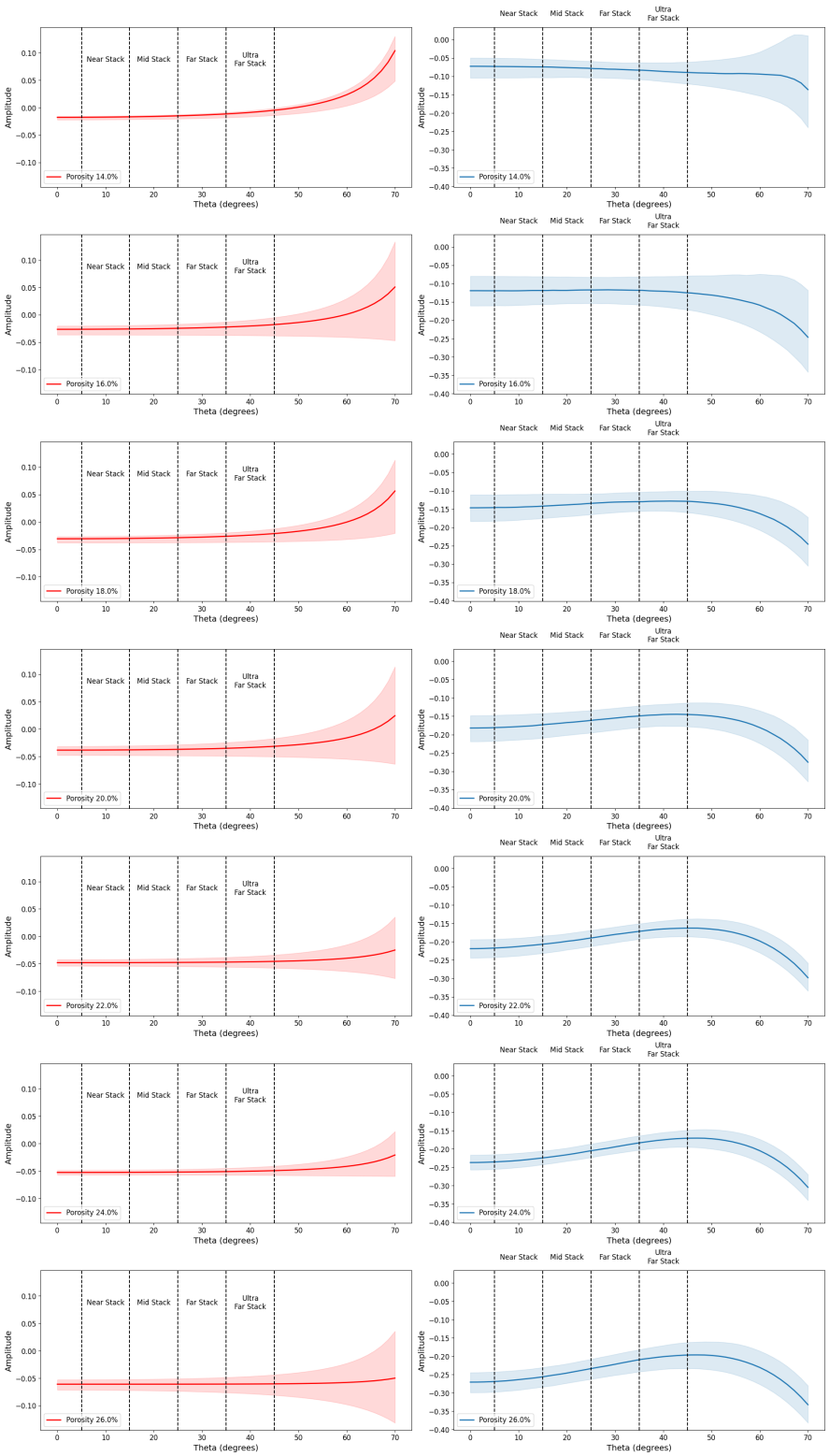

APPENDIX 18 ROTLIEGEND AMPLITUDE VERSUS OFFSET FOR HYDROGEN FLUID SUBSTITUTION. RED IS RESERVOIR – RESERVOIR CONTACT, BLUE IS SEAL – RESERVOIR CONTACT

Symbol	Quantity
σ'	Effective pressure
ph	Hydrostatic pressure
ρ	Density
g	Gravity
$\nabla\sigma v$	Overburden pressure gradient
σv	Overburden pressure
Z	Depth
T	Temperature
∇T	Geothermal Gradient
v	Velocity
K	Bulk Modulus
G	Shear Modulus
Vp	Compressional Velocity
Vs	Shear Velocity
Kfl	Bulk Modulus of fluid mixture
S_w	Water Saturation
K_w	Bulk Modolous of Water
K_{fn}	Bulk modulous of input fluid
ρ_{fn}	Bulk density of input fluid
Φ	Porosity
ρ_{bulk}	

$\boldsymbol{\rho_{new}}$	Bulk density of fluid substituted rock
$\boldsymbol{\rho_{matrix}}$	Bulk density of rock matrix
K*	Dry frame bulk modulus
$\boldsymbol{K_{new}}$	Bulk modulus of fluid substituted rock
$\boldsymbol{K_o}$	mineral matrix modulus
F	Volumetric fraction
$\mathbf{K_1}$	Bulk modulus of system component

APPENDIX 19 TABLE OF TERMS AND ABBREVIATIONS USED WITHIN CHAPTER 5